Pushing the Limits for Directly Cooled Molecules

by

David L. Reens

S.B., Massachusetts Institute of Technology, 2011

M.S., University of Colorado, 2014

A thesis submitted to the

Faculty of the Graduate School of the

University of Colorado in partial fulfillment

of the requirements for the degree of

Doctor of Philosophy

Department of Physics

2019

This thesis entitled:
Pushing the Limits for Directly Cooled Molecules
written by David L. Reens
has been approved for the Department of Physics

—————————————————————————

Prof. Adj. Jun Ye

—————————————————————————

Prof. Eric Cornell

Date —————————————————

The final copy of this thesis has been examined by the signatories, and we find that both the content and the form meet acceptable presentation standards of scholarly work in the above mentioned discipline.

Reens, David L. (Ph.D., Molecular Physics)

Pushing the Limits for Directly Cooled Molecules

Thesis directed by Prof. Adj. Jun Ye

The subfield of cold and ultracold molecules is growing increasingly mature, with exciting results from laser cooled species, from precision measurement experiments, and from atomic dipolar competitors. These exciting developments have placed an appropriately stimulating pressure on direct cooling experiments to hurry along and deliver on long expected promises of high number densities and in-trap collisional effects. Towards this end, this thesis reports on several fundamental improvements in the key techniques employed. The first plugged magnetic traps for cold dipolar molecules are presented. Deceleration is modified to enable unprecedented improvement in the transverse trapping capability of the devices. Beam skimming is also made more effective, trap loading more efficient, and designs are initiated which will allow hold times of unprecedented length.

Acknowledgements

First and foremost I acknowledge my lovely wife. Abby, you have an incredible love and appreciation for the simple things in life- diligence, routine, and data collection! Without you as a life partner, I am certain I would have traded in the PhD life for a flashy but fleeting trendy job ages ago. I'm so glad we've stuck it out together. It's been a worthwhile struggle, and we're coming out stronger in so many ways. Kudos for finishing first.

I am also very grateful to my family for their support and encouragement of me as a scientist. I owe much of my self-confidence as a researcher to my mother's limitless confidence in my capabilities. During our shared high school experience thanks to her role as math teacher, her joyful celebration of my accomplishments shaped my goals and my future.

Contents

Chapter

Tables

Table

Figures

Figure

Chapter 1

Introduction

In the beginning, God created hydroxyl radicals, and it was good. God used a complex expansion and condensation process beginning with higher energy forms of matter such as quark gluon plasma that thankfully are no longer relevant to anything, except certain other PhD theses. Later on, God created atomic physicists, who neither know anything nor are aware of this. Fortunately, through centuries of "serendipitous" discovery and other unscrupulous tactics, God managed to orchestrate that this same group of physicists would continue to make dramatic advances relevant to life, the universe, and the obtaining of PhD's, right up to the present day.

1.1   Atomic Physics

Atomic physics is a very exciting branch of physics, concerned with atoms or molecules as a whole and not their subatomic constituents, and especially the interaction of atoms with one another and with light. Some of the core questions of the field have in some sense been solved for quite some time, such as the nature of an atom and all the finest details of the energy levels of atoms and molecules. In other areas, the field has greatly matured only much more recently, such as in the ability to cool an ensemble of atoms into a regime where not only their internal degrees of freedom are quantized, but their external motional degrees of freedom as well, thereby enabling the realization of Bose-Einstein Condensation [1, 2]. Another even more recent example of the development of the field can be found in the detection of gravitational waves [3], more specifically the interferometer used for this purpose. This device relies on coherent and high power laser sources and

the finest understanding and management of the interaction between light and materials, especially optical coatings, and even the quantum mechanical manipulation of quadratures to reduce noise sources by spin-squeezing.

A significant contingent within atomic physics has in recent years moved in the direction of quantum information science, especially with regard to the trapped ion modality of quantum computing, where two or several states within a trapped ion serve as a quantum bit of information [4, 5]. While still only boasting rather modest near-term gains, such as the noisy, intermediate-scale quantum (NISQ) regime [6], this qubit modality at least provides some unique opportunities for atomic physicsts to compete with Josephson junctions and other modalities more the purview of condensed matter physics. Keeping a focus on scientific rather than technological aspects, quantum information science affords unique opportunities for application to scientific computing, and early quantum computation demonstrations have focused on analog quantum simulations of real scientific phenomena [7, 8].

Lastly I'll mention precision measurement, an amusing avenue of advancement whereby atomic physicists leverage our measurement accuracy to learn something completely fundamental by understanding something simple to death and beyond. This branch of atomic physics has been around since the beginning and is in some sense a natural evolution out of the spectroscopic beginnings of the discipline [9]. Some of the highlights include the electron magnetic moment [10], providing a part per trillion comparison between standard model quantum field theory and experiment, and the measurement of time itself, which has seen incredible advances in the modern era [11].

1.2   Molecules

Against this brief smattering of more modern directions of atomic physics, I am now pleased to delve with more focus into the molecular subfield of atomic physics. Molecules boast a number of exciting realized and hypothetical contributions, across all of the major focus areas of atomic physics [12]. The recurring theme is that their rotational and vibrational degrees of freedom intro-

duce new features that are both challenging to control and very useful if controlled. For example, in trapped ion quantum computing, the most realistic pathways to scalability demonstrated thus far involve the performing of 2-qubit gates via the mechanical motion of the trapped ions. Though advantageous as far as scalability is concerned since such manipulations can be achieved with conventional electronics, many challenges including heating issues, fidelities, and gate times exist [13]. Molecular trapped ions offer new opportunities for circumventing the need for motional manipulation, such as dipole-dipole couplings for gates [14].

In the study of quantum gases, manipulation of interactions between atoms have long enabled studies of pairing and BEC-BCS crossover [15]. Nevertheless, availability of a quantum gas with constituent particles themselves possessing anisotropic interactions has long attracted great interest in the field. Great strides have already been made in this direction, especially with magnetic atoms with unusually strong magnetic dipole moments such as Erbium and Dysprosium. These are already cutting into the territory once hoped for by molecular cooling enthusiasts with the startling discoveries of self-bound quantum droplets [16] and liquid-He reminiscent roton modes [17]. Still, it could be argued that these unexpected results connected to the dipolar character of the underlying particle only confirm the validity of the quest for quantum degenerate systems of an ever widened pool of candidate particles.

With regard to precision measurement, molecules offer a number of exciting possibilities, perhaps most notably with respect to measurements of the electric dipole moment of the electron, recently measured to zero within $10^{-28}e$ cm [18] and $10^{-29}e$ cm[19]. These results are fundamentally enabled by the internal electric fields present inside molecules. Additional possibilities include extending such studies to polyatomics [20], studying time variations [21], or studying nuclear effects [22].

1.3   Molecular Cooling

Several strategies exist for getting molecules cold, which is the primary challenge associated with their further usefulness to atomic physics. Firstly there is the possibility of using already

ultracold alkali molecules, associating them together loosely via scattering resonance techniques, but then utilizing precise spectroscopy of high-lying molecular states to coherently transfer them to ground states. A nice survey of these techniques is available here [23, Sec. 1.3], and exciting recent work with polar potassium rubidium molecules produced in this manner is being performed right here in the Ye group [24].

1.3.1   Laser Cooling

A different approach is to instead select a molecule with some favorability for traditional laser cooling techniques. First proposed in titanium monoxide by Benjamin Stuhl during his dissertation work on this experiment [25], and later realized with yttrium monoxide [26], more advanced magneto-optical trapping schemes exist which are amenable for use with molecules. Since then, numerous molecules have been successfully slowed and trapped, including strontium fluoride [27] and calcium fluoride [28], with the latter even loaded into optical tweezer arrays. Recently, it has been exciting to observe the application of various advanced techniques to these molecules for rapid further progress in cooling, such as lambda-enhanced gray molasses [29] and blue-detuned magneto optical trapping [30]. These advances have been particularly satisfying for the community given the long time spent waiting for these groups to master the molecule slowing process in order to load magneto optical traps, something which all groups involved spent something like four years achieving. So far no group has brought these laser cool-able species below about 5 μK, although the yttrium oxide has prospects for doing so via narrow-line cooling [31].

Another related but distinct technique that could in principle apply to a much broader class of molecules but still relies on lasers is sawtooth-wave adiabatic passage (SWAP) cooling [32]. Somewhat controversial in its reliance on stimulated emission and the opaque role of spontaneous emission in the process, SWAP cooling is nevertheless a valid technique which may be useful for some species. For a time, the YO experiment considered its implementation, or a modification using triangular waves, but this may have been superseded by opportunities with the techniques described above.

1.3.2   Direct Cooling

Although sometimes used to refer to any technique other than the association of ultracold molecules, I will use the term "Direct Cooling" to refer to those cooling techniques which do not rely on lasers to transfer entropy, but instead make use of conventional and more broadly applicable collision-based cooling mechanisms. Two primary directions in this regard are the supersonic expansion [33] and the cryogenic buffer gas beam [34]. Although both rely on thermalization by collisions between noble gas buffer atoms and the species of interest, their principles of operation and the characteristics of the molecules they generate are quite different. The supersonic expansion technique is ideal for generating a high phase space density with a large lab frame velocity offset, and the cooling happens all in one shot right from room temperature thanks to an expansive flow process described further in Sec. 2.1. The cryogenic buffer gas beam generates molecules with greater breadth in velocity space but a much lower initial kinetic energy [34, Fig. 1]. These properties make the cryogenic buffer gas beam ideal for experiments with good prospects for further phase space compression by laser cooling, but with difficulty in performing slowing, exactly the case for the laser cool-able diatomics. In contrast, the supersonic expansion is ideal for experiments with no clear path to higher phase space densities, but robust options for removing lab frame velocity in a phase-stable manner, i.e. Stark or Zeeman deceleration. These techniques, though general compared to laser based methods, require a careful understanding of the molecule of interest, for which purpose we now transition into more directly practicable background information.

1.4   The OH Molecular Hamiltonian

All of our ability to successfully exploit and manipulate OH radicals is underpinned by a robust understanding of its internal structure undergirded by decades of careful spectroscopy. Early spectroscopic results are still directly useful in determining where to set detection lasers [35], although many of these parameters are now more usefully catalogued in the NIST webbook [36]. As in many areas of modern quantum physics, careful understanding begins with classical Hamiltonians

followed by quantization and then a perturbative approach to better and better models of the system.

A well trodden pedagogical progression exists for the problem of the Hydrogen atom. One begins with classical descriptions of electrons orbiting a hydrogen nucleus, moves to semiclassical angular momentum quantization, and finally on to the exact Hydrogen quantum mechanical wavefunction solution [37, Sec. 4.2]. A similar progression exists for Molecules, and begins with the simplified quantum mechanics of rigid rotors and springs. The former end up applying well to the rotational degrees of freedom of the molecules, and the latter to their vibrational degrees of freedom.

1.4.1   The Rigid Rotor

For the rigid rotor, we imagine some extended rigid body with moment of inertia I_z about its center of mass in a particular direction z, which may be calculated in the usual way:

$$I_z = \int\limits_V \rho r^2 dA dz, \tag{1.1}$$

where the integral covers the whole volume of the body with density ρ, and r gives the distance from the infinitesimal volume element to the axis parallel to z through the center of mass of the body. Classically, lacking any environmental coupling, this body may indefinitely rotate about its axis of rotation with any angular velocity ω, and posses a rotational kinetic energy given by:

$$U = \frac{1}{2} I_z \omega^2, \tag{1.2}$$

and an angular momentum given by:

$$L = I_z \omega \tag{1.3}$$

We can extend into the quantum domain following Bohr's loose quantization rule and requiring the angular momentum to be quantized in units of $\hbar$:

$$L = l\hbar = I_z \omega, \tag{1.4}$$

with l an integer, so that the allowed values of the angular velocity and energy become:

$$\omega = l\hbar/I, \qquad U = \frac{1}{2I}l^2\hbar^2 \tag{1.5}$$

with the natural consequence that for larger inertia I, the spectrum of allowed rotations becomes increasingly continuous. This turns out to differ only slightly from the true situation, at least as it pertains to the specific case of linear rotors and diatomic molecules, where we find:

$$U = \frac{1}{2I}(l^2 + l)\hbar^2. \tag{1.6}$$

It is instructive to follow this through more thoroughly [38, Sec. 2.8]. For the case of a linear rotor, where the body's mass is essentially confined to a single axis in space, a single momentum of inertia I characterizes the system, and for the even simpler case where the mass is located at only two points separated by R, we can evaluate Eq. 1.1 but with the following density distribution:

$$\rho(r) = m_1\,\delta\left(r - R\frac{m_2}{m_1 + m_2}\right) + m_2\,\delta\left(r + R\frac{m_1}{m_1 + m_2}\right), \tag{1.7}$$

where m_1 and m_2 are the two masses separated by a distance R, and the values in the delta functions create the situation where the radial coordinate r attains its zero value at the center of mass of the distribution. Evaluating Eq. 1.1 then leads to the result:

$$I = \frac{m_1m_2^2 + m_2m_1^2}{(m_1 + m_2)^2}R^2 = \frac{m_1m_2}{m_1 + m_2}R^2 = \mu R^2, \tag{1.8}$$

where μ is the reduced mass of the system. Now the Hamiltonian for this system is simply the rotational energy:

$$\hat{H} = \frac{1}{2\mu}\nabla^2 \tag{1.9}$$

which upon moving ahead with the Schrödinger Equation, gives the spherical harmonic eigenfunctions:

$$\hat{H}Y_{lm}(\theta, \phi) = E_l Y_{lm}(\theta, \phi), \qquad E_l = Bl(l + 1), \qquad B = \frac{\hbar^2}{2I}. \tag{1.10}$$

Here B is referred to as the rotational constant, and θ, ϕ give physicist spherical coordinates relative to an axis orthogonal to the axis of the linear rotor, i.e. an axis along which the system has angular

Table 1.1: Parameters leading to the value of the rotational constant B are shown, together with its semi-classically inferred value. Spectroscopically determined values agree quite well. Radii and spectroscopically determined rotational constants from [36], except RbCs from [39] and YbCs from [40].

Molecule	μ (amu)	R (Å)	B_{semi} (GHz)	B (GHz)
H_2	0.5	0.74	1850	1820
OH	0.94	0.97	573	567
LiH	0.88	1.60	227	225
YO	13.6	1.79	11.6	11.6
CaF	12.9	1.97	10.1	10.1
SrF	15.6	2.08	7.52	7.51
YbF	17.1	2.02	7.24	7.22
RbCs	51.9	4.4	0.503	0.497
YbCs	75.2	5.4	0.230	0.207

momentum I, **not** the axis of the rotor itself. It is interesting to ask what the wave-functions associated with these eigenvalues are, in terms of their spatial probability distribution. In the case of $l = 0$, quantum mechanically the molecule is in a spherically symmetric state with equal probability of finding a nuclei anywhere on the surface of its own spherical shell, with a radius corresponding to the distance of that nuclei from the center of mass. This is a satisfyingly bizarre quantum mechanical state of affairs, especially given that relative to the quantum mechanics of the light electron, these coordinates describe the locations of heavy atomic nuclei.

It is interesting to compare the values of B calculated naïvely from Eqs. 1.10, 1.8 to the spectroscopically determined values, as shown in Tab. 1.1. Very good agreement is obtained, at least when using the spectroscopically determined internuclear distance, which is therefore not quite fair as far as theory experiment predictions are concerned. Nonetheless, it is reasonable to conclude that the rigid linear rotor model is a good description of the situation for diatomic molecules. The bulk of the remaining deviations relate to centrifugal effects, by which I broadly refer to the interaction between the rotational and the vibrational components of the Hamiltonian, a nice segue into the following section.

1.4.2 The Vibrational Hamiltonian

In much the same way as the canonical simple harmonic oscillator problem in quantum mechanics, at its core the vibrational Hamiltonian may be represented as a harmonic potential describing the energetics of the internuclear distance of the molecule. This potential may be specified beginning with the full Hamiltonian describing all of the electrons and nuclei in a molecule, and then separating the electronic and nuclear portions based on a hierarchy of timescales known as the Born-Oppenheimer approximation [41, Sec. 8.1]. Essentially, the nuclear positions are taken as parameters to the computation of the electronic wave functions, and so by parametrically solving the electronic Hamiltonian for all nuclear distances and rotations, the energetic landscape governing the dynamics of the nuclei emerges. It is therefore somewhat difficult to directly specify the form of the interatomic potential experienced by the nuclei, but the results from this procedure turn out to be closely represented by the Morse potential:

$$V(x) = D \left(1 - e^{-\beta x} \right)^2. \tag{1.11}$$

This potential has a minimum at $x = 0$, defined to be the equilibrium distance, often R_e, of the vibrational oscillation. Below $x = -R_e$, this coordinate is unphysical, at which point the potential is still finite, but usually quite large relative to the relevant energetics. It tends to D the dissociation energy as $x \to \infty$. For small x, expanding near zero gives a harmonic form as we would expect:

$$V(x) \approx D \left(1 - (1 - \beta x + \beta^2 x^2/2 - ...) \right)^2 \approx D\beta^2 x^2 - D\beta^3 x^3 \tag{1.12}$$

This potential is therefore an anharmonic oscillator, with a cubic anharmonicity that enhances restoring force in one direction but weakens it in the other. As far as energy level spacing is concerned, the weakening direction has the dominating effect, tending to reduce the energy level spacing at higher energies. Another important property of the Morse oscillator is that only a finite number of levels are supported, which is also the case for true molecular potentials, unlike electronic energy levels, for which the so-called Rydberg series of their energy levels is countably infinite.

The Morse oscillator is a close enough match to true molecular potentials, that the results

Table 1.2: Spectroscopically determined vibrational constants are shown for several molecules of interest [36].

Molecule	μ (amu)	R_e (Å)	w_e (THz)	$w_e x_e$ (GHz)
H_2	0.5	0.74	132	3640
FH	0.95	0.92	124	2700
OH	0.94	0.97	112	2550
N_2	7	1.10	70.8	427
LiH	0.88	1.60	42.2	696
YO	13.6	1.79	25.8	87.0
CaF	12.9	1.97	17.4	82.2
SrF	15.6	2.08	15.1	66.0
YbF	17.1	2.02	15.1	66.0
RbCs	51.9	4.4	1.48	-

of molecular spectroscopy are often expressed in terms of the coefficients that describe the Morse oscillator whose rovibrational energies best match the actual level spacings of the molecule. It is useful therefore to write down the rovibrational level spacings predicted by the Morse oscillator:

$$E(\nu, J)/hc = w_e(\nu + 1/2) - x_e w_e(\nu + 1/2)^2 \tag{1.13}$$

$$+ B_e J(J + 1) - D_e J^2(J + 1)^2 \tag{1.14}$$

$$- \alpha_e(\nu + 1/2)J(J + 1) \tag{1.15}$$

Here ν gives the vibrational quantum number and J the rotational quantum number. These energies come by using Eq. 1.11 in the rovibrational hamiltonian one can obtain by applying the Born-Oppenheimer approximation [38, Eq. 2.157] to the full molecular Hamiltonian. The value of each of the parameters w_e, x_e, B_e, D_e, and α_e may be written in terms of the β and D of Eq. 1.11, and the reduced mass μ and equilibrium nuclear distance R_e of the molecule, see [38, Eq. 2.183]. The value of the vibrational parameters w_e and $x_e w_e$ for a few molecules of interest are shown in Tab. 1.2.

1.5   Angular Momentum Coupling

By far the most significant challenge to understanding and working with molecules relates to their complex angular momentum coupling. The various sources of angular momentum in the molecule are often described using a hierarchy of successively weaker couplings which specifies the Hund's case of the molecule, or rather of one particular state of the molecule.

1.5.1   Revisiting J=L+S

Before diving in, we begin with the simplest angular momentum coupling example, but with an eye toward its generalization to the molecular situation. Electrons have orbital angular momentum and spin in the hydrogen atom, but a state of definite orbit and definite spin is not necessarily an eigenstate of the Hamiltonian, because of "coupling" that may exist between these states by the Hamiltonian governing the evolution of the system. Specifically, the orbit and the spin influence one another via the magnetic fields they generate, so that the Hamiltonian has a term proportional to their dot product. This classic problem may be resolved by defining true eigenstates of the Hamiltonian using a different quantum number which describes the total angular momentum of the system. We say that L is "weakly" coupled to S in the sense that the level shift caused by including or ignoring the coupling term is small compared to the effects of the L and S terms independently.

1.5.2   Coupling Many Spins

Every atomic nucleus or unpaired electron in the molecule may contribute angular momentum to the coupling story, either spin or orbital. The latter is known as orbital angular momentum when carried by electrons, and simply rotation when carried by nuclei. The coupling story is then addressed essentially by writing terms down in order of the magnitude of their leading coefficient in the full Hamiltonian. These terms can either be coupling terms or specific terms, and we are free to treat them in order, defining as appropriate a combined quantum number to include a given
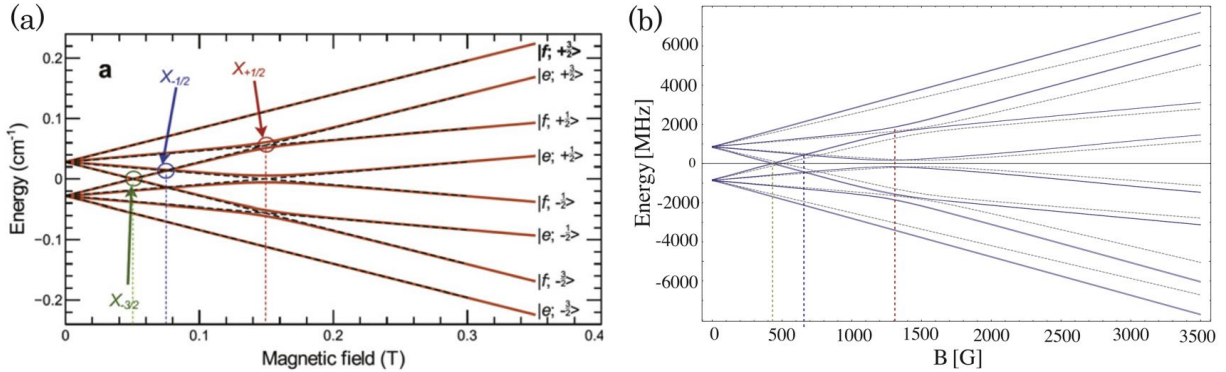
Figure 1.1: Inclusion of higher lying states of the OH Hamiltonian in [43] accounts for the mixed Hund's case and gives a significant 20% level correction to level crossings. A snippet from [44, Fig. 1] is shown in (a), and panel (b) has the results from [43].

coupling effect before moving on to higher order, lower energy coupling effects later on down the line. One way this is often indicated is to draw diagrams that indicate the magnitude of an effect by the length of a vector, and indicate the use of a coupled basis by the definition of a new vector which is the sum of the other two. The first two vectors may be considered valid possible instantaneous values of the angular momenta they represent were they measured, but only the final sum vector is actually conserved by the Hamiltonian. The ordering of these sources of angular and their coupling strengths generally follow one of a few set patterns which are known as Hund's cases. These are well enumerated and diagrammed in [42, Sec. 2.2.1-4].

1.6   Stark and Zeeman Effects

These effects may be well understood on their own, as described in [45, Sec. 2.3.1-2.1], but combining them can be a very challenging thing to do properly. During my thesis, it was discovered that use of the Hund's case (a) assumption, considered valid at least for the lowest rotational states of OH [23, Sec. 2.2], led to significant errors in the location of avoided crossings between states. Essentially, the magnetic moment of the molecule is not quite perfectly coupled to the internuclear axis, so that rotational averaging of the molecule's angular momentum from the molecule frame to

the lab frame does not reduce the magnetic moment from 2 μ_B to 1.2 μ_B as one would calculate for Hund's Case (a), but instead only to 1.4 μ_B. One way to describe this is to simply include more terms in the Hamiltonian used for computing the Stark and Zeeman effect of the molecule. This was done in [43], where direct reference was made to one of the figures in our earlier work [44], see [43, Fig. 12], reproduced here as well 1.1. We had in fact discovered the correction much earlier in 2013, but did not have a good way to publish our findings on their own. For future work, wherever it counts, the full Hamiltonian has been implemented in Matlab and is available for future use in the experiment.

Chapter 2

Creation

Like all things, Jun Ye's hydroxyl radical experiment also begins with creation; specifically, the creation of hydroxyl radicals via discharge during pulsed supersonic expansion. Such a supersonic expansion occurs when gas at pressure is allowed to escape into vacuum via a small orifice. No better resource on the supersonic expansion or free jet seems to exist besides [33], although a more modern compendium of results does also exist [46]. I will begin with supersonic expansions and the thermodynamics thereof, before moving to the implications for our work and some specific valve technologies.

2.1   Supersonic Expansion

Suppose that an ideal gas is trapped in a certain volume V_1 and at a certain pressure P_1, when one of the walls enclosing the volume is suddenly removed, and the gas is allowed to expand into a much larger volume V_2. To determine the long term properties of the system, one can use the fact that neither heat nor work were transferred out of the gas, so that its energy E must remain fixed, and therefore also its temperature, following the well-known intrinsic formula relating the temperature of an ideal gas to its internal energy, $E = C_V N T$. Here C_V denotes the specific heat of the gas at constant pressure, and N the number of particles present in the system. It would follow that $P_2 = P_1 \cdot V_1/V_2$, and that the entropy would be significantly increased. To determine by how much, we can use the thermodynamic relation for the internal energy E of the system:

$$dE = TdS - PdV, \tag{2.1}$$

which since $\Delta E = 0$ for this process since it transfers , leads us to:

$$\Delta S = \frac{1}{T} \int P dV = \frac{1}{T} \int\limits_{V_1}^{V_2} \frac{P_1 V_1}{V} dV = N k_B \log\left(\frac{V_2}{V_1}\right), \tag{2.2}$$

Since $P(V) = P_1 V_1 / V$ for fixed T and since $P_1 V_1 = N k_B T$. This is also intuitively valid, since the entropy ought to correspond to the logarithm of accessible micro-states. With nothing else changing about the momentum distribution before and after the event, only the system size contributes to an increase in accessible micro-states, by an amount given by the ratio of volumes before and after.

Although the foregoing example is ubiquitous in the problem sets assigned to physicists and mechanical engineers during thermodynamics classes, the corresponding short term behavior is rarely if ever treated. At first glance, it may seem that in the short term, i.e. times t after barrier removal smaller than that required for the reestablishment of a pressure equilibrium, the suddenness of the event and its obvious lack of reversibility would make it somewhat intractable to the methods of statistical physics. To the contrary, much progress can be made once some additional details and assumptions are specified. Suppose that the initial volume is allowed to expand into a much larger volume, but only through a rather small opening. Suppose further that the expansion process is in a flow equilibrium, so that gas is constantly supplied to the initial volume in order to maintain a constant pressure, and gas is constantly pumped out of the back of the much larger volume. This supposition includes what is known as the continuum hypothesis, which stipulates that the gas may be treated as a fluid of smoothly varying density on all scales, and essentially requires a short mean-free path and a suitably high local density [47, Sec. 1.2]. These assumptions create a very similar environment to the one realized in many molecular beam apparatuses, known as a supersonic expansion. Now consider a small sub-volume V_1 within the high pressure volume, close to the small opening. Since the speed of egress is fast compared to diffusion timescales, we may assume that this volume is isolated from the rest of the gas, and consider its fate as the molecules within follow the flow lines of the fluid. As we follow the flow lines, this volume expands, performing work on the surrounding environment, but not exchanging any heat with it. Paradoxically, the process is then adiabatic, despite the significant and non-zero ΔS calculated above for the long term behavior. The

Table 2.1: Final supersonic expansion velocities for various gases according to Eq. 2.4, using $T = 300°$K. For H_2 I have used the ideal gas heat capacity since rotations are hardly populated at room temperature. For UF_6, inclusion in this chart is largely fanciful in any case, but rovibrations are unlikely to be efficiently cooled so I have again used the ideal gas heat capacity.

Gas	Speed (m/s)
H_2	2490
^{3}He	2030
^{4}He	1760
Ne	790
Ar	560
Kr	380
Xe	310
UF_6	190

work done during expansion primarily serves to accelerate the volume just ahead along the flow, and the magnitude of the acceleration is such that sound waves are significantly outpaced [33, 42], hence the "supersonic" in the expansion.

As the gas expands, it continues to work on the environment until it has exchanged all of its internal energy, in principle reaching $T = 0$ and satisfying Bernoulli's flow equation by converting its initial enthalpy entirely to kinetic energy:

$$H_i = C_P N k_B T_i = \frac{N}{2} m v_f^2. \tag{2.3}$$

For a monoatomic ideal gas, $C_P = 5/2$, and we have:

$$v_f = \sqrt{\frac{5 k_B T_i}{m}}. \tag{2.4}$$

The final velocities obtained from this equation for noble gas carriers are shown in Tab. 2.1. In practice, these speeds are not always obtained by the species of interest within a noble gas buffer, often due to velocity slippage in cases of significant mass imbalance between the carrier and the species of interest. Another source of discrepancy comes from excess heating, either due to the mechanism of operation of the valve [45, Sec. 3.1.3.1], or the mechanism of generating the species of interest, see Sec. 2.2.2 below.

Table 2.2: Final supersonic expansion temperatures for noble gas carriers in an Even-Lavie valve according to Ref. [49, Fig. 12], using $T = 300°$K.

Gas	Temp (°mK)
^{4}He	33
Ne	180
Ar	930
Kr	2400

As the gas rarifies, the continuum flow hypothesis breaks down, and the mean free path between collisions of molecules becomes long enough that the assumption of an isolated sub-volume of the flow becomes invalid. What this means is that below a certain pressure, the gas can no longer perform work on itself during expansion, and a limiting nonzero expansion temperature is reached. In practice, the remaining internal energy of the gas associated with this nonzero final temperature is not a significant perturbation on the final velocity of the beam, but it does influence the phase space density available for later use. The remaining internal energy of the gas manifests most measurably as an extra spread on the final velocity obtained during the expansion. Also known as the translational temperature, its direct calculation is possible but complex [48], but it is not overly difficult to measure, at least approximately, using a pulsed source and measuring at a near and distant point along the propagation of the pulsed expansion. When this is done with a miniaturized solenoidal Even-Lavie valve [49], the values shown in Tab. 2.2 are obtained for a selection of rare gases. Various factors can influence this, and often clustering effects can prevent utilization of the narrowest possible distributions for a seeded beam, see discussion in [45, Page 47].

2.1.1 Rovibrational Temperatures

An additional effect requiring careful accounting is the degree of thermalization of the particles in their frame of reference after the expansion. One piece of this is the degree of thermalization of the rotational and vibrational degrees of freedom of molecules seeded in the beam with the translational degrees of freedom. Generally it is found that these degrees of freedom do not thermalize as well as translation, with vibrations thermalizing much worse than rotations. Much attention has

been given to this subject, particularly given its very clear manifestation in an experimental observable, namely the relative population of the various rovibrational levels as probed by laser induced fluorescence or other state selective means. It has even been found that the rotational levels fail to be well described by any meaningful temperature, even towards the beginning of the expansion [50]. Studies specific to hydrides and even to the hydroxyl radical have been performed [51].

2.1.2   Translational Disequilibrium

Compared to rovibrational levels where nearly complete information is available, it is rather difficult to measure the translational temperature of the beam in the direction transverse (orthogonal) to the beam-line. Evidence exists for a disequilibrium between transverse and longitudinal frame of reference temperatures [52, 53, 33]. This is especially important for consideration of the effective initial size of the beam as seen by devices downstream. In the continuum flow region of a supersonic expansion, the fluid obeys a kind of hyperbolic flow pattern, which has the property that after a few nozzle diameters flow-lines actually appear to originate from a single point [33]. As the molecules leave the continuum regime and the cooling process halts at nonzero temperature, this breaks down, so that individual molecules no longer appear to originate from a single point.

A useful way to understand these phenomena is to work in transverse phase space, where the velocity of molecules in one of the directions transverse to the beam is plotted against their position in that same direction. If the cooling were to continue indefinitely and all molecules appeared to originate from a single point, the transverse phase space distribution function describing the ensemble at a fixed large time t after passing through the orifice would look something like:

$$d(x,v) = \delta(vt - x)e^{-(v^2/2\sigma_v^2)}, \tag{2.5}$$

where d is the phase space distribution function, and δ the Dirac delta function. The delta function term enforces the criterion that molecules originate at $x = 0$, since with velocity v they may only be found at $x = vt$. The additional gaussian term assumes some generic velocity spread with a standard deviation of σ_v. The nonzero final transverse temperature convolves extra spread in the
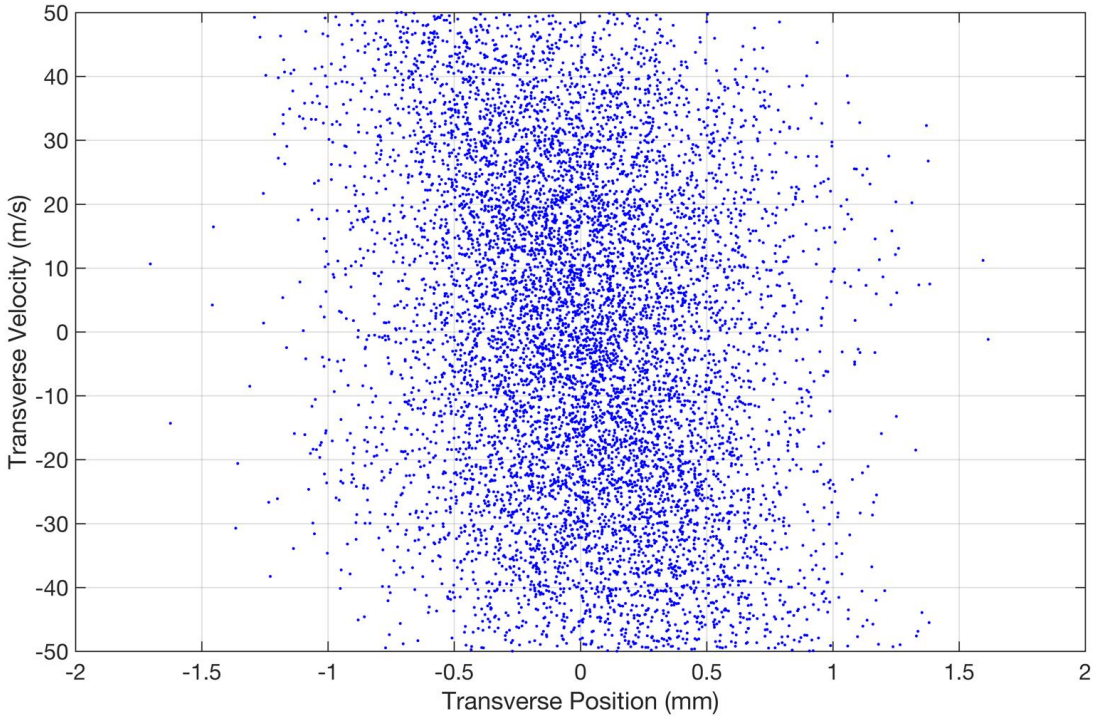
Figure 2.1: This scatter plot samples a distribution function designed to be reflective of that which may be generated in an Even-Lavie valve, see Sec. 2.2.1. The quitting surface, where continuum flow ceases, is assumed to lie 3 cm distant from the 500 μm nozzle, and a transverse temperature of 200 mK in both transverse and longitudinal directions is used.

velocity direction over this narrow distribution, which is relevant for the use of hexapole focusers as discussed in Chapter 4.

An example of transverse phase space generated by propagating molecules perfectly from a source point and then adding nonzero transverse temperature at a certain distance is shown in Fig. 2.1. The distance is chosen to be representative of the transition between continuum and molecular flow, which is often termed the quitting surface. This distance is referred to as the quitting surface in the literature [33]. In Fig. 2.1, the molecules are back-propagated after the extra temperature included at the quitting surface, so that the distribution shown can be thought of as an effective source distribution in the same plane as the actual nozzle. The distribution is quite

tall vertically, which is a reflection of the fact that the beam expands on the surface of a sphere, so that transverse velocities even approaching the forwards velocity magnitude of 810 m/s in this case should in principle be populated. In practice such large transverse velocities are unusable, since even with an arbitrarily powerful focusing device molecules with very large transverse velocities also have forwards velocities reduced relative to the better collimated portion of the beam. For this reason, I use an unphysical directed-ness parameter in generating distributions such as the one shown in Fig. 2.1, which has a FWHM polar angle of $\pi/12$, since the other molecules are not relevant for subsequent focusing and deceleration. Actual directed-ness of supersonic expansions tend to follow an angular distribution with polar angle θ according to $\cos^3(\theta)$ [33], and some claim increased directed-ness through the use of conical expansion regions [54, Fig. 11].

2.1.3   Experimental Transverse Temperature

It is possible to access some of this information experimentally by observing the angular distribution of a beam, especially downstream of some additional collimating aperture. We can adopt similar terminology to that used in optics, although no corollary exists here to the possibility of constructive and destructive interference. The point spread function gives the distribution in a detector plane after convolution with the distribution found in the aperture plane. Transverse temperature controls the width of this point spread function, causing a sharp edged aperture to cast a nonetheless blurry shadow in the detector plane. See Fig. 2.2 for an illustration of this. One way to measure this blurriness would be with an angle resolved, or adjustable position detector of some kind, but an easier alternative is to translate the distance between the source and aperture, thereby increasing and decreasing the size of the blurry spot in the detector plane.

We detected this effect during our work on skimmer cooling [55], where the skimmer, a device designed to collimate a beam with minimum interference described in Chapter 3, serves as the aperture. An important caveat is that any aperture has the potential to interfere with the beam, so that the blurriness observed could be an artifact caused by the aperture, and not a true representation of the original beam. Data from [55, Fig. 2c] are repeated here in Fig. 2.3 with
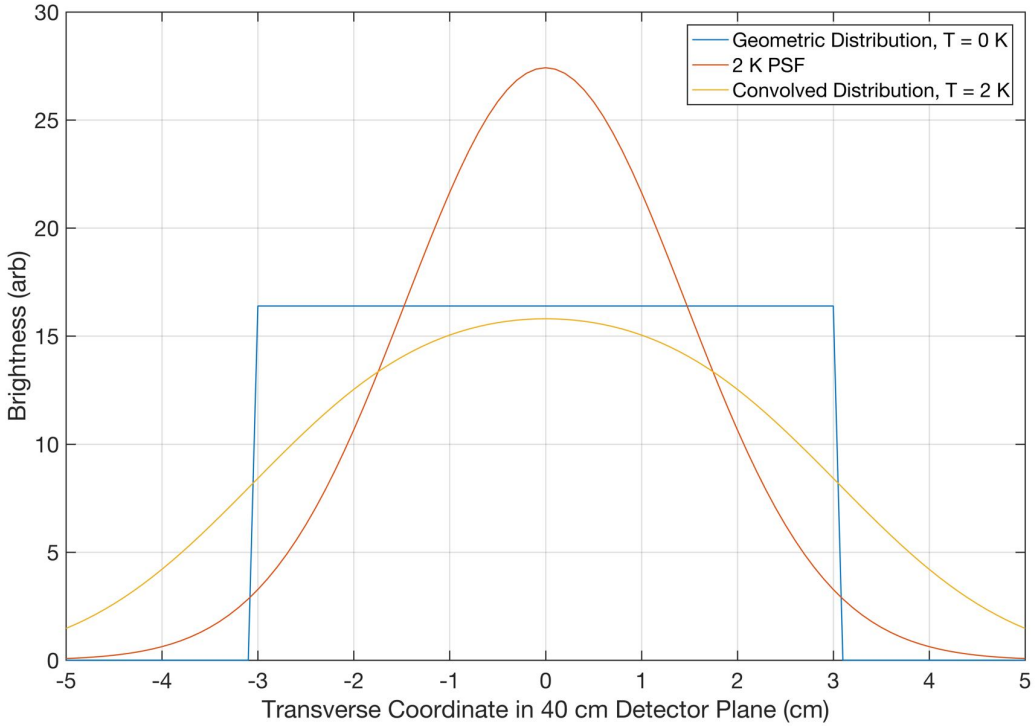
Figure 2.2: Transverse temperature lends a point spread function (PSF) to the image of apertures in the detector plane of a molecular beam. These distribution functions reflect a 20 cm distance between the source and the aperture, and a 3 mm aperture. This investigation was first performed in June 2018, and relevant files may be found in a code appendix I intend to add at some point.

an expanded discussion of these transverse effects that is not available in [55]. For a suitably small transverse temperature, we would expect that once the valve is close enough to the aperture that the detector area is fully illuminated by the beam, signal no longer increases as a function of reduced valve skimmer coordinate. This is at odds with the data shown in Fig. 2.3, where the signal is seen to increase even below a 3 cm valve-skimmer distance. At this valve-skimmer distance, considering the 3 mm skimmer opening and 40 cm detector distance, the zero temperature spot size of the beam would be a 4 cm diameter circle, well overlapping our fast ion gauge detector (6 mm x 18 mm). One way to make sense of this discrepancy is to introduce a bimodal transverse temperature distribution:

$$d(v) = \alpha e^{-v^2/2\sigma_c^2} + \beta e^{-v^2/2\sigma_h^2}, \tag{2.6}$$
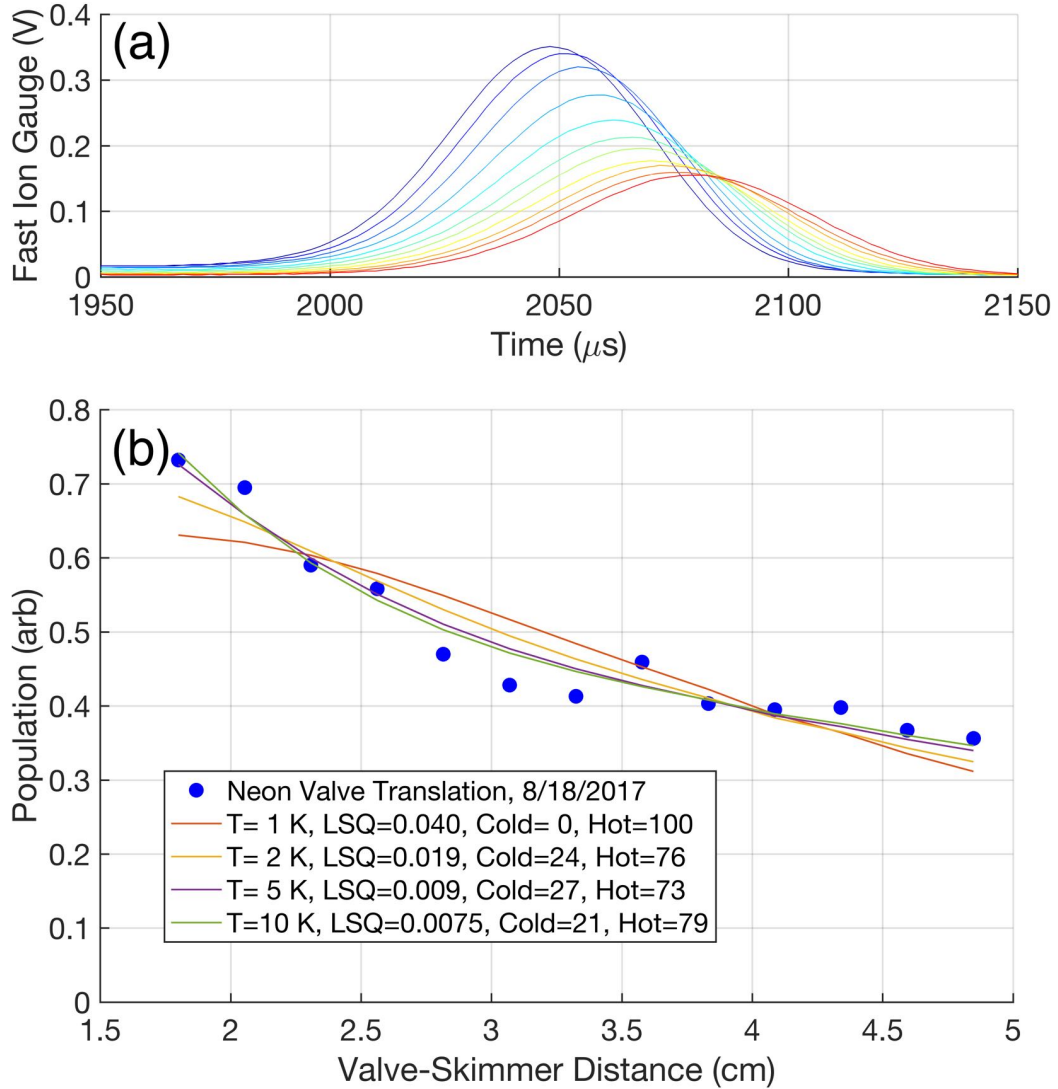
Figure 2.3: (a) Time of flight traces taken with varying distance between the valve and the aperture, with blue closest (1.8 cm) and red farthest (4.8 cm). The area under the curves are computed, leading to the data-points in the next panel. (b) Fit attempts allowing a variable fraction of the population in a second, warmer temperature distribution.

where d the distribution function consists of two normal distributions weighted by α and β, with widths σ_c and σ_h where the latter is hotter than the former and thus respecting $\sigma_c < \sigma_h$. This hypothesis has some scientific support and relates to the relatively hot collisions that can occur for molecules which do happen to collide well after the quitting surface [52, 33]. Varying the fraction assumed cold and the hot temperature, various fits are obtained as described in the legend

of Fig. 2.3b. The cold fraction is assumed to be at 200 mK, the measured longitudinal temperature, which well overlaps the detector at all valve-skimmer distances included here and essentially contributes only a baseline offset for the fitting. The warm fraction is assumed responsible for the upturn at closest distances, leading to the various fractions and temperatures shown in the legend. The temperatures required for obtaining any agreement with the experimentally observed upturn are not surprising. In [52, Abstract, 3rd Paragraph], effective transverse source size for the hot distribution are claimed to be $4 - 8$ times that of the cold distribution, implying a temperature larger by that factor squared. The fraction populating the hot distribution is much more surprising, with [52] reporting only $30 - 50\%$.

The primary alternative hypothesis is that the results obtained in Fig. 2.3 are not a pure reflection of the transverse properties of the supersonic expansion, but rather are the result of some degree of interference effects from the aperture itself. The surprising thing here would be that the interference effects actually lead to an increase in signal, whereas the usual result of interference is only the reduction of signal. It could be that this is a compound effect of some kind, for example that the close proximity of the valve may reduce interference with the aperture in a certain range. This could be caused by a favorable match between the angle of the conical skimmer faces and the position of the source, leading to a reduced cross section presented to the beam by the skimmer. Another possibility is that ions generated in the discharge, see Sec. 2.2.2, have a cleaning effect that enhances the performance of the cryogenic skimmer. This is not out of the question, as in-situ noble gas ion cleaning techniques are a legitimate surface preparation strategy [56].

2.2   Pulsed Valves

Pulsed valves solve what is otherwise a significant dilemma for a vacuum system, and enable significant improvements in brightness compared to their continuous analogs. The key challenge for a pulsed valve is to rapidly transition from leak-tight to fully formed, minimally impeded flow. Many strategies exist for achieving this, and many have been utilized right here in Jun's OH experiment. A current loop, solenoid, and drum-mode piezo valve have been used, well described

in [45, Sec. 3.1.3.1-3]. The latter proved particularly well suited for stable long-term operation, and continued to serve our needs well into 2017. An impeccable description of this valve is available here [57, Sec. 3.4.1.1], and of course its original publication [58]. In what follows, I focus on two pulsed valves with which I have played a more direct role.

2.2.1 Miniature Solenoid

Towards the middle of my thesis work, a decision was made to lengthen the decelerator and switch to a lighter neon carrier gas. The use of neon opens up many opportunities for possible increases in source brightness, at the expense of increased beam forward velocity. Neon has a lower viscosity, reduced propensity for clustering and colder final temperature relative to krypton, the previously employed carrier gas. Additionally, velocity slippage, a phenomenon whereby the species of interest reaches a different speed than the carrier, is reduced with OH due to the more comparable mass. The reduced clustering issues also make it possible to consider running at dramatically increased pressures, and also heating the valve to run at correspondingly enhanced water pressures. The use of high pressures has an important effect on the operating mechanism for a pulsed valve, since this can significantly increase the mechanical force which must be exerted in order to open the valve. This seems particularly problematic for piezo valves, which seem already somewhat limited in actuating distance and applied force. For this reason, together with the change to a longer decelerator, we decided to purchase an Even-Lavie valve [49, 54], considered to be a kind of gold standard in high density pulsed molecular beams, although with more challengers of late [a] . Refer to Fig. 2.4 for a labeled view of the valve together with a custom designed and self-manufactured mounting structure. The valve utilizes a highly miniaturized solenoid type design, which actuates a ferromagnetic plunger that actually maintains its magnetic susceptibility down to cryogenic temperatures, allowing the valve to continue to function at those temperatures and opening up new possibilities for Helium beams and other physical chemistry pursuits. It also

---

[a] David Nesbitt claimed that this valve was comparable [59] to the Even-Lavie valve in email communication to Hao, Jun, and I
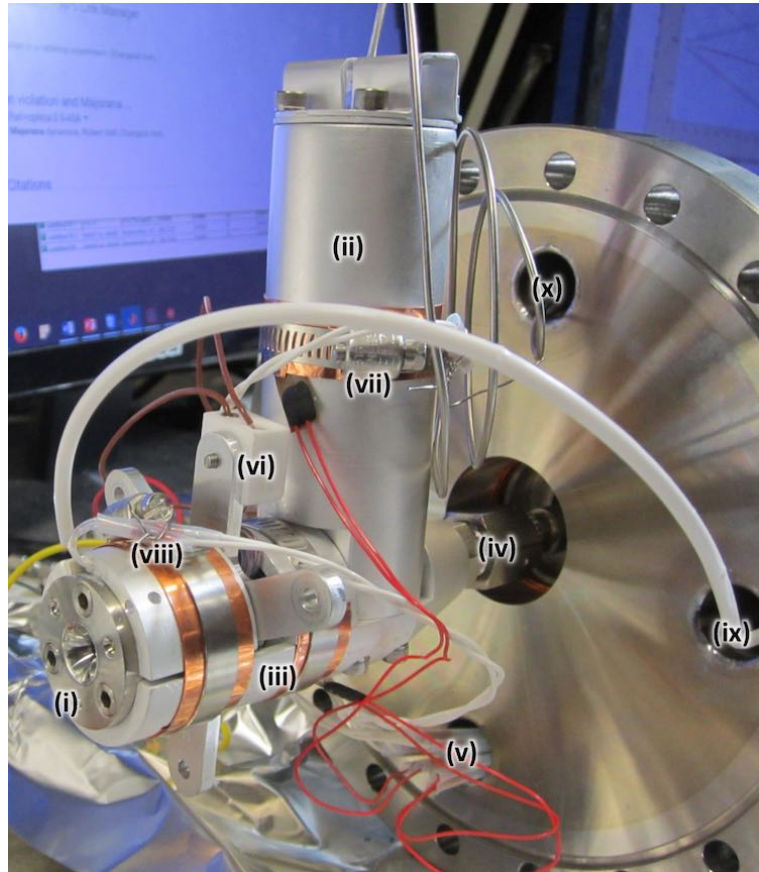
Figure 2.4: The Even-Lavie valve, mounted in a thermally stabilized aluminum rig. (i) The stainless steel body of the valve itself protrudes from the front of the aluminum rig. (ii) This vertical aluminum cylinder is in fact a tube, containing within a water reservoir consisting of an NPT fitting with glass fiber filter papers inside for localizing some liquid water vapor. (iii) A half-closed cylindrical holder for the valve body sits down here, and connects to the valve via hose-clamps. These hose clamps tighten onto copper sheets which help transfer heat to the upper aluminum slices which surround the valve for optimum thermal equilibration. (iv) The valve mounts up to a VCR connector, by means of a VCR plug with 1/4"-28 threaded hole feature. This VCR connector formerly served as a gas line for the previous piezo valve. (v) A frighteningly frustrating eight-pin mini-CF connector transfers wiring for two thermistors and two heaters. Teflon tubes prevent unintentional grounding between pins. (vi) This Teflon block is original to the valve, and strain-relieves the feedthroughs for the wires which actuate the solenoid. (vii) This clamp tightens the aluminum cylinder onto the water reservoir within (the cylinder has a cut to allow flex). A small vacuum compatible heater (Minco) is mounted underneath the clamp. (viii) The leads to an Omega thermistor are connectorized to a teflon wire twisted pair and strain relieved via stainless steel wire to the hose clamp. The thermistor is glued into the upper aluminum cover piece on the front, to the left of this label and directly above the valve nozzle. An identical thermistor connects to the back of the water reservoir. (ix) High voltage RF feedthrough for the dielectric barrier discharge. (x) Ultra-thin 1/16" Swagelok gas line for minimum dead volume at high pressure.
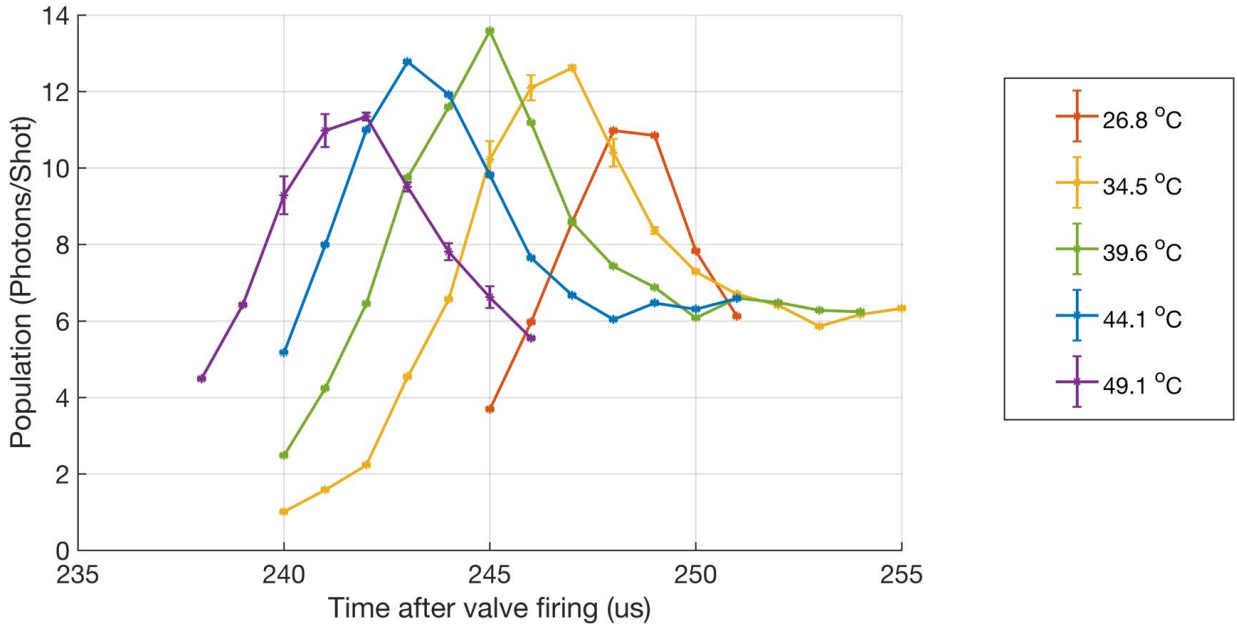
Figure 2.5: Free flight of OH radicals past a detection region in the source chamber as a function of the temperature of the valve housing. An optimum is found close to $40\,^{\circ}$C, only $\sim 20\%$ above the room temperature value.

boasts operation up to extreme pressures of 100 bar, potentially a game changer for high brightness generation of OH radicals.

The purchase of the valve was not a pleasant experience, and involved over a year of waiting and much haggling about paperwork and international agreements. The performance of the valve was also somewhat lackluster, with OH brightness in the source chamber actually only half that achieved with neon in our previous piezo valve. Tuning the temperature of the system did not yield any significant change in the performance of the system either, see Fig. 2.5. Increased temperature would have been necessary to capitalize on the possible gains of a higher pressure source region. This is because OH radicals are formed from water as described below in Sec. 2.2.2, and the partial pressure of the water strongly depends on temperature close to room temperature (hence all the weather here on planet earth). Great care was taken to optimize all relevant parameters, including discharge frequency, length, and delay; valve opening current and time; filament position and current. Many plots similar to that in Fig. 2.5 may be found in the data folders and logbooks from

May-June of 2017. On the bright side, the valve was successful in delivering an impressively low total gas load, and an impressive flux of neon atoms, potentially a crucial enabler of our skimmer cooling results [55]. In addition, the low translational temperature of neon is essential for our as yet unrealized dream of studying collisions between neon and OH in the midst of the beam [60, Chapter 7].

2.2.2   Discharge

For working with OH, or any other free radical, it is essential to integrate together with the valve body a mechanism for generating the radicals during the supersonic expansion process. Generally, their reactive lifetime is too short to enable any other solution, and therefore a delicate balance arises between generating them far enough into the expansion process so that they do not have time to react, but not so far that they don't have time to be thermalized to the buffer gas during the expansion. Various techniques exist, including both radio frequency and pulsed electric fields, and also UV photolysis of some precursor species. All three of these have been attempted on this experiment, with the use of pulsed electric fields having been used over the majority of the experimental history prior to the Even-Lavie valve, which was purchased together with a so-called dielectric barrier discharge radio frequency source. One exception was an attempt made at using photolysis of HNO_3, described in [45, Sec. 3.1.4.2], which produced only half the output of the piezo valve, and led to some rather hazardous laboratory conditions [b].

A surprising observation we made during the testing of the Even-Lavie valve was that production efficiency of OH radicals continued to improve well beyond the recommended operating point of the device, yielding an additional factor of two by going beyond the maximum recommended RF discharge of 1.6 kV or so. This suggested to us that the RF discharging mechanism of the Even-Lavie valve could be the primary limiting factor associated with its performance for our operation. This led us to be quite interested in the possibility of using a DC discharge with a high pressure neon source, something which has at this point not yet been tested.

---

[b] Private Communication with Brian Sawyer during DAMOP 2019.

2.2.3   Lorentz Force Opening Mechanism

The Lorentz force exerted on a wire by a magnetic field containing the wire can also be exploited for operating valves. A key advantage of this is the reduced obstruction of the required hardware for gas flow. This style was designed in Nijmegen in the Netherlands [61], and a similar design was undertaken in our shop, though not yet completed or tested at the time of this writing. A primary motivation of the undertaking was the lead time of the Even-Lavie valve, but when this at last arrived, the effort was dropped. Based on the performance of the Even-Lavie valve however, the possibility of operating this valve remains interesting, and a potentially viable way of actually leveraging the possibilities in principle afforded by having switched to a supersonic expansion in neon.

The JILA valve design was performed by Kyle Thatcher, and contains many nice optimizations relative to the original [61], especially an externally tunable positioning of the sealing device, which is shown in Fig. 2.6. The valve also features careful material engineering to enable operation into the 100 bar regime, although the relation between opening current and stagnation pressure will need to be explored. A traditional DC discharge stack sits in front, and is also capable of higher voltages than usual, motivated by our experience with the Even-Lavie valve.

2.3   Conclusion

The major undertakings that have occurred during this and all theses of the OH experiment demonstrate the challenge and difficulty associated with maximizing the performance of a beam source. A new effort associated with leveraging the seemingly promising characteristics of a neon seeded beam has begun, with minimal results thus far. One thing worth noting is that switching back to the older piezo valve should at least provide a decent two to four fold gain relative to the performance of the Even-Lavie valve obtained thus far, although this valve may play much less well with the cryogenic techniques discussed in the next chapters because of its increased flux. Should an effort be deemed worthwhile, the new JILA version of the Nijmegen valve could serve as an
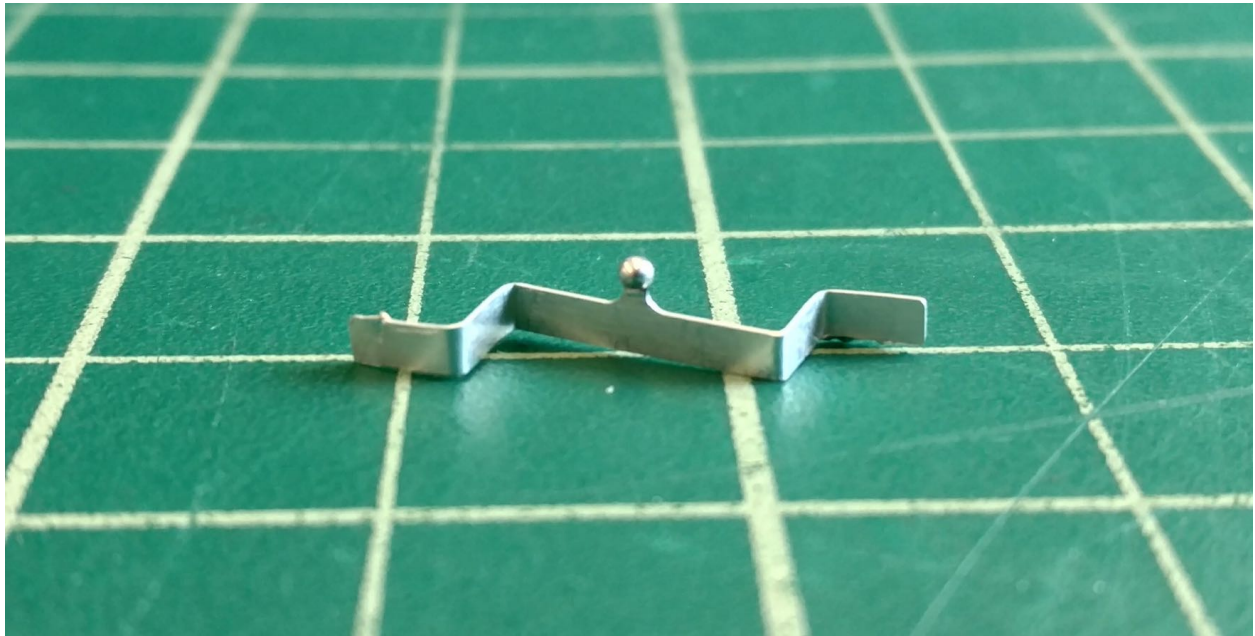
Figure 2.6: This high spring coefficient aluminum alloy wire sits within a large magnetic field and pulls open a valve due to the Lorentz force resulting from a brief 1000 A current pulse. The design was taken from [61] and manufactured by Kyle Thatcher in the JILA machine shop.

excellent starting point for exploring the frontiers of optimum OH production in the neon regime.

Chapter 3

Skimming

The creation was all too soon marred and cast into disarray. Molecules whose trajectories led them into difficult circumstances, such as forceful impact with the chamber walls, did loudly proclaim their misfortune by initiating damaging shockwaves upon the entire population. And so it became necessary to separate these malcontents from their fellows, and to restrict from access to the promised land all those who failed to follow the straight and narrow path that leadeth unto salvation. The device chosen to perform this separation of straight line followers from their fellows, of the wheat from the chaff, became known as a molecular beam skimmer.

3.1 Aerodynamic Skimming

Traditional skimming techniques focus on shaping a trumpet-like structure in just the right way so as to minimize the chance of rejected molecules subsequently reentering the beam [62, 63]. To a good approximation, molecules encountering the surface may be assumed to leave with a cosine distribution of trajectories. This cosine distribution also describes the the likelihood of a patch of surface being struck by particles in a gas above that surface. For simple reasons of geometrical flux, a given patch of surface is more likely to encounter particles approaching along a normal to the surface, than at shallower angles, and quantitatively, the distribution function is proportional to the cosine of the angle between the normal and the actual line of incidence. It follows that the same should be true for molecules exiting a surface, at least in the thermodynamic limit for a gas interacting with a surface. For this reason it is advantageous to have the surface strongly

tipped away from the beam, and to have the surface razor thin around its opening, so that as much as possible the molecules which interact with the skimmer are directed strongly away from the beam-line. With this way of thinking, it might seem ideal to separate the beam with a very long hypodermic tube, but interactions with the inner surface of the skimming structure are also a concern. Molecules impinge on the inner surfaces due to the inherent transverse temperature and spreading of the unperturbed beam, and also due to molecules which interact unfavorably with the tip of the skimmer, and for this region it is better to have the inside of the skimmer open up and not be shaped like a tube [62, Sec. 2.4]. The precise details of the shape can be exactly computed in the case of a continuum flow of molecules [64], but since the advent of pulsed supersonic expansions, these details are no longer relevant since skimmers are no longer positioned in the regime of continuum flow of the valve, which only made sense with the much higher overall fluxes and much lower instantaneous fluxes of continuous beam sources.

3.2   Cryogenic Skimming

Cryogenic skimming can make a significant improvement to the situation thanks to the high probability of adsorption of molecules directly onto a cold surface, which much more thoroughly addresses the problem of separating unwanted molecules without their having an opportunity to negatively influence the others [65]. Even in the case of incomplete sticking, a partial accommodation of molecules to the low temperature surface reduces their velocity, making it less likely that they will travel back into the beam before it has passed. This work is thoroughly described in both our PCCP publication [55] and in Hao's thesis [60, Chap. 5]. I will focus here on the question of how these gains may best be transferred to the loading and operation of a Stark decelerator. For this purpose, the key result worth recapitulating from our skimmer cooling work concerns the absolute comparison between the state of the art in room temperature skimming and that in cryogenic skimming, see Fig. 3.1. A gain of nearly a factor of thirty is found in the improvement that results from the use of the cryogenic technique. This gain may be understood to arise from a combination of "geometric" and "cryogenic" gains, where the former refer to the reduction in valve-detector
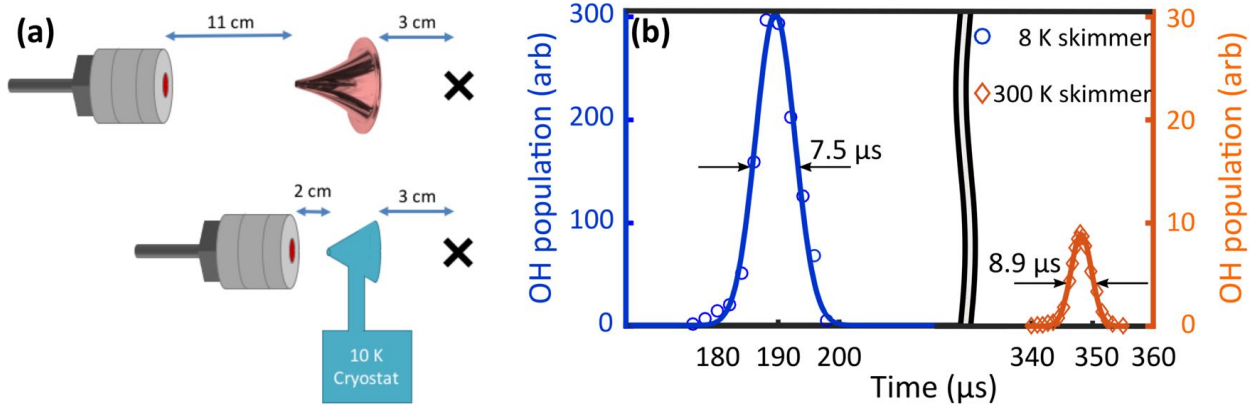
Figure 3.1: (a) Experimental diagram for the skimmer comparison. The "X" marks the location of LIF detection. (b) Spatial hydroxyl radical density is measured after cryogenic and conventional skimmers with the valve-skimmer distance optimized for greatest density in both cases. A factor of thirty enhancement is observed.

distance afforded by the reduced valve-skimmer distance and correspondingly increased solid angle, and the latter refers to the remaining gain directly associated with clogging mitigation. It should be noted that this geometric gain is potentially suspect in the sense that at some point these gains correspond to molecules which may contribute to the increased spatial density observed after the skimmer but are too hot transversely to be loaded into the decelerator anyway. To first order, this is not the case for the molecules which contribute to the observation in Fig. 3.1, since with a minimal detector transverse size for optimum density measurement, and an assumed ~ 2 mm transverse effective initial source size, molecules hit the detector with a transverse velocity spread of:

$$\frac{2 \text{ mm}}{8.4 \text{ cm}} \times 810 \text{ m/s} = 19 \text{ m/s}. \tag{3.1}$$

By comparison, traditional deceleration accepts a spread closer to 10 m/s, but SF mode pushes this out to 18 m/s, and VSF out to 24 m/s, see Fig. 4.2.
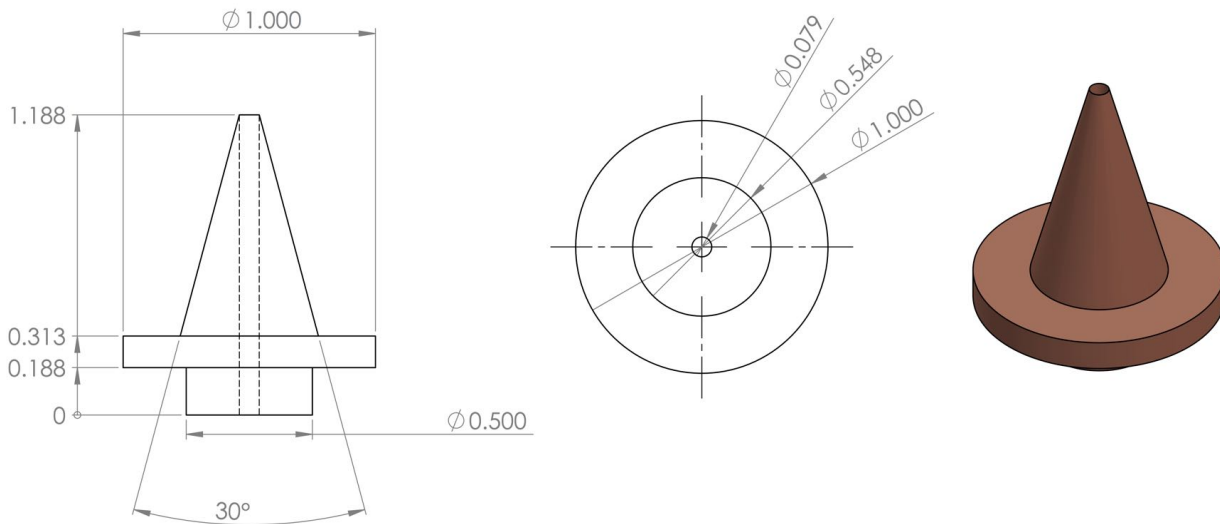
Figure 3.2: Mechanical drawing of the volcano skimmer, units are inches, 0.079" = 2 mm. With a valve mounted right at $2-3$ cm from the skimmer tip, the optimum found with no decelerator, 9x reduced flux from 50% hole diameter reduction and doubled distance of aperture to valve.

3.3 Decelerator Coupling

Our first attempt at coupling molecules into the decelerator did not show a significant increase in signal upon cooling down the skimmer, as had been observed with the skimmer by itself. This is a strong indication of clogging, since the cryogenic skimmers should feature severe clogging at room temperature due to their rather blunt shape. The obvious hypothesis is that skimmer cooling was successfully mitigating skimmer clogging, but the increased flux through the skimmer simply led to decelerator clogging instead. We first sought to address this through the use of modified skimmer geometries, which I will describe here, before moving on to more advanced strategies involving hexapolar focusing as described in the next chapter.

3.3.1 Volcano Skimming

One obvious way to reduce the flux of molecules encountering the room temperature surfaces of the electrodes present in the Stark decelerator is to require the molecules of interest to go through a longer, narrower hole than previously. To achieve this, we installed a modified skimmer which was

The details of these fillets aren't important.
We just want it to be aerodynamic.

B
B

A
A

0.375
0.125
0.078
0

0.079

∅0.039

35°

SECTION B-B

25°
35°

0.090

∅0.206

SECTION A-A

0
0.020
0.138
0.375

This feature aligns with ID
of mounting part.
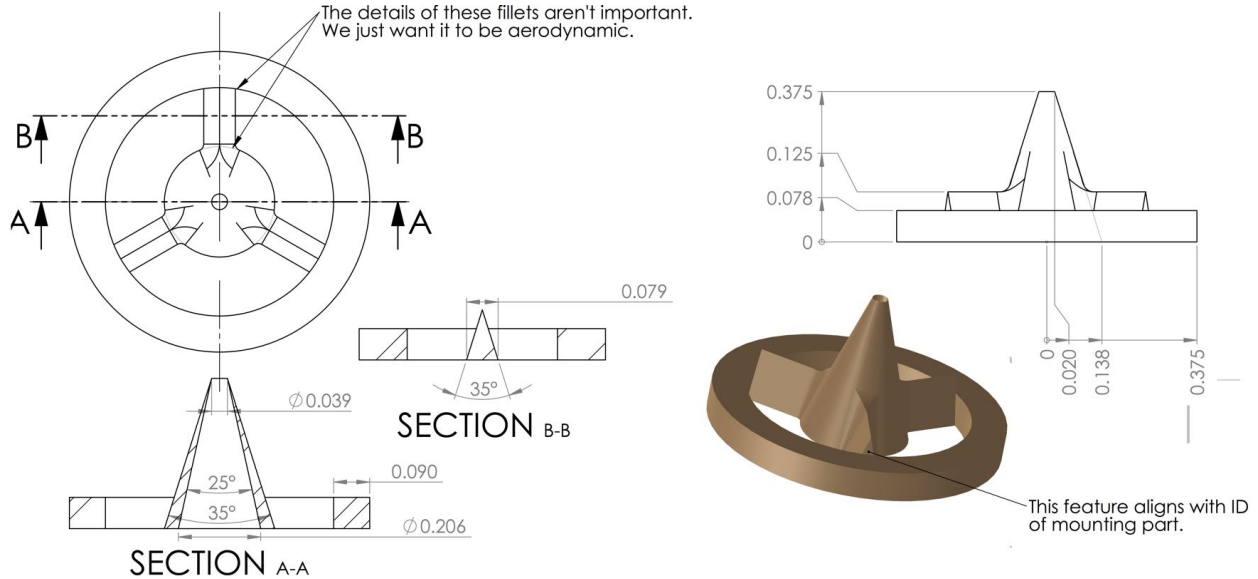
Figure 3.3: Mechanical drawing of the second skimmer attachment component of the double skimmer. This rather complex design was machined via CNC from a single block of 99.9995 (5N5) copper for high thermal conductivity. Dimensions are in inches, $0.039'' = 1$ mm.

essentially just a cone with a hole drilled through, see the mechanical drawing shown in Fig. 3.2. Using naïve solid angle arguments, this ought to have reduced flux onto the decelerator rods by more than an order of magnitude relative to the previous design. In practice, the volcano skimmer also performed poorly, with no significant gain during cool-down. One likely explanation for this is that the skimmer opening was too restrictive, and adsorption not complete enough to avoid clogging in this geometry. To assess the relative contribution of volcano skimmer clogging and decelerator pin clogging, we also performed tests with Argon as a carrier gas. This ought to have a significantly improved adsorption probability relative to neon, and could have led to a performance enhancement if clogging in the skimmer were truly to blame. A comparable ratio of hot and cold temperatures with Argon was observed, suggesting that either both gases had rather poor first-bounce adsorption probabilities or that clogging on the decelerator pins remained the primary issue.
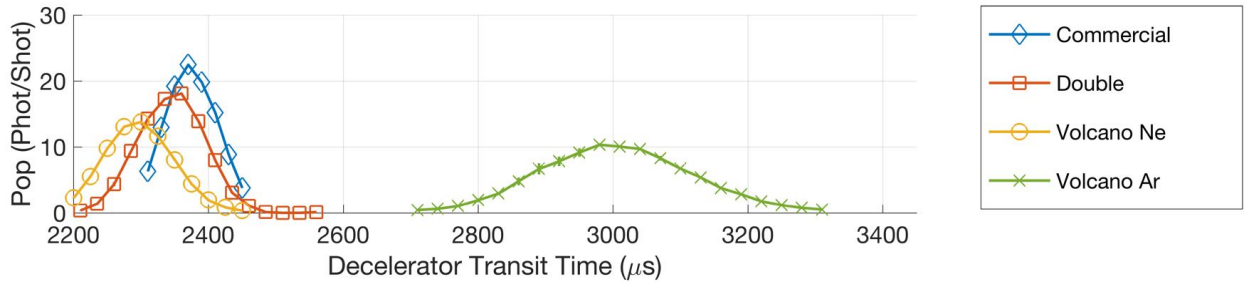
Figure 3.4: Several Skimmers are attempted, and none are found to improve upon the best guided molecule flux obtained via conventional skimming. The variation in arrival time of the measurements correspond to the different valve skimmer distances used in the various cases, and also to the variation in the initial speed of carrier gases between the case where Argon is used and the others. These data were collected on March 16 and April 26 of 2018.

3.3.2 Double Skimming

Suspecting clogging in the volcano structure, we designed an alternative with similar flux reductions as far as the decelerator was concerned, but with much better egress options for limiting any clogging within the structure itself, see the mechanical drawing shown in Fig. 3.3. The device was designed to occupy a small space and integrate seamlessly with our existing mounting structure for quick manufacturing turnaround. Essentially, a miniature skimmer was machined in one piece with an outer ring for soldering directly on to the back of another skimmer. Any clogging associated with internal wall reflection in the volcano skimmer should be greatly reduced in the device, while enacting even stricter flux limitations thanks to the further reduced 1 mm opening hole. In practice, the device performed only slightly better than the volcano skimmer. Our key figure of merit for performance is shown in Fig. 3.4. Here the detected OH molecules after guiding through the length of the decelerator are shown comparing the conventional room temperature skimmer to the volcano and double skimmers. In stark contrast to Fig. 3.1, here only a loss is found between the conventional and cryogenic devices.
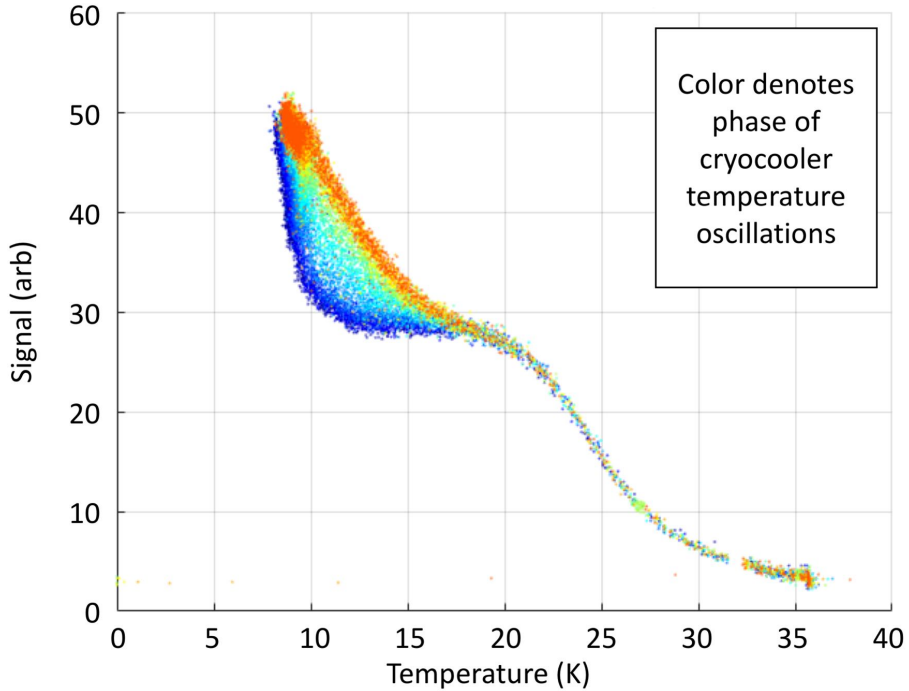
Figure 3.5: The low temperature behavior for cryogenic skimming shows a distinct lack of saturation, and a broadening of signal variation. Binning data by phase of the pulse tube cooler temperature variation reveals the strong role this plays. Results are somewhat encouraging of prospects for a lower temperature measurement.

3.4   Lower Temperatures

Some of our results suggested a performance that was still strongly improving as a function of further reduced temperature by the time our pulsed tube cryostat had reached its lowest temperature, see Fig. 3.5. This motivated us to pursue a liquid Helium cooled skimmer, so as to achieve a further factor of two reduction in temperature, and potentially expose an even more dramatic gain in molecule number relative to what had already been observed. These attempts did not lead to an improved performance, and were not reported in [55], but some lessons worth sharing were learned.

One of our most surprising early observations was the wildly varying variance of the observed signal as a function of skimmer temperature. In fact, at first the observation was even more bizarre than what is shown in Fig. 3.5, where three distinct data branches were visible in the region between

$35 - 20°$K, as can still be seen in the experiment logbook. This turned out to be an artifact of 60 Hz noise on the thermometer spectrum, and is an interesting example of the ways that noise sources can interfere with data interpretation especially on a parametric plot. In any case, with this issue easily filtered away, it also became clear that the broad variation in signal variance, especially between $20 - 8°$K, was induced by the rather large $2 - 3°$K amplitude temperature oscillations of the second stage of our Cryomech PT807 pulsed tube cooler. Such fluctuations are not untypical of a purely copper system, which has a negligible heat capacitance in these temperature ranges, and therefore directly writes the fluctuating temperature of the cryogenic fluid onto the system of interest. A similar observation was recently communicated [66], and resolved through the use of a helium heat transfer stage interrupting the direct copper heat link. We found a very strong dependence of the observed flux through the skimmer on not only the instantaneous temperature of the skimmer but whether it was in the midst of becoming colder or hotter. It is a bit of a mystery why such a dependence would exist. I spent some time searching for any reason that a time-lag might exist between the collection of OH signal and of cryostat temperature data, since this could masquerade as such a dependence, but nothing turned up. Assuming the dependence is in fact real, one reason could relate to details of the adsorption process and of the surface layer on the cryogenic skimmer. For example, bringing the adsorbed neon back up from its lowest temperature could function as an annealing step which changes the spring constant of the solid in a way that is more favorable for further adsorption.

In any case, the observation suggests that lower temperatures could provide further benefit, as mentioned above. I devised an unconventional flow type cryostat designed for bringing only the skimmer and a small thimble worth of liquid Helium down to low temperature. The device is pictured in Fig. 3.6. A long 1/2" SS tube protrudes deep into the vacuum chamber, such that a 3/8" OD helium fill line is able to protrude all the way down without making significant contact and while leaving room for cold Helium gas to escape back upwards, further cooling the fill line during egress. In terms of manufacturing, the solder joint between copper and steel constitutes the most challenging step. This was performed using a more aggressive ZnCl based flux, and required a
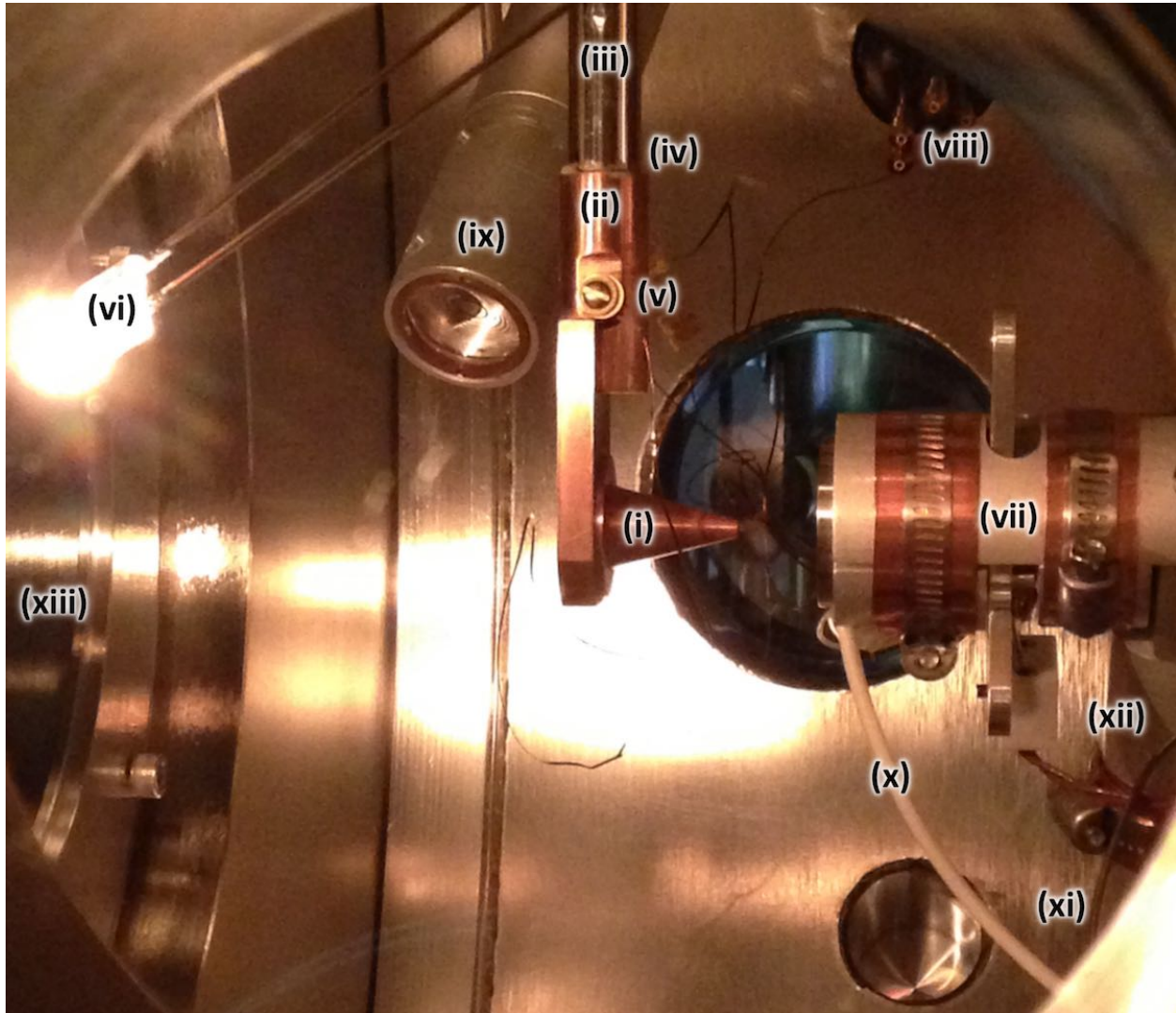
Figure 3.6: A thimble sized flow cryostat at the bottom of a long, thin-walled Stainless Steel tube is seen soldered to a copper skimmer. (i) Copper skimmer, 3 mm orifice, 30° external included angle, 25° internal. (ii) Copper liquid Helium reservoir, soldered to a copper skimmer backplate and thence to the skimmer. (iii) Thin-walled Stainless Steel tube, found in the shop. Not exorbitantly thin, something like 0.01". (iv) Copper to SS solder joint. (v) Lakeshore DT-670 Silicon Temperature Diode. (vi) Tungsten filament for seeding the discharge, taken from Hans' Halogen bulb by removing the glass on the diamond saw. (vii) Even-Lavie valve and aluminum mounting frame. (viii) Quad-lead feedthrough for Temperature Diode. (ix) Un-anodized lens tube structure for mounting LIF collection lens about 5 cm from the beam-line. (x) High voltage RF wire for driving the dielectric barrier discharge during the supersonic expansion from the Even-Lavie valve. (xi) 1/16" OD gas feed line for Even-Lavie valve just visible. (xii) Thermal mounting block containing water reservoir.

few times to get right. Another initial failure arose from the use of an UltaTorr fitting with gasket directly contacting the OD of the 1/2" tube. This poor choice led to the freezing and failing of said gasket due to the cold Helium gas flowing just within. A workaround was to use a 1" UltraTorr fitting to bridge the vacuum barrier and provide some position tunability, and connect a 1" tube to the thin walled 1/2" SS tube with the cold cryogen running through it via Swagelok, thereby leaving plenty of room to apply a heater for the gasket in between. Further details are labeled in Fig. 3.6.

Several of the first attempts at transferring Helium to this device were fraught with major challenges, particularly with regard to temperature stabilization, which are worth discussing further here. In our experiments with the pulse tube cooled skimmer, we often detected a strong sensitivity to whether or not the valve was operated during cool down. In particular, it was found that operating the valve was actually crucial to the resulting performance of the system. We were usually unable to recover the performance of the system without first heating close to room temperature. This strongly suggests that the performance relates to the influence of water or other high temperature freezing species on the cryo-adsorption process for neon onto the copper skimmer. For example, suppose that a layer of solid ice is actually detrimental to neon adsorption, and the formation of such a layer is the key process leading to reduced performance under some operating conditions. This could explain the observed requirement of operating the valve during cool down, provided the regular bombardment of the skimmer surface with neon was sufficient to disturb the formation of such a layer. It could also explain the observed failure to restore performance by partial warming, since warming only above the neon freezing point could actually be a very efficient way to help the water mixed in with the neon to settle down into a solid layer.

In any case, during our first attempts with the Helium cooled skimmer, we inadvertently created a temperature bouncing phenomenon, see Fig. 3.7. The system temperature was found to erratically vary between 20°K and 5°K, as shown in panel (b) of Fig. 3.7. We hypothesize that this resulted from the situation where the narrow size of the copper reservoir allowed a bubble of Helium gas to sit between the base of the copper reservoir and the liquid Helium above. The bubble would
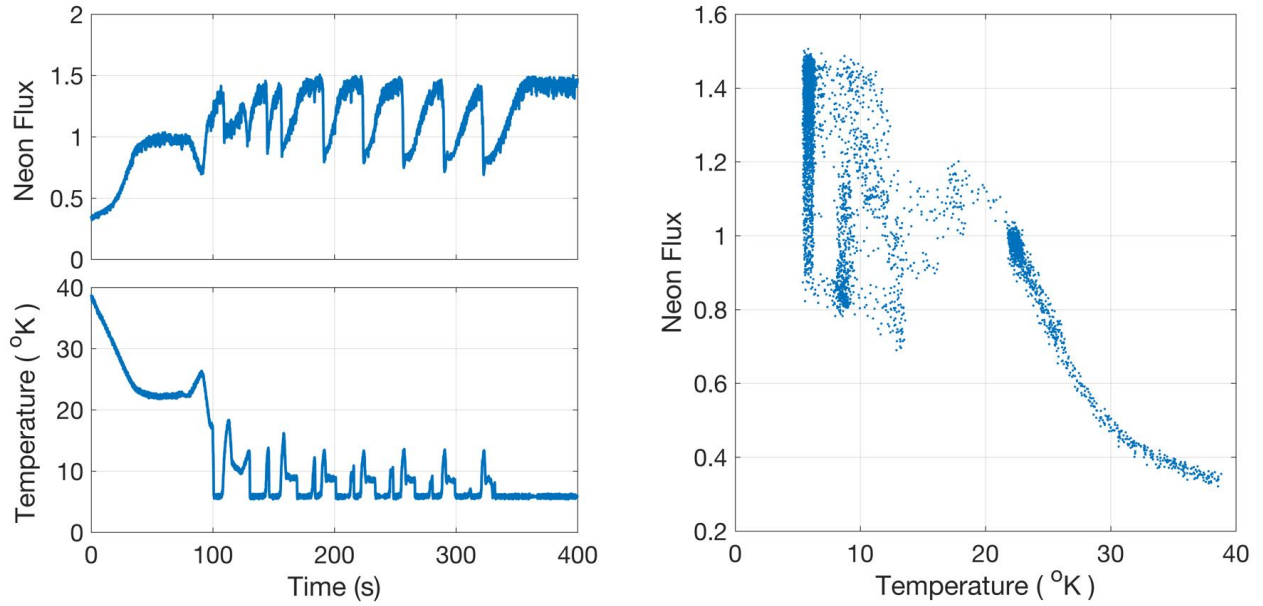
Figure 3.7: Neon flux and temperature are monitored during the cool down procedure for a liquid helium cooled skimmer. (a) Neon signal, measured by fast ion gauge, creates a voltage dip on the collector of the indicated magnitude over the measured timespan. (b) Temperature, measured via DT-670 Lakeshore Silicon diode, exhibits an erratic quasi-periodic temporal variation, likely driven by highly nonlinear characteristics of the liquid Helium flow including bubble formation and surface tension inhibiting heat transfer. (c) Parametric plot showing strong hysteresis behavior in the sense that the observed signal depends not only on the instantaneous temperature but its time history.

grow in size as the heat load on the skimmer continues to transfer to the Helium, until eventually the bubble would interrupt the flow of liquid helium out of the transfer tube and into the thin-walled stainless steel tube. At this point, the liquid Helium working its way up between the transfer line and the thin-walled tube would quickly evaporate, allowing Helium gas to escape from the bubble above the reservoir and allowing new liquid helium to drop suddenly down on to the reservoir once more. By increasing the pressure of Helium gas applied to the Helium dewar during the transfer, we were able to overcome this temperature bouncing mode of operation, although the pressures required (5 psi or so above room pressure) are very high as far as Helium dewars are concerned, which usually have relief valves at 10 psi and very stern warnings about the dangers of overpressure. The high pressures used for transfer also limit the temperature obtained at the skimmer, since the evaporation temperature of liquid Helium has a significant pressure dependence [67, Sec. A].

3.5   Conclusions

Although we have successfully demonstrated very significant gains associated with skimmer cooling on its own, leveraging these gains for deceleration has proven elusive. A more reliable and robust method is desired for mitigating clogging not only in the skimmer but also in the ensuing coupling process to the decelerator. While cooling of the decelerator itself certainly comes to mind as a possibility, the best blend of manufacturing plausibility and prospects for clogging mitigation were determined to be a cryogenic focusing hexapole, described further in the next chapter.

Chapter 4

Hexapole Focusing

And it came to pass that all those molecules who contrived to survive the great segregation described in the previous chapter, were set about a grueling and strenuous exertion of the mental faculties. Indeed, the focus requested of them was of such a severity as to literally bend their wills and their trajectories. And in more modern terminology, the subject of this chapter is the focusing of molecular beams for optimized coupling between their source and any ensuing scientific apparatus. The work described in this chapter is in progress, and has thus far only yielded a factor of two improvement in decelerator flux, when used together with the cryogenic skimming techniques described in Chapter 3, and compared against conventional room temperature skimming with no focusing. As a consequence of the ongoing nature of this work, I have deemed it particularly worthwhile to include many details of potential relevance to those who may wish to carry this work a few steps farther.

4.1   Phase Space Matching

To understand the action and possible usefulness of a hexapole, it is essential to become familiar with thinking and working in phase space. By phase space I simply mean the two dimensional space spanned by the position of molecules in the ensemble on one axis and their velocity on the other. Technically speaking phase space ought to refer to the position-momentum space, but for our molecules the resulting units would be cumbersome. The usefulness of working in phase space stems from the straightforward correlation between the various transformations that

may be applied to the ensemble and how they are manifested in phase space, as is summed up in Tab. 4.1. Free propagation results in molecules with larger velocity coordinate deviating towards larger spatial coordinate, and vice versa. I always work in the frame of reference of the ensemble, so that the centroid of the initial ensemble is assigned the $(0, 0)$ coordinate. The action of a hexapole is to create a spring-like harmonic restoring force in the transverse directions, in which case it may be proven that motion in phase space is circular, provided the velocity axis is scaled by the angular frequency of the harmonic restoring force into spatial units: $v' = v/\omega$. Beginning with the spring-like restoring force:

$$\ddot{x} = -kx/m_{\mathrm{OH}} = -\omega^2 x, \tag{4.1}$$

and obtaining the solution for the position and velocity under simple harmonic motion:

$$x(t) = \sin(\omega t + \phi), \qquad v(t) = \dot{x}(t) = \omega \cos(\omega t + \phi). \tag{4.2}$$
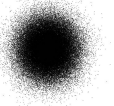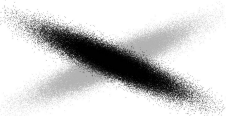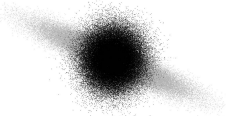
If we now scale the velocity units by ω, we obtain:

$$\left(x(t)\right)^2 + \left(\frac{v(t)}{\omega}\right)^2 \quad = \quad \sin^2(\omega t + \phi) + \cos^2(\omega t + \phi) \quad = \quad 1. \tag{4.3}$$

By appropriately choosing the frequency of the hexapole and the length of time spent within, it is possible to prepare the ensemble for a revival of the initial distribution after some additional free propagation afterwards, see the third and fourth rows of Tab. 4.1.

Furthermore, it is possible to engineer the applications of hexapole rotation and free flights to achieve compression along one axis, accompanied by density preserving dilation in the opposite axis. These results parallel the magnification or demagnification of an image achieved by a lens between an image and object plane depending on whether the lens is positioned closer to the image or the object plane. One key distinction however between the behavior of an optical lens and that of a hexapolar lens is that the latter is almost never operated in the short-lens regime, which has a significant impact on how one thinks about its behavior. Molecules are often rapidly transiting a hexapole in the longitudinal direction, which means that the device needs to be long in order to apply the desired rotation of the transverse phase space. By carefully following an ABCD matrix

Table 4.1: Phase space manipulations are described and visualized. Velocity is the vertical axis, Position the horizontal. Gray shows the ensemble before the action, black afterwards. The first four actions are applied subsequently, the last two are applied directly after initialization.

Action	Effect	Visualization
Initialization	Some approximately Gaussian Distribution	
Free Propagation	Upper Region to Right, Lower to Left	
Hexapole Focusing	Clockwise Rotation	
Additional Free Propagation	Spatial Density Revival	
Free + Hex + Long Free	Velocity Compression	
Free + Hex + Short Free	Spatial Compression	

approach, instead of a simple lens-maker equation for the locations of image and object planes, we obtain [68, Eq. 9]:

$$L_3 = \frac{L_1 + \frac{1}{\kappa}\tan(\kappa L_2)}{L_1 \kappa \tan(\kappa L_2) - 1}, \tag{4.4}$$
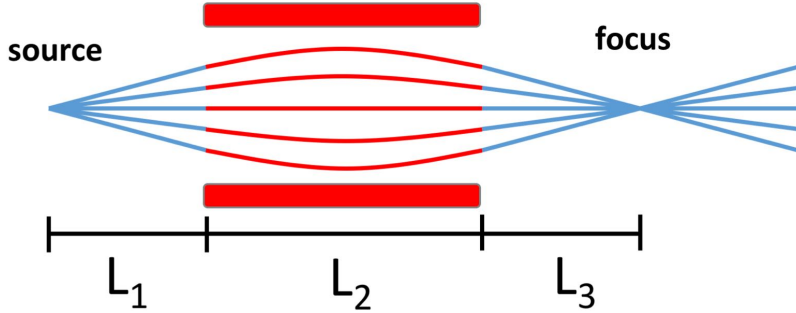
Figure 4.1: Sample trajectories of molecules focused by a hexapole of length L_2 after traveling L_1 to arrive and an additional L_3 afterwards.

where $\kappa = \omega/v$ is an inverse length unit directly related to the hexapole strength and inversely to the beam speed, and the L_i are as described in Fig. 4.1. In the limit of small L_2, this equation can be reduced to something more familiar. First, using $\tan(x) \sim x$,

$$L_3 = \frac{L_1 + L_2}{L_1 L_2 \kappa^2 - 1} = \frac{L_1}{L_1 L_2 \kappa^2 - 1}, \tag{4.5}$$

and now inverting,

$$\frac{1}{L_3} = L_2 \kappa^2 - \frac{1}{L_1}, \tag{4.6}$$

so that for $f_H = 1/L_2 \kappa^2$ we recover the lens-maker formula:

$$\frac{1}{L_1} + \frac{1}{L_3} = \frac{1}{f_H}. \tag{4.7}$$

This focal length has the dependences we would expect, since it reduces (i.e. the lens strengthens) with larger L_2 or with larger ω. This recovery of the lens-make formula applies for spatial focusing, and if a similar focusing were desired in momentum space, this would correspond to collimation.

This compression of velocity and dilation of position or vice versa is often utilized for optimizing the transfer of molecules in an ensemble between a source and a device, or between devices, a procedure known as phase space matching. To flesh this out a bit further, all the devices worked with in the laboratory can be characterized by a phase space acceptance, in principal a six dimensional region but in practice only ever considered in terms of two conjugate dimensions at a time. The phase space acceptance typical of the Stark decelerator for example is indicated in Fig. 4.2, and
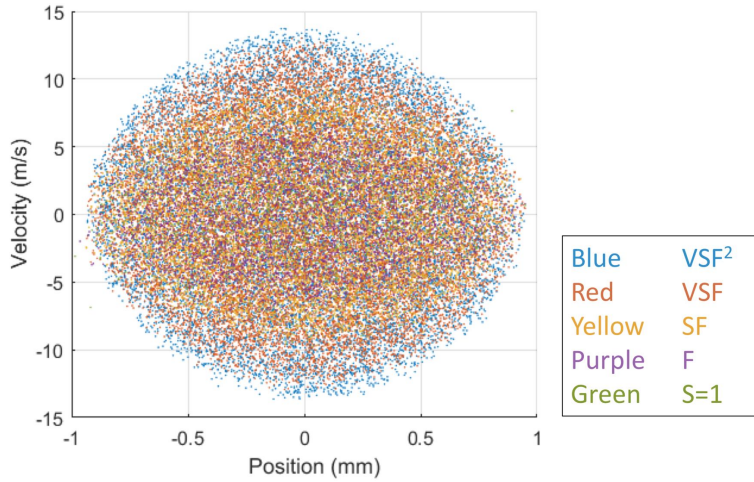
Figure 4.2: Transverse phase space acceptance of a Stark decelerator operated in various modes. Each mode has a different characteristic ratio of velocity width to spatial width. Some colors are hard to perceive, but all have a width close to 2 mm and varying heights between 10 and 30 m/s.

discussed further in Chap. 5. Unfortunately the phase space generated by a supersonic expansion is rather difficult to ascertain, as discussed previously in Sec. 2.1.2. One thing which can be said for certain however is that the initial transverse velocity width generated by the supersonic expansion is much larger relative to anything else in the experiment. This follows from simple intuition as the supersonic expansion only generates a mildly directed beam, which therefore expands significantly transversely away from the valve. Projected onto transverse phase space, such an ensemble should have a variation of transverse velocity that is on the same order as the forward velocity of the beam, i.e. hundreds of meters per second. These velocities are much larger than the maximum stable transverse velocities in decelerators, which are usually around ten meters per second. Nonetheless, the valve may still generate a distribution that is quite narrow in its initial transverse spatial spread. If the initial distribution is narrower spatially than the 2 mm of the decelerator, there will be opportunities for an improved loading of the decelerator with appropriate magnification of the device designed to compress velocity and dilate position as in row 5 of Tab. 4.1.
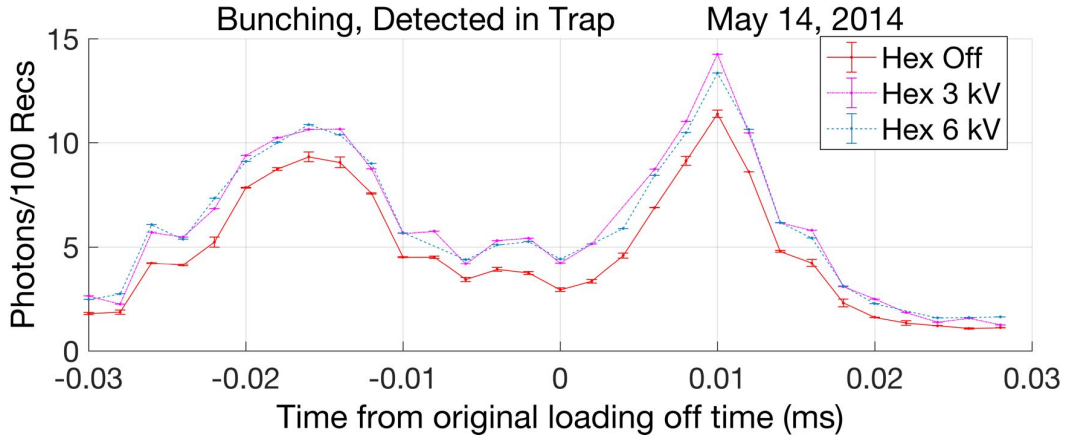
Figure 4.3: Three traces showing OH population after bunching with the hexapole set at different voltages. A scant 17% effect is observed.

4.2   History

In the first generation of the experiment, a 5 cm hexapole was employed and successfully enhanced the molecule number just afterwards by as much as a factor of 16 [69, Fig. 6]. What is less clear however is whether this enhancement really exceeds what could have been had by simply mounting the decelerator closer to the valve and skipping the hexapole entirely. By the time Hao and I were running the second generation of the experiment [70], the hexapole was only providing a 17% effect, as shown in Fig. 4.3. I can find no earlier record of the performance of this hexapole, so it is difficult to say whether this observation of no effect with the voltage on/off stems from some HV issue that developed later, from transition between Jordan and PZT valves, or an alignment issue or some other effect.

If it is indeed the case that the hexapole in the second generation decelerator never had a significant effect, there are a few possible explanations. One relates to the influence of skimmer clogging, which can alter the trajectories of molecules so that they appear to have originated from the skimmer tip. The skimmer tip is too close to the hexapole relative to its focal length for it to have much influence, hence the observation of little effect. Another possibility is that the initial distribution of molecules in transverse phase space is simply much larger than the phase space

acceptance of the decelerator, so that even with no hexapole and pure free propagation, the initial distribution still thoroughly overlaps the acceptance of the decelerator. This explanation would even jive with the observed influence of the hexapole in [69, Fig. 6], since that observation was made with a detector directly after the hexapole. This detector could have observed a legitimate hexapole induced spatial density enhancement, but entirely composed of molecules with transverse velocities above the threshold for decelerator acceptance.

4.3   Cryogenic Hexapole 1

Against this dubious backdrop, we decided in the summer of 2018 to begin work on a new hexapole for use with the third generation decelerator. Our motivations were quite different however from those that motivated the poorly performing hexapole of the second generation. Instead of seeking to optimize coupling between the valve and decelerator, we were seeking to intentionally distance the two for the sake of reduced clogging potential, without sacrificing the gains in phase space density we had obtained by cryogenically cooling the skimmer. This was largely motivated by observation of significant decelerator clogging, as described previously in Chap. 3. The new hexapole would this require cooling to cryogenic temperatures, so as to avoid the clogging observed in the decelerator. In a sense, one can think of the cryogenic hexapole as comparable to cryogenically cooling the decelerator, only much more practically attainable.

4.3.1   Hexapole Fundamentals

A hexapole consists of six alternately charged poles, which generates close to the axis an electric field with the functional form:

$$\left|\vec{E}(r)\right| = 3V_0 \left(\frac{r^2}{r_0^3}\right), \tag{4.8}$$

where V_0 is the magnitude of the voltage to which each rod is charged, with alternating sign, and r_0 is the smallest radius which reaches from the axis to the surface of a pin. For a molecule with a linear response to the electric field, this quadratic dependence of the electric field magnitude

results in a harmonic potential, with the exception of the relatively small region close to the axis where the field is too small to polarize the molecules. This exception causes a perturbation to the ideal focusing behavior, but is not very significant for OH [69, Fig. 2b], although more so for other species [68, Fig. 1]. Specifically, with $V_0 = 13$ kV and $r_0 = 5$ mm, which lead to the typical field strengths characteristic of our traps and decelerators, electric fields up to 100 kV/cm are generated, compared to 3 kV/cm for polarizing the radical.

4.3.2   Core Electrode Design

My first attempt at a cryogenic hexapole design leveraged some rather complex technologies. Fearing the possibility of gas mediated discharge of the hexapole electrodes due to the high densities of molecules shortly after the skimmer, I planned to have the electrodes encased in sapphire tubes, so as to avoid the availability of conduction electrons at their surfaces. These sapphire tubes would in turn sit within a copper block, for maximal thermal conductivity, mechanical alignment, and to provide additional adsorbing surfaces for the Neon. The fields generated in the planned configuration at its intended voltages are shown in Fig. 4.4. In panel (a), note how the fields inside the sapphire are particularly small, a byproduct of its large dielectric constant close to 11. In panel (b), the electric fields along two axes are shown, one through the electrodes and the other between them. A quadratic guiding curve is also shown, which corresponds to an angular trapping frequency for OH radicals of $\omega = 20.6$ kHz.

This all of course requires patterning of a honeycomb-like structure on the inside of a long copper block, something which may be readily achieved using a technique known as wire electric discharge machining, wherein a thin sacrificial wire at high voltage is used like a bandsaw blade, and is slowly moved through another metal. Electric discharges between the wire and the metal being cut cause material to be removed, and the wire is constantly fed so as to avoid its disintegration. This was achieved according to our specifications without any hitches by the CIRES shop, a shop located at the time of this writing in the chemistry department at CU.
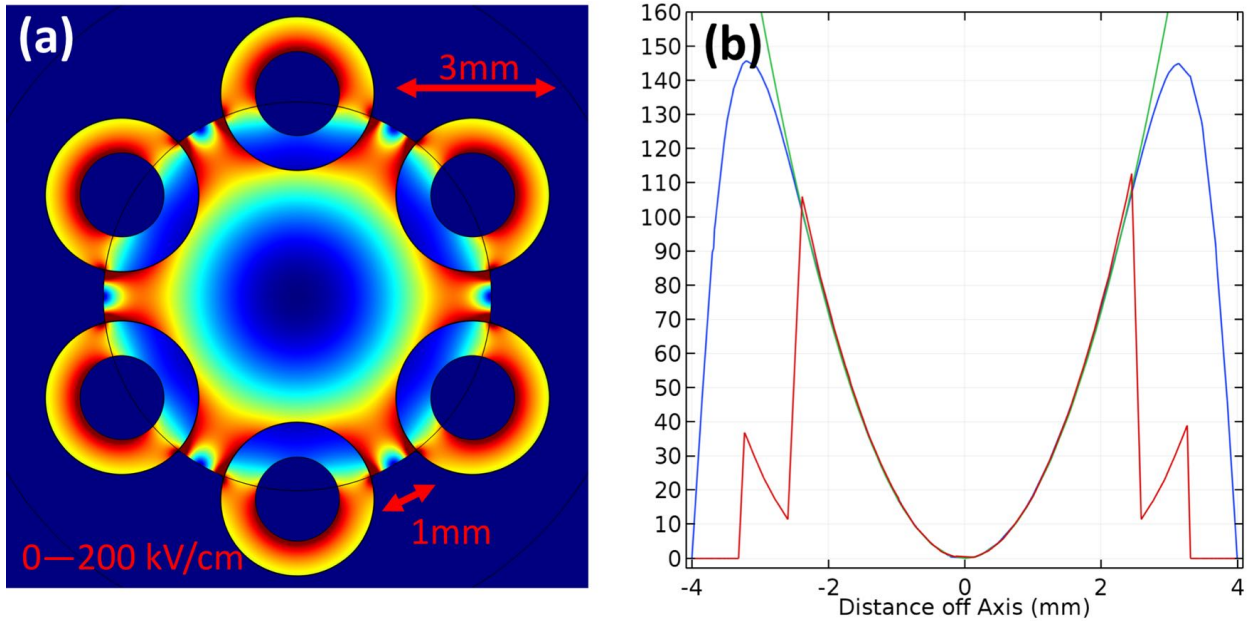
Figure 4.4: (a) Electric field magnitudes and geometric size of the first generation hexapole, composed of 1/16" steel electrodes mounted within 1/8" sapphire tubes mounted within a 1" copper block. Note how the fields inside the sapphire are particularly small, a byproduct of its large dielectric constant close to 11. (b) Field Strength (also kV/cm) verse distance off axis along various axes as described in the main text.

4.3.3   Thermal Design

Some of the thermal considerations pertinent to the design are illustrated in Fig. 4.6. The final

mechanical design differs slightly from what is shown in this figure, but the thermal considerations

remain the same. The large copper block within which the hexapole sits has a skimmer affixed to

the front and an aperture to the back, and a large clamp-like structure conveys sufficient thermal

conductivity without requiring Indium solder. Confirming this required careful consideration of the

force-dependent thermal contact between the clamp and the hexapole, and also between the braid

and the clamp. Thermal conductivity across gold-gold and copper-copper pressure interfaces have

been measured [71, Fig. 2.7], and exceed grease joints above a certain pressure, see the discussion

in [71, Sec. 2.6.4]. As can be observed below in Fig. 4.7, we settle for a gold-copper joint, which

naively would fall somewhere between the gold-gold and copper-copper performances. Of course

nothing is certain, see for example in [72, Fig. 5.8] how mixing copper particles into epoxy can actually worsen its thermal conductivity in some temperature ranges. It is also important to figure out how tight the clamp should be made, so as to benefit from the pressure-dependent thermal conductivity, without irreversibly deforming the copper parts. I studied this using finite element analysis via Solidworks Premium Simulation package, see Fig. 4.5. One interesting point worth mentioning is that the geometry of the device leads to a factor of 2π hoop stress amplification, where the force between the clamp and the cylinder is actually 2π times bigger than the force applied to the bolts. This can be derived by conceptually dividing the geometry in half through the bolts and analyzing the static free body diagrams of each component, a standard exercise in statics. The conclusion is that 1000 kg on each of two bolts would give 240 W/$^\circ$K for gold-gold and 3 W/$^\circ$K for copper-copper, found by taking the 10 $^\circ$K 50 kg data in [72, Fig. 5.8] and multiplying up to 12000 kg including the hoop stress amplification. Of course, this brings to mind the question of validity of the linear scaling of conductivity all the way up to such large forces. In [73], extremely high loads were investigated, and although their cryogenic hydraulic ram apparatus failed catastrophically during the investigation, they were able to confirm that conductivity increased 50-fold for forces increasing 20-fold up to 4700 lb, a super-linear scaling to very high forces.

The emissivities guessed for the surfaces shown in panel (b) of Fig. 4.6 turned out to be optimistic, perhaps because they were approximate room temperature emissivities and not cryogenic, or maybe due to adsorbed gas layers further increasing emissivities. A key challenge of the design pertains to how voltage is to be fed into the electrodes located inside the sapphire tubes. A few iterations were made on the design before this was achieved with acceptable surface path-length reduction and suitable mechanical rigidity. The HV distribution rings visible in Fig. 4.6 ended up having too much flexibility on their own, so plastic Ultem cuffs were glued directly onto the Sapphire rods, simultaneously increasing surface path length for arcs and adding the required rigidity.

An additional consideration for the hexapole is the matter of its alignment with the beam-line. There are two primary strategies by which satisfactory alignment may be obtained:
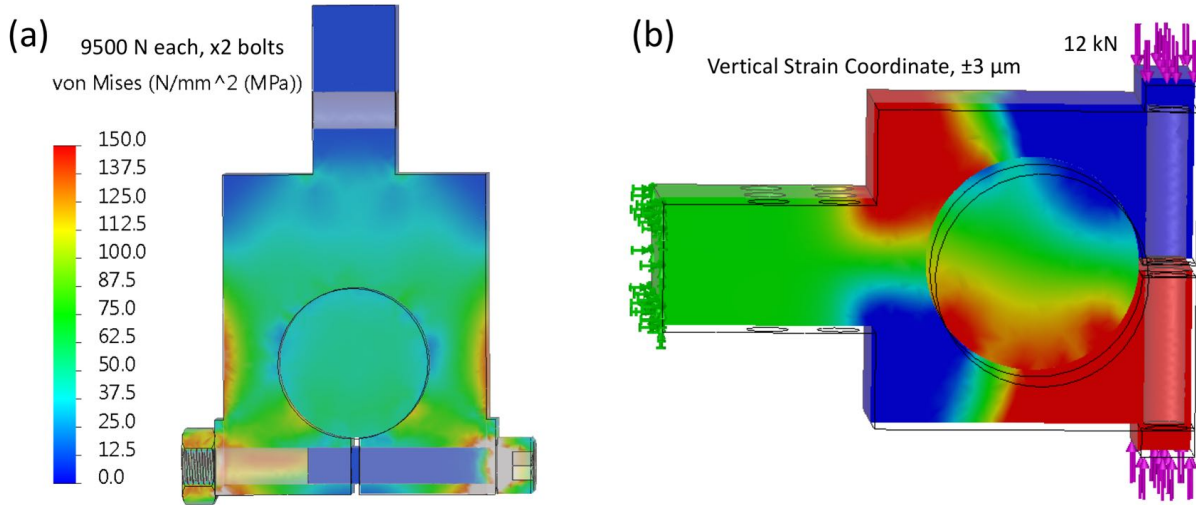
Figure 4.5: (a) Stress resulting from clamp tightening. One of two pairs of bolts and nuts intersect the shown plane near the bottom, and tighten on a rectangular block, the clamp, which then grabs hold of a copper rod, the hexapole mounting rod. The hexapole is not visible within this rod. Coloration indicates the stress induced by the tightening in the clamp, the rod, and the bolts. Annealed copper yields at only 70 MPa or so, and this stress is exceeded in several places, indicating that 9500 N is on the upper end of what should be used on the bolts, and would accompany some yield on the edges of the clamp. (b) Strain in the vertical direction only, so as to view what happens to the clamped hexapole mounting copper rod. Only 3 μm radial compression is observed, small compared to the 3 mm diameter sapphire tubes later inserted into the rod.

(1) Contrive a way for alignment to be tweaked from outside of the vacuum chamber, so that final alignment may be guided by actual system figures of merit such as molecule yield after the hexapole.

(2) Provide in-vacuum fine-adjust knobs only, and engineer a protocol by which alignment may be obtained before pump-down, and not subsequently lost during either pump-down or cool-down.

Strategy (1) was employed for our cryogenic skimming work as described previously in Chap. 3, but was deemed insufficient for this hexapole work, primarily due to unavailability of the requisite
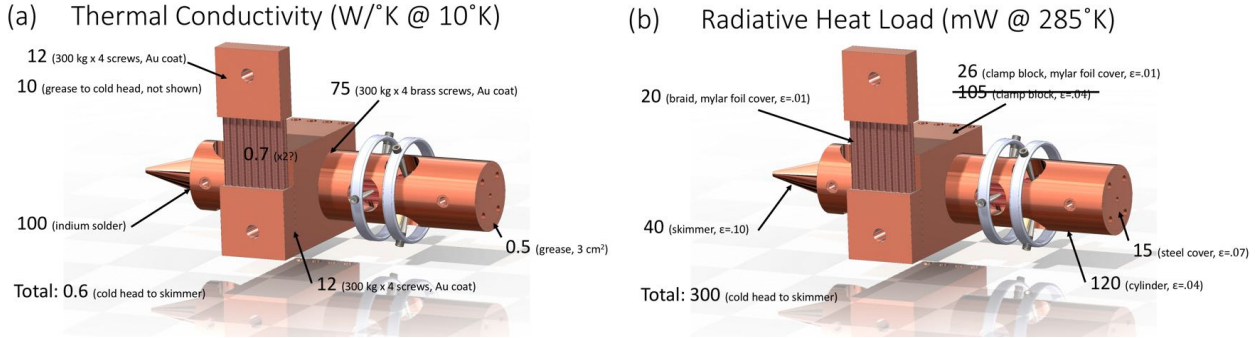
Figure 4.6: (a) Conduction of thermal joints in W/°K. In the final design, two braids were used, for a total conductivity closer likely above 1 W/°K. (b) Radiative heat loads on exposed surfaces in mW.

degrees of freedom. Unlike the skimmer, which only really requires two translational degrees of freedom in order to achieve beam alignment, the hexapole has four alignment parameters, and potentially five depending on whether it is desirable to translate the device along the beam. There seemed no straightforward way to achieve this across the vacuum envelope, especially given how far above the hexapole the tuning bellows sits. Thus strategy (2) was pursued, and the problem of cool-down induced misalignment addressed via a flexible heat linkage[a].

The principal challenge of utilizing a flexible heat linkage is finding a different way to achieve mechanical rigidity without violating thermal isolation. For this purpose, I selected Ultem (or PEI, polyetherimide), a dimensionally stable engineering thermoplastic with poor thermal conduction and good mechanical properties. Ultem rods 1/8" wide and 7/8" long can be seen in Fig. 4.7(i), which also illustrates other pertinent details of the mounting assembly. Many polymers feature admirably low thermal conductivity, and the subject of polymer thermal conductivity is treated more fully in [72], Chap. 5. The same selection was once made for cryostats at the RHIC [74]. In order to make estimations of the thermal conductivity for long, thin cylinders made of unfilled Ultem 1000 connected between room temperature and the cold apparatus, it is necessary to properly treat the thermal gradient which will necessarily build up within the material. I address this first

---

[a] Technology Applications Inc, braid P6-502. Tyler Link, at the time of this writing, is always ready to send long emails about his products, at any hour of the day. Contact him directly for a product manual.
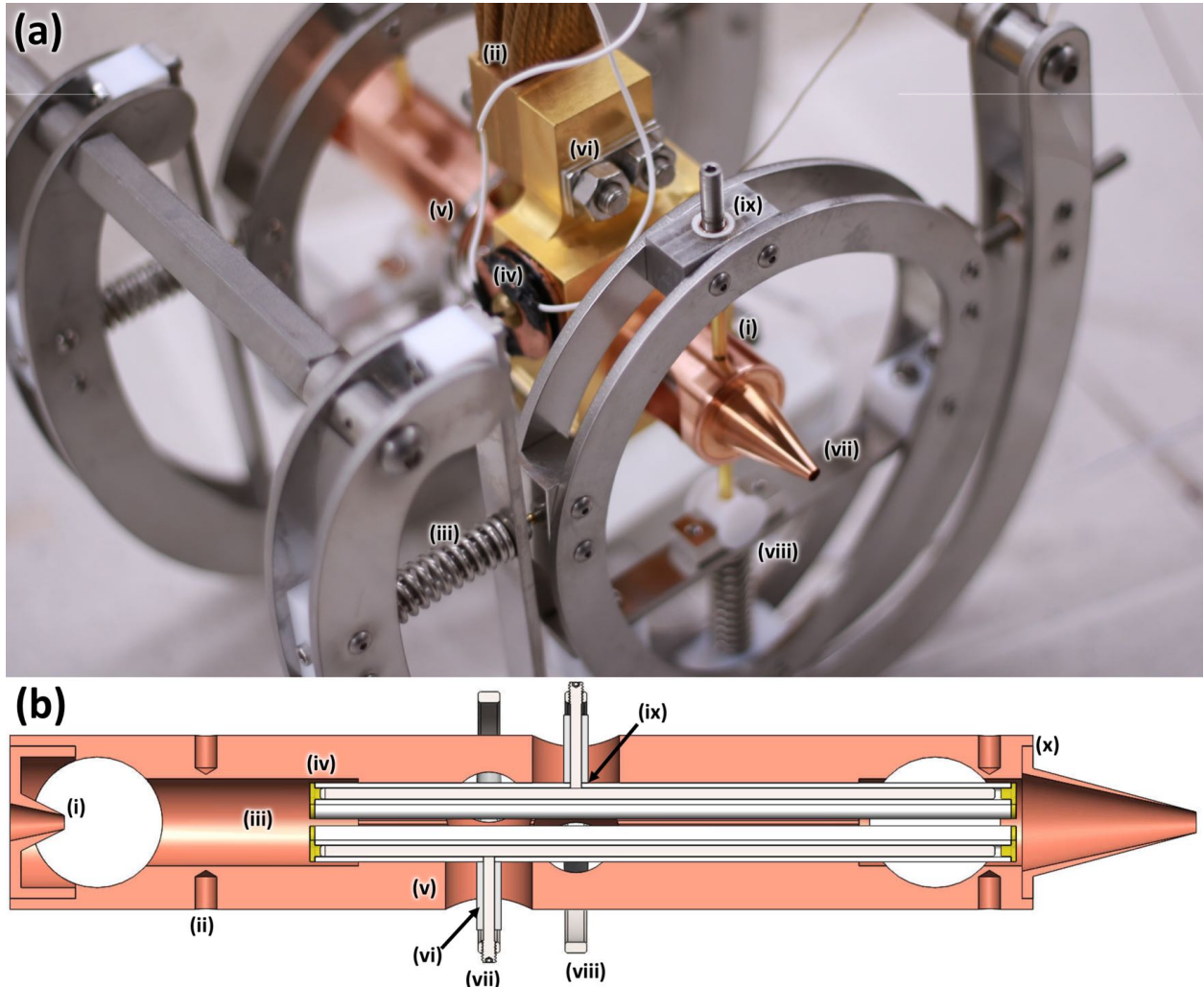
Figure 4.7: (a) A view of Hexapole 1 after assembly. (i) 1/8" x 7/8" Ultem rods to insulate but support the structure. (ii) Flexible heat linkage, 1.4 W. (iii) Springs enabling fine positioning, four in total. (iv) Nichrome heater coil. (v) Blurry HV distribution ring barely visible. (vi) Invar plate spacers behind steel 1/4-28 nuts. (vii) Custom Skimmer, 3 mm opening. (viii) Teflon kinematic cylinder visible for translating but allowing twist. (ix) Fine adjust knob, 3/16-100, mounted in a phosphor bronze bushing, torr-sealed into a steel block. (b) A mechanical section view focusing on the scientific portion of Hexapole 1. (i) A rear skimmer, one piece with an outer rim that allows grease-only installation. (ii) Drill holes for slip-fitting thermally insulating Ultem mounts. (iii) Recess drilled for increasing surface path between the open end of the sapphire rod and the mounting block. (iv) Plastic caps glued onto the rods for further voltage safety. (v) One of six HV holes, $\varnothing 1/2$", used for feeding voltage to the electrodes. (vi) Plastic stubs for increasing surface arc distance in the vicinity of the feedthroughs. (vii) HV Pin which pokes down through the stubs and contacts electrodes. (viii) Distribution rings which HV pins thread into. (ix) Curved contact line where plastic stubs were glued to sapphire tubes. (x) Recessed solder joint for cryogenic skimmer.

in a very general sense. Suppose a material has a thermal conductivity $c(T)$ which varies with temperature T and is connected as a cylindrical rod between reservoirs at temperatures T_L and T_H. The total heat transfer rate, $\dot{Q}$, must be the same through every slice of the rod, neglecting radiative heat loads, and will induce a temperature change through a thin slice dx of the rod of the amount

$$dT = \frac{\dot{Q}}{c(T) \cdot A/dx}, \tag{4.9}$$

where A is the cross sectional area of the rod. Rearranging and integrating:

$$\int_{T_L}^{T_H} c(T)dT = \int_0^L \frac{\dot{Q}dx}{A}, \tag{4.10}$$

$$\bar{c}\Big|_{T_L}^{T_H} = \dot{Q}L/A, \tag{4.11}$$

where $\bar{c}$ is the antiderivative of c. We may proceed using the data from [74] for slightly glass-filled Ultem 2100, which shows 0.04 W/m°K at 10 °K, 0.4 W/m°K at 300 °K, and an approximately straight line on a log-log plot in between. It follows that $c(T)$ may be approximated as:

$$c(T) = \alpha T^\beta, \quad \beta = \frac{\log\left(\frac{0.4}{0.04}\right)}{\log\left(\frac{300}{10}\right)} = 0.68, \quad \alpha = \frac{0.4}{300^{0.68}} = 8.5 \times 10^{-3} \text{ W/m/(°K)}^{\beta+1}, \tag{4.12}$$

so that,

$$\bar{c}\Big|_{T_L}^{T_H} = \frac{\alpha}{\beta+1}T^{\beta+1}\Big|_{10°K}^{300°K} = 73 \text{ W/m}, \tag{4.13}$$

and finally with $A = 7.9$ mm^2 and $L = 20$ mm, we have rearranging Eq. 4.11:

$$\dot{Q} = 73 \text{ W/m} \times 7.9 \times 10^{-6} \text{ m}^2/(0.02 \text{ m}) = 0.029 \text{ W}. \tag{4.14}$$

A table of thermal conductivity integrals with $T_L = 4$°K and various T_H is provided in [71, App. A2.1]. No value is included for Ultem, but the listed polymers have very similar values to that found above in Eq. 4.13, for example Teflon is listed as 70 W/m. It is also worth pointing out that the conductivity integral between room temperature and 4 °K only differs from that between room temperature and 50 °K by 10%. This is symptomatic of the asymmetric distribution of thermal gradient, with most of it occurring in a very small section, and the majority of the plastic closer to room temperature since this is where the thermal conductivity is larger.
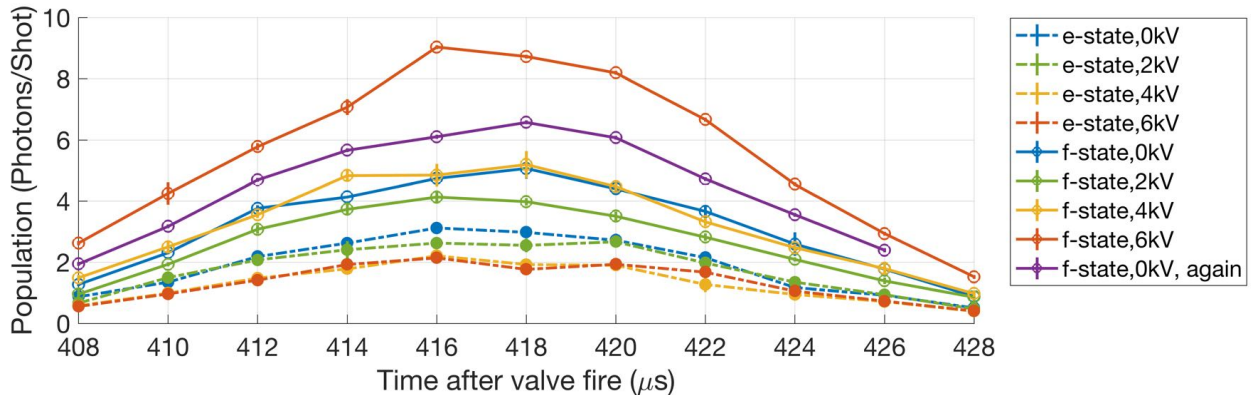
Figure 4.8: Flight profiles of OH after the Hexapole. Voltage is seen to have an effect. The effect is sometimes disordered, and shows strong hysteresis. Note how for the $|e\rangle$ state, signal decreases monotonically with voltage, as one might expect, but for the $|f\rangle$ state, signal first decreases before increasing. Upon returning to the 0 kV trace, the value is larger than both the original 0 kV and 2 kV traces. These traces were recorded chronologically in the same order as the legend. The data were collected on November 27, 2018, with a 16.5 cm valve position setting, which in this setup corresponded to a 10 cm true valve skimmer distance, a 9.7 °K hexapole temperature, and an ND1 filter on the fluorescence collection stack.

4.3.4   Performance

The hexapole did not even come close to performing as intended, particularly as far as high voltage is concerned, with arcing behavior observed at only one third of the designed operating voltage. One of the first datasets is shown in Fig. 4.8. A surprising effect was observed, whereby the signal was first decreased and then increased. At first it was suspected that this could relate to the focusing behavior of the device in some way, since by analogy with lenses over-focusing can be problematic. This does not make sense at such low voltages however, and does not explain the even more surprising observation of hysteresis behavior, where the signal with the hexapole off was observed to decrease dramatically after having operated the hexapole at voltage for a while.

Ultimately, these effects were attributed to the buildup of very significant patch charges on the surface of the sapphire, significant enough to simulate the hexapole having been charged to several kilovolts of voltage. This effect was in fact anticipated during the design stage, and a workaround developed- regular polarity reversal. In the design stage, it was expected that charges
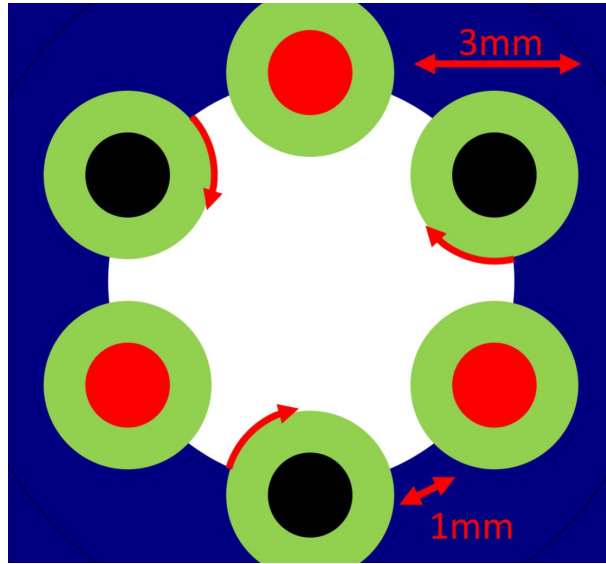
Figure 4.9: This schematic diagram illustrates how surface charges donated from the conductive grounded hexapole mounting block (blue) are able to rather efficiently coat the surface of the sapphire tubes insulating the positively charged hexapole electrodes (black).

might buildup due to ionization of carrier gas upon interaction with the electric field and the cryogenic sapphire surface, but in fact a more potent mechanism exists, see Fig. 4.9. Despite fillets designed for minimizing surface currents, conduction electrons from within the grounded copper block are likely able to migrate out onto the surface of the sapphire tubes. This also suggests that charging the hexapole with only negative voltage and ground could help reduce the effect, since the copper block only has negative charges to donate to the surface, not positive.

While true voltage alternation requires complex tri-polar switch output configuration, effective alternation may be achieved with a unipolar setup by connecting each set of three hexapole electrodes to the output of a switch which connects between ground and minus high voltage. The switches can then take turns charging the hexapole, so that the field direction reverses each time, rod polarity is always negative relative to the grounded copper block, and unipolar push-pull architecture is maintained. Operating in this manner did indeed resolve patch charge issues, and led to the data shown in Fig. 4.10. One downside of this mode of operation is the reduced maximum hexapole voltage which may be applied, assuming that availability of MOSFET switches limits the
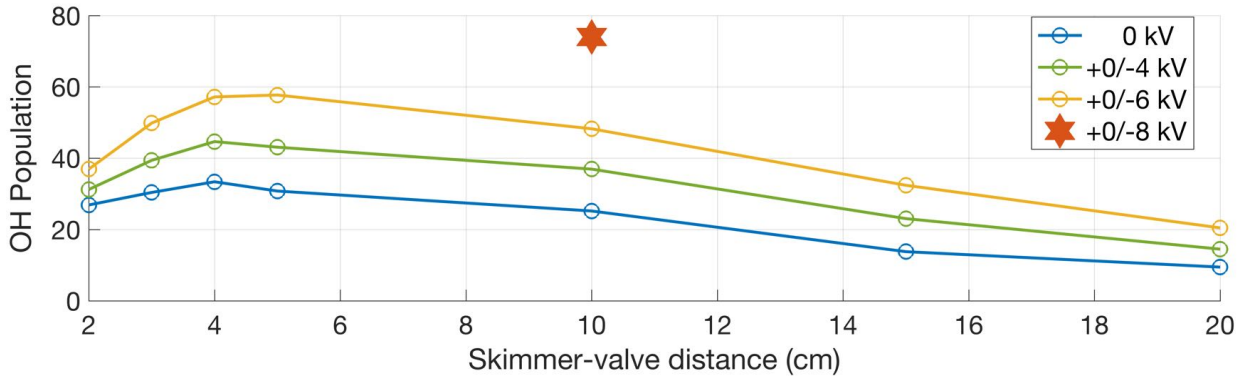
Figure 4.10: Peak OH population, various valve-skimmer distances, several voltages. Much longer averaging and runtimes without hysteresis and with sensible trace ordering. Vertical axis is arbitrary, the numbers may be derived from an area integrating script applied to raw data traces akin to those in Fig. 4.8.

maximum absolute value of voltage. There is also the important question of what influence the non-bipolar hexapole voltages have on fringing field distributions. Generally speaking, the fringe field magnitude should become much larger, since now on average the hexapole rods are charged instead of neutral. To some extent, this may be a welcome effect as far as maintaining polarization is concerned, since without any electric field, the well focused $|f, \pm\frac{3}{2}\rangle$ molecules would be liable to re-project into $|f, \pm\frac{1}{2}\rangle$ after spending time in a region of little or no field.

As far as the thermal performance of the device, a thermal conduction of 1.4 W/°K was achieved, based on the observed second stage cryostat temperature of 7.2 °K, which suggests via the capacity of the device that a 3 W heat load is incurred. This, together with the measured temperature of 9.4 °K close to the hexapole suggests that 3 W leads to 2.2 °K temperature rise, hence the stated 1.4 W/°K. While the thermal conductivity is as intended, the heat load is much higher than predicted. This prompted a thorough investigation that ultimately implicated blackbody radiation as the culprit. At one point we even disconnected the hexapole from its mounting structure so as to take away any heat load due to the thermally insulating mechanical Ultem mounts. These were completely exonerated, as the observed temperature after their removal did not detectably improve.

4.4   Cryogenic Hexapole 2

Primarily motivated by the failure of the first Hexapole to hold the desired voltages, we undertook a new hexapole with a completely different high voltage strategy. Fearing significant delays to our long term goals, I pushed for significant reuse of our earlier design, especially with regard to the mounting structure. The result is shown in Fig. 4.11. The mounting structure and thermal clamp are completely reused, but the copper hexapole mounting block is replaced with a thin copper sheath for transferring heat to the skimmer, inside of which sits an Ultem plastic mounting tube, and inside of that a more traditional stainless steel hexapole. The steel is allowed to reach some equilibrium temperature set by the balance between weak heat transfer through the Ultem tube to the cryogenic copper transfer tube, and radiative coupling of the high emissivity Ultem to the room temperature vacuum chamber. A room temperature skimmer is used as a back aperture, and HV distribution is simplified and achieved via steel setscrews that also fix the position of the internal hexapole. These screws sit in a plane orthogonal to the section plane and are thus not visible.

Cryogenic hexapole 2 was a very quick turnaround relative to hexapole 1, with first tests occurring within one month of those for hexapole 1. The second hexapole performed significantly better as far as voltage application, by more than a factor of two. However it seemed to be clogging limited, showing an earlier falloff with respect to reducing valve-skimmer distance, and a weaker peak signal compared with hexapole 1. These results are summarized in Fig. 4.12. One obvious explanation for this would be the increased temperature of the hexapole, a sacrifice made in light of the importance of first verifying voltage capability before anything else. It is unsettling however that the first hexapole appears to perform better even at larger distances where the clogging should not yet dominate. This could be attributed to differences in the alignment of the collection system and laser, but it is difficult to say.
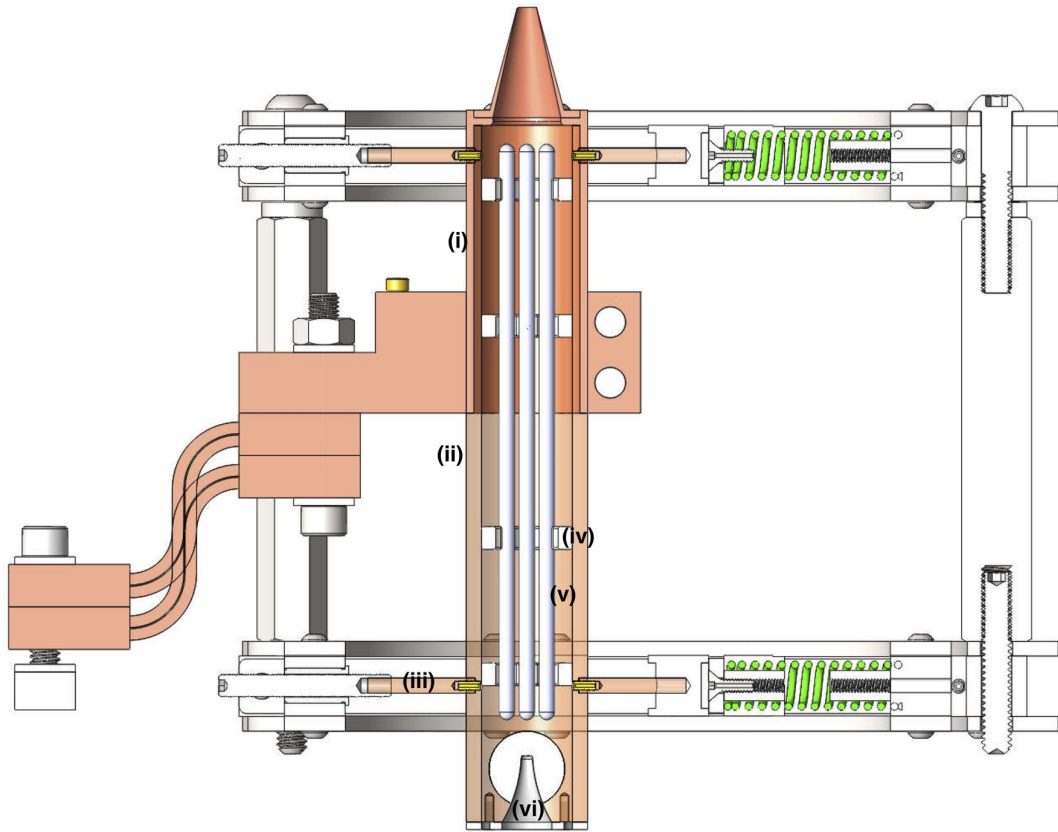
Figure 4.11: This section view shows Hexapole 2, and how it was designed to fit inside of the same mounting structure used for Hexapole 1. (i) A copper transfer sheath transfers heat from the skimmer. (ii) An insulating Ultem tube extends the entire length of the hexapole, allowing a stainless steel hexapole to be voltage isolated within. (iii) Ultem stalks are used like in Hexapole 1, but this time with threaded PEEK 2-56 screws connecting them directly to the Ultem sheath. (iv) One of four HV rings mount to every other hexapole rod in two places each. The rearmost rings also connect to HV wires via setscrews mounted in the Ultem orthogonal to the section plane and this invisible here. (v) One of six hexapole rods, about 50% longer than in Hexapole 1, chosen so as to increase effective hexapole position tuning flexibility by varying the turn-on and turn-off of the device. (vi) Commercial rear skimmer, with nearby gas egress openings visible in the Ultem tube.

4.4.1   Cryogenic Hexapole 2.5

Hoping to obtain the best of both worlds, an updated version of Hexapole 2 was created capable of reaching full cryogenic temperatures while leveraging the favorable voltage performance of Hexapole 2. A section view showing this is available in Fig. 4.13. Relative to Hexapole 2, Hexapole 2.5 features HV safety shoulders built together with the HV tube as a single piece, so
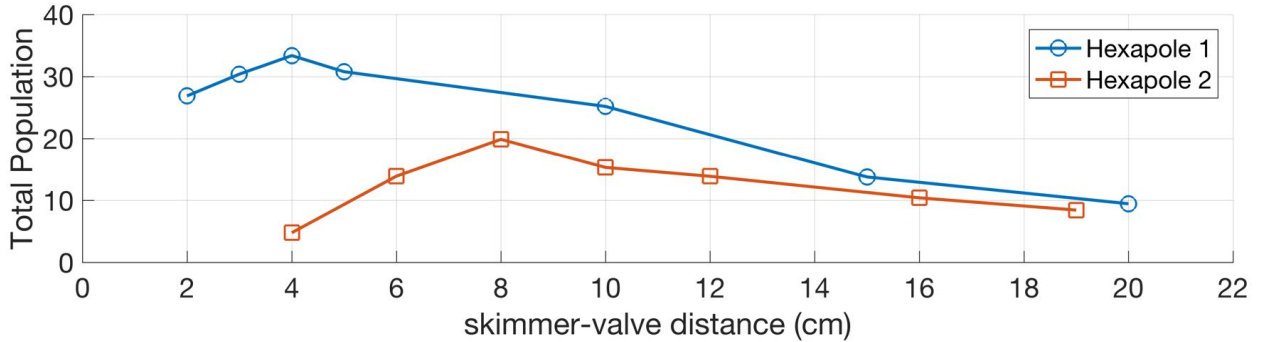
Figure 4.12: Hexapoles 1 and 2 are compared regarding maximum signal with no applied voltage as a function of valve-skimmer distance. The second hexapole turns over at larger distance and appears slightly lower in the large distance wing relative to the first. The original figure was generated on January 7th, 2019.

that a cryogenic copper shield can slide over the entire Ultem HV tube instead of only covering a small portion and serving as an interconnect to the cryogenic skimmer. To our chagrin, the device featured a significantly worsened high voltage performance relative to Hexapole 2, which ultimately turned out to be a fault related to surface arcing on the Ultem tube itself, despite this not having limited behavior in Hexapole 2. This was confirmed by successively disassembling the device, pumping back down, and applying high voltage. Even with all of the shielding and even the mounting structure removed, leaving only the Ultem mount and the steel hexapole within, the arcing persisted.

The reason for the poor performance of the Ultem remains a mystery. Organic polymers are not inherently bad, as evidenced by the ubiquitous use of polymethacrylate, or acrylic, in HV situations [75]. In fact, organic polymers often outperform glasses and ceramics, possibly due to their reduced dielectric constant, which controls field amplifications near voids and triple points [75, pp. 776]. Another possible explanation of the difference in performance between Hexapoles 2 and 2.5 relates to their surface treatment, with the latter much more smooth than the former. Evidence exists for a benefit to surface roughness [76, Sec. 8.3.11]. It is also possible that cryogenic temperatures negatively influence performance, as observed for some polymers [77, Sec. 14.4].

As far as cryogenics are concerned, hexapole 2.5 performed better than any other, validating
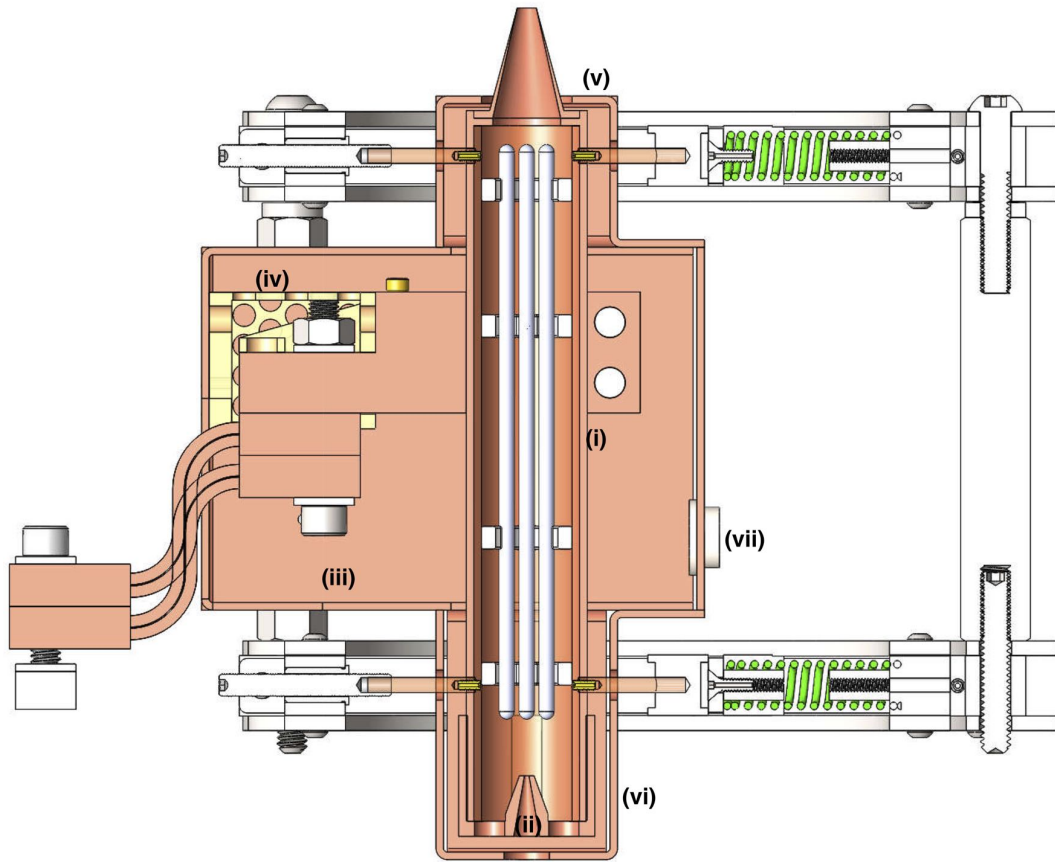
Figure 4.13: This section view shows Hexapole 2.5. (i) The outer copper sheath extends past the thermal block, all the way to the rear of the hexapole, and the Ultem tube inside is 1/16" thick everywhere, rather than 1/8" for half of its length in Hexapole 2, see Fig. 4.11. (ii) The rear skimmer is machined together with a cylindrical can designed to mate to the outer diameter of the outer copper sheath, like the rear aperture of Hexapole 1 except in that design the mate was on the ID. Holes outside this aperture skimmer allow steady state gas egress. (iii) A large box-like first-stage radiation shield is installed. (iv) An Ultem part directly mounts the radiation shield to the second stage thermal clamp, but with extremely low thermal conduction thanks to a 3D printed hole array. (v) A smaller shield boxes covers the front of the hexapole, except for the skimmer cone. This screws into the larger shield box. (vi) Another shield box covers the rear, except for an egress hole for the beam. These shield parts are all bent to shape and then annealed. (vii) Macor bushings insulate $\varnothing 1/2$" holes for HV feedthroughs. The other sits inside the smaller rear shield box in the un-shown sector.

the blackbody shielding technique incorporated. Surprisingly, this did not lead to significant clogging mitigation relative to hexapole 2 at zero electric field where the high voltage performance is not relevant. In fact, by varying temperatures, the magnitude of the cryogenic benefit was directly
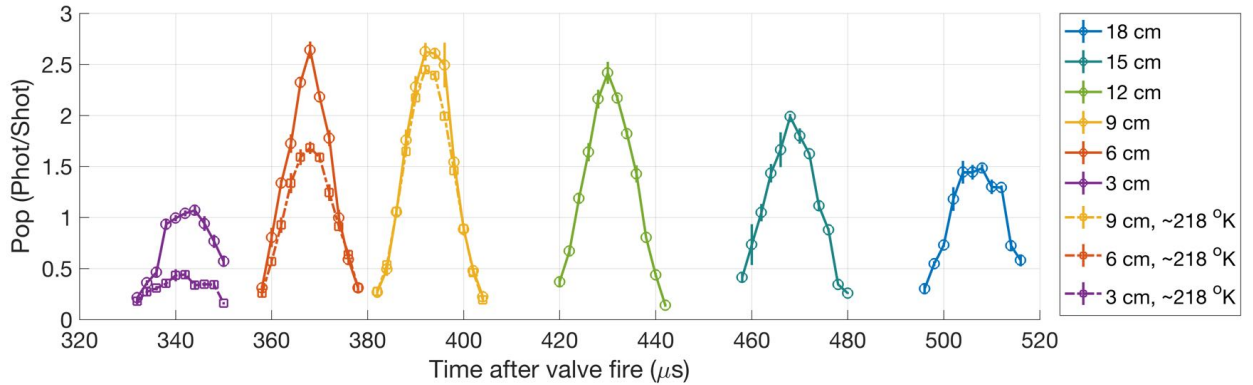
Figure 4.14: Time of flight traces for different valve-skimmer distances and at two temperatures elucidate the clogging performance of Hexapole 2.5.

investigated, and found to be far smaller than anticipated, see Fig. 4.14. One explanation for this could be the negative influence of surfaces positioned orthogonally to the beam-line, such as those formed by the HV distribution rings in Hexapoles 2 and 2.5 but not on Hexapole 1. Another explanation could relate to the adsorptive properties of the materials involved in the two hexapoles. In Hexapole 1, the surfaces presented to the molecules were lightly greased sapphire and semi-rough copper from the wire-EDM process, while in Hexapole 2 and 2.5 the surfaces are un-greased highly polished steel. It is conceivable that the former would perform better, in which case one simple test would be to lightly grease the stainless steel.

Some of the technologies involved in the cryogenic performance of Hexapole 2.5 are worth some further discussion. Firstly, the plastic component visible in Fig. 4.13(iv) demonstrates the power of 3D printable thermoplastics for custom thermally insulating structures with good mechanical rigidity. Thermal simulations of this part indicate conductance in the vicinity of $10\,^{\circ}\mathrm{K/mW}$, which includes a factor of 2.5 achieved by the convenient removal of material in a hole pattern 4.15 This patterning not only reduces thermal conductivity, but also aids in the removal of 3D printing scaffold material and reduces print time. It is also possible to reduce the thermal conductivity of 3D printed parts by reducing infill, so that voids are intentionally left inside of a structure. This seems inadvisable given the likelihood of virtual leaks to the vacuum chamber, although this may
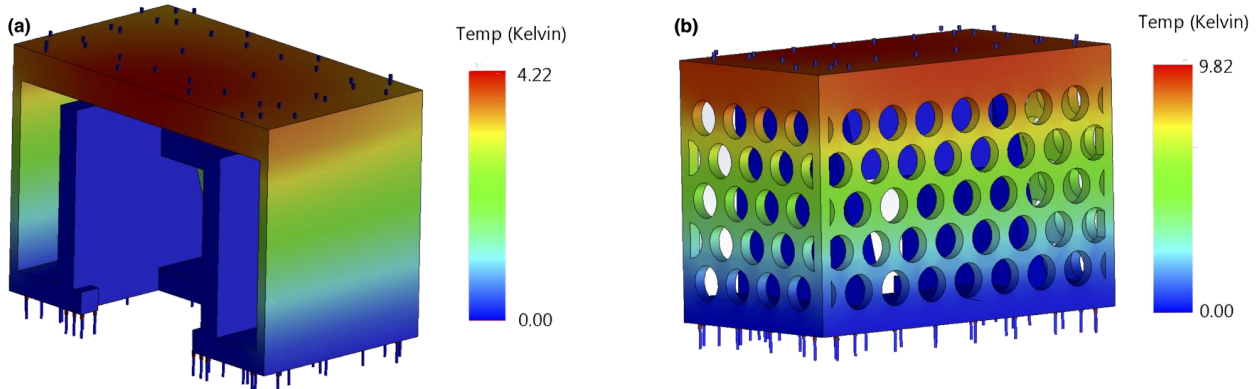
Figure 4.15: Thermal simulations of an Ultem isolator used as a mechanical interconnect between Hexapole 2.5 and its radiation shields, with (b) and without (a) extra holes. In each case, a 1 mW load is applied across the device, and the base is fixed at 0 °K, so that the reported temperature on the upper surface of the device rises with smaller conductance.

not be relevant for parts that will sit between two cryostat stages and therefore lie entirely below the freezing point of all relevant gases after cool-down. Secondly, the radiation shields are manufactured using sheet-metal bending techniques. Sheet-metal bending techniques are not often utilized in the laboratory, often reserved for high throughput manufacturing, but in Hexapole 2.5 they really enable geometries that would be vastly more challenging to achieve with traditional fastener-based methodologies. Using appropriate design modules in Solidworks, the radiation shields are designed to be folded into the desired shape after first being water-jetted out of copper sheet. At the time of this writing, water-jetting is available in the physics shop with nearly next-day service and only 1-2 hour operator costs. Bending is hard to do accurately, but this is generally not required for radiation shielding, and if accuracy is required, commercial CNC bending is available with 0.005" tolerances on hole positions for the final folded part[b] . The act of bending reduces thermal conductivity by work-hardening the joint, but where conductivity is critical, this can be addressed by annealing.

---

[b] Rapid Sheet Metal offers 10-day service and something like $500 per design, way less with quantity.

Table 4.2: The historical record of coupling molecules into the decelerator, with and without hexapoles, is presented. Hexapole 1 is seen to provide the greatest peak signal by 48%, and the greatest total flux by 75%.

Date	Situation	Velocity Spread (m/s)	Peak Signal (photons/shot)	Total Flux (arb)
Aug. 2, 2018	No Hexapole, 8° K Skimmer	10.7	3.2	95
Aug. 21, 2018	No Hexapole, Hot Skimmer	11.1	4.8	156
Dec. 04, 2018	Hexapole 1	14.1	7.1	275
Jan. 07, 2019	Hexapole 2	11.7	3.3	119

4.5   Guided Flux

One important way to gauge the performance of these hexapoles is to study the flux of molecules which they are able to couple into the decelerator when it is run in a guiding mode. We can use this to compare the hexapoles together with earlier measurements without a hexapole to get at the key question of whether a cryogenic hexapole is capable of improving performance relative to the non-cryogenic, hexapole-free, commercial skimmer approach. A selection of several measured fluxes in guiding spanning the hexapoles discussed here are shown in Tab. 4.2. In all cases, the skimmer used features a 3 mm opening diameter, and the DC guiding voltage used is 6 kV, a value which gives a transverse phase space acceptance comparable to that of F mode decelerator operation, see Sec. 5.2.3. Overall, only Hexapole 1 is seen to outperform the commercial skimmer option, and that by less than a factor of two. It is still an accomplishment to have exceeded the previous best, but a far cry from the thirty-fold gain comparing a room temperature and cryogenic skimmer without any coupling to the decelerator [55].

4.6   Cryogenic Hexapole 3

After an interlude for attempts at collisional studies in the decelerator and between parallel plates, it was time to move on to other things, but the lessons learned on the first two and a half hexapoles could one day be brought to full fruition in a final iteration of the device. By abandoning the emphasis in Hexapoles 2 and 2.5 of reusing the mounting structure developed for Hexapole 1, it should be possible to further increase the surface path distance between electrodes, by say an additional factor of 3-5 beyond the factor of 3 already implemented between Hexapoles 1 and 2. In addition, by carefully following the principles of triple point shielding laid out in [78, Sec. 4.3.3], extra safety should be reachable. In particular, true shielding of the triple points that exist between the Ultem tube and the internal HV distribution mounts of Hexapoles 2 and 2.5 is not really possible given the external copper tube and requirement of sliding installation inside.

In addition to making a further dramatic increase in surface arcing path-length and triple point shielding, the next generation hexapole will need to address the observation of limited cryo-adsorption performance. In addition to the reduction or removal of orthogonal surfaces and the investigation of surface materials and the performance of grease, another possibility would be to reduce all surfaces, even parallel ones, presented to the beam-line. One way to move in this direction would be to reduce the radius of the hexapole rods, which would introduce some dodecapolar deviations from the ideal hexapole fields, likely a minor effect on top of the clogging behavior. Another rather drastic possibility would be to remove the front skimmer entirely. It is difficult to predict what would result from this, but if the skimmer is still reducing the beam flux relative to what it could be with no skimmer, a big win could be obtained. Simultaneously, without the skimmer the flux onto the hexapole rods would be significantly increased, exacerbating any clogging issues associated with these surfaces.

An important factor to keep in mind is the effective transverse size of the source coming from the valve. If the valve generates molecules with a broad enough spread in their initial transverse coordinate relative to what the decelerator can accept, this can pose a limit on what can be obtained

by adding a hexapole. The reason for this is that with a suitably broad initial distribution, even an extended time in free flight may be incurred without significant broadening of the portion of phase space that overlaps with the acceptance of the decelerator. It is difficult to measure this initial transverse spread of the molecules, but simulations of transverse oscillations in the decelerator suggest the value may be somewhat large, see Sec. 5.3.

4.7   Conclusions

Several cryogenic hexapoles have been designed and tested. High Voltage issues have proven more pervasive than initially expected. Clogging issues within the hexapole have proven difficult to fully understand. As far as the absolute comparison between what may be obtained with a cryogenic skimmer and hexapole and what may be obtained with a traditional skimmer, thus far nearly a factor of two gain has been demonstrated, despite the high voltage and clogging underperformance.

Chapter 5

Optimized Deceleration

Over the past two decades, Stark deceleration has enabled groundbreaking collisional [79, 80, 81] and spectroscopic [82, 83, 84, 85] studies of a variety of species [86]. Subsequent trap-loading greatly enhances interrogation time for such studies [87] and opens the door for further cooling and manipulation [44, 88]. Stark deceleration preserves the high densities generated by supersonic expansions, and these perform best with the lightest and fastest carrier gases. This therefore promotes the continual hunt for more efficient and longer devices. In the following the conventional decelerator geometry will be discussed, followed by an extensive discussion of alternative techniques and improvements, which are shown both theoretically and experimentally to provide promising improvements in molecule flux and decelerator efficiency. Finally some details of the manufacture of an actual device, the third generation of the OH experiment, are provided.

5.1 Conventional Decelerator Geometry

Much like related work in charged particle accelerators [89], a neutral particle decelerator is required to satisfy two key principles:

(1) A particular candidate particle known as the synchronous molecule must be manipulated as desired by the device, e.g. slowed from $800 - 50$ m/s.

(2) Other particles of similar initial conditions to the synchronous molecule must also possess similar final conditions.

This second principle is known as phase stability, and is crucial to the overall performance of the device as far as flux or brightness is concerned.

Neutral particle decelerators face an incredible setback relative to charged particle accelerators, in that it is vastly harder to apply forces on neutral particles. Specifically, the device I will soon describe can accelerate hydroxyl radicals at ~ 200 km/s/s. If hydroxyl cations were instead placed in the largest electric fields generated by the device of about 100 kV/cm, they would experience an acceleration given by:

$$\frac{q_e \cdot E_{\text{max}}}{m_{\text{OH}}} = 5.5 \times 10^9 \text{ km/s/s.} \tag{5.1}$$

This constitutes a factor of over ten million. But is this truly fundamental, or technically limited?

Applying forces on neutral particles requires the application of gradients in electric field magnitude, and the magnitude of these gradients depends on the miniaturization of the geometry the electrodes. It becomes challenging to develop a truly fair comparison, but underneath all of the details about electrodes and geometries, electric fields are always generated by charged particles, regardless of whether they are conduction band electrodes in some material. The force on a neutral particle by a charged one scales as r^{-4}, while that between charged ones scales as r^{-2}.

In any case, once the factor of ten million setback is taken into account, neutrals have the nice property that the forces which act on them depend only on the magnitude of the external fields, and not its direction. This makes it possible to generate large magnitude electric fields with the direction of the field orthogonal to the beam-line, which is precisely the trick utilized in the first Stark decelerators [90]. The design of this decelerator was replicated here in the Ye group, first at a length suitable for expansion with Xenon, then later with Krypton, and most recently with Neon. Pairs of cylindrical pins are arranged alongside the beam-line, so as to apply a large but localized field magnitude across it for maximum field magnitude gradient. Successive pairs are rotated ninety degrees relative to one another, which is relevant to transverse confinement, and every fourth pin is connected up to the same backbone electrode.

Diagrams such as that shown in Fig. 5.1 are useful in understanding the operation of the

Configuration A
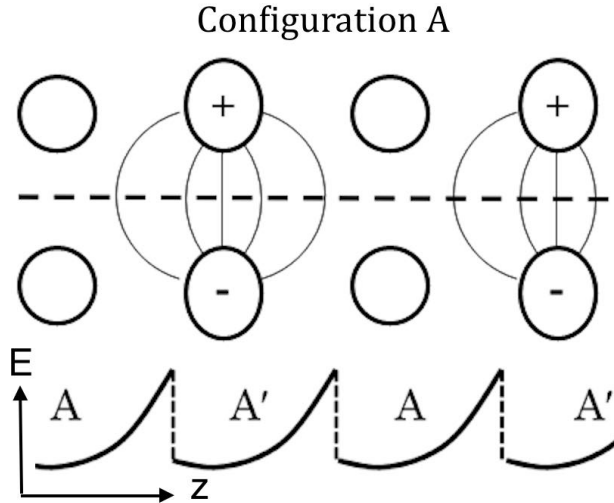
Figure 5.1: Voltages, electric fields, and on-axis potential energy in a conventional pin decelerator [90]. Pin rotation indicated by representation as slight ellipses rather than circles. Electric fields density corresponds to the potential experienced by molecules. The horizontal dashed line indicates the central axis of the device, and the potential energy of the target or synchronous molecule as it transits this axis is shown below the pin pairs. A' indicates the translation (and rotation) of the drawn configuration of fields and voltages to the next pin pair(s). Vertical dashed lines indicate change in potential energy of a molecule during a switching event between configurations.

device. Molecules approach a region of strong electric field, trading kinetic energy for internal potential energy to compensate for their Stark shift, which describes the dependence of their internal energy on external electric fields. In the case of molecules whose internal quantum state shifts upwards in increasing external electric fields, i.e. with a positive Stark shift, entering a region of strong field results in a reduction of speed. At some point, the strong electric fields are turned off, and a different region of strong electric field is turned on further along the beam-line. If the strong fields are turned off before the synchronous molecule reaches the strongest fields, i.e. partway up the hill, phase stability is obtained, because a molecule that is ahead of the synchronous one will therefore exchange a greater quantity of kinetic energy for potential energy by climbing farther up the hill before the turn-off event. This molecule thus experiences a force restoring it to the location of the synchronous molecule. Of course if a molecule is too far ahead, it may pass all the way through the region of highest field prior to the turn-off event. Such a molecule is no longer phase
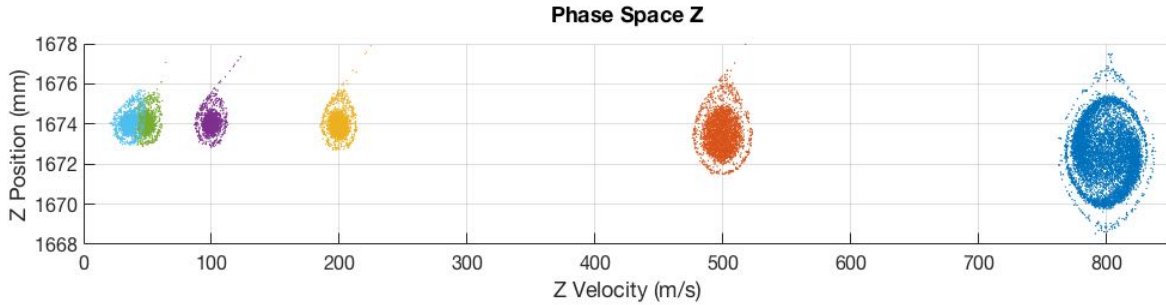
Figure 5.2: Longitudinal phase space plots of a Stark decelerator with varying final velocity. From left to right, $v_f = 33, 50, 100, 200, 500, 800$ m/s. Note how the size of the populated area reduces as the final speed is reduced. This is a direct reflection of how closely the synchronous molecule approaches the charged pin-pair, which in turn controls how far ahead a non-synchronous molecule may be while still experiencing a restoring force. Note also how the size reduces much more significantly between $800 - 500 - 200$ m/s then for any of the other speed reductions. This is described further in the main text.

stable and will travel farther and farther from the synchronous molecule. Thus there is a tradeoff between the deceleration capability of the device and the volume of its phase stable region.

This can be seen more directly from simulations of its behavior, such as in Fig. 5.2. The area of the region populated by molecules reduces as the deceleration is increased. However, the change in area seems to plateau and then stop, somewhere between $200 - 500$ m/s since all velocities below 200 m/s show nearly the same area. This can be attributed to the fact that all of these low speeds require nearly the same energy to be removed per stage of the decelerator, since the total energy removed can be calculated by the potential energy difference before and after the decelerator:

$$\Delta\text{PE} = \frac{1}{2}m_{\text{OH}}\left(v_i^2 - v_f^2\right). \tag{5.2}$$

Once $v_f << v_i$, ΔPE no longer various strongly with v_f:

$$\Delta\text{PE} \sim \frac{1}{2}m_{\text{OH}}v_i^2\left(1 - \left(\frac{v_f}{v_i}\right)^2\right). \tag{5.3}$$

With no variation in ΔPE, we expect no further change in the area of the regions populated in Fig. 5.2.

An important corollary of this idea relates to the parameterization typically used for spec-

ifying decelerator operation. Since the devices are periodic, it is convenient to parametrize the longitudinal coordinate with an angle, called the phase angle, and chosen to vary by 180° between one pin-pair and the next, so that a single voltage configuration applied to the device repeats itself after 360°. This parametrization also allows us to work independently from the choice of pin size and pin spacings for a given device. A decelerator is often operated so that a synchronous molecule with a given speed would always experience a turn-off event at the same phase angle ϕ (or $\phi+180°$), which then allows the operation of the device to be specified by only that angle. It follows from Eq. 5.3 however that very slight changes in ΔPE can lead to dramatic changes in the final velocity of the synchronous molecule, which also applies to ϕ since ΔPE $\propto \sin(\phi)$ and our device operates far from $\phi = \pi/2$. In earlier iterations of the code used for programming the switching sequence of our decelerators, it was necessary to specify the phase angle down to the thousandth of a degree in order to get the desired final speed within a few meters per second, which in turn required carefully hand-exploring the function mapping phase angles to final speeds.

It is also worth discussing some other features of the longitudinal phase space plots shown in Fig. 5.2. Almost all final speeds show a bullseye type pattern, with a halo of outer particles surrounding an inner core. This is discussed extensively in [91], and relates to the inefficiencies in the device that are the subject of the next section. However, there is additional structure evident within the inner core, especially for the molecular packet with 800 m/s final velocity. These molecules have not had their speed modified significantly by the simulated device, in which case the activity of the device is better described as "bunching" the molecules than "slowing" them. In the experiment, these bunched molecules would travel together with a large population of unaddressed molecules with initial longitudinal velocity and position unsynchronized with the timing of the device. These unaddressed molecules are nonetheless transversely focused, and in some cases with better efficiency than target molecules, and so constitute a rather large background signal relative to the molecules of interest. The reason these unaddressed molecules are not evident in this simulation is that the simulation only initializes molecules that are likely to be addressed, for reasons of runtime.

This in turn relates to the substructure evident in the inner core of the bunched molecules in

Fig. 5.2. This substructure is an artifact of incomplete phase space filling in the simulation, i.e. if the right molecules had been included in the initialization, the inner core would be more uniformly filled out and not feature any swirling. It is useful to keep an eye out for such artifacts as a way of monitoring whether the initialization assumptions of a simulation is valid. This swirling is not necessarily only an artifact however, and can in fact be relevant in the experiment as well. In [92], the rotating nature of the inner core in phase space is intentionally understood and exploited for minimizing the velocity spread of a beam exiting a decelerator.

5.2   Alternative Geometries and Configurations

Alongside the history of achievements enabled by Stark deceleration runs a parallel ongoing saga surrounding their efficient operation. Many important steps have been made, not only in understanding the flaws of the conventional pulsed decelerator [91, 93], but also in addressing them through the use of overtones [94, 95], undertones [96], or even mixed phase angles [92, 97]. Even with these advances, the outstanding inefficiencies of the pulsed decelerator, particularly with regard to transverse phase stability, have motivated alternative geometries such as interspersed quadrupole focusing [93] and traveling wave deceleration [98, 99, 100]. Although traveling wave deceleration takes a strong step in the right direction toward truly efficient operation, it comes with costs in system complexity and high voltage engineering. These costs can be partially addressed by the use of combination pulsed and traveling wave devices [101], or even using traveling wave geometry with pulsed electronics [102, 103]. Others continue to pursue brand new geometries aiming to enhance transverse acceptance without abandoning more reliable pulsed electronics [104].

5.2.1   Flaws in Conventional Deceleration

I begin here by describing more precisely these flaws in the conventional pulsed decelerator. It is useful to distinguish between two primary categories of performance breakdown:

(1) Breakdown associated with the discontinuous nature of the geometry.

(2) Breakdown associated with the nature of the phase stable region.

The first breakdown mechanism follows directly from the geometry of the conventional pulsed decelerator. Focusing only occurs in a given transverse direction every other pin pair. So if the speed of the beam is decreased enough, there is clearly a point at which molecules will be adversely affected. The same issue exists for the longitudinal direction. Switching events are required for molecules to experience restoring force in the longitudinal direction. When molecules do not encounter pin pairs with enough frequency, molecules again are adversely affected. Discontinuity breakdowns are thus further classified by their transverse and longitudinal manifestations– over-focusing and reflection loss– discussed further in [93]. These breakdowns can in general be described by a lower bound on the velocity of the beam:

$$v_z >> L f_{\mathrm{osc}}, \tag{5.4}$$

where z indicates the propagation direction, L indicates the distance between successive pairs of pins, and f_{osc} is the oscillation frequency of the molecules about the synchronous molecule. This latter parameter is not strictly well defined across the entire ensemble, but accepts a range of possible values according to the anharmonicity of the restoring force experienced by molecules with different deviations from the synchronous molecule. For typical operating conditions, $f \sim 1-2$ kHz.

This anharmonicity is at the core of the second kind of breakdown in performance of the pulsed decelerator, a breakdown which results in unwanted decreases in the flux of the device even without any of the issues associated with achieving low final speeds. In fact, the effect is already clearly manifested for devices operated in bunching mode without any slowing, refer to Fig. 5.3 for the following discussion. One way to understand these flaws is to think in terms of an unwanted coupling between transverse and longitudinal modes [91]. In other words, molecules are best focused transversely on their closest approach to the charged pin pair, and therefore molecules which deviate significantly from the synchronous molecule in the longitudinal direction experience better transverse focusing. It follows that the two directions of motion are strongly coupled to one another, and any full description of their equations of motion will not be separable. It also
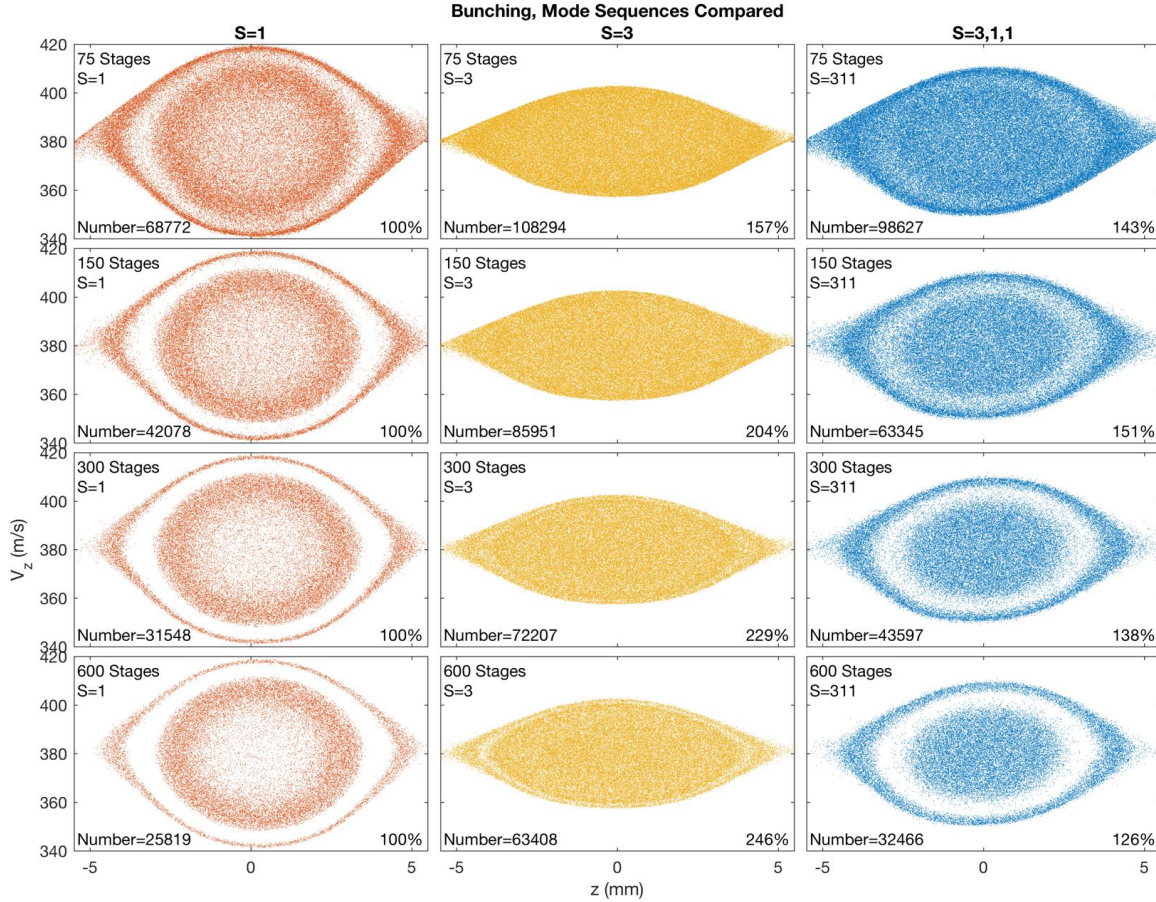
Figure 5.3: Longitudinal phase space plots after several types of bunching for several decelerator lengths. Column-wise, operation is in S=1, S=3, and a hybrid of these that I term S=311. Indicated percentages are comparable by rows, but suffer from a pernicious simulation artifact. Some molecules are included which actually pass through decelerator pins. The effect adversely influences the comparative survival numbers, but not the observed projection of phase space onto the longitudinal direction.

follows that molecules would survive better at greater distance from the synchronous molecule in longitudinal phase space, which agrees nicely with the observed sparsity close to the center of the left four plots in Fig. 5.3. The dead band and outer ring are best explained in terms of parametric amplification phenomena [91].

One way to address this is to allow the molecules to pass all the way through a charged pin pair, and only switch the fields after they climb a second hill. This is known as overtone opera-

tion [94], where the term stems from the fact that even without intending it, the standard operating mode supports overtone operation for molecules that happen to begin at triple the intended speed. Or one may intentionally reduce the switching frequency by a factor of three, typically indicated by the overtone parameter S as S = 3 operation, in which case standard operation may be referred to as S = 1. This gives rise to the much more homogeneous set of phase space plots in the center column of Fig. 5.3. Despite improved homogeneity, the plots are thinner than those for S = 1 by a factor of $\sqrt{3}$, which stems from the fact that molecules experience restoring force in the longitudinal direction with one third frequency. They can therefore deviate from the synchronous molecule by only a third as much kinetic energy as before, or $1/\sqrt{3}$ less deviation in velocity. An even more important drawback of S = 3 operation is that only a third as much energy may be removed per unit distance.

It is also possible to use a hybrid approach that we term S = 311. In this operating mode, one allows the synchronous molecule to climb all the way over a hill only every third time. It should be noted that $S = 31$ operation, where the synchronous molecule climbs all the way over a hill every other time, is not as useful because this molecule would only experience extra focusing in one of the transverse directions. This mode has the advantage of sacrificing less deceleration capability, since it is 60% as effective as S = 311 since 3/5 of all possible hills are climbed, but also addressing some of the coupling issues. As can be seen in the last column of Fig. 5.3, the sparsity closest to the synchronous molecule at the center of the phase space is addressed, although a parametric amplification dead band still persists. Unfortunately this mode also features an increased sensitivity to low speeds. Typically, S = 1 operation stops performing due to low speed breakdown below 50 m/s, and S = 3 below 150 m/s. The cutoff has not been studied thoroughly for S = 311, but a hybrid alternative exists, which is to use S = 311 for the bulk of the deceleration except when the speed drops below 150 m/s, at which point one returns to S = 1 for a brief enough time that the transverse-longitudinal coupling does not lead to excessive loss. In practice, this has yielded factor of $2 - 3$ improvements in the number of molecules which may be slowed or trapped in our experiment. I spent some time seeking to determine the source of the discrepancy between

this improvement and the smaller one predicted by the simulations leading to Fig. 5.3, and only years later caught a simulation bug relating to molecules with large transverse deviation ghosting their way through decelerator pins without being removed.

5.2.2   Alternative Geometries

Perhaps the most important class of alternative geometries for deceleration are those that are continuous in nature. These include both Stark [98] and Zeeman [105] varieties, and in principle provide a complete solution to breakdowns associated with the discontinuous nature of pulsed geometries, although in practice they face various low-speed challenges of their own.

The Stark devices, also known as traveling wave decelerators, feature cylindrical symmetry and use sinusoidal voltages to generate a macroscopic moving trap which can be translated or decelerated, and even brought to rest, at least provided high voltage amplifiers with bandwidth down to DC operation. The most common and as far as I can tell the only geometry used thus far, in three or four different groups, is that described in [98] with 0.8 mm diameter wires bent into 4 mm inner diameter rings, and connected up to eight different backbone electrodes. Their total phase space acceptance, at least for lower decelerations, is an incredible improvement over $S=1$ operation, skip ahead to Fig. 5.8 and compare $S=1$ to TW in panel (b).

There also exist a host of proposals for alternative pulsed geometries, including this one with interspersed quadrupole focusing stages [93], this one with charged wires for improved transverse behavior [104], and even a magnetic device with interspersed hexapole stages for use with NH molecules [106]. The first two may become less important thanks to the results discussed in the next section. Perhaps the earliest attempted device appears to have used actual parallel plates and relied on their fringing fields for focusing [107], as would have been necessary given the speed of available switches at the time.

I would be remiss if I did not introduce a few new geometry proposals of my own, as have my predecessors [45, Sec. 5.5], [23, Sec. 7.3]. The first, motivated by the trapping configuration discussed further in Sec. 6.4, is to add magnetic focusing to each decelerator pin. The idea would

be to use dual domain magnetic pins to superimpose 2D magnetic quadrupole focusing fields on top of the entire decelerator. This has the potential for a vey substantial benefit as far as transverse performance is concerned, see the vastly enhanced phase space volume shown in Fig. 5.4. Unfortunately, this design would suffer from very significant spin flip losses due to the presence of orthogonal magnetic and electric fields, see further discussion in Sec. 6.4.2. Molecules would likely shuffle back and forth between $|f, \frac{3}{2}\rangle$ and $|f, -\frac{3}{2}\rangle$, with any favorable focusing effect completely washed out. A molecule besides OH with a $J = \frac{1}{2}$ ground state (CH, CF, NO [108, 109]) could be much more likely to benefit from this scheme, since these molecules do not feature the electric field enhanced spin-flip behavior derived for $J = \frac{3}{2}$ OH molecules in Sec. 6.4.4. I do not provide a formal proof of this, but the path to the proof is that the spin-flip enhancement requires the Zeeman effect to have cubic order with orthogonal fields. This cubic order relates to the order of perturbation theory required to get a coupling between the $|f, \frac{3}{2}\rangle$ and the $|f, -\frac{3}{2}\rangle$ states, since their m number differs by 3. In a $J = \frac{1}{2}$ molecule, the m number differs by only one, so that the Zeeman effect would remain linear. I have also confirmed this by numerically diagonalizing sample Hamiltonians with $J = \frac{1}{2}$.

And secondly, it is my distinct pleasure to introduce the double-pin decelerator, a brand new design, specially featured thus far only here in this thesis. The double pin decelerator uses a pair of pins everywhere that a normal decelerator would feature only a single pin. Instead of overlapping each other, pairs of double pins point directly towards each other, with a well-controlled tip-to-tip spacing. Manufacturing of the device is therefore somewhat more sensitive, although the regions of the pins which need to be highly polished are reduced, and the tips of pins are by far the best polished portions when tumble polishing is performed. The key idea behind the use of pairs of pins is to obtain a focusing effect in both transverse directions each stage. It could also be thought of as a pulsed ring decelerator with each ring split in half to enable more significant deceleration forces by building up field between the two halves. The idea is to make use of two different field distributions obtained by charging the device up in different ways. One is like in conventional deceleration, when a pair of double pins are oppositely charged; the other occurs when the pair are
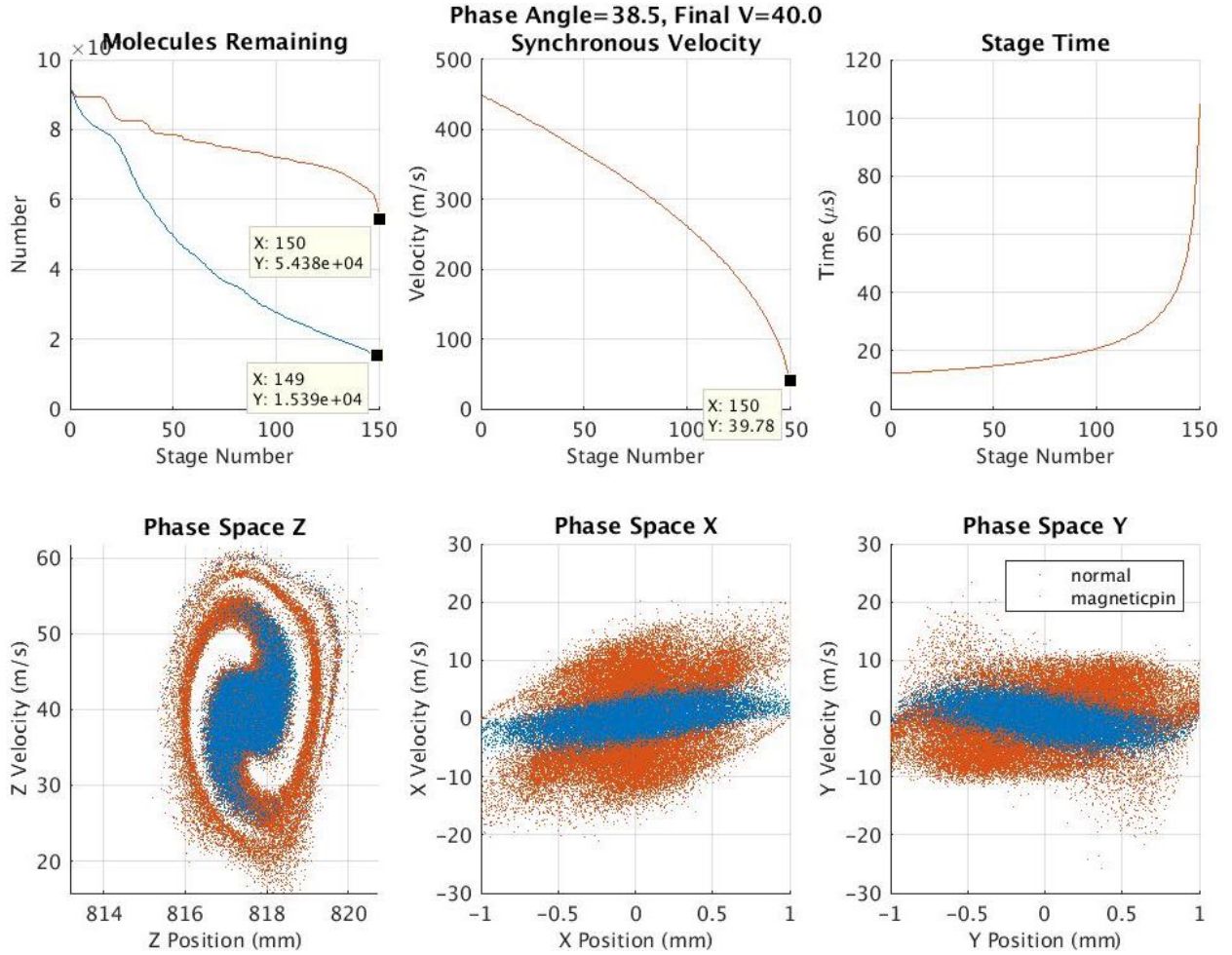
Figure 5.4: By adding magnetic domains to the pins of a conventional Stark decelerator, dramatic gains in transverse performance can be obtained. Here a factor of three is found, even with dramatically under-filled simulated phase space is evident by the swirling structure in the longitudinal phase space.

charged to the same voltage, but preceding and following pairs of double pins are charged to an opposite voltage. The field distribution resulting in the latter case would ideally resemble that in a ring decelerator. This concept is also very relevant for the conventional geometry, and discussed at length in the next Section, Sec. 5.2.3.

The field distributions generated by the device are shown in Fig. 5.5. The transverse focusing effect when pairs of pairs are charged to the same voltage is a big win compared with conventional operation, and even a modest win over a conventional decelerator with alternative field distributions
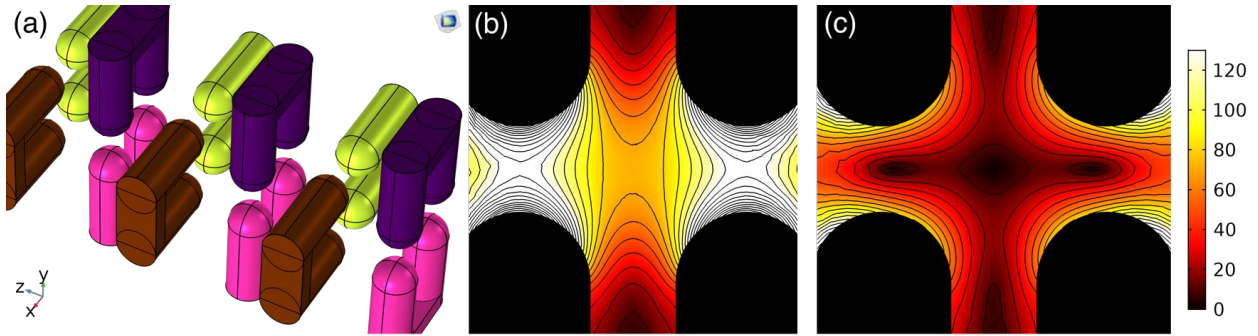
Figure 5.5: (a) Geometry view showing arrangement of the double pins. (b-c) $x - y$ planar cuts through a pair of double pins showing the magnitude of the electric field, color axis kV/cm, contours every 10 kV/cm. Pins have 3 mm diameter, 1.5 mm adjacent spacing, 2 mm point to point spacing, and 2 mm stage to stage spacing. (b) The slowing hill with the pair oppositely charged. 40% less height than conventional deceleration and some defocusing. (c) Now with the pair charged to the same voltage and un-shown preceding and following pairs of double pins charged to the opposite voltage.

run in the most promising of the alternative modes described further in Sec. 5.2.3. However it features a good bit of asymmetry, and has much better focusing for molecules that deviate along $\pm\vec{x}\pm\vec{y}$ compared with $\pm\vec{x}$ or $\pm\vec{y}$, see Fig. 5.5c. It also has 40% less slowing power than a conventional decelerator, and some defocusing in one direction while slowing. These drawbacks could be partially addressed by shaping the double pins more like half of a ring, but this would drastically reduce manufacturability.

5.2.3   Alternative Field Distributions

As far as the conventional geometry is concerned, a much more effective route to improved performance is to mix alternate field distributions into the deceleration scheme that feature strong restoring force in the transverse directions, refer to Fig. 5.6. In the conventional $S = 1$ operating mode [86], molecules approach a charged pin-pair, climbing a hill in potential energy. The hill is abruptly switched off partway up the hill, allowing molecules to have phase stability as discussed above. But it follows that molecules spend a significant portion of their flight passing between grounded pins. Conventionally, pins are always charged in bipolar pairs, in which case few field
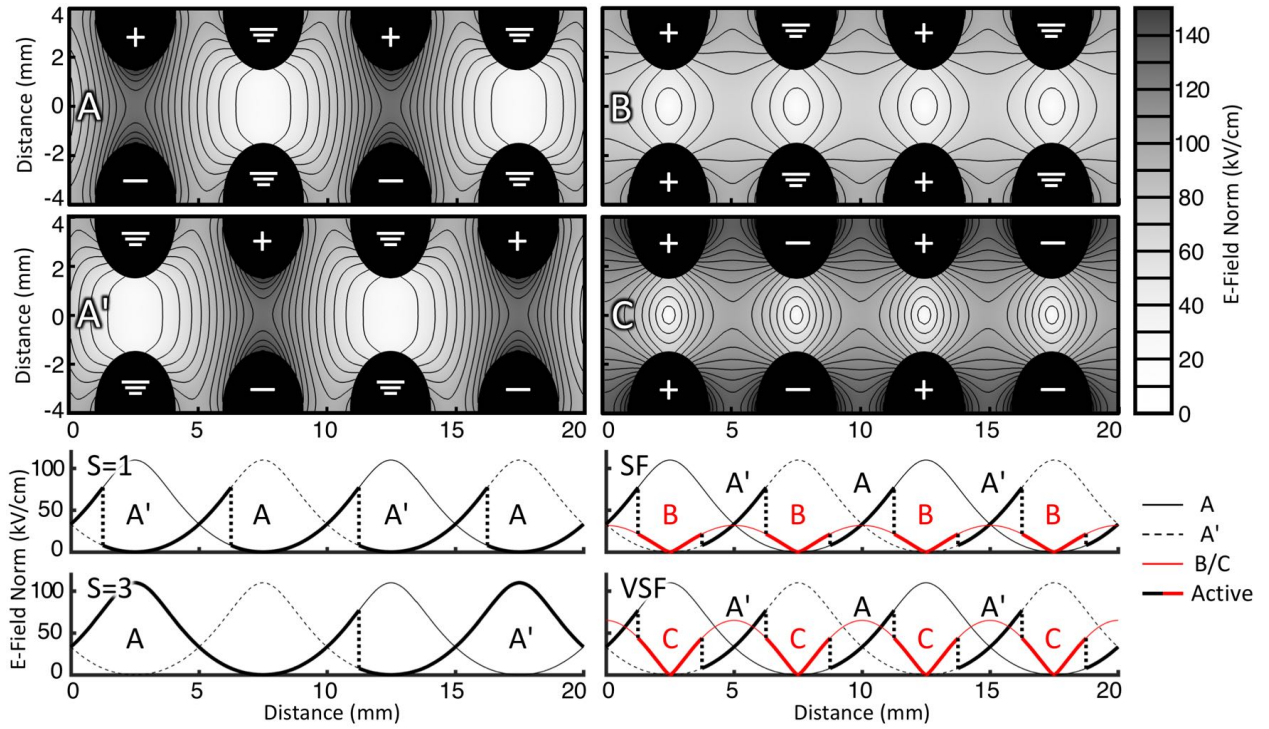
Figure 5.6: Alternate field distributions which can be used alongside the conventional one for greatly enhanced performance. Configurations B and C feature strong transverse focusing in the regions where molecules would normally pass between grounded pin pairs. On-axis energy diagrams are shown for several modes of operation incorporating these alternate configurations, with primes indicating translation to the next pin pair. In addition to S = 1 mode and its S = 3 overtone [94], a strong focusing (SF) and a very strong focusing (VSF) mode are introduced.

lines run toward the grounded pin-pairs, and those that do actually create a slight defocusing effect. This defocusing is not obvious in Fig. 5.6 because those plots are generated by slicing so as to include the decelerator axis but also make a 45° angle with all pin axes. This choice has the distinct advantage of allowing the plane to intersect all pairs of pins, making it much more clear where they are. However, the defocusing effect is significantly stronger in the plane orthogonal to the grounded pin pairs, and is thus obscured.

Useful alternate configurations can be created by applying voltage in a way that is not balanced between adjacent pin pairs. Once an imbalance exists, by charging up both pins in a pair to the same non-zero voltage, by only charging one pin in a pair, or even by unbalancing the de-

celerator power supplies[a] , the field lines will run between pin-pairs. Near the grounded pin-pair, these field lines create a focusing 2D quadrupole structure, much like this one used intentionally for trapping and controlling spin-flip losses [88]. By implementing these configurations when the synchronous molecule is flying between the grounded pin pair, but retaining the use of the conventional configuration for hill climbing, the longitudinal behavior of the device is unaffected while the transverse behavior is vastly improved. Regarding spin-flip losses, use of these configurations is cause for concern relative to the conventional $S = 1$ mode, since the molecules regularly pass close to small regions of zero electric field. I have done some rudimentary modeling of this effect, and found it not to be a concern. This is discussed further in Sec. 5.4. Utilizing the field distribution that results when both pins in a pair are brought to the same voltage gives rise to a new strongly focusing operation mode (SF), and utilizing the distribution where the adjacent pin pair is also brought to the voltage opposite the first gives a very strongly focusing mode (VSF).

It is also possible to obtain some of these effects without the need for rods being charged to three different voltages, by making use of the field distribution generated by turning on only a single pin, a somewhat focused mode (F). This is especially significant for being realizable immediately on existing devices with no new electronics, and offers 4-fold gains at trappable speeds, see the actual experimental data shown in Fig. 5.7. Operation in F mode requires alternating between the two choices of which pin in a pair should be charged and which should be grounded, in order to balance out the asymmetry of the resulting field distributions. The field distributions and on axis energy diagrams indicating when they are to be used are also shown in Fig. 5.7.

An important feature of the required time sequence of field distributions is that in switching from A to E configuration, a single rod may be switched off and the other left on, so that relative to $S = 1$ operation, the total number of switching events for each rod is unchanged. This is important because it means that the total energy dissipation in the high voltage system is unchanged, so that no improvements to the thermal dissipation capability of existing high voltage systems are

---

[a] It was once noted that unbalancing the power supplies led to improved performance on a conventional pulsed Stark decelerator. S. Hoekstra, private communication.
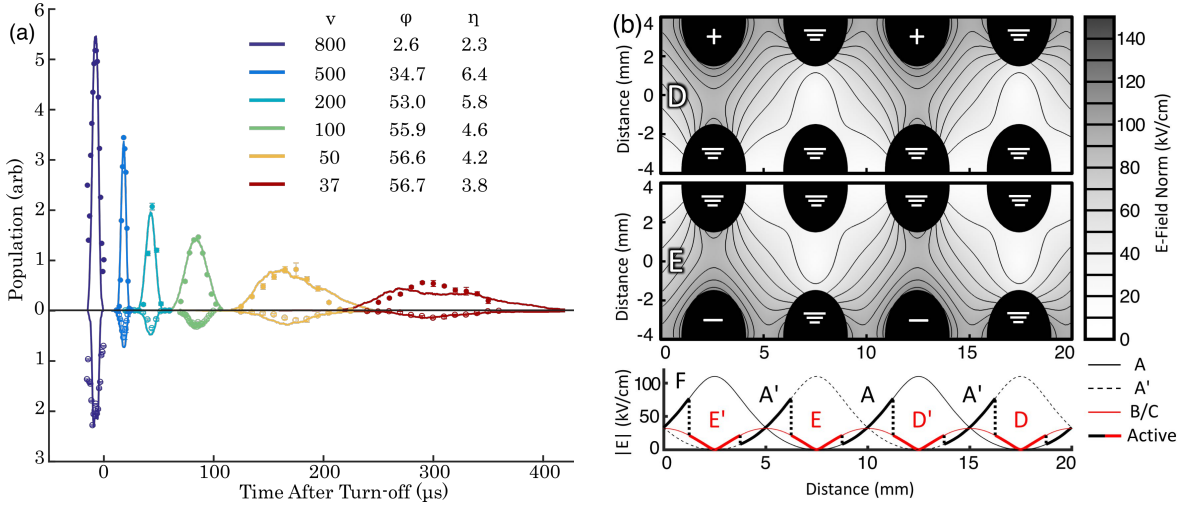
Figure 5.7: (a) Experimental Data Comparing S = 1 and F mode. Fourfold or greater improvements are found across many final velocities. F mode traces are shown with positive sign, and S = 1 with negative for visual comparison. Simulations are performed and reported as solid lines; good agreement is obtained. (b) Diagrams like in Fig. 5.6, but for F mode. At bottom, the potential energy of the alternate distributions (red) are still those for configuration B of Fig. 5.6 for reasons of simplicity, but the labels are as appropriate for F mode.

necessary. This discussion ignores the fact that turning off a single rod without the other also turning off actually requires more energy ($\sim 20\%$) than turning both off at the same time, see Sec. 5.5.5. In practice however, extra capacitance in the decelerator will primarily influence the thermal load on the external limiting resistors, which are usually not chosen within 20% of failure, and can have a cooling fan added easily. For the high voltage FETs themselves, cooling power can be a more sensitive parameter, but with the limiting resistors in place, most of their heat load actually comes from discharging their internal parasitic drain source capacitance, which therefore depends only on the number of switching events and not the capacitance of the load.

5.2.4 The Effective Moving Trap

In order to quantitatively analyze these and other operation modes, we can work in the non-inertial moving frame of the molecules, where any feasible mode generates an effective trapping potential with deceleration included as a fictitious force. This approach is usually reserved for

continuous deceleration schemes [98, 105], but is equally valid for pulsed schemes provided their velocity satisfies Eq. 5.4. The effective trap for on-axis molecules in the longitudinal direction has been discussed at length [110, 111], but computation of the full 3D effective trap has not been reported previously. The 3D effective trap is evaluated numerically for various operation modes to obtain the equipotential surfaces in Fig. 5.8d. It is found that for $S = 1$, the effective trap has holes. Molecules moving away from the trap center along the x and y axes experience almost no restoring force at all. This can be considered the underlying reason for the transverse-longitudinal coupling problem discussed above. Such couplings are in some contexts useful for maintaining ergodicity in a trapping geometry [112], but with one dimension featuring a very low energy barrier, they lead to loss.

Motivated by the holes evident in $S = 1$ mode, a new figure of merit that may be used to compare the performance of various modes of operation is introduced: the minimum depth of their effective moving traps. Here minimum depth refers to the smallest energy above which a molecule with that energy can find a way out of the trap. Having a single value to characterize effective traps allows doing so systematically across many modes and across many magnitudes of the applied deceleration, see Fig. 5.8a. Remarkably, F mode offers comparable trap depth improvement to $S = 3$, but with no sacrifice in deceleration capability. The SF and VSF modes make still more dramatic improvements, with the latter even rivaling traveling wave (TW) deceleration [98]. Note that for SF and VSF, the alternate configurations are not utilized in a symmetric manner about the grounded pin pair as for F. Instead, allowing them to be used asymmetrically opens up a new degree of freedom, which is optimized so as to maximize the minimum depth.

It is useful to discuss this tuning a bit further. A very similar process was used in [96], where multiple switching events were employed during a single stage. The present case is similar in having two different switching events in a stage, one happening at the usual position, call it ϕ_1, and another, ϕ_2, happening earlier. In [96], extra switching events still only made use of configurations A and A', but enabled greater transverse focusing power and also opened up other opportunities for more specifically tailoring the effective trapping potential. The same is true in the present case,
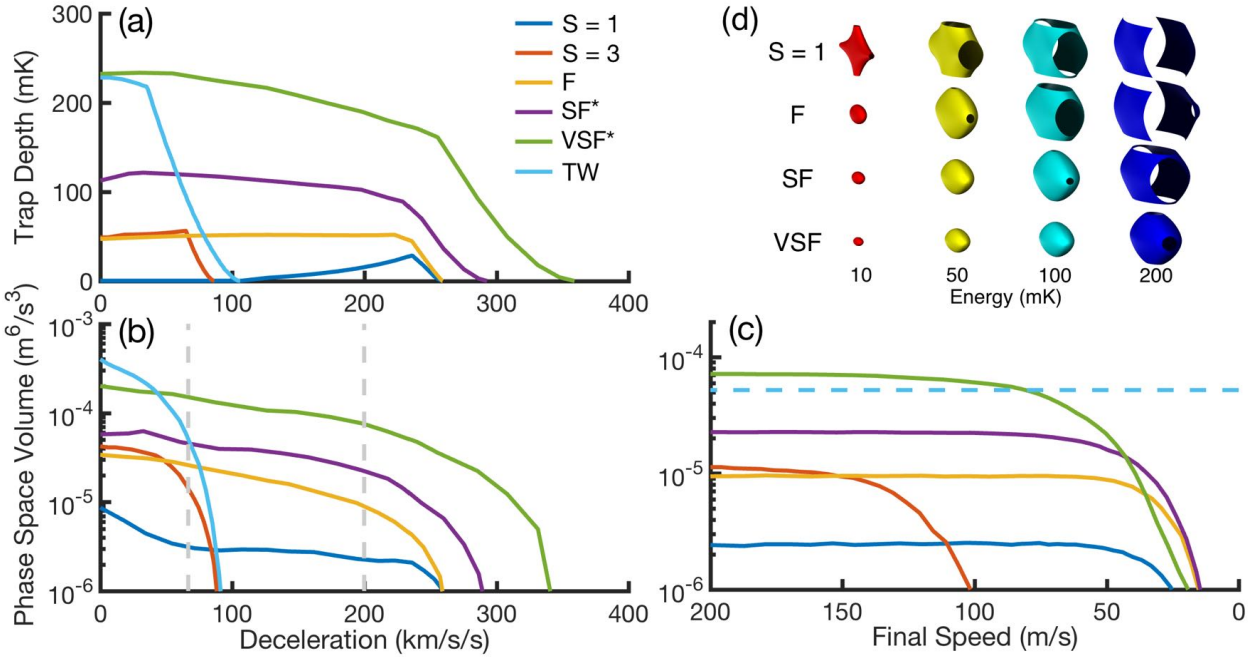
Figure 5.8: Characterizing the moving trap under different modes of operation. In addition to the conventional S = 1 and S = 3 modes, newly defined strong focusing (SF), very strong focusing (VSF), and focusing (F) modes are shown. Traveling wave (TW) deceleration is also compared, assuming 10 kV peak to peak, to our knowledge the largest voltage used to successfully decelerate to rest with a TW device. In panel (a) the trap depth at the lowest point of escape is shown as a function of deceleration for different operating modes. The stars on SF and VSF indicate ϕ_2 tuning, see the text. In panel (b) the initial phase space volume remaining within these effective traps after a 3 ms hold time is shown, and in panel (c) a full decelerator simulation is performed as a function of final velocities, with hold time fixed also at 3 ms and deceleration fixed as indicated by the gray dashed lines in panel (b). For TW a full simulation is not performed, since low speed losses are less significant, but the dashed line shows the value corresponding to 67 km/s/s in panel (b). In panel (d) equipotentials give a feeling for the effective trap as a whole, which is helpful for visualizing the derivation of the minimum trap depth in panel (a). The effective traps shown correspond to $\phi = 45°$, about 180 mK. The propagation axis is to the right, and transverse directions are up and diagonally outwards.

as far as the increased opportunity for specific tailoring. Perhaps the simplest decision is to simply set $\phi_2 = -\phi_1$, which has the extra benefit of making no change to the relationship between phase angle and deceleration rate relative to S = 1 operation, since the molecule doesn't gain or loose any extra energy while in the alternate configuration. This decision gives good results across a wide range of values of ϕ_1, but not close to $\phi_1 = 90°$, where ϕ_2 becomes nearly identical to ϕ_1 and the
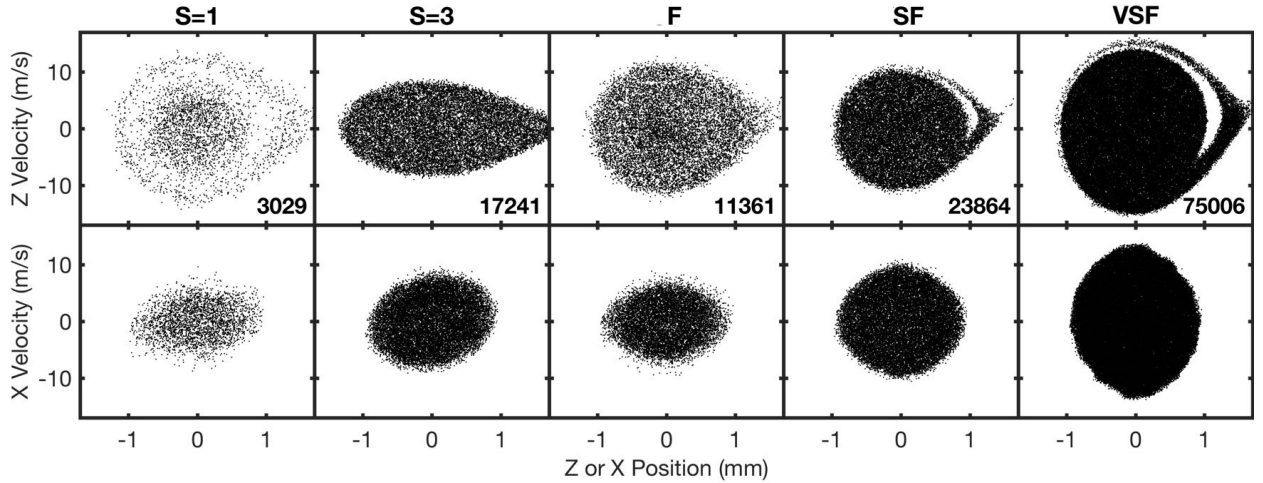
Figure 5.9: Longitudinal Phase Space Fillings are shown for several operation modes as labeled. All modes are initialized with the same uniformly distributed phase space, and the surviving number of molecules is indicated for each pair of panels. Note dramatic improvements in homogeneity and planar density, without significant broadening to larger velocity classes except for VSF. Molecules travel 333 stages, begin at 900 m/s, and slow at 200 km/s/s (67 km/s/s for S = 3).

alternate configuration is hardly employed at all. It is also a poor decision close to $\phi_1 = 0°$, since in this case ϕ_2 becomes nearly 180° off from ϕ_1 and the normal configuration is hardly used. The switch back and forth from the normal configuration is essential to obtaining restoring force in the longitudinal direction, so this would also be a poor choice. Instead, by tuning the location of ϕ_2 to optimize the minimum trap depth and not always choosing $\phi_2 = -\phi_1$, SF and VSF modes can be more fully leveraged. This is evident in the phase space plots shown in Fig. 5.9. F mode can be seen to feature greater depth longitudinally than transversely based on the larger projected area of the population, but for SF and VSF the projected area is comparable between the transverse and longitudinal planes. This is a direct reflection of the fact that ϕ_2 has been tuned for optimal minimum trap depth, because what happens in this case is that longitudinal depth is exchanged for transverse by increasing the time spent in the transversely focusing direction.

We can make further use of the effective trap by directly employing it to simulate the fate of particles confined for 3 ms, the duration of a typical deceleration sequence (Fig. 5.8b). The results show a very close qualitative match to the trends predicted by the minimum trap depth. The

most notable exception is found in S = 1 mode at low decelerations, where extremely deep holes dominate the minimum trap depth, but the small effective cross sectional area of the holes still allows molecules to survive in greater number than at higher decelerations where the minimum trap depth actually improves. As far as the comparison with TW is concerned, it is important to point out that we use the rather small 2 mm pin-pair spacing and 2x2 mm^2 opening area of our device, while TW devices use 4 mm diameter rings. If VSF mode were used with a 3x3 mm^2 device [95] or a 4x4 mm^2 [113], phase space volume would increase significantly, depending approximately on the cube of pin-pair spacing, and thus outperforming TW. Deceleration does also reduce linearly with pin-pair spacing, since this influences the number of pins that may be fit next to one another in a given longitudinal distance.

Of course the validity of using the effective trap in this manner depends on the final speed after the deceleration sequence. This effect can be isolated by also performing a full Monte-Carlo simulation of the various deceleration modes, without use of the effective trap approximation. By varying only the final speed, and keeping deceleration and run-time exactly fixed by appropriately varying initial speed and decelerator length, we obtain the results shown in Fig. 5.8c, an exact isolation of the low speed effects from other phase space effects. The asymptotically flat profiles at high enough speeds validate the effective trap picture, as do the quantitative agreement between the asymptotic values and the corresponding points at 200 km/s/s and 67 km/s/s in Fig. 5.8b.

The beginning of the low-speed breakdown depends on the intended use of the decelerator, and especially how far the molecules will be expected to travel unguided afterwards. In Fig. 5.8c, the molecules still confined within a 3 mm diameter circle after 5 mm free flight after the end of the sequence are shown. This is a conservative representation of what is required for trap-loading, but for collisional experiments a larger flight distance may be required. Note how F and SF cut off at even lower speeds than S = 1, but VSF cuts higher. This can be attributed to the fact that VSF actually features an increased transverse trap frequency relative to the others, while F and SF improve over S = 1 mostly by plugging holes and not by increasing the trap's depth or frequency. This restricts the usefulness of VSF mode for OH or other strongly dipolar species at low speeds

to devices that combine with a TW device as in [101]. For less strongly dipolar species however, VSF will more easily respect the low velocity transverse oscillation bound, and may not feature an altered low speed cutoff relative to SF or F.

Despite the lack of experimental validation for SF and VSF mode at the time of this writing, it is clear that alternate field distributions present an exciting and viable alternative to conventional deceleration, obviating the need for more advanced geometries and offering very significant gains in flux in almost all cases. Brand new opportunities are opened up by the increased efficiency, such as more favorable outcomes for targeting heavier or less polar species, or even the deceleration of beams seeded in Helium. Alternate field distributions are sure to play a central role in Stark deceleration moving forwards.

5.3 Transverse Trap Oscillations

A common technique for characterizing any trapping apparatus is to intentionally perturb the population so as to directly observe oscillations caused by the trapping force. This is performed for example in our OH magnetic trap [114], see Fig. 4, to ascertain the trapping frequency. The same can be performed for the effective moving trap formed by a given deceleration mode. We first investigated this with the goal of better understanding the behavior of OH molecules in the decelerator so as to extract the influence of collisions with Neon beams from single particle behavior. Experiments were performed with the goal of understanding and manipulating the trapping behavior formed by the two dimensional potential created by the decelerator operated in a guiding mode. The key idea is to initialize the trap with a broad position and low velocity distribution, so that a breathing mode is excited, see Fig. 5.10a-e. Some time later the trap is briefly switched off. Depending on whether this window corresponds to the outgoing or ingoing portion of the breathing mode, this brief lack of trapping will lead to more or less loss respectively, see Fig. 5.10f-h. This transverse trap may also be computed numerically, depending on the choice of field distribution, and gives rise to transverse potentials as shown in Fig. 5.11.

Breathing modes were detected as expected, and an effort was undertaken to infer the initial
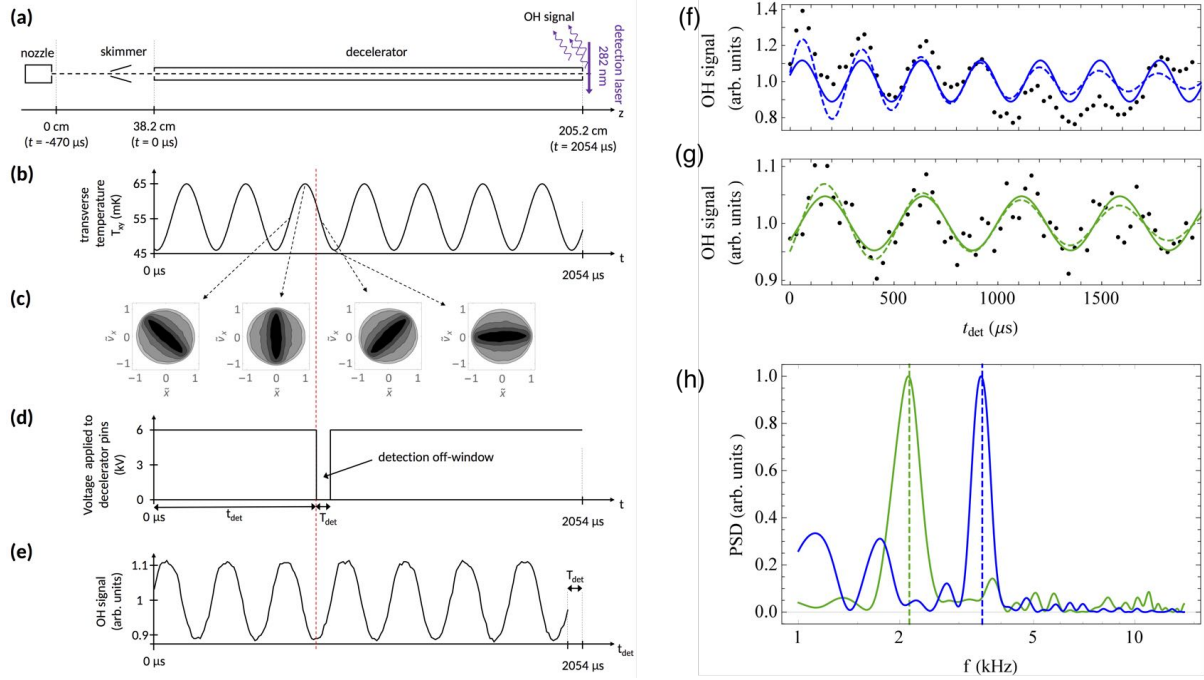
Figure 5.10: Transverse Oscillations in the Decelerator. (a) Schematic timing diagram for the experiment. (b) Transverse temperature (velocity spread) as a function of propagation time. (c) Phase space views demonstrating the rotation that gives rise to velocity spread variations. (d) Schematic timing diagram for application of a detection off-window for time T_{det} after a hold time of t_{det}. (e) Resulting signal in simulation. (f-h) Experimental data for guiding with 6 kV (blue) or 2.2 kV (green) applied voltage. (f) Sine (solid) and damped sine (dashed) fits to the experimental 6 kV data (black dots). (g) Same for 2.2 kV. (h) Fourier transforms of the experimental data with dashed lines indicating the simulated breathing mode frequency.
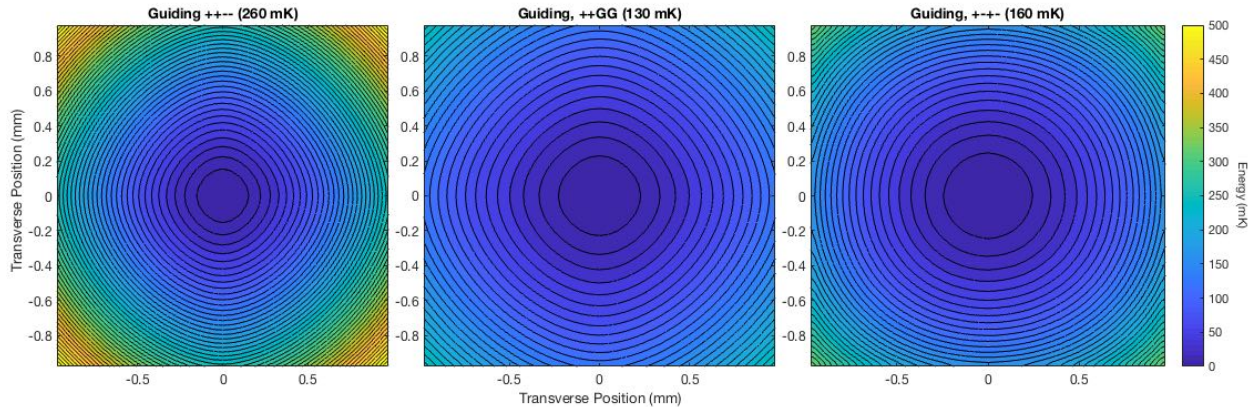
Figure 5.11: Transverse Traps formed by Different Field Distributions. Field distributions are generated in COMSOL, converted to internal potential energy, and then averaged longitudinally.

population distribution generated by the valve from the observed oscillations. This turned out to serve as a probe of skimmer interference, since it was found that a distant source of the expected temperature could not reproduce the shallowness of the oscillation amplitude observed, although there are of course other deviations between model and experiment which could lead to a reduction in fringe contrast. It was also found that by intentionally turning the trap off at the right moment could serve as a manipulation of the transverse phase space distribution for the sake of reduced transverse temperature.

It would be ideal to use this technique also as a means of studying the transverse or longitudinal frequencies in the traveling potential well in deceleration mode, but this has not yet been undertaken. Greater signal to noise would be desirable, at the time of this writing unavailable due to intentional space added between the source and the decelerator for studying collisions between parallel plates.

5.4   Non-adiabatic Transitions

The Landau-Zener formula may be used to approximate the relevance of non-adiabatic transitions in a given situation:

$$P = e^{-\pi \Delta^2 / \left(\hbar \frac{\partial E}{\partial t} \right)}. \tag{5.5}$$

Here Δ gives the minimum energy gap between two approaching eigenstates, and $\partial E / \partial t$ gives their rate of approach. Working in frequency units, we can simplify this to say that non-adiabatic transitions are negligible provided that:

$$G >> \sqrt{E \cdot \nu}, \tag{5.6}$$

where G is the closest approach of the states in frequency units, E is the initial energy spacing between the states in frequency units , and ν is the frequency characterizing the variation speed of the system. This is a convenient rule of thumb– just compare the minimum gap to the geometric mean of the inverse timescale and the typical energyscale.

For example, in the absence of any magnetic field, parity flips from $|f\rangle$ to $|e\rangle$ are highly unlikely thanks to the lambda doublet spacing of 1.7 GHz. Compare this with the geometric mean of 100 GHz and 1 MHz where the latter is appropriate for the microsecond turn-off of the fields during switching events and the former is the energy scale set by the magnitude of electric fields in the decelerator. The geometric mean is 300 MHz or so, below 1.7 GHz indicating that these transitions are not a concern.

On the other hand, transitions between $|f, \frac{3}{2}\rangle$ and $|f, \frac{1}{2}\rangle$ are a much greater concern, and have been observed during propagation of molecules in decelerators [115], and also during switching events of decelerators [116]. The Stark effect treats $|f, \pm\frac{3}{2}\rangle$ the same, and also $|f, \pm\frac{1}{2}\rangle$, but the latter have one third the response of the former, so transitions between them are essentially loss. Moreover, these states are degenerate at zero field and don't have any fixed barrier as do the states of different parity. Of course, states being degenerate does not necessarily lead to loss if the Hamiltonian driving their evolution does not have any amplitude connecting the states in question. For states of differing m quantum number, the Hamiltonian will only couple them when molecules are experiencing a rotation of the electric field vector. In $S = 1$ operation, suitably fast rotations, together with very small values of the electric field, cannot occur on-axis, but may occur for off-axis molecules that experience weaker fields close to the grounded decelerator pins. I investigated the loss probability for off-axis molecules, for the first time as far as I can tell, and the results I obtained are shown in Fig. 5.12. Only a small fraction of molecules are lost, perhaps something like 0.1% over the length of the decelerator. Being more quantitative would require simulating a denser grid of trajectories close to the pins.

Although free propagation doesn't lead to non-adiabatic transitions off axis, there is still the question of non-adiabatic transitions during the switching of the electric fields. I also checked this, for the first time as best I can tell, for a 3D grid of possible positions relative to the synchronous molecule, see Fig. 5.13. I find that non-adiabatic transitions are possible only if the molecule is significantly behind the synchronous molecule, shielded by the grounded pins just prior to their being rapidly switched on. These positions are not longitudinally phase stable anyway, unless the
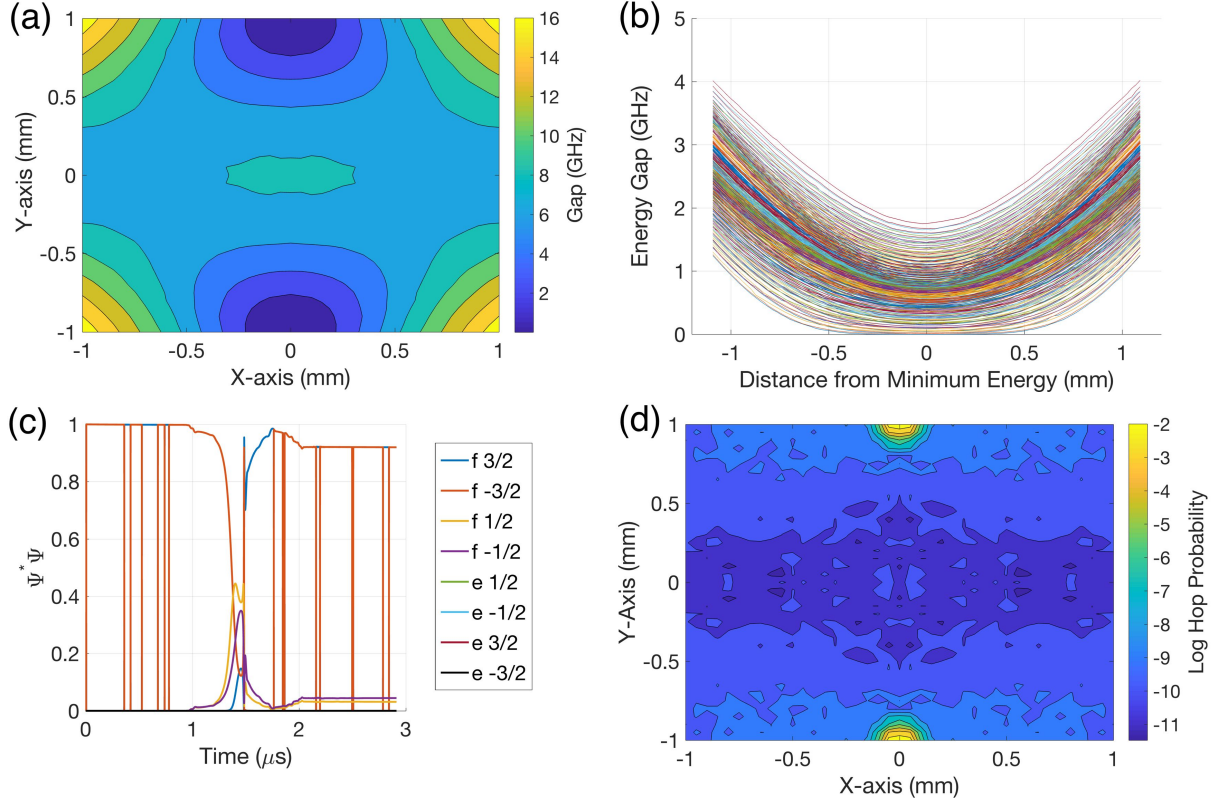
Figure 5.12: (a) Minimum energy gap along straight line trajectories parallel to decelerator axis and intersecting the transverse plane as shown. (b) Resulting energy gap as a function of propagation distance for a grid of trajectories. (c) Sample solution of the time-independent Schrödinger equation for a trajectory that shows a 10% chance of hopping to the $|f, \frac{1}{2}\rangle$ state. Many sharp jumps are seen between $|f, \pm\frac{3}{2}\rangle$, these are irrelevant and an artifact of an unphysically small bias magnetic field. (d) Inferred hopping probability as a function of position in the transverse plane.

decelerator is being operated in an acceleration mode, in which case some locations off axis do seem to feature a significant chance of non-adiabatic transitions. The real thing to do would be to repeat this study with alternate field distributions in mind. These would be likely to feature a significantly enhanced chance of free propagation transitions close to the electric quadrupole created by the alternate configurations between the grounded pin pair. As far as the chance of switch-induced non-adiabatic transitions, those would seem to be reduced by the alternate field distributions, since in $S = 1$ mode they were worst with the molecules beginning in a region of small field, and the alternate distributions generally add electric field in the regions where it was
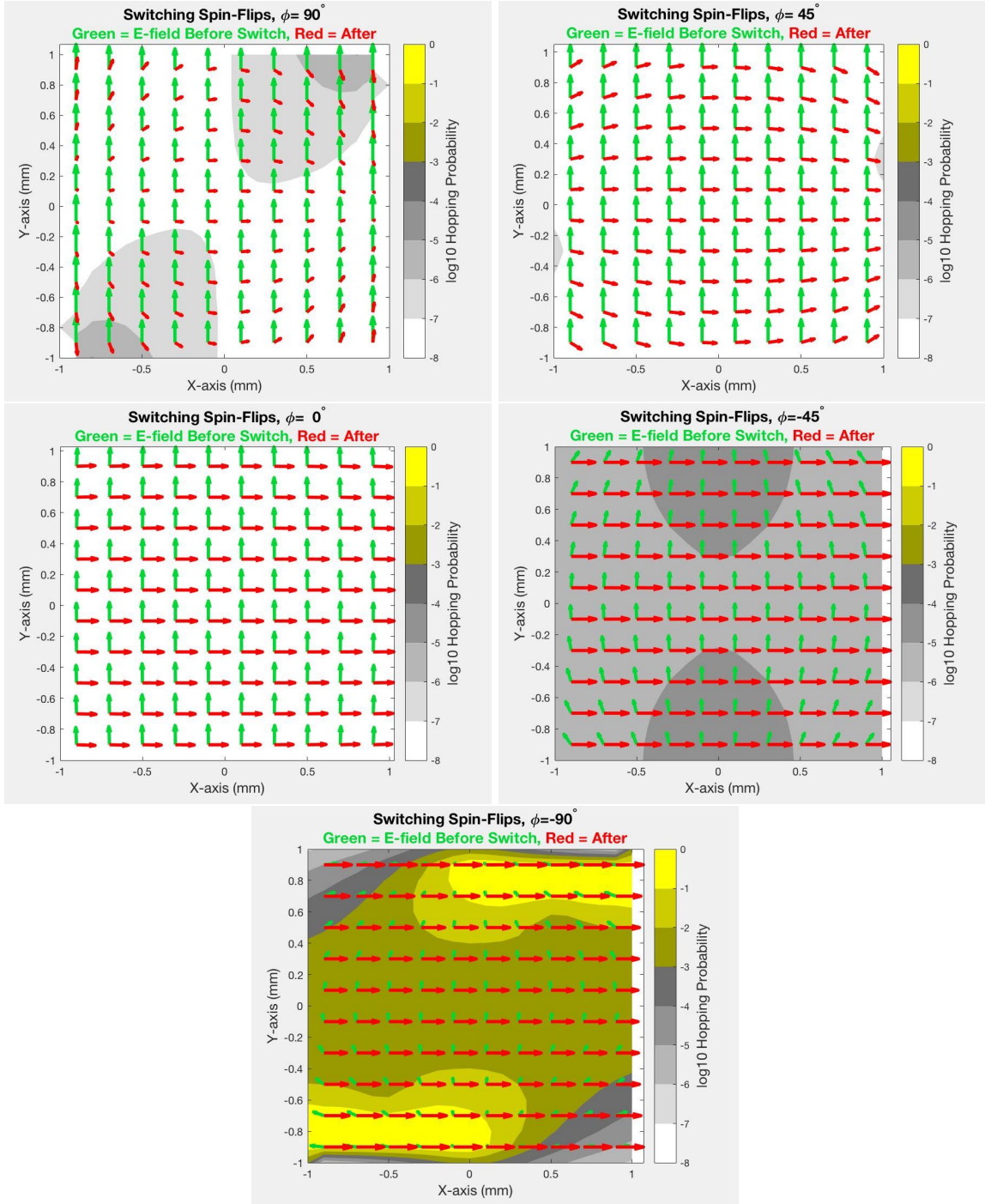
Figure 5.13: Loss per switching event in several $x-y$ planes of different z coordinate parametrized by phase angle $\phi = 90°$, $45°$, $0°$, $-45°$, and $-90°$, from left to right and top to bottom. Significant loss only in the $-90°$ plane, where phase stable molecules do not reside anyway.
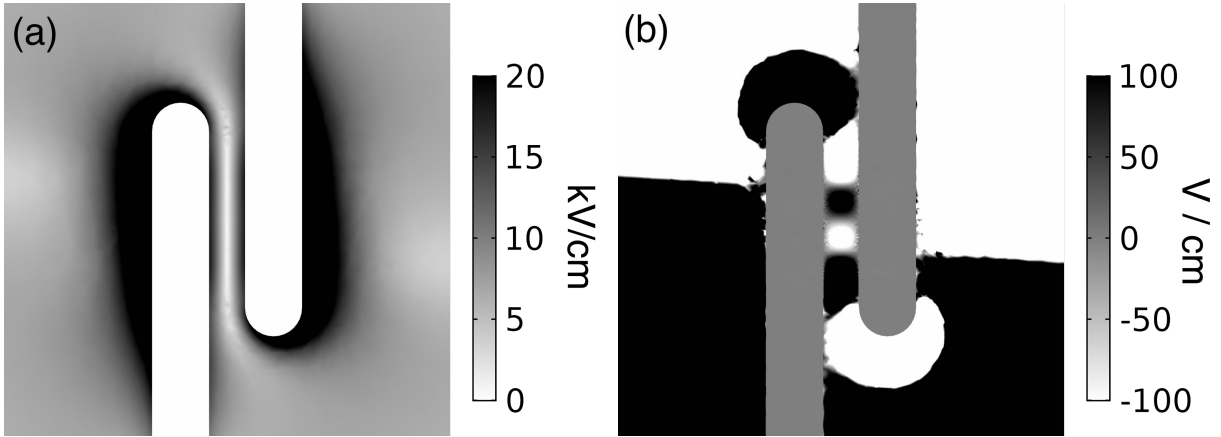
Figure 5.14: Together these panels demonstrate that the electric field is zero not along a line but only at a single point. (a) Electric field magnitude in the transverse plane bisecting a pair of pins. A line of near-zero field is evident. (b) Electric field in the same plane, but only its projection on the line of near-zero field, and zoomed in a few orders of magnitude in the grayscale axis. The checker-like structure close to the central axis shows that there is not a line of zero field but actually a 3D electric quadrupole structure, with very slight restoring force in the vertical direction. This is relevant to reducing non-adiabatic transitions through intentional misalignment.

previously small or absent. However significant the non-adiabatic transitions in the new operation modes, one way to address them is to intentionally vary the length of decelerator pins, so that one pin is longer than the other in a pair. What this does is push the electric field zero off of the decelerator axis, creating some extra protective energy splitting even for molecules passing dangerously close to the electric field zero. It is not obvious that there is a single point of zero electric field, something I endeavor to demonstrate in Fig. 5.14. In panel (a), there appears to be not a point but a line between the pins where the electric field is zero valued. However, if we zoom in on the energy axis (Fig. 5.14b) and consider the coefficient of the field which points along this seeming linear electric field zero, we find that this component is in fact nonzero except in a single point. Of course it comes very close to zero, but not much of an extra protective field is required to reduce the effect of the spin-flip loss significantly. Thanks to the variation in length of our decelerator pins, a known side effect of tapered pin mounting as described in Sec. 5.5.2, our decelerator may benefit from reduced sensitivity to these spin-flip issues.

5.5   Decelerator Manufacturing

Beginning in Fall of 2015, an effort was undertaken to manufacture a new decelerator capable of slowing an OH beam generated with neon as a buffer gas. This effort was begun in parallel with ordering of a new Even-Lavie pulsed valve [54], which boasts significant gains especially for lighter carrier gases[b] . Initially argon was considered, but foolish zeal on the part of the author led to neon, although at least he was talked out of helium.

5.5.1   Modeling

Simulations were used to determine the optimal length for the device, or at least a length that would slow OH beginning at Neon speeds without comparable performance to the previous generation, see Fig. 5.15a. It was determined that something closer to 350 stages should be ideal for loading the magnetic pin trap at $\phi \sim 55°$, and so a 333 stage device was planned. Sensitivity of decelerator performance to pin pair spacing was also studied, and found not to have a significant effect, see Fig. 5.15b. Thinking in terms of the effective trap, this reduction shrinks the spatial extent of the longitudinal trap, but increases the velocity extent of the transverse traps, since the transverse focusing becomes more frequent. The spacing was reduced from 5.461 mm in the previous generation to an even 5 mm.

5.5.2   Mechanical Considerations

In order to address manufacturing costs and installation time associated with such a long device (up from 142 stages previously [70], and 69 before that [69]), we spent some time investigating the possibility of separate modules or of extensions mechanically affixed to the existing rods. Ultimately it was decided that the challenges associated with getting such things right were not warranted by our length, and that it would be best to tackle everything with one long set of rods, mounted in a cage made of several stages, see Fig. 5.16. One significant change that was developed

---

[b] It is difficult to verify such a claim, which concerns the relative performance of different valves with different carrier gases. The claim of better performance for an Even-Lavie valve only with lighter carrier gases comes from verbal discussions with SYT van de Meerakker during his sabbatical at JILA in the winter of 2015-2016.
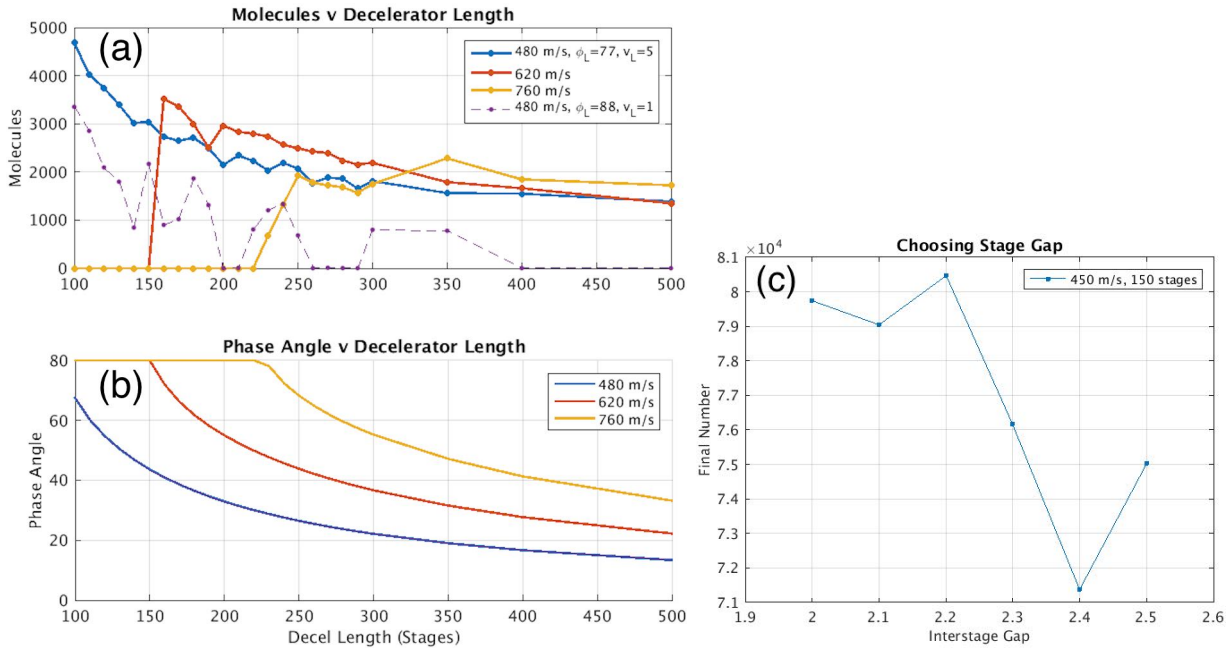
Figure 5.15: Simulation results for deceleration and loading verses decelerator design parameters. (a) Loading efficiency is studied as a function of three initial speeds and various decelerator lengths. A ramping of the phase angle is used in the final few stages for further optimized loading. Increased length is observed not to facilitate improved trap population beyond some initial threshold value, likely due to the inefficiencies of the deceleration modes used at the time. (b) The selection of phase angle to achieve slowing to rest as a function of decelerator length is also shown. (c) The interstage gap is also studied.

out of a partnership with a local manufacturing company[c] was to use locking tapers on both the pins and their mounting holes to fix them in place. This halved manufacturing costs for the rods, and removed the need for setscrews, which created a serious galling hazard on the previous device and led to several near-disasters when re-polishing pins. A special tool was developed for pressing the tapered pins into their holes, or removing them, without scratching any polished surfaces[d] . We had also run into high voltage issues when using MoS_2 powder dissolved in isopropyl alcohol as a lubricating agent for said setscrews. A key downside of the tapers was that they ended up creating a large sensitivity of final installed pin length on pin polishing procedure, since an extra unit thickness removed from the outside of the tapered pin causes the pin to sit 48 units deeper into its

---

[c] Hirsh Precision Products, INC.
[d] The design is publicly available on Instructables

hole (since the standard taper rate for locking tapered pins is a quarter inch per foot). Fortunately the length of pins along their axis of symmetry has only a minimal effect on the fields experienced by molecules in a pin-style Stark decelerator. An additional challenge is that installation of many tapered pins acts as a fairly effective wedge for causing the main rod to bend ever so slightly. After installation, we worked very hard to adjust the mounting structure so as to force the decelerator into proper alignment. Lacking all requisite degrees of freedom, we settled for a precision tuning of the pin pair spacing, in the hope that as long as that remained correct, the molecules would be able to follow any slight bends in the device. Finding a way to work with a larger diameter rod may have been preferable. The tapered pins may be a good choice for other designs, especially if a vendor is used who can offer both surface quality and tolerancing at the same time[e] .

It is worth setting out a figure of merit to describe the extent to which such slight bends would be acceptable. For velocity v, a bend radius r causes an acceleration $a = v^2/r$. For a given operation mode, we can characterize the transverse trap as a harmonic potential $U = \frac{1}{2}m\omega^2 x^2$. In the case of a bent decelerator, this potential is a non-inertial frame, and the bending acceleration can be included as a fictitious force which causes the molecules to shift off of center in the trap. The magnitude of this shift is given by the x_s which satisfies:

$$\left.\frac{\partial U}{\partial x}\right|_{x_s} = m_{\text{OH}}\frac{v^2}{r}, \tag{5.7}$$

from force balance. Solving:

$$x_s = \frac{v^2}{r\omega^2}. \tag{5.8}$$

For SF mode, $\omega \sim 1.0$ kHz, for F mode, $\omega \sim 0.7$ kHz. Assuming that $x_s \sim 0.2$ mm is acceptable, 10% of the pin pair spacing, the allowed bend radius for 800 m/s molecules is $3.2, 6.5$ km for SF, F modes. Along the length of a 1.7 m device, such bends amount to offsets of $1, 0.5$ mm. Based on the observation that we are able to shine a laser beam all the way through the device, albeit without the expected 2 mm square-like shape, bends in the device are unlikely to be significantly

---

[e] We worked with TriGON Precision for polish after having Hirsh Precision Products INC manufacture the pins. They often expressed their preference to have manufactured the pins themselves in the first place, since we were asking them to get a high quality polish without removing too much material.
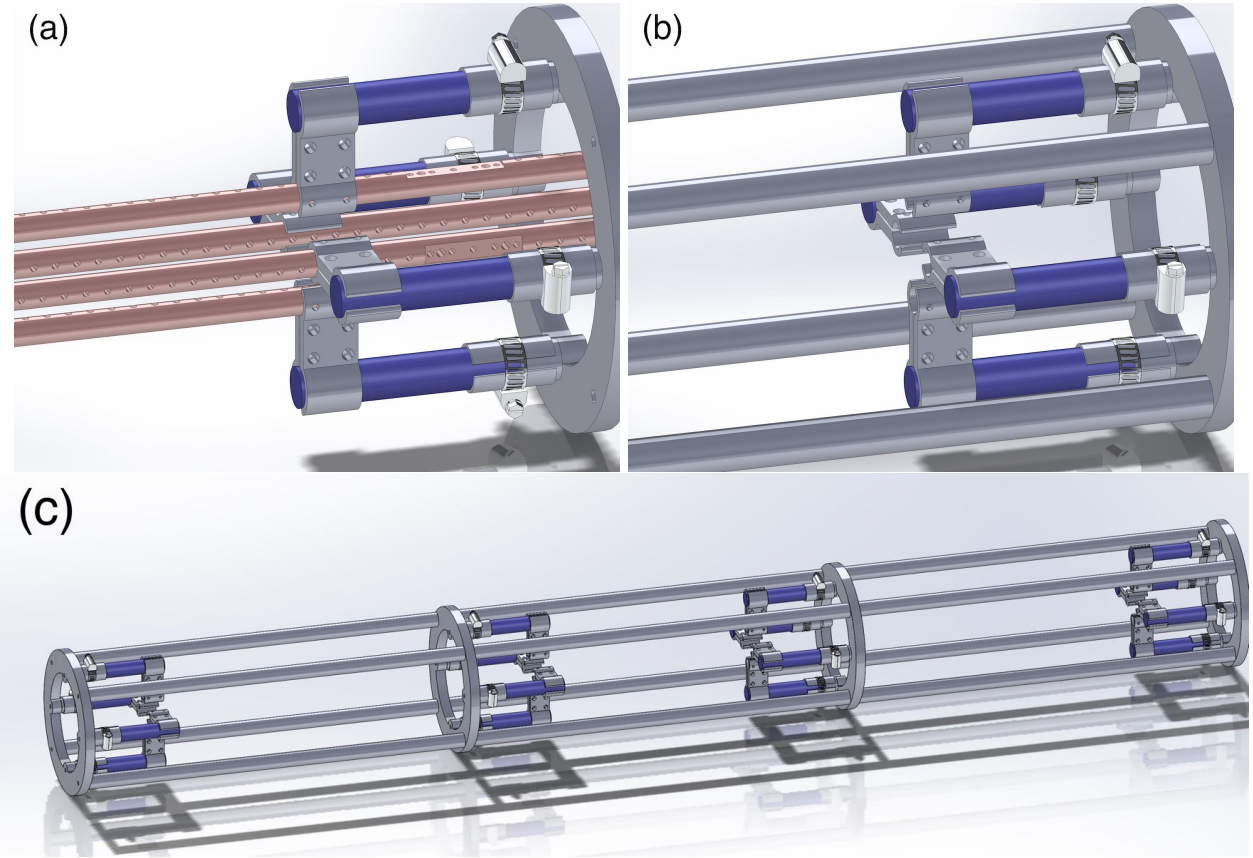
Figure 5.16: Mounting structure of third generation Stark decelerator. Note large safety high voltage surface distance along glass rods, blue. (a). Clamping pieces grab on to the actual decelerator rods. A mounting flat, a vestige of an earlier design, is visible on the decelerator rod. (b) Decelerator rods hidden, cage connection rods shown. (c) Full view of the cage structure.

larger than these numbers, but likely on this order.

5.5.3   High Voltage Arcing

With the new design, an effort was made to address challenges that had developed with the mounting of the previous generation, which had been facilitated by MACOR, a machinable glass ceramic material. The MACOR was found to allow surface currents, which also were un-phased by the surface path-length extension grooves that had been added to reduce their likelihood, as can be seen in Fig. 5.17. There was never a clear indication that these surface arcs were actually causing a reduction in molecule yield, but nevertheless it seemed wise to make an attempt at improving the
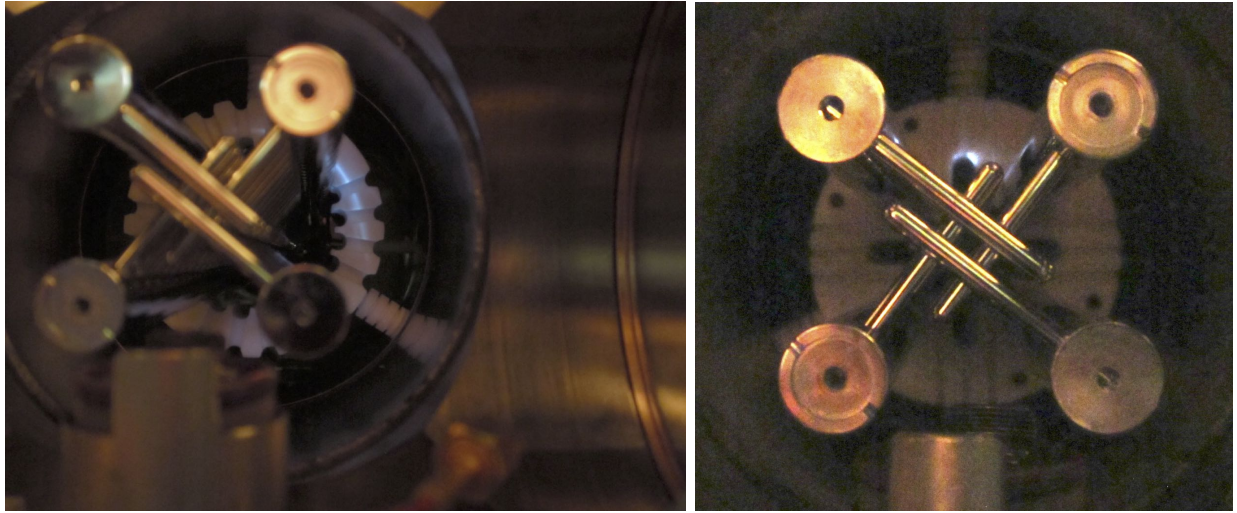
Figure 5.17: MACOR surface arcs. At left, arcing on an insulator original to the manufacture of the second generation device [70]. At right, arcing on a redesigned version, undertaken concurrently with a re-polishing of the last twenty decelerator pins performed in the fall of 2014. Here it is evident that the path-length extension grooves are not helpful.

situation. In reviewing literature [78, Sec. 4.3.3] and consulting other opinions, it was found that the previous geometry did not respect recommended considerations regarding so-called "triple-points" where vacuum, dielectric, and conductor meet. It is advised to have the triple-points recessed or otherwise manipulated so as to minimize the electric field at their locations [75]. This is achieved in the new design, as well as increasing the safety distance and removing reliance on sharp insulator features, by the geometry visible in Fig. 5.16 and heavily influenced by [91, Fig. 4]. Borosilicate glass rods were selected for their vacuum and insulating properties, with alumina rods as a close second.

5.5.4   High Voltage Electronics

In the design of the new decelerator, the capacitive load presented by the decelerator was an important consideration. For a long enough device, it would in principle become necessary to purchase a new set of switches capable of providing higher currents. Fortunately, prior to the design effort which culminated in the third generation decelerator system, it was realized that the

capacitance of the cables connecting the high voltage switches to the decelerator actually dominated the capacitance seen by the switches. It was thus possible to operate the original electronics with the new decelerator at even lower load than previously, thanks to a systematic effort of relocating electronics so as to minimize all high voltage cabling, especially between the transistor switches and the decelerator rods. Considerable influence in the design and execution of this effort was taken from [117, Fig. 4.6].

An even more significant challenge constitutes the management of multiple output states as required for the realization of the SF and VSF modes discussed above. Such an effort was successfully undertaken in the operation of certain traps discussed later in this thesis, but only at very low repetition rate. In considering circuitry involving the use of multiple transistor switches arranged in series or parallel it is essential that all parasitic elements of the devices are taken into account, especially the parasitic capacitances in parallel with the drain and source terminals, which can form the dominant current load as seen by other transistor switches in the circuit. At the time of this writing, careful collaboration with engineers at Behlke GMBH resulted in the selection of a device[f] that should be capable of operating SF mode, and VSF if a second such device is ordered. The device has yet to arrive after requiring a rebuild following a miscommunication pertaining to the specification of options for the switch.

5.5.5   Capacitance Matrix

It is also relevant to again consider the capacitive load associated with switching between various distinct field distributions. In this case, it becomes necessary to treat the full system of electrodes not as a single capacitor but actually as a network of different capacitors most efficiently captured in the form of a capacitance matrix C_{ij} satisfying:

$$Q_i = C_{ij}V_j, \tag{5.9}$$

---

[f] Behlke HTS-301-151-SiC, options HFB, ILC, ALL-OFF-BIPOLAR.

so that a vector of charges on each conductor can be obtained given a vector of voltages on each. Surprisingly, in our system the capacitance between a pair of rods with parallel pins is actually slightly less than that between a pair of rods whose pins are orthogonal, see the matrices reported in Fig. 5.18. The entries in these matrices are computed experimentally using a capacitance meter, the SR720. It is not possible to measure C_{ij} simply by connecting an LCR meter only to nodes i and j. What happens in this case is that the nodes other than i and j float to various unknown voltages, and confound the measurement.

We opted instead to partition the nodes into two groups, short these groups to one another, and then measure the two point capacitance between those groups. Consider for example the case where rods 1-3 are shorted together, and 4 is grounded. When the capacitance meter applies a test voltage V_T to rods 1-3 and measures the stored charge Q_T, this can be related to the C_{ij}'s as follows:

$$Q_T = \sum_{i=1}^{3} Q_i = \sum_{i=1}^{3}\sum_{j=1}^{5} C_{ij}V_j = V_T \sum_{i=1}^{3}\sum_{j=1}^{3} C_{ij}. \tag{5.10}$$

That is to say, we measure the total sum of a sub-matrix of the full matrix C_{ij}. It is clear that such measurements may be added and subtracted so as to obtain each C_{ij} independently.

Another interesting property of the capacitance matrices shown in Fig. 5.18 is their positive diagonal and negative off-diagonal. This is as expected, as can be proven by considering the case where all V_i are zero except for one, $V_j = V > 0$. To achieve such a configuration, positive charge must have flowed onto conductor j, which would then require negative charge to flow from ground onto conductors $i \neq j$. It follows that $C_{ij} < 0$ whenever $i \neq J$.

An important corollary of the multi-capacitor system is that the transient dynamics of the system do not follow the usual RC behavior, as shown in panel (c) of Fig. 5.18. When one considers the response of the system to a specific impulse vector of voltages, the system will respond on a few different timescales according to the eigenvalues of the matrix. In panel (c), which is a first order dynamical simulation applying just such an impulse using the experimentally measured capacitance matrix, the current through the resistor connecting to one of the rods is seen to first briefly increase

(a) Experiment (LCR SR720 Probe)

(pF)	Rod 1	Rod 2	Rod 3	Rod 4	GND
Rod 1	206	-56	-64.5	-62	-33
Rod 2	-56	208	-65	-63	-37
Rod 3	-64.5	-65	210	-57	-33.5
Rod 4	-62	-63	-57	206	-33.5
GND	-33	-37	-33.5	-33.5	140

(b) COMSOL Simulation

(pF)	Rod 1	Rod 2	Rod 3	Rod 4	GND
Rod 1	199	-43	-55	-55	-46
Rod 2	-43	199	-55	-55	-46
Rod 3	-55	-55	199	-43	-46
Rod 4	-55	-55	-43	199	-46
GND	-46	-46	-46	-46	184

(c)
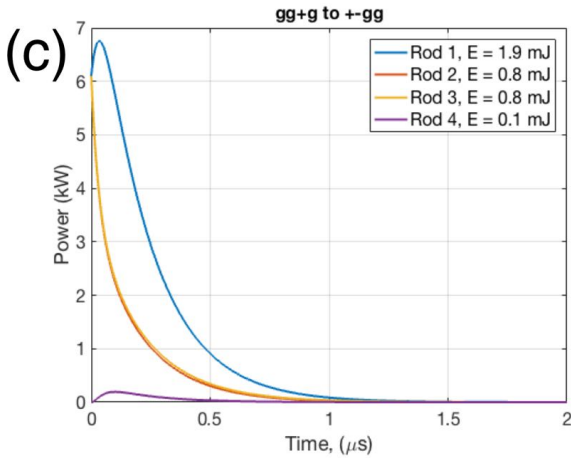
Figure 5.18: Capacitance matrices from LCR meter and simulation for third generation decelerator. (a) Capacitance matrix by measurement and (b) by COMSOL simulation. (c) Example of the multi-timescale dynamics that can occur when solving the transient response of a capacitive system to sudden changes in the voltages applied to the electrodes. Traces are simulated dynamics using the experimentally determined capacitance matrix.

with time before then decreasing exponentially in a less surprising manner.

5.5.6   Differential Pumping

One key downside of Stark decelerators compared to conventional alkali Zeeman slowers is the lack of feasible differential pumping schemes. This challenge stems from the difficulty of mounting anything close to the Stark decelerator without violating high voltage safety on some level. Electric fields also interact more strongly with most materials compared with electric fields, and so there is
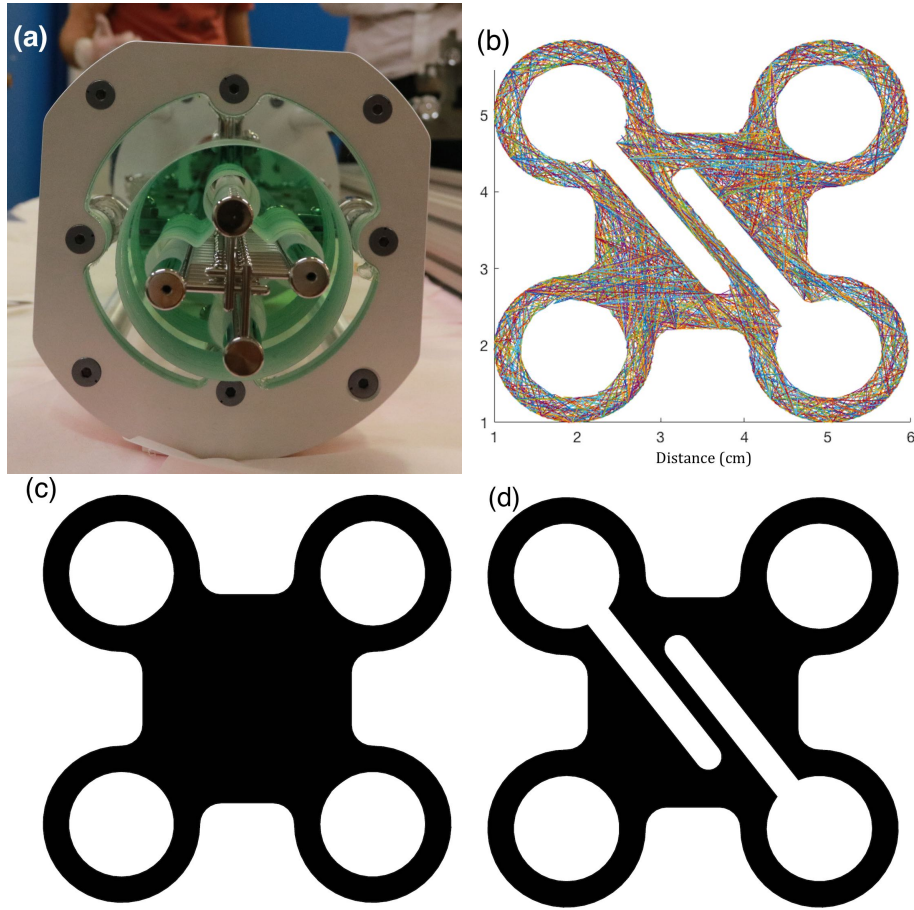
Figure 5.19: Glass baffle for differential pumping. Conductance of about 20 L/s for Neon. (a) Manufactured from a stack of water-jetted glass slabs, glued together with a low outgassing epoxy. (b) Sample output from pipeConductance.m, a conductance calculation package developed for this application[g]. One tenth of the chords used for calculation are shown. Calculation is well converged as far as chord inclusion is concerned. (c,d) Profiles used for specifying cross sections for conductance calculation. Conductance is 24.2 L/s for (c), 12.7 L/s for (d).

no tube like structure that could be mounted inside the pairs of decelerator pin without shunting away most of the field lines, not to mention surface arcing. Nonetheless, in the third generation of the experiment a technique was developed for differentially pumping the end region of the Stark decelerator from the other vacuum regions, using a glass baffle structure which comes close to the decelerator on all sides but without making any surface contact, see Fig. 5.19.

I devoted some effort to determining the vacuum conductance of the unusual cross section

---

[g] See the MATLAB file exchange or my Github page.

one obtains by mounting something close to the outside of a Stark decelerator. While commercial software exists for determining conductances and pump-down times for arbitrary geometries, these options would require very high mesh densities and very long computation times given the small scale and detail of the geometry. A better option is to work in two dimensions where general expressions amenable to numerical integration exist [118, Eq. 14]. Of course the decelerator is not quite translationally invariant in the molecular direction, because the pins are discontinuous. A worst case can be had by assuming no pins installed, and comparing this to the case of only two or four rows of pins being installed, see panels (c) and (d) of Fig. 5.19. My conductance calculations are nicely packaged and publicly available[g]. Conductance would be 24.2 L/s without any pins, 12.7 L/s with two solid rows of pins, and 8.6 L/s with four solid pin rows. Given our 500 L/s pumping speed in the chamber downstream of the baffle, the baffle therefore affords something like a twenty-fold differential pressure reduction in the gas load coming through the baffle from the beam source. This could be measured somewhat easily using a leak valve, but we have simply never bothered. Excellent suppression of Neon is observed, with an RGA mounted in the trap chamber not even detecting whether or not the pulsed valve is turned on, at least with a skimmer in place in the source chamber.

Chapter 6

Molecular Trapping

Some of the earliest successful trapping of neutral molecules began with CaH in John Doyle's group in a dilution fridge with ^{3}He buffer [119]. Stark decelerated and electrostatic trapped ammonia followed soon later [120]. Since then extensions to many species have occurred. In this chapter we focus on OH molecules, whose strong Stark shift to mass ratios make them favorable for attempts to attain high enough densities to observe collisions between members of the ensemble.

6.1   History of OH traps

The history of OH trapping in the Ye group has grown substantial enough to warrant a tabular environment 6.1. Each attempt has brought new challenges and experiences, and steady progress has been made in a number of key areas. The Magnetoelectrostatic Trap (MET) installed during Brian Sawyer's time [70] was a heroic first attempt that included a few-turn magnetic coil run at a startling 1400 A, and 2000 A briefly during loading. Later it was decided to trade the role of the fields used for loading, and great gains in magnetic field strength and simplicity were attained by switching to permanent magnets with the "Ring" trap [79]. A key improvement occurred when it was discovered that patch charges on the Ultem mounts originally used for affixing the magnetic trap to the Stark decelerator could have a significant impact on spectroscopic efforts [114, Fig. 6]. This was addressed by designing primarily stainless steel mounts, so that molecules only had line of sight to grounded conductors, although still with insulators installed between the decelerator and trap but relocated elsewhere.

Table 6.1: The Ye Group Molecule trapping endeavor. All but the last have been experimentally realized.

Name	Type	Depth (mK)	Uses
MET	Magnetic Quadrupole, Electric Hexapole	250	First Demonstration [70]
Ring	Magnetic Quadrupole	100	He, D_2, ND_3 Collisions [87, 79]
Ring	Above, but new mounts	100	E-field Induced Collisions, Evaporation [114, 44, 121]
Tricycle	Magnetic Quadrupole	300	10x density, spin-flip loss
Pin	2D Magnetic and Electric Quadrupoles	500	Solved spin-flip loss [88]
Cryocycle	Magnetic Quadrupole	200	Lifetime, Fluorescence Enhancements

6.2 Tricycle over Ring Trap

In pursuit of increases in density and molecule number, an iteration on the Ring trap was performed, dubbed the "Tricycle" trap due to the three rectangles formed when examining planar cuts through the ring and rear magnets used to generate the trap, see Fig. 6.1. This was first installed in 2014, and improved on the Ring trap in several key ways:

(1) Replaced rear ring with its core, removing an outer toroidal trap and tripling depth.

(2) Significantly improved loading dynamics.

(3) Increased trap gradient, thanks to a $\sim 40\%$ reduction in size.

6.2.1 Toroidal Destabilization

This first achievement was one of the primary goals of the iteration, since the influence of the toroidal minimum present in the Ring trap was difficult to ascertain. Molecules ought to have been able to explore the toroidal region, but based on the observed distribution of molecules as a function
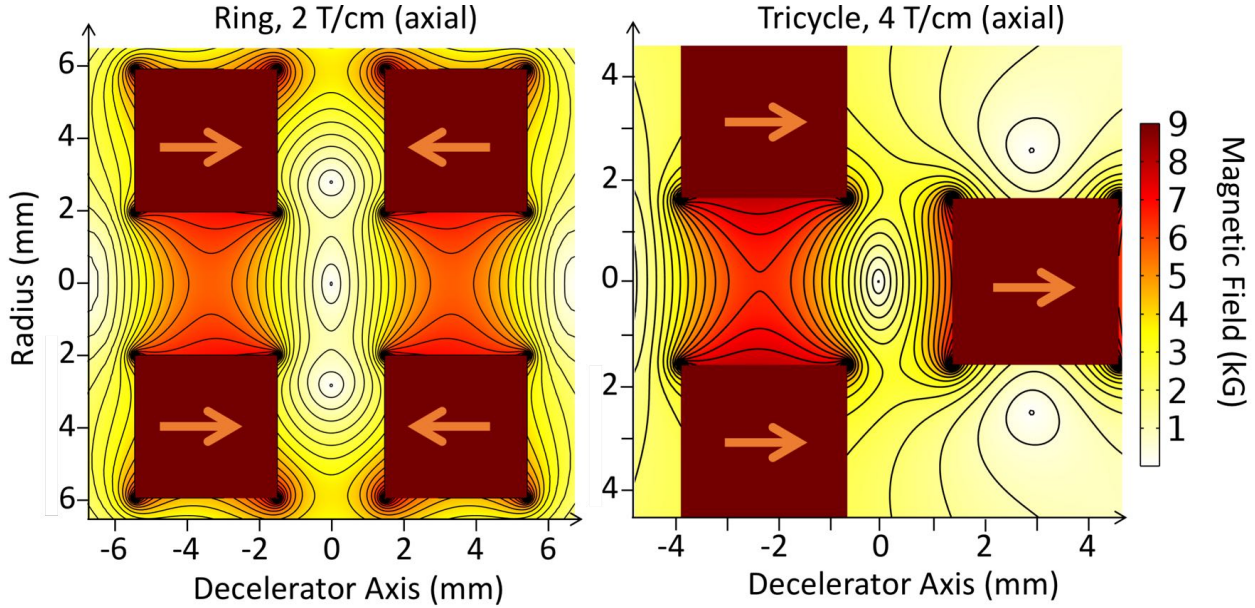
Figure 6.1: Cross Sections including the cylindrically symmetric axis for both the Ring and Tricycle traps. Arrows indicate magnetization directions up to an overall sign. Magnetic trapping fields are shown, demonstrating the destabilization of the toroidal minimum of the Ring trap. Contours every 500 G. Steel mounting electrodes are not shown in either case, but are installed on the outer diameter of the magnets and affixed to them with setscrews.

of magnetic field, they did not appear to be doing so for unknown reasons. At the time it was highly desirable to be able to perform the same evaporation type experiments, but in a geometry without a toroidal minimum. The removal of the toroidal minimum can be best understood by thinking about the traps using the principle of superposition. The Ring trap may be thought of as the result of superposing two different quadrupole traps, one formed by cylinders of diameter given by the ID of the rings, and the other formed by cylindrical magnets of diameter given by the OD of the rings. The smaller quadrupole trap is nice and tight, but the magnets block the beam path. The larger trap is larger and weaker, and its field lines move in the opposite direction, since its magnets are oppositely magnetized relative to the smaller quadrupole trap (so that they cancel each other out in the centers of the rings, allowing molecules to pass through). The larger trap works against the smaller, but is much weaker than it at least near the center of the geometry, so that the smaller trap remains tight near the trap center. Further outside, where the fields generated by the smaller

quadrupole trap are less significant, the outer quadrupole dominates, creating the outer toroidal minimum. If instead of overlapping a larger quadrupole trap with the smaller, we just overlap a single disk magnet, then no significant outer trap is created, just as in the Tricycle trap.

In fact, in the limit of large OD of the single ring magnet of the Tricycle trap, the geometry exactly approaches that of a pair of small disk magnets, but with the crucial modification of an entry hole for the molecules to be delivered. This is because for a disk magnet, the on-axis magnetic field is given by:

$$B(z) = \frac{1}{2} B_r \left(\frac{z+t}{\sqrt{R^2 + (z+t)^2}} - \frac{z-t}{\sqrt{R^2 + (z-t)^2}} \right), \tag{6.1}$$

where B_r is the remanent flux density of the permanent magnet, t is its half thickness, and z the distance from the magnet center, and R gives the cylinder radius. In the limit of large R we obtain:

$$B(z) = \frac{1}{2} B_r \left(\frac{z+t}{R + (z+t)^2/2R} - \frac{z-t}{R + (z-t)^2/2R} \right), \tag{6.2}$$

and taking it to cubic order:

$$B(z) = \frac{1}{2} B_r \left(\frac{z+t}{R} - \frac{(z+t)^3}{2R^3} - \frac{z-t}{R} + \frac{(z-t)^3}{2R^3} \right) \tag{6.3}$$

$$= \frac{1}{2} B_r \left(\frac{2t}{R} - \frac{3z^2 t}{R^3} + \frac{t^3}{R^3} \right). \tag{6.4}$$

So we see that as R grows, $B(z)$ shrinks close to the magnet with $1/R$, but the flatness of the field increases, so that the term proportional to $z^2 t/R^3$ which describes the second order fall off of the field away from the magnet reduces as $1/R^3$. In other words, the magnetic field just outside of a disk magnet does indeed shrink as one increases its radius, although the volume occupied by this smaller magnetic field increases. It is especially advantageous to have a small field from the large superimposed disk of the tricycle trap, since this extra field acts to shift the trap center into the hole of the ring and out of view of the detection laser. For this purpose, the Tricycle trap features a 19 mm outer diameter ring magnet, up from 12 mm in the Ring trap.

6.2.2   Loading Improvements

The Tricycle trap features some loading improvements over the Ring trap, although the precise extent is difficult to pin down. The main reason for an expectation of improvement lies in the phase space dynamical behavior of the two geometries. In analyzing any trap loading scenario, it is important to pursue the analysis with both intuition and simulation. The latter on its own will lack the guidance necessary for truly identifying an optimal scenario, while the former is unlikely to be able to fully disentangle interdependent factors influencing performance.

On the intuitive side, it is useful to apply the same reasoning as in the decelerator by focusing on phase stability. Electric fields useful for loading are generated by charging up the surfaces of the magnets in the traps. These loading fields are mirror symmetric about the center of the Ring trap. This means that if a loading sequence is designed so that the synchronous molecule ends up exactly in the trap center, the synchronous molecule will be required to roll up to the top of a hill and then stop there. Molecules with slightly more forward velocity than the synchronous molecule will end up quite a ways down the other side of the hill by the time the loading fields are switched off, and vice versa. It follows that longitudinal phase stability during loading requires that the loading be performed on a slope, not a peak.

It is possible to generalize these ideas further, while still remaining in the intuitive domain. If it is true that the loading fields ought to feature a slope at the location of the trap center where the synchronous molecule comes to rest, what is the ideal value for that slope? Also, is there a similar ideal value for the slope of the loading fields in the region in front of and beyond the trap center? We can answer these questions with a simplified thought experiment, refer to Fig. 6.2. Suppose we have a population experiencing a harmonic trapping potential with a characteristic width δz in real space and δv in velocity space, and centered at $z_0 = 0$ and $v_0 > 0$. One way to controllably transfer this population to $v_0 = 0$ without unwanted stretching of the population would be to load it into a much larger harmonic potential with oscillation frequency ω centered at $z = 0$ and $v = 0$. Because harmonic potentials always execute rotations in phase space with ellipticity controlled by
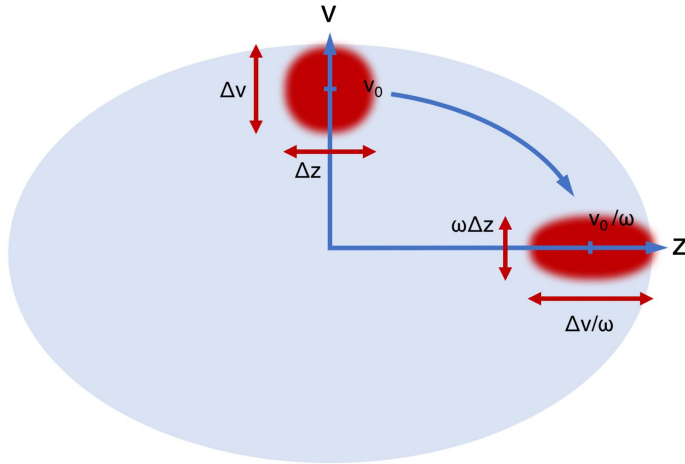
Figure 6.2: Phase space diagram depicting the action of the ideal phase space conservative loading fields derived from a large external harmonic potential. The region of phase space acted on by the external potential is indicated as a light blue ellipse. The region of phase space populated initially is shown in red along the v axis. The region populated after rotation is shown along the z axis also in red. Widths and origins are as indicated.

their oscillation frequency, the population would then be smoothly transferred over the course of a quarter oscillation to be centered at $z = v_0/\omega$ and $v = 0$, with widths $\omega\delta z$ and $\delta v/\omega$. If ω is chosen equal to $\delta v/\delta z$, i.e. to have the same strength as the trapping potential prior the initiation of the loading sequence, then the original widths in position and velocity are precisely maintained. On the other hand, ω could be tuned so as to optimize coupling between the initial traveling trapping potential and the trapping potential to be used after loading.

In addition to this harmonic loading potential, it would be ideal to also maintain a transverse trap simultaneously. The ideal fields would have a magnitude with the following spatial dependence:

$$|E(x,y,z)| = \frac{1}{2}m_{OH}\left(\omega_z^2 z^2 + \omega_r^2 r^2\right) \tag{6.5}$$

where ω_z and ω_r are the longitudinal and transverse trap frequencies. Neglecting the nonlinearity of the Stark shift for OH molecules close to zero field, such a harmonic potential could be generated transversely with a hexapole, but to do it simultaneously in the transverse and longitudinal directions would require an octopole moment, such as could be generated with three rings and two
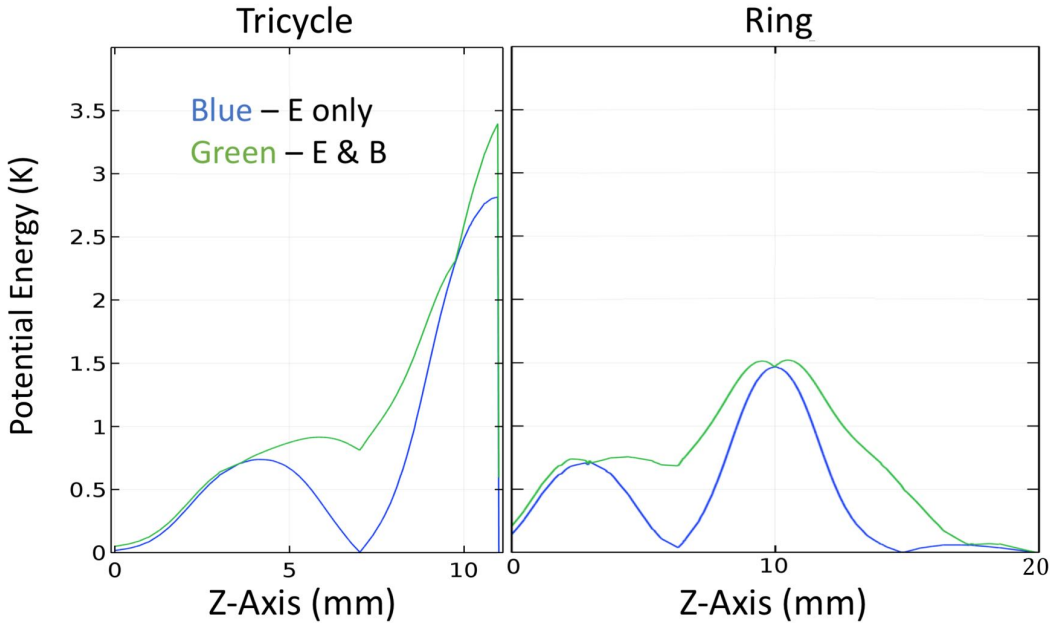
Figure 6.3: Potential energy along axis for Ring and Tricycle traps. The trap center is located at $z = 10$ mm in both cases. Note the more favorable slope of the loading potential in the vicinity of the trap center for the tricycle trap. Field magnitudes arise from application of ± 12.5 kV for the Ring trap and also for the Tricycle. In practice almost half this voltage was applied on the Tricycle for optimal operation, perhaps due to arcing effects or non-adiabatic transitions during loading discussed below in Sec. 6.3.

end-caps with the end-caps at $+V$, the outer rings grounded, and the inner one at $-V/2$ so as to approximate spherical boundary conditions following the second Legendre polynomial [122]. This would of course be very unlikely to be able to be crammed into the small space between the end of a decelerator and a trap, and unlikely to be able to be charged up to a high enough potential energy for stopping an appreciable speed v. It is much more likely that an efficient solution would be obtained by abandoning the harmonicity and instead focusing on the reduced criterion of loading fields that respect phase stability by having a slope at the location of what will be come the trap center and which also provide some transverse confinement. The slope of the loading field at the location of the trap center would ideally match the slope that the ideal harmonic trap with frequency ω would have at that point, $m_{\text{OH}}\omega v_0$.

In practice, Fig. 6.3 shows what we are able to obtain for loading fields comparing the Ring

and Tricycle traps. Note the role of the magnetic field, which is non-negligible. The tricycle trap comes much closer to the harmonic ideal discussed above. For the ring trap, the extra effect of the magnetic field actually depresses the potential energy at the trap center below a wider plateau, making it formally impossible to bring the synchronous molecule to rest at the trap center. In practice, the experimentally determined ideal application time of loading fields likely corresponds to the synchronous molecule being brought close to rest but out in front of the trap center. This unideal situation should result in a higher loaded temperature in the ring trap compared with the tricycle trap, 87 mK compared with 61 mK in simulation. In practice however, the measured spectra of molecules in the Ring trap fits better to a thermal distribution and to a lower temperature compared with the tricycle trap, see Fig. 6.5. Before discussing this further, we first revisit the process of spectroscopy in these traps.

6.2.3   Microwave Spectroscopy

A critical tool for understanding the behavior of populations in our magnetic traps is microwave spectroscopy performed on the parity changing transition between $|f, \frac{3}{2}\rangle$ and $|e, \frac{3}{2}\rangle$ states. This transition is ideal for spectroscopy, because it has a very small but nonetheless nonzero differential Zeeman shift of 26.6 MHz/T, which allows molecules to be resolved according to their magnetic field, while also allowing the entire trap to be surveyed over a very narrow bandwidth of microwave frequencies. The narrowness of the band is crucial for avoiding the complexities associated with the delivery of microwaves to the trapping region. If it were necessary to instead use microwaves to transfer molecules directly from a trapped to an un-trapped state by flipping their magnetic quantum number, $|f, \frac{3}{2}\rangle$ to $|f, -\frac{3}{2}\rangle$, scanning the trap would require scanning the applied microwave frequency between 1.7 and 16 GHz. While this is no problem for the microwave synthesizer itself, obtaining a suitably level passband in the components responsible for delivering the microwaves to the molecules would be unfeasible. In particular, the microwaves are delivered to the trap using a bias tee setup, nicely described in [114, Fig. 5], and the transfer function through the isolation capacitors is particularly troublesome, see Fig. 6.4. In contrast, with the entire pop-
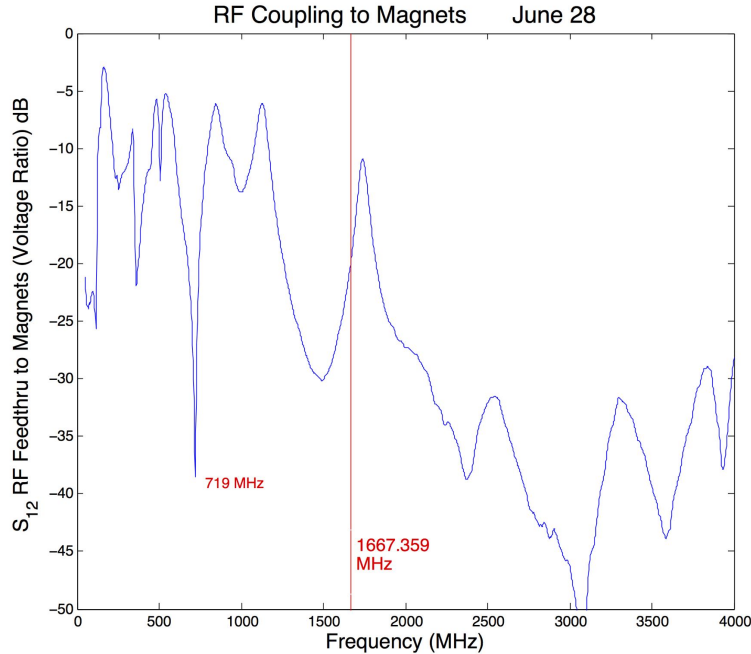
Figure 6.4: Microwave transfer function from vacuum feedthrough to magnet surfaces. Large variations are observed across the GHz scale required for performing spectroscopy along m-changing transitions, but not on the MHz scale required for $|f, \frac{3}{2}\rangle$ to $|e, \frac{3}{2}\rangle$ spectroscopy.

ulation sitting below 0.5 T, only 13 MHz needs to be scanned out of 1.7 GHz, and no significant attenuation variation is expected or measured.

In addition to the use of microwaves to transfer population, the spectroscopy relies on a few further steps. First, molecules in the $|e, \frac{3}{2}\rangle$ state remain trapped, and must be removed. This is done by first applying a bias electric field to allow molecules to escape via avoided crossings, like those shown in Fig. 1.1. In [114], it was nicely demonstrated that this is effective for removing molecules in the $|e\rangle$ state. Second, the process is repeated many times, with varying wait times so as to avoid any pathological resonance between the application of microwaves and the oscillation of molecules in the trap, which could result in certain privileged classes of molecule orbits always avoiding the microwaves. Third, comparison is made between the total laser induced fluorescence with and without the application of the spectroscopic sequence. When this is done, spectra such as shown in Fig. 6.5 are obtained.
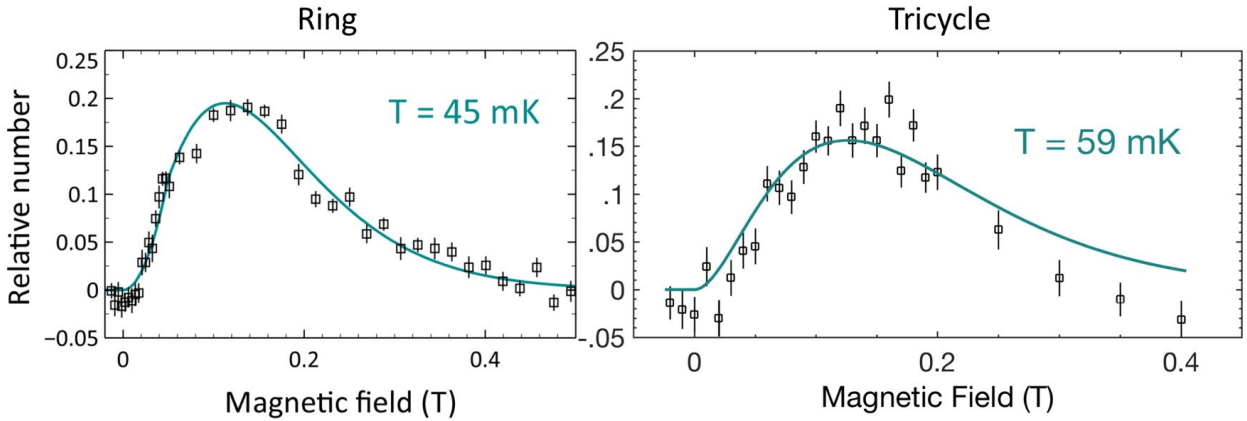
Figure 6.5: Spectra in the Ring and Tricycle traps after loading without forced evaporation. The former was published in [44, Fig. 3a], though repeated many times by the author afterwards. The latter was collected on Feb. 24, 2014.

6.2.4   Limitations to Spectroscopy

One key limitation to microwave spectroscopy via the procedure described is the spatial variation of sensitivity of the technique. The influence on microwave frequency dependent intensity has already been claimed negligible, but microwave intensity at any given frequency varies significantly across the cloud. This goes against the rule of thumb that electromagnetic intensity shouldn't vary significantly on length-scales below a wavelength, 18 cm in this case. This is because the microwaves are in the near field regime with respect to the conductors that form the trapping potential. The microwave fields may to a good approximation be taken to be dominantly electric and equal to the DC electric field distribution generated during loading but with magnitude oscillating at the microwave frequency. This means that their intensity should vary as shown in Fig. 6.6ab. In particular, the microwave intensity falls off quickly as molecules approach the openings of the magnets of the Ring trap. Furthermore, the efficiency of microwave transfer also features a polarization dependence. Since the $|f, \frac{3}{2}\rangle$ to $|e, \frac{3}{2}\rangle$ transition has $\Delta m = 0$, there is a dependence of the Rabi frequency describing the intensity of the microwave drive on the cosine of the angle θ between the electric and magnetic fields, see panel (c) of Fig. 6.6. This ends up favoring molecules on the axis of the trap.
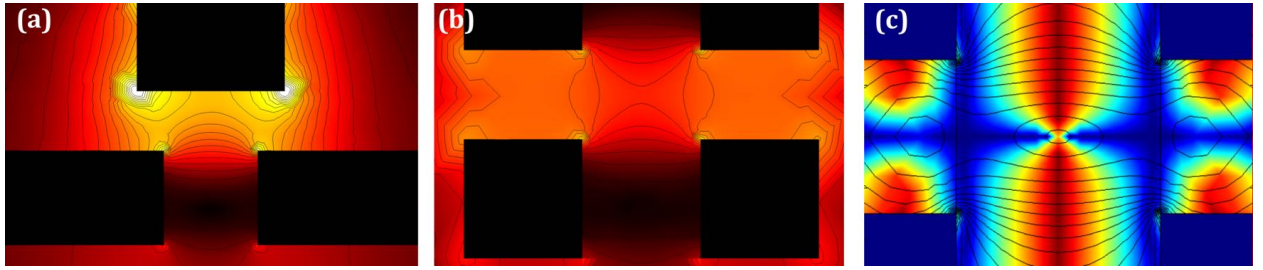
Figure 6.6: The near field intensity close to the (a) Tricycle trap and (b) Ring trap. Colors and contours are relative to the magnitude of the microwave drive, but may be thought of as ranging from 0 to 100% as color ranges from black to red to yellow to white, with contours at 5% intervals. Colors are comparable between the two traps, assuming the same microwave intensity on the surface of the conductors. These are also the DC field distributions for loading the traps, in which case color ranges from 0 to 200 kV/cm with contours every 10 kV/cm and 25 kV applied across the magnet surfaces. Rings are 3 mm apart for the Ring trap and in the Tricycle trap magnets are 2 mm apart. (c) The angle between electric and magnetic fields is shown, from red, 0, to blue, $\pi/2$ radians. Magnetic field contours every 500 G are superposed.

In mid 2013, an effort was made to perform spectroscopy along the $|f, \frac{3}{2}\rangle$ to $|e, \frac{1}{2}\rangle$ transition, with the goal of addressing the issue that $|e, \frac{3}{2}\rangle$-state molecules with total energies below the lowest crossing of the $|e, \frac{3}{2}\rangle$ and $|f, -\frac{3}{2}\rangle$ states at 410 G are unable to find their way out of the trap, see Fig. 6.7. The results were quite different from those performed along the $|f, \frac{3}{2}\rangle$ to $|e, \frac{3}{2}\rangle$ transition, perhaps due to polarization differences since this transition would feature dependence on $sin(\theta)$, but more likely reflective of the microwave coupling bandwidth issues discussed above.

Another point is the spatial dependence of the fluorescence collection system. Fig. 6.8 shows how the solid angle for photons to hit the lens varies with trap position, but beyond this there is of course the question of laser coverage. The laser is always optimized for signal, making it quite likely to be well overlapped with the trap center, but for the larger magnetic field ranges, there are regions of the trap that are likely not well exposed to the laser, especially inside the rings of the traps, since the laser impinges from the side.

Some of these spatial variations may be mitigated by an ergodic hypothesis. If the molecules can be assumed to be exploring all regions of phase space, then variations in detection efficiency may not significantly perturb the spectra or prevent it from representing the thermal state of the
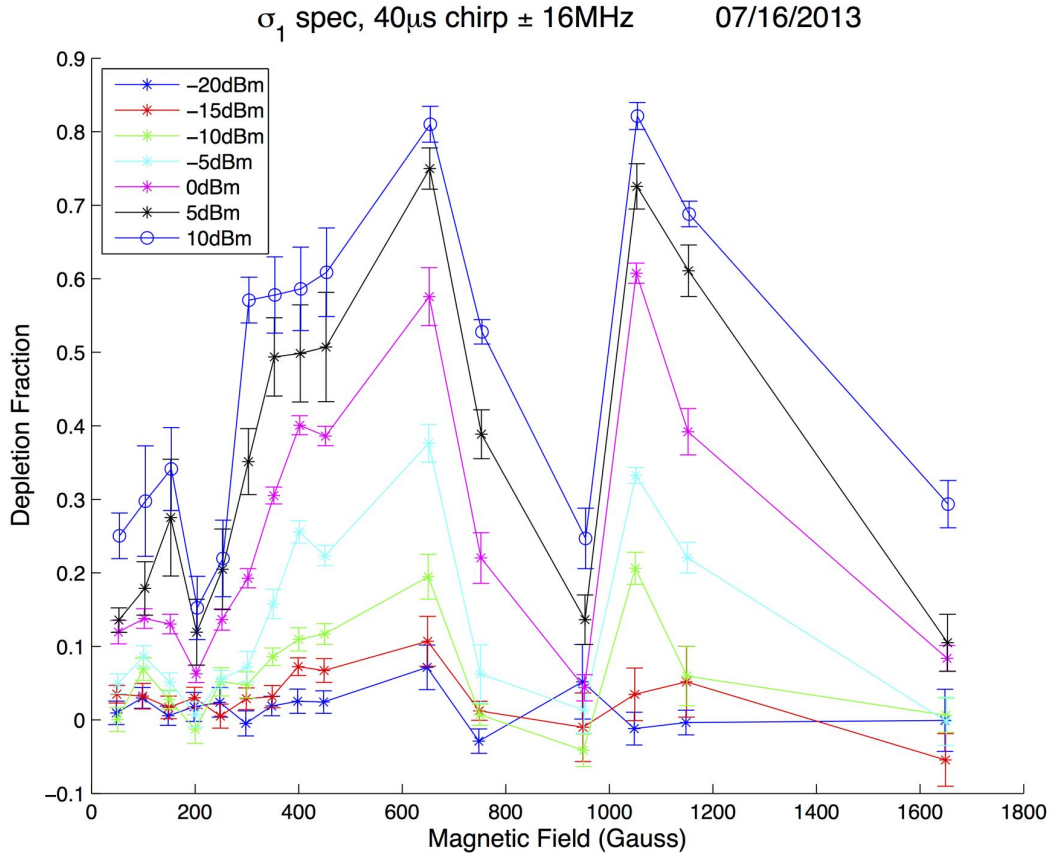
Figure 6.7: Depletion spectroscopy performed by microwave transfer from the $|f, \frac{3}{2}\rangle$ to $|e, \frac{1}{2}\rangle$ state. The dip between $800 - 1000$ G is likely an artifact of coupling efficiency challenges.

ensemble. Essentially, any blind spots in the spectroscopic procedure can be averaged away by the motion of the molecules themselves, since a molecule which is flipped from $|f, \frac{3}{2}\rangle$ to $|e, \frac{3}{2}\rangle$ by microwave outside of the view of the laser may after just a partial trap oscillation find its way back into view. Unfortunately, the ergodic hypothesis seems not well supported in this case, especially for the Ring trap where cylindrical symmetry guarantees angular momentum as a conserved quantity, unless strong elastic collisions capable of cross-dimensional thermalization were present. Since ideally spectroscopy would be a tool to help confirm the thermalization status of the ensemble, having this as an assumption becomes circular.

In any case, a final limitation of the spectroscopy worth discussing is that in principle it ought to be performed in a regime where the distribution is not significantly altered by the spectroscopy.
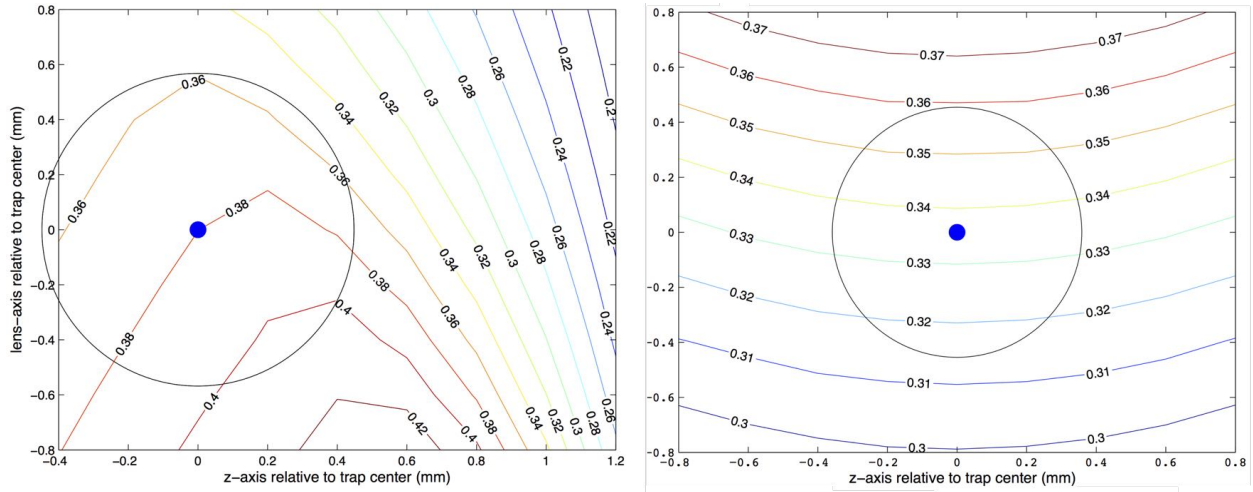
Figure 6.8: Collection solid angle for the Tricycle (left) and Ring (right) traps. Colors do not quite match between the two panels but are labeled in steradians. For the tricycle trap, the lens is located far below, while for the ring trap it is located far above. Electrodes are to the left and right of the plots. In both cases, solid angle variations within 500 μm of the trap center are on the 10% level only, although larger variations occur for molecules regularly reaching $3 - 5$ kG, a deviation of over 1 mm from the trap center.

This is difficult to respect in practice, because the less significantly the population is perturbed, the smaller the resulting signal and the longer the averaging time. In practice, the spectroscopies performed in the Ring and Tricycle trap usually push the boundary with respect to the perturbation threshold, with points collected at the peak of the distribution often featuring 30% population removal. Pushing this boundary threatens to add an artificial smoothing on top of the true magnetic field variation of the cloud, since even if one magnetic field were actually populated less fully than its neighboring magnetic field regions, so many microwave pulses are applied that even molecules which spend a small fraction of their time at that magnetic field end up having a decent likelihood of being removed. We can observe this effect to some extent by varying the number of microwave pulses used in the spectroscopic sequence, see Fig. 6.9. For the most part, the techniques agree with one another, but as far as the statistical likelihood of fitting to Maxwell-Boltzmann distributions, the single pulse spectra appears much more triangular, rising too far above the low and high field wings in the center.
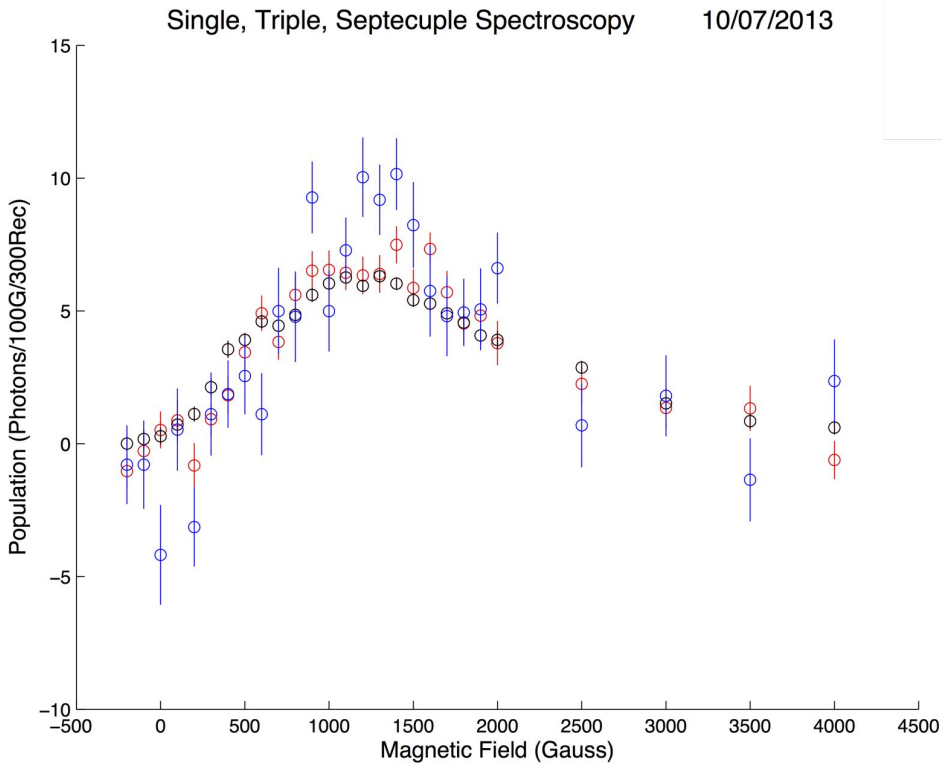
Figure 6.9: Three spectra obtained with differing numbers of microwave pulses. General agreement is good, but the single pulse spectra deviates more noticeably. This is an indication of the potential smoothing effect of including many pulses as discussed in the text.

6.2.5   Ring and Tricycle Thermometry

The obtained spectra in the two traps were shown above in Fig. 6.5. Several important features are worth discussing here. First of all, the Ring trap fits nicely to a Maxwell-Boltzmann distribution, which in a linear trapping geometry should scale with magnetic field in the following way:

$$p(B) \propto B^2 e^{\mu_B B/kT}. \tag{6.6}$$

The exponential term gives the expected Boltzmann suppression factor as a function of increasing potential energy, while the B^2 term is proportional to the volume degeneracy factor. In other words, the volume corresponding to a magnetic field B within dB is an ellipsoidal shell in the linear trap, whose surface area grows proportionally to B^2 since the trap is linear. Of course

there are already the limitations discussed above in Sec. 6.2.4, but in fitting Eq. 6.6 we must also account for deviations from the linear quadrupole geometry. Close to 1100 G, molecules should be exploring the region between the central and toroidal traps, a plateau which ought to contribute a large volume degeneracy factor, although perhaps this should be suppressed due to polarization. Close to the axis however, there is also a significant change in field gradient that occurs above and below ~ 1.5 kG. Contour lines are much more closely above than below, so that in principle the volume degeneracy factor should be different for the two regions.

In the tricycle trap, the fit is more dubious. Points clearly fall below the fit at high magnetic fields, and also seem to lie below at the lowest fields as well. On the other hand, given that the tricycle trap opens to the environment above 3 kG, it may be that falling below the Maxwell-Boltzmann fit line is the more natural thing to occur in this situation. Alternatively, there is another factor at play here worth mentioning- the influence of the nuclear spin of the molecule. This comes not from the ^{16}O, which has a spin nucleus, but from the hydrogen. It does not create any significant perturbation to the trapping potential experienced by the molecules at the energy scales we are considering here, but because the differential Zeeman shift between the $|f, \frac{3}{2}\rangle$ and $|e, \frac{3}{2}\rangle$ states is a hyperfine effect, some relevant features emerge. Specifically, at low magnetic fields we have to work in the coupled hyperfine basis $F = I + J$, and the $|f, m_{\mathrm{J}} = \frac{3}{2}\rangle$ state actually includes two substates, $|F, m_F\rangle$ equal to $|2, 2\rangle$ and $|2, 1\rangle$. The former experiences a fixed differential Zeeman shift relative to its opposite parity partner, but the latter experiences a varying differential Zeeman shift at low fields, see Fig. 6.10a. This has a significant effect on how a Maxwell-Boltzmann spectra ought to look for a population uniformly split between the two substates. Essentially, the shift grows significantly closest to zero field, so that as the microwave is scanned across what would correspond to a 500 G for the $|2, 2\rangle$ state, only a third of that is scanned for the $|2, 1\rangle$ state. In the Tricycle trap, including this effect leads to an improvement in the fitting of the distribution relative to excluding it as shown in Fig. 6.10c, while in the Ring trap the reverse is likely the case.

Uniform splitting is indeed what we would expect, even after carefully thinking through adiabatic transitions during loading described soon in Sec. 6.3. None of the spin-flip and non-

adiabatic effects give significant bias to one nuclear spin orientation over the other; the nuclear spin orientation does often change after spin flips or non-adiabatic transitions, but with both populations present before, both are present afterwards. This jives with thermodynamic intuition, since the ensemble temperature of ~ 50 mK is far hotter than the energy splitting arising from the nuclear spin of only 40 MHz or 2 mK. Equal population is also more or less consistent with the observations in 6.24, where small stray electric fields perturb measured population distributions due to avoided crossings which appear in two different locations corresponding to $|2, 2\rangle$ and $|2, 1\rangle$.

6.2.6   Summary

The performance of spectroscopy deviates from the ideal in several key respects, which are spatial variation of sensitivity due to polarization, fluorescence collection, and microwave intensity variations; and oversampling beyond the small perturbation regime. The functional form of the expected distribution deviates from the ideal given in Eq. 6.6 due to significant variations of the volume element relative to a linear quadrupole, including the toroidal plateau, and the gradient enhancement above 1.5 kG. Nuclear spin effects should influence this functional form still further. In light of all this, the close fit of the microwave spectroscopy on the Ring trap at left in Fig. 6.5 to the functional form given in Eq. 6.6 is not a reliable indication of the degree of thermalization of the ensemble. Similarly, the lack of a close fit to the microwave spectroscopy on the Tricycle trap is not a reliable indicator of any lack of thermalization in that ensemble. This spectroscopy should rather be used as a general indicator, assigning a representative temperature at the 10% level, but not making any guarantee of the presence or absence of thermalization.

Thermalization aside, microwave spectroscopy may still be used to compare the spatial density achieved in the two traps. To do so, it is necessary to make some historical comparison of relative molecule numbers, and also to choose a size within which to count molecules for both cases. Doing so leads to the numbers shown in Tab. 6.2. Taking the measured photon number, multiplying by the fraction below 1 kG, dividing by collection solid angle, and multiplying by gradient cubed gives the numbers shown in the density column of Tab. 6.2, for an overall fourfold
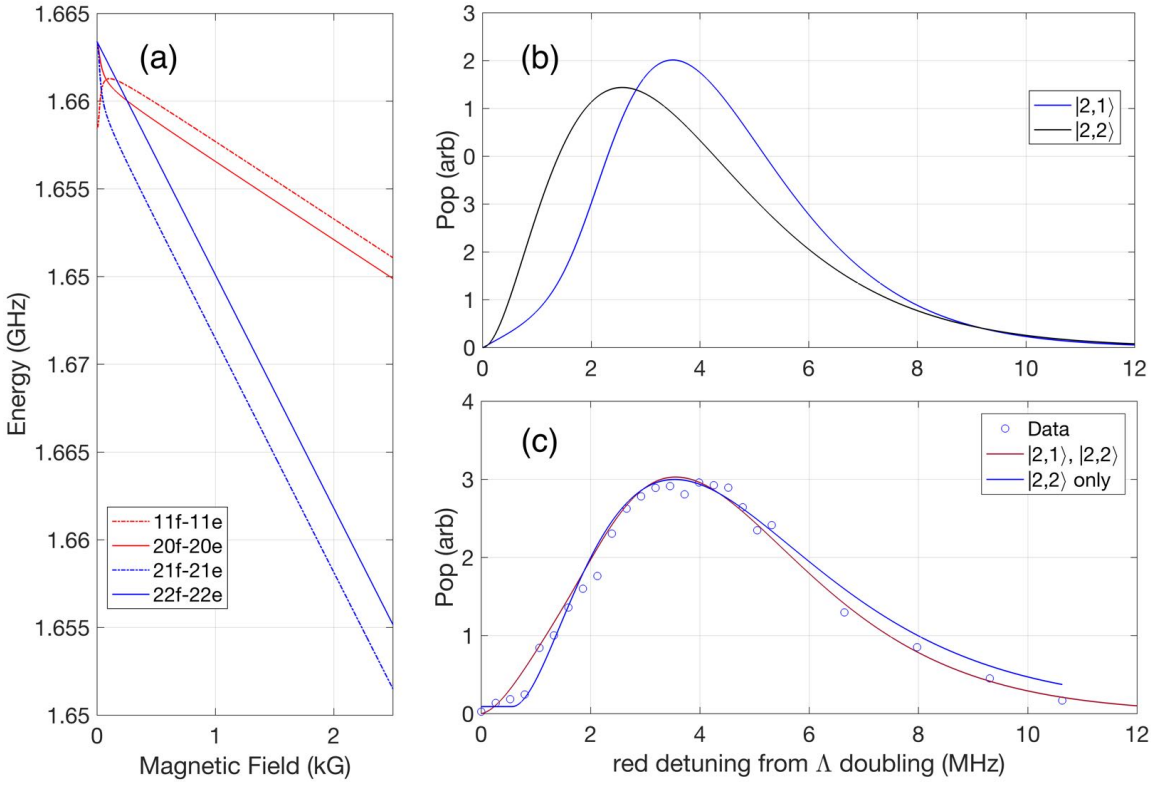
Figure 6.10: Inclusion of nuclear spin in differential Zeeman shift calculations is shown to significantly influence microwave spectroscopy. (a) Microwave frequencies for targeting different states are shown as a function of magnetic field for the four substates of what in the $|J, m_J\rangle$ basis are the $|f, \frac{3}{2}\rangle$ and $|f, \frac{1}{2}\rangle$ states. (b) Distribution functions for the $|F = 2, m_F = 2\rangle$ state and for the $|F = 2, m_F = 1\rangle$ state versus microwave frequency. (c) The differential Zeeman shift of the $|2, 2\rangle$ state is used to convert between microwave frequency and magnetic field. Data collected on March 13, 2014 are shown. The green line shows what the Boltzmann distribution function accounting for the presence of both states would look like, and is a fit to 37 mK. Blue only includes $|2, 2\rangle$ and fits to 52 mK with a zero point offset.

Table 6.2: Historical Data are consulted in comparing the trap population between Ring and Tricycle traps. In the tricycle trap, the number below 1 kG are counted, giving rise to the reported fraction, while in the ring, the number below 1 kG are counted. This reflects the doubly strong gradient in the Tricycle trap.

Trap	Num	Fraction	Ω	Gradient	Density
Tricycle	78 ± 3	$22 \pm 3\%$	0.38	2	360 ± 60
Ring	110 ± 2	$28 \pm 4\%$	0.34	1	91 ± 13
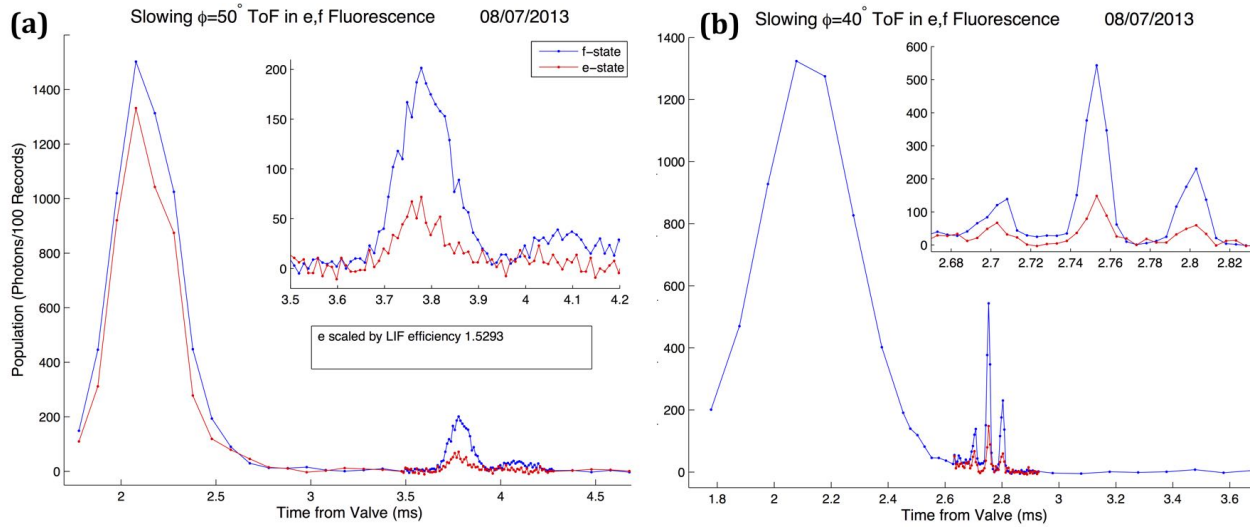
Figure 6.11: $|e\rangle$ parity molecules are observed after two different decelerations. (a) $\phi = 40°$ deceleration. (b) $\phi = 50°$ deceleration. Insets zoom in on the decelerated packet. Note also the relative peak heights of the un-decelerated and decelerated molecules.

improvement in spatial density in the Tricycle trap.

6.3 Adiabatic Transitions during Loading

In early 2014, we were startled to discover that $|e\rangle$ state molecules were able to survive the decelerator, and were appearing in significant numbers in our detection scheme at various final speeds and even after loading the trap, see Fig. 6.11 This discovery led to a renaissance in our understanding of transitions between states. Essentially what is happening is that molecules which are in the $|f, -\frac{3}{2}\rangle$ state during the deceleration are able to adiabatically transition to the $|e\rangle$ state due to the presence of the magnetic field in the detection region, despite the fact that the molecules are not trapped and are only briefly flying through the trap. We realized that the magnitude of electric field required to allow adiabatic transitions between the $|f, -\frac{3}{2}\rangle$ and $|e, -\frac{1}{2}\rangle$ states was actually quite small, only a few V/cm. Since molecules pass through regions well in excess of 1200 G where these states cross on their path into the trap region, all of the molecules in the $|f, -\frac{3}{2}\rangle$ state would deterministically make this transition assuming a rather small stray field.

During the loading of the molecules, a similar fate may befall the $|f, -\frac{3}{2}\rangle$ molecules delivered by the decelerator. When the loading fields are finally switched off, these molecules do not maintain their $|f, -\frac{3}{2}\rangle$ character, but rather follow a tangle of adiabatic crossings, and therefore retain their energetic hierarchy. That is to say, $|f, -\frac{3}{2}\rangle$ molecules remain in the second highest energy state, which can be either $|f, \frac{1}{2}\rangle$ or $|e, \frac{3}{2}\rangle$ depending on the magnitude of the magnetic field at the molecule's location during the rapid turn-off of the electric fields used for loading. In light of this, statements such as the following, "perfect OH rotational, Λ-doublet, and hyperfine state purity is achieved" [79, Page. 19061, Top Right] become somewhat ironic. An example of how significantly this turns out to be false is shown in Fig. 6.12. Many molecules are remaining in $|e\rangle$ parity states, regardless of whether an extra bias field is left on or off after loading. It is unclear whether this is a result of molecules regularly adiabatically transiting between $|f, \frac{1}{2}\rangle$ and $|e, \frac{3}{2}\rangle$, or whether something different is going on, such as a more complex orbital route including states of even lower energy. Either way, one clear way to address the problem is to include regular switching of the electric field to address any partially trapped orbitals including $|e\rangle$ parity segments. From Fig. 6.12, a single switching event already significantly reduces the problem.

To complicate matters further, another kind of adiabatic transition, perhaps more appropriately termed a spin-flip, can also occur close to zero magnetic field in the presence of electric field. At zero magnetic field, there is also a degeneracy between states, not of opposite parity but of the same parity and differing m number. Depending on the angle between the electric and magnetic field [a], these states are brought much closer together, facilitating spin-flips. This is described further in the Appendices of both [121] and [88, App. A], and is also depicted visually in Fig. 6.13 The upshot for loading is that molecules which cross the plane including the magnetic zero almost certainly flip between $|f, \pm\frac{3}{2}\rangle$ given the very large magnitude of the loading fields.

It therefore follows that many of the molecules which end up in the $|f, \frac{3}{2}\rangle$ state after loading

---

[a] In fact, all of the opening and closings of avoided crossings between states have dependencies not only on the magnitude of the electric field but on this angle as well. Their exact functional form may be computed via perturbation theory on the OH ground state Hamiltonian, which is actually analytically solvable since its eigenvalues always come in pairs and therefore the system reduces to a quartic polynomial system, which has analytic expressions for its roots. The perturbation has to be taken to various orders depending on how different the m number or the parity are of the two states that are interacting.
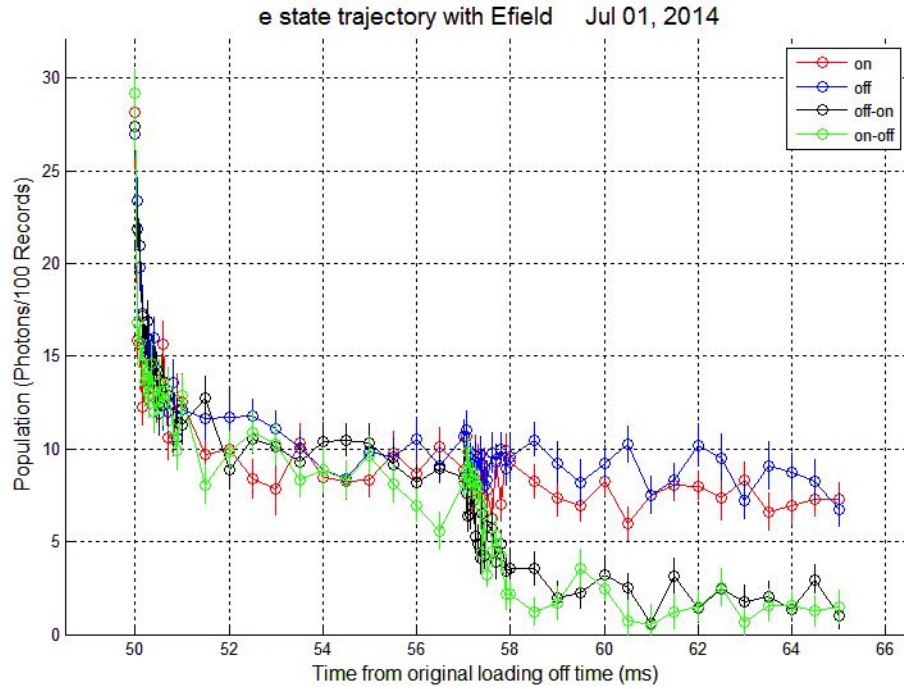
Figure 6.12: $|e\rangle$ parity molecules stably remain in the trap under either constant bias electric field or zero electric field, but not switching between the two.
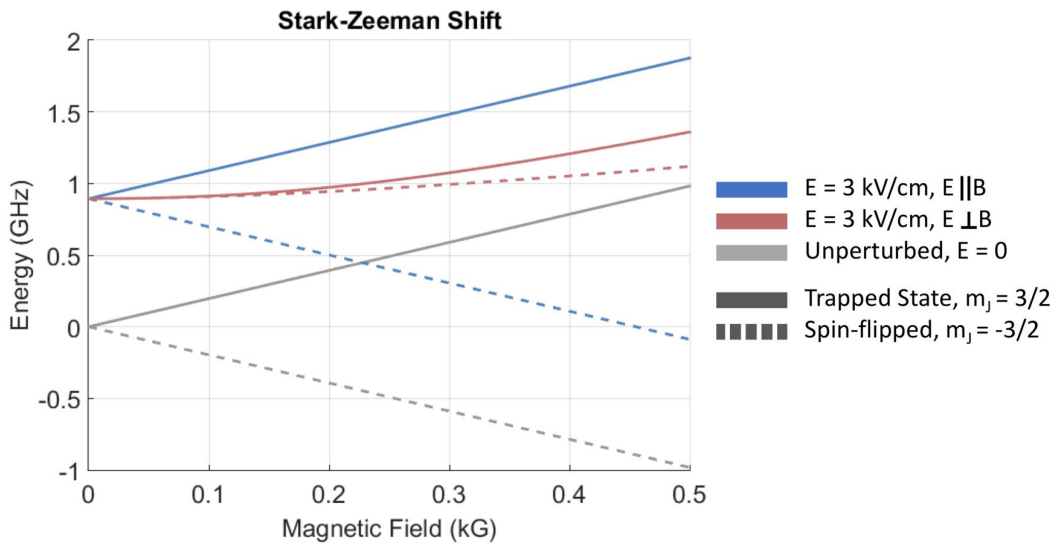
Figure 6.13: The $|f, \frac{3}{2}\rangle$ and $|f, -\frac{3}{2}\rangle$ state with varying B-field and three E-field conditions. The states are squeezed together when the electric field is orthogonal to the magnetic, which in the Ring and Tricycle happens along the plane parallel to the magnet surfaces through the trap center.

have in fact experienced the loading fields as $|f, -\frac{3}{2}\rangle$ molecules, and therefore with a different on-axis potential than the two already shown in Fig. 6.3 which include or exclude the magnetic field. This on-axis potential is added in red in Fig. 6.14. The magnetic field is seen to reduce the magnitude of the potential experienced by the $|f, -\frac{3}{2}\rangle$ states relative to $|f, \frac{3}{2}\rangle$ wherever the magnetic field is non-zero. Although with near-unit flipping between the two across the trap center, the $|f, -\frac{3}{2}\rangle$ states actually experience a larger stopping potential than the $|f, \frac{3}{2}\rangle$. Because the $|f, -\frac{3}{2}\rangle$ molecules experience a reduced potential except past the trap center, they should arrive earlier, having traveled at a larger speed than their $|f, \frac{3}{2}\rangle$ counterparts. It should therefore be possible to deterministically load $|f, \frac{3}{2}\rangle$ molecules just before the plane and $|f, -\frac{3}{2}\rangle$ molecules just after, so that the latter actually convert to $|f, \frac{3}{2}\rangle$ during the loading. It would be interesting to demonstrate this experimentally by sitting on the e-state LIF transition during the loading and seeing whether tuning of the time-length of application of the stopping fields actually varies the initial loading of the $|e\rangle$ state. It should be possible to observe variation, and it should be the case that a minimum in loading of the $|e\rangle$ state would correspond to an optimally deterministic transitioning of $|f, -\frac{3}{2}\rangle$ molecules into $|f, \frac{3}{2}\rangle$ during the loading sequence.

6.3.1   Multi-pulse Loading

The field distributions used for loading the Ring trap feature an extra bump in between the end of the decelerator and the beginning of the trap, refer back to Fig. 6.3. This bump could in principle be used to perform last minute slowing or bunching prior to trap loading, especially if it were strengthened in magnitude by also turning on the last decelerator electrodes to the same voltage. We attempted this in 2014, and obtained the disappointing results shown in Fig. 6.15, among many other such datasets. This was also our first attempt at using Behlke switches in series, at least for serious tri-polar output voltages and not only trap-floating voltages, and in the end led to one of my first broken Behlke switches. At the time, we assumed HV issues, or perhaps that the bump was essential for transverse focusing, but the idea of loaded molecules actually existing as $|f, -\frac{3}{2}\rangle$ during loading never occurred to us. With regards to $|f, -\frac{3}{2}\rangle$ molecules, the extra switching
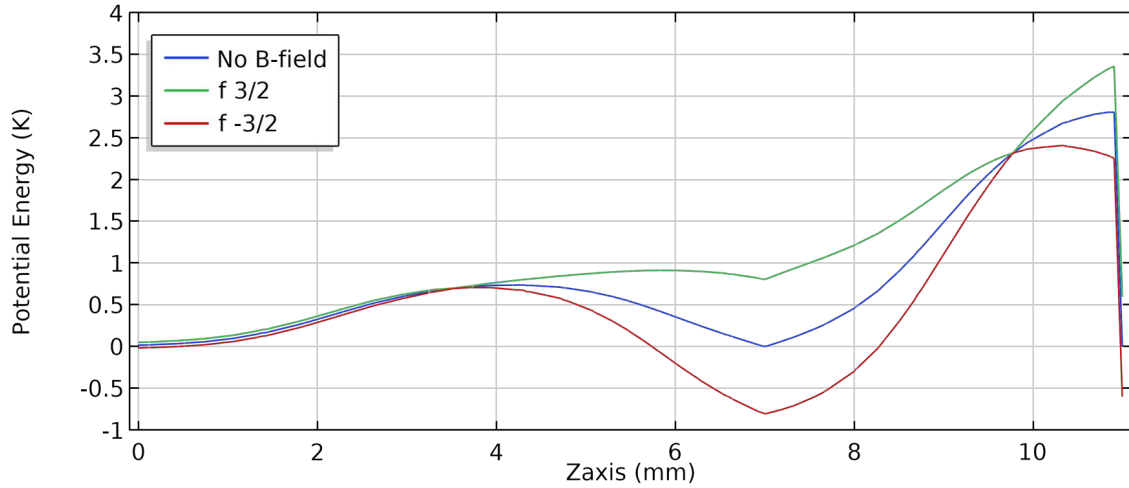
Figure 6.14: The potential for molecules in the $|f, -\frac{3}{2}\rangle$ state during trap loading. The trap center can be seen close to 10 mm based on the single-point overlap of the three traces indicating an isolated magnetic zero. Due to the spin-flip inducing behavior of superimposed electric and magnetic fields close to magnetic zeros, molecules in the $|f, -\frac{3}{2}\rangle$ state to the left of the zero transition uniformly into $|f, \frac{3}{2}\rangle$ to the right of the zero, and vice versa. The kink seen close to 7 mm corresponds may at first come as a surprise. This occurs in all three traces and is therefore an electric field effect. It turns out to be the zero of a weak electric quadrupole trap formed by the loading fields at the center of the frontal ring magnet of the Tricycle trap, as can be seen more clearly by studying Fig. 6.6(a).

events and extra flight time with varying magnetic field and no electric field out in front of the magnets where the extra bump is created could lead to those molecules being transferred to various other sub-levels. This would reduce the flux of $|f, -\frac{3}{2}\rangle$ molecules through the trap center to then spin-flip into trapped $|f, \frac{3}{2}\rangle$ molecules.

6.4   Pin Trap

Originally motivated by an attempt to repeat the electric field inelastic collisions reported in [121], but this time in the tricycle trap, it was discovered that electric field induced single particle loss via spin-flips were in fact a dominant mechanism, overwhelming an effect attributable to inelastic collisions. In this section, we recapitulate the conversations also available in [88], which describe this mechanism in the most coherent way we were able to contrive.
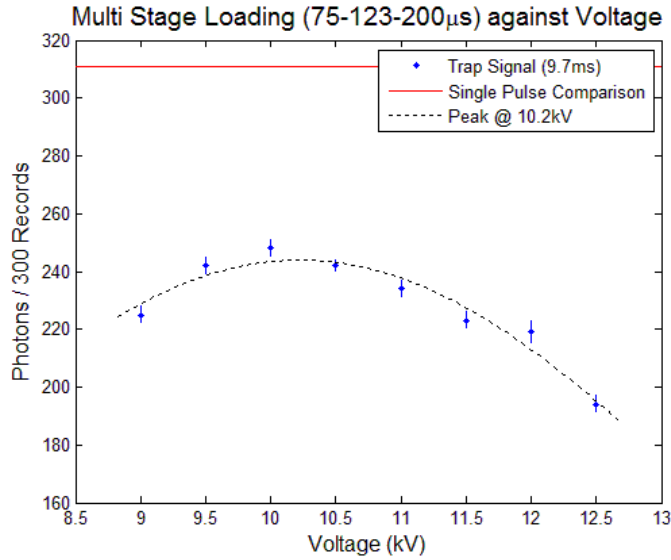
Figure 6.15: Breaking up the loading pulse into an extra slowing pulse followed by loading only leads to a reduction in trapped molecules.

6.4.1   Introduction

A diverse array of direct cooling strategies have succeeded on various molecules [119, 90, 123, 105, 124, 125, 126, 127], including those now enabling molecular collision studies [79, 128, 129, 130]. Many of these molecules will require secondary strategies like evaporation or sympathetic cooling to make further gains in phase space density [131, 44, 132]. They also may face a familiar challenge: spin flip loss near the zero of a magnetic trap, but dramatically enhanced for doubly dipolar molecules, relative to atoms, due to their internal spin dynamics in mixed electric and magnetic fields.

Spin flips were directly observed for magnetically trapped atoms near $50\,\mu$K and overcome with a time-orbiting potential trap [133] or an optically plugged trap [2], enabling the first production of Bose-Einstein condensates. Non-laser-based molecular cooling experiments begin at modest temperatures and require trap strengths typically only attained with quadrupole fields [119, 87, 134, 135, 136]. In the 2 T/cm magnetic quadrupole used in our previous studies of hydroxyl radicals (OH) [44], spin-flips should not have had a significant influence until the μK

regime, but the application of electric field changes this. Electric fields applied to magnetically trapped dipolar species offer interesting opportunities to study anisotropic collisions and quantum chemistry [121]. They can also be useful for control over state purity [114]. But the electric field can also dramatically enhance spin-flip losses, due to internal spin-dynamics that we corroborate with direct experimental evidence for the first time in the present work. We achieve this with a novel trap geometry that also allows complete removal of the loss with minimal sacrifice of trap strength.

6.4.2 Loss Mechanism

The internal spin-dynamics leading to spin-flip enhancement are subtle, having eluded two previous investigations: In Ref. [137] the analogues of atomic spin-flip loss for molecules in mixed fields were modeled. It was concluded that no significant loss enhancement due to electric field would be evident. However, this conclusion holds only for the approximate Hamiltonian used in that study, not more generally. In Ref. [138] it was correctly noted that Hund's case (a) molecules maintain a quantization axis in mixed fields. The states of the molecule were shown to align with one of the two quantization axes set by the vector fields $\vec{X}^{\pm} = d_{\text{eff}}\vec{E} \pm \mu_{\text{eff}}\vec{B}$ [b] , μ_{eff} and d_{eff} the effective dipole moments of the molecule in uncombined fields. The key idea is that Hund's case (a) molecules have both dipole moments fixed to their internuclear axis, so that in the molecular frame, the energy shifts from the two fields combine like vectors. It was also shown that the combined Stark-Zeeman energy shift of the molecule is proportional to the length of either $\vec{X}^{\pm}$, depending on the choice of quantization axis, with proportionality given by an m quantum number. This basis was dubbed "Hund's Case X," and it was asserted that the existence of the Hund's Case X quantization axis would prevent flips near the zero of a quadrupole trap. As we now describe, the loss is actually enhanced, but this Hund's Case X basis actually proves very useful in explaining why.

---

[b] The authors use $\mu_{\text{eff}}\vec{B} \pm d_{\text{eff}}\vec{E}$. We reverse this to provide a more physical connection to our experiment, where the electric field is fixed.
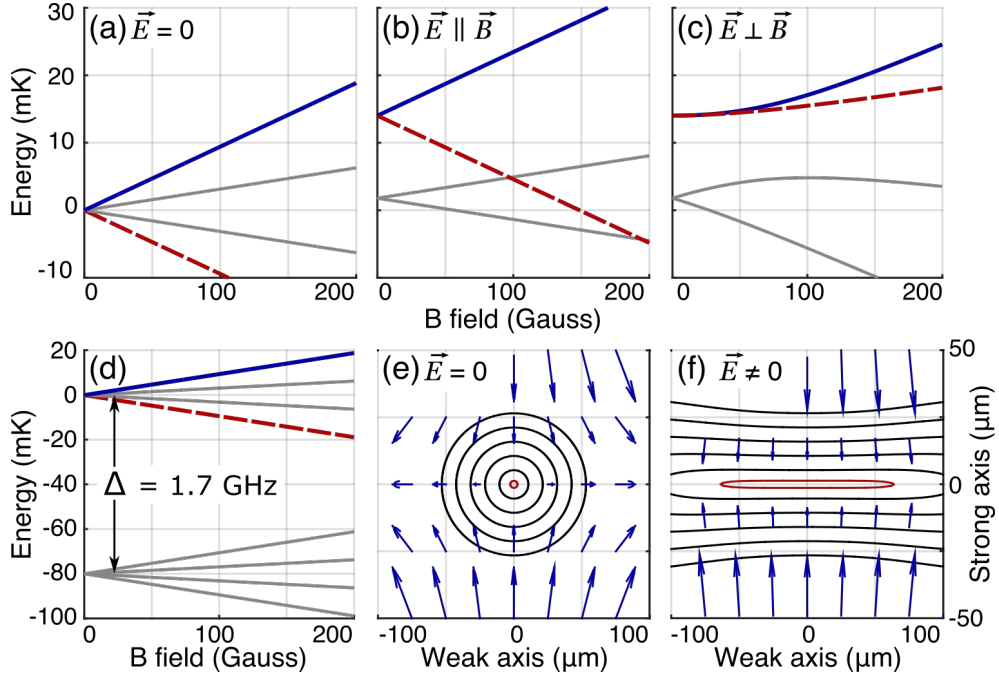
Figure 6.16: A uniform electric field, added to magnetically trapped molecules for dipolar studies or other purposes, enhances spin-flip losses. Note in particular the increased size of the lowest contour (red) in panel (f) relative to panel (e); this result can be understood by considering Zeeman shifts under various conditions as shown in panels (a-c) and described further now. Four Zeeman split lines in OH's $X^2\Pi_{3/2}$ manifold are shown (a-c), with the doubly stretched state in blue and its spin-flip partner in dashed red. These states are shown with no electric field (a), with $|\vec{E}| = 150$ V/cm and $\vec{E} \parallel \vec{B}$ (b), and with $\vec{E} \perp \vec{B}$ (c). Note the vastly reduced red-blue splitting in the latter case. The ground state consists of two parities and four m states each, usually labeled $|\text{parity} = f, e; \ m = \pm 1/2, \pm 3/2\rangle$. The negative parity, electrically strong field seeking manifold sits Δ below (d). The application of electric field generally drives these parities further apart, but within each parity manifold the exact modification depends on the relative field orientations (b-c). In panels (e-f), energy splitting contours are shown every 40 MHz near the zero of a 2 T/cm magnetic quadrupole trap for OH molecules [114] with $\vec{E} = 0$ (e), and with uniform $E = 150$ V/cm along the strong axis of the quadrupole (f). The vectors are $d_{\text{eff}}\vec{E} + \text{sign}(\vec{E} \cdot \vec{B})\mu_{\text{eff}}\vec{B}$, the proper quantization axis for well-trapped molecules as described in the text.

We begin with an intuitive picture. In order to remain well trapped in combined fields, a molecule must remain weak field seeking with respect to both fields, i.e. doubly stretched. This means that the quantization axis to which it aligns should correspond to the vector field $\vec{X}^{\pm}$ with maximal length at the molecule's location. In a geometry where the fields are continuously rotating, the maximal length vector field can be either of $d_{\text{eff}}\vec{E} \pm \mu_{\text{eff}}\vec{B}$, depending on whether the fields are

oriented closer to parallel or antiparallel. Consider a molecule in a magnetic quadrupole trap with a uniform electric field. This trap has two hemispheres, a parallel hemisphere where the fields are closer to parallel, and vice versa. The hemispheres are separated by a plane where $\vec{E} \perp \vec{B}$, which intersects the trap center. Now suppose a molecule in the doubly stretched state begins in the parallel hemisphere. To be doubly stretched, it must be aligned to the sum quantization axis set by the vector field $\vec{X}^+ = d_{\text{eff}}\vec{E} + \mu_{\text{eff}}\vec{B}$. If its trajectory carries it near the trap center where the magnetic field is small, the electric field does indeed maintain the quantization axis and the molecule's alignment with it. However when the molecule enters the antiparallel hemisphere, the magnitude of this quantization axis now decreases with increasing magnetic field. This molecule has therefore spin-flipped from the doubly stretched state to a magnetically strong field seeking state. These states are degenerate in the plane where $\vec{E} \perp \vec{B}$, leading to loss.

This intuition agrees with a more rigorous analysis of the energy splitting G between the trapped state and its spin-flip partner. By diagonalizing the approximate eight state ground molecular Hamiltonian for OH, subtracting the relevant state energies and Taylor expanding, we find:

$$G(\mathcal{B}_\perp, \mathcal{B}_{||}, \mathcal{E}) = 2\mathcal{B}_{||} + 4.3 \cdot \mathcal{B}_\perp^3 \frac{\Delta^2}{\mathcal{E}^4} + \mathcal{O}(\mathcal{B}_{||}^2, \mathcal{B}_\perp^4) \tag{6.7}$$

Here $\mathcal{B}_{\perp,||} = \mu_{\text{eff}}\vec{B} \cdot \hat{e}_{\perp,||}$, where $\hat{e}$ is the unit vector in the labeled direction relative to the electric field. $\mathcal{E} = |d_{\text{eff}}\vec{E}|$, Δ is the lambda doubling (see Fig. 6.16d). The relevant splitting is not quite zero where $\vec{E} \perp \vec{B}$ and $B_{||} = 0$ thanks to Δ, but nonetheless reaches a deep minimum; the remaining Zeeman splitting is reduced from linear to cubic in magnetic field (Fig. 6.16). This Zeeman splitting suppression is in fact a known phenomenon in the precision measurement community [139, 140], and experimentalists have exploited it to suppress the influence of magnetic fields in electron EDM measurements. However, in the case of applying mixed fields during trapping, this suppression is not beneficial but rather detrimental.

To deduce the effect of this loss plane on the ensemble, we consider molecular trajectories in light of the Landau Zener formula:

$$P_{\text{hop}} = e^{-\pi\kappa^2/2\hbar\dot{G}}, \tag{6.8}$$

Table 6.3: Enhancements (η) and loss rates (γ) for OH with typical applied fields. Zero field values are equivalent to traditional spin-flip loss. Electric field is required during evaporation and spectroscopy to open avoided crossings [44, 114], or applied to polarize the molecules and study collisions [121].

E (V/cm)	55 mK		5 mK		Purpose
	η	$\gamma\,(s^{-1})$	η	$\gamma\,(s^{-1})$	
0	1	0.02	1	1.3	Zero Field
300	5	0.1	9	11	Evaporation
550	17	0.3	40	50	Spectroscopy
3000	1000	19	1600	2000	Polarizing

which relates the probability of diabatically hopping between two states P_{hop} to their energetic coupling κ and their rate of approach $\dot{G} = v_z dG/dz$. Here z and v_z are normal to the $\vec{E} \perp \vec{B}$ plane, and we neglect the components of $\dot{G}$ due to the other coordinates since from Eqn. 6.7 it is clear that G grows predominately in one direction. We can also set κ to the minimum energy gap along the trajectory, which is found in the plane. This facilitates direct numerical computation of the loss rate (γ) by integrating the molecule flux through the plane for a thermal distribution, weighted by the hopping probability. The expression is more fully derived in Chapter 7. We perform these integrations for OH over the velocity distribution in a 2 T/cm magnetic quadrupole [87] under various electric fields in Tab. 6.4.

We have also developed an algebraic scaling law, which yields the electric field induced loss enhancement factor

$$\eta = \frac{3}{11} \left(\frac{d_{\text{eff}} E}{\sqrt{\kappa \Delta}} \right)^{8/3}, \tag{6.9}$$

see Sec. 6.4.4 for the full derivation. Here κ represents a characteristic energy scale for spin-flips that can be derived by setting $P_{\text{hop}} = 1/e$ in Eqn. 6.8 and using a typical value of v_z. This means that for electric fields with $d_{\text{eff}} E > \sqrt{\kappa \Delta}$, the loss enhancement is almost cubic with electric field. Crucially, it is not Δ that sets the relevant scale, as one might naively suppose given that this is the energy beyond which the Stark effect is linear and the molecule is polarized. Instead it is $\sqrt{\kappa \Delta}$, which is in general much smaller; $\kappa = 5$ MHz for OH in our trap, while $\Delta = 1.7$ GHz.

Returning to the numerical approach, the direct integration of flux is a key improvement

relative to our previous work [121], where electric fields were applied to study collisions. The mechanism of molecular spin-flip loss was identified, and an attempt was made to deconvolve it from the collisional effect of the electric field. Revisiting this with the direct integration of flux, we find a three-fold larger loss magnitude, enough to explain a significant portion of the effect previously attributed to collisions, see Chap. 7. In light of this, it becomes especially important to perform direct, un-convolved experimental verification of both the magnitude of the loss effect and the validity of our loss-flux calculations. We now present the new trap where this is achieved.

6.4.3   Experiments and Results

Our idea is to use a pair of 2D quadrupole traps, one magnetic and the other electric, with orthogonal centerlines (Fig. 6.17):

$$\vec{B} = B'x\hat{y} - B'y\hat{x} \qquad \vec{E} = E'y\hat{y} - E'z\hat{z} \tag{6.10}$$

We achieve these fields in a geometry that matches our Stark decelerator [123]. This geometry features large spin-flip loss, since $\vec{E} \perp \vec{B}$ in both the $x=0$ and $y=0$ planes, and from Eqn. 6.7, $G = \mathcal{B}_\perp^3 \Delta^2 / \mathcal{E}^4$ will be generally very small due to the large $\mathcal{E}$. However, by adding a small magnetic field $\vec{B} = B_{\text{coil}}\hat{z}$ along the centerline of the magnetic quadrupole with an external bias coil, a dramatic change can be made to the surfaces where $\vec{E} \perp \vec{B}$ with minimal perturbation of the trapping potential.

B_{coil} morphs the $\vec{E} \perp \vec{B}$ surface from a pair of planes into the hyperbolic sheet given by $x \cdot y = z \cdot B_{\text{coil}} / B'$ (Substitute Eqn. 6.10 into $\vec{E} \cdot \vec{B} = 0$). This means that $\vec{E} \perp \vec{B}$ is pushed away from the z-axis where $\vec{B}$ is smallest. In Fig. 6.18, the surfaces where $\vec{E} \perp \vec{B}$ for several B_{coil} magnitudes are calculated and shown wherever $G \leq \kappa$. The loss regions ought to be tuned far enough from the trap center that molecules cannot access them. This is indeed what we observe, note the striking difference in trap lifetimes in Fig. 6.19a. With only $200\,\text{G}$ bias field (the trap is $5\,\text{kG}$ deep) the loss is suppressed below that due to background gas.

To further verify our understandings of the loss mechanism, we translated one of the magnetic
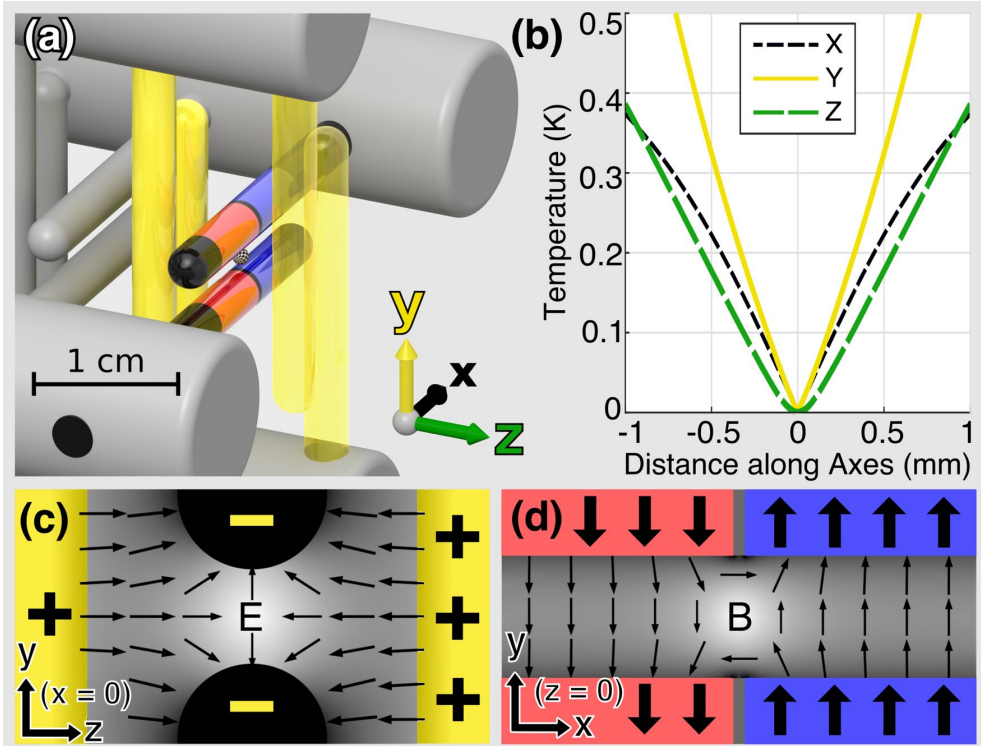
Figure 6.17: The last six pins of our Stark decelerator [87] form the trap (a), which is 0.45 K deep with trap frequency $\nu \approx 4$ kHz (b). Along y the trap is bounded by the 2 mm pin spacing. The yellow pins are positively charged and the central pin pair negatively, which forms a 2D electric quadrupole trap with zero along the x-axis. This is shown for the $x = 0$ plane (c), with yellow pins artificially projected for clarity since they don't actually intersect the plane. The central pins are magnetized, with two domains each. Blue indicates magnetization along $+\hat{y}$, red along $-\hat{y}$. These domains produce a magnetic quadrupole trap with zero along the z-axis, shown in the $z = 0$ plane (d).

pins along $\hat{x}$. This pin translation disrupts the idealized 2D magnetic quadrupole by adding a small trapping field $\vec{B} \propto B'z\hat{z}$, which significantly alters the topology of the $\vec{E} \perp \vec{B}$ surface and the overall loss rate in the trap. We also compute loss rates for all values of pin translation and B_{coil} by numerically integrating the loss flux through these unusual loss surfaces via the Landau-Zener formula, just as for the simpler quadrupole geometry discussed previously. The calculated populations after 30 ms in the trap have a reasonable agreement with the measurements (Fig. 6.19b). The direct integral calculation uses only the temperature of a purely thermal distribution as a free parameter,
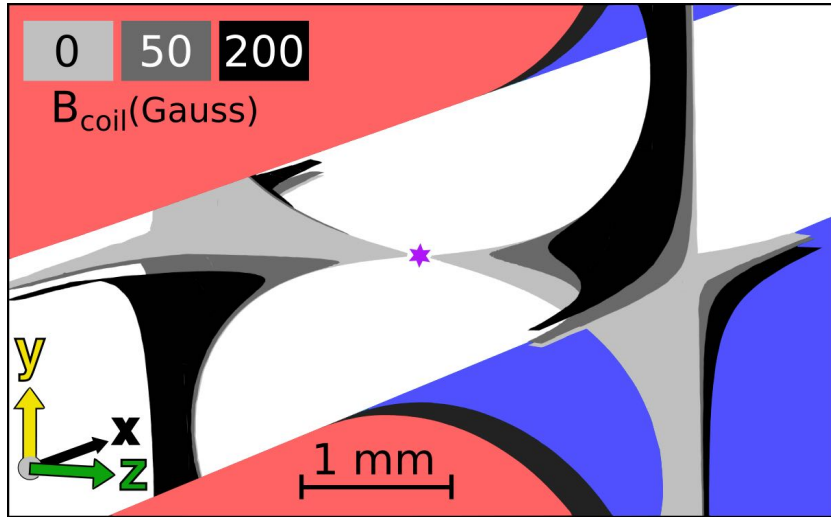
Figure 6.18: Surfaces where spin-flips can occur are shown for three values of B_{coil} in light gray, dark gray, and black. The magnetic pins are shown as in Fig. 6.17 for context. The purple star marks the trap center, to which molecules are confined within a ~ 1 mm diameter.

and does not involve computation of any trajectories. The temperature fits to 170 ± 20 mK [c] . An intuitive explanation for the intriguing double well structure in Fig. 6.16 is that B_{coil} first translates the magnetic zero along the z-axis, overlapping it with larger electric fields at first before moving it out of the trap.

With strong experimental confirmation of the molecular spin-flip loss enhancement, we can move on to generalize beyond OH. Hund's case (a) states are most susceptible in the sense that smaller electric fields are sufficient to cause a significant problem, but with enough electric field any state exhibiting competition between electric and magnetic fields for alignment of the molecule or atom will be susceptible. One way to avoid competition is for the fields to couple to unrelated parts of the Hamiltonian, which happens to a limited extent for Hund's case (b) states without electron orbital angular momentum (Σ states, $\Lambda = 0$) [138]. In these states, which include most laser-cooled molecules thus far, the electric and magnetic fields couple to rotation and spin respectively, which are only related by the spin-rotation coupling constant. This constant is usually in the tens of MHz [132], so molecular spin-flip loss remains quite significant. The inclusion of hyperfine requires

---

[c] Calculation performed in COMSOL: Source Code
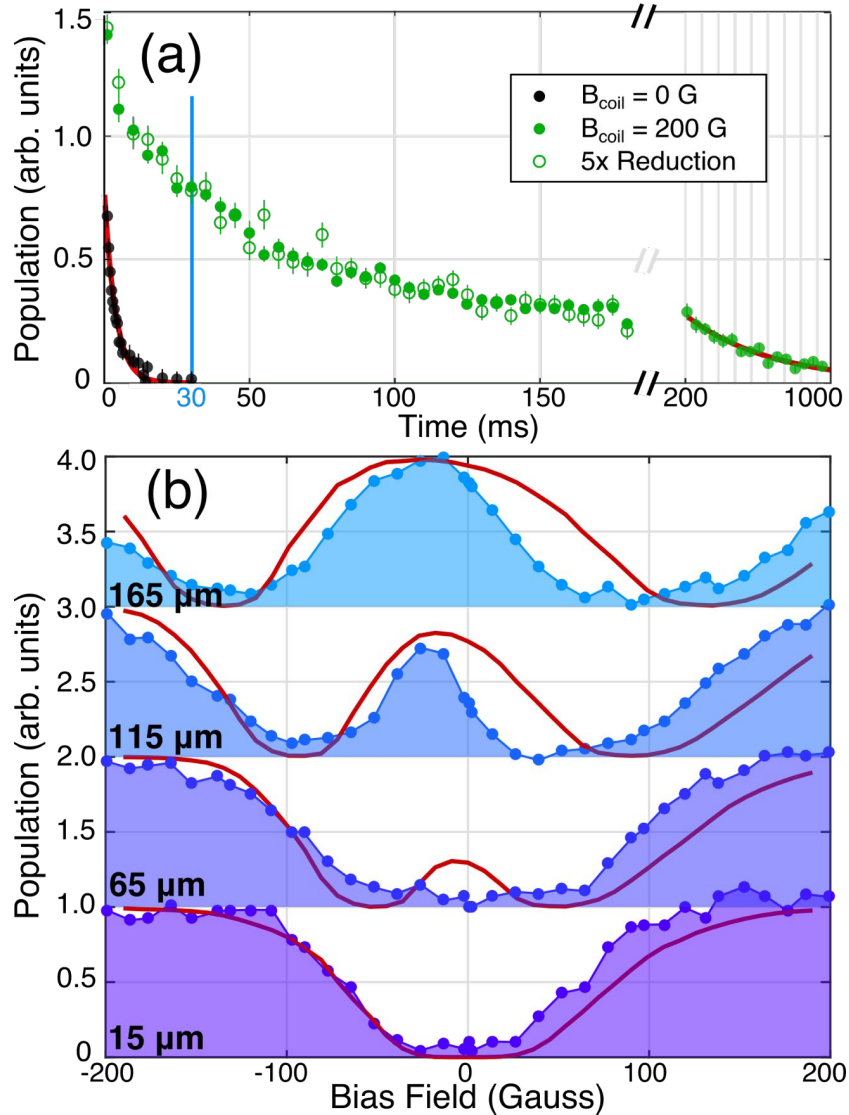
Figure 6.19: Time traces (a) without bias field (black), with bias field (green dots), and with modulated density (green circles). One body fits (red) give loss rates of 200 s^{-1} without bias field and 2 s^{-1} with full bias field at long times, in agreement with our background gas pressure. At the fixed time 30 ms, population is shown as a function of both pin translation and bias field (b), for several values of pin translation, labeled relative to perfect alignment. Fits (red) are calculated by integrating the molecule flux of a thermal ensemble through surfaces where $\vec{E} \perp \vec{B}$.

a careful case-by-case investigation. For OH, it would initially seem to add an extra splitting that could protect from spin-flips, but in fact the loss plane is only shifted slightly away from $\vec{E} \perp \vec{B}$ and retains the same area. For Yttrium Monoxide [26], certain hyperfine states can avoid

spin-flip loss entirely when electric fields are applied. These states are characterized by significant electron-spin-to-nuclear-spin dipolar coupling, which results in a protective gap regardless of field orientation.

It is also instructive to consider the related case of a pure electrostatic trap. Here there is always some zero field parity splitting that prevents the orientation-reversing spin flips we have been discussing. However, this same splitting pushes all states with the same sign of m, the field alignment quantum number, very close to one another, leading to loss via Landau-Zener transitions other than the m to $-m$ spin-flip [116]. Intriguingly, the addition of a homogeneous magnetic field can actually suppress this loss [115].

The present trap, in addition to providing the desired experimental testing ground for molecular spin-flip loss, produces large $5\,\mathrm{T/cm}$ trap gradients useful for maintaining high densities to facilitate collisional studies. This is in contrast with other strategies for plugging the hole of a magnetic trap which often lead to a reduction in trap gradient. With loss removed, we observe a population trend whose initially fast decay rate decreases over time (Fig. 6.19a, green dots), suggesting a two-body collisional effect. We test this by reducing the initial population fivefold but without changing its spatial or velocity distribution, and then scale the resulting trend by five (green circles). This technique is described further in Chapter 7. If collisions had contributed, this new trend would show less decay, but we observe no significant change. This seeming lack of collisions is likely due to the much higher initial temperature of $170\,\mathrm{mK}$, in contrast to the earlier work at and below $50\,\mathrm{mK}$ [44]. An alternative hypothesis for the population trend is the existence of chaotic trap orbits with long escape times [141]. The understanding of electric field enhanced spin-flip loss brings an important consequence to the use of RF knife under electric field employed in the forced evaporation, especially at low temperatures. We present the effect of evaporation at intermediate temperatures (~ 30 mK) in Chapter 7. Moving forward, we aim to increase the density by means of several improvements [54, 65].

6.4.4 Scaling Law Derivation

Here we derive the loss enhancement scaling law presented in Eqn. 6.9, and repeated here:

$$\eta = \frac{3}{11}\left(\frac{d_{\mathrm{eff}}E}{\sqrt{\kappa\Delta}}\right)^{8/3}. \tag{6.11}$$

The key idea is to compare the surface areas of the loss regions with and without electric field. There is no exact loss region where a molecule is guaranteed to spin flip, but rather its velocity and direction contribute to the Landau-Zener probability (Eqn. 6.8). Nonetheless, for the purposes of a scaling law, we can assume the average thermal velocity v_T, and choose a probability threshold of $P > 1/e$. These assumptions allow us to define the loss region as the contour surface of energy κ where

$$\kappa = \sqrt{2\hbar\dot{G}/\pi} = \sqrt{4\hbar v_T B'/\pi}. \tag{6.12}$$

Here $\dot{G}$ is the rate of change in the energy gap between the trapped state and its spin flip partner, and B' is the magnetic field gradient along the strong axis of the trap.

We assume that the electric field is applied parallel to the strong axis of the quadrupole trap, which makes the loss plane, as defined by $\vec{E} \perp \vec{B}$, perpendicular to this axis. This matches the geometry that has been realized in our experiment [121], and is the worst case, but by no more than a constant factor of $2\sqrt{2}$ relative to other directions the electric field could have.

Before application of electric field, the κ valued energy contour is the surface of an oblate ellipsoid of long radius $r_0 = 2\kappa/\mu_{\mathrm{eff}}B'$. Its area is then $2\pi\alpha\,r_0^2$, where $\alpha(e) = 1 + (1/e - e)\tanh^{-1}(e)$ generally for eccentricity e, and $\alpha \sim 1.38$ for the present 2:1 ellipsoid. When electric field is applied, the energy gap near the trap zero takes an unusual functional form. To derive it, we first assign spatial coordinates r and z denoting directions within and normal to the loss plane, respectively. Next we diagonalize the ground state hamiltonian of OH in mixed fields, see App. A of Ref. [114], or similarly for another species. Subtracting the energies of the trapped state and its spin-flip partner, and then series expanding the result yields:

$$G = 2\mu_{\mathrm{eff}}B'|z| + \beta\frac{(\mu_{\mathrm{eff}}B'r/2)^3\Delta^2}{(d_{\mathrm{eff}}E)^4}f(d_{\mathrm{eff}}E/\Delta), \tag{6.13}$$

plus higher order terms in r and z. Here $\beta = 625/144 = 4.3$ and f is a rational expression that approaches 1 for small arguments: $f(x) = (1 + 1.28x^2)/\sqrt{1 + 1.44x^2}$. The key feature, as discussed in Sec. 6.4.2, is the cubic dependence G exhibits on r which leads to much more severely oblate contours.

Now we can use Eqn. 6.13 to compute the surface area of the $G = \kappa$ contour. We specialize to the regime where $d_{\text{eff}}E < \Delta$, so that $f(d_{\text{eff}}E/\Delta) \sim 1$. The radial extent of the surface can be solved by inverting $\kappa = G|_{z=0}$:

$$r_E = \frac{1}{\mu_{\text{eff}}B'} \sqrt[3]{\frac{8\kappa(d_{\text{eff}}E)^4}{\beta\Delta^2}}. \tag{6.14}$$

The axial extent remains $z = \kappa/\mu_{\text{eff}}B'$ for all $\vec{E}$. For large enough E, r_E dominates over this axial extent, so that the area is effectively $2\pi r_E^2$ and the loss area enhancement becomes $\eta = r_E^2/(\alpha r_0^2)$. Putting everything together:

$$\begin{aligned} \eta &= \frac{1}{\alpha}\left(\frac{1}{\mu_{\text{eff}}B'}\sqrt[3]{\frac{8\kappa(d_{\text{eff}}E)^4}{\beta\Delta^2}}\right)^2 \Big/ \left(\frac{2\kappa}{\mu_{\text{eff}}B'}\right)^2 \\ &= \frac{1}{\alpha\beta^{2/3}}\left(\frac{1}{2\kappa}\sqrt[3]{\frac{8\kappa(d_{\text{eff}}E)^4}{\Delta^2}}\right)^2 \\ &= \frac{3}{11}\left(\frac{d_{\text{eff}}E}{\sqrt{\kappa\Delta}}\right)^{8/3}. \end{aligned} \tag{6.15}$$

Now we address the domain of validity of this result. When E is small, Eqn. 6.13 only has a narrow range of validity, since the electric field only dominates in a very small region near the trap center. Outside, G retains a nearly linear dependence on r. This means that Eqn. 6.14 only holds for E above some threshold. For smaller E, r_E will simply not be significantly perturbed from its zero electric field value of $r_0 = 2\kappa/\mu_{\text{eff}}B'$. The implication for the enhancement factor in Eqn. 6.15 is simply that it is only valid when it predicts an enhancement significantly greater than unity. In other words, Eqn. 6.15 holds when $d_{\text{eff}}E > 1.6\cdot\sqrt{\kappa\Delta}$, but below this η gradually returns to unity. Eventually when $d_{\text{eff}}E > \Delta$, the factor of $f(d_{\text{eff}}E/\Delta)$ in Eqn. 6.13 is better approximated by $1.1\cdot d_{\text{eff}}E/\Delta$, which leads to the modification $\eta = 0.26\cdot(d_{\text{eff}}E)^2/\kappa^{4/3}\Delta^{2/3}$. Thus for these larger E-fields, the enhancement factor reduces in its dependence on electric field from order $8/3$ to order 2. At this point, the loss is typically too large for trapping, see Tab. 6.4.

6.4.5   Conclusions

Molecule enhanced spin-flip loss arises in mixed electric and magnetic fields due to a competition between field quantization axes. We conclusively demonstrate and suppress this effect using our dual magnetic and electric quadrupole trap, which is also an ideal setting for further progress in collisional physics thanks to its large trap gradient. Our calculation of the magnitude of spin-flip loss via flux through surfaces where $\vec{E} \perp \vec{B}$ enables detailed predictions of how its location and magnitude ought to scale with bias field and trap alignment, which we experimentally verify. Our results correct existing predictions about molecular spin-flips in mixed fields and pave the way toward further improvements in molecule trapping and cooling.

6.5   Trap Escape and Dynamical Phenomenon

Early during my thesis work, it was common to infer significant information pertaining to the collisional behavior of ensembles based on the observed loss rates of molecules from traps. One effect which significantly influences the observed trends is the behavior of molecules in the $|f, \frac{1}{2}\rangle$ and $|e, \frac{3}{2}\rangle$ states after loading. Molecules are loaded into these states from the $|f, -\frac{3}{2}\rangle$ state which is decelerated, as described above in Sec. 6.3. An additional important effect however is the escape of molecules from the expected $|f, \frac{3}{2}\rangle$ state but with surprisingly long lifetimes. A common rule of thumb floating around in the atomic physics community is that molecules or atoms which are not well trapped ought to find their way out of the trap within a quarter trap oscillation. This viewpoint neglects the potential complexities associated with the dynamics of molecular orbits. In the effective moving trap which characterizes deceleration for example, almost all molecules lie above the true trap depth when operating in S = 1 mode, but many survive the ~ 5 oscillations they undergo in the ~ 3 ms they spend in the decelerator, refer back to Chap. 5 for more information.

More generally, the stability of orbits in dynamical systems is an exciting question in classical physics, with applications to the planets of our solar system, chaotic systems, and so on [142]. One intriguing study applies tools of dynamical system analysis to the trapping of atoms in a crossed

optical dipole trap [141]. Not only do they demonstrate chaotic behavior in this comparatively simple trapping geometry, but as a corollary they find single particle trajectories with very long escape times over 10^4 times the oscillation period [141, Fig. 11]. I studied the escape dynamics from the Ring, Tricycle, and Pin traps, generating the trajectory information shown in Fig. 6.20. Energies of molecules are given in units of GHz, and there are 2.0 GHz/kG for OH molecules. It is remarkable that molecules survive at these energies, which are therefore far above the minimum trap depth of ~ 5 GHz in the Tricycle, similar in the Ring, and ~ 8 GHz in the Pin trap.

I therefore followed this up by studying chaos indicators for trajectories in the magnetic pin trap. This can be done by studying the evolution of orbits with infinitesimally varying initial conditions, in which case a new higher order equation of motion may be found which describes the evolution of the variation itself. Specifically, if the evolution of the system is described by:

$$\frac{\partial x}{\partial t} = F(x, t), \tag{6.16}$$

where x is a point in 6D phase space and F describes the "flow" of the system, then it is possible to specify a modification to the initial position δx and study:
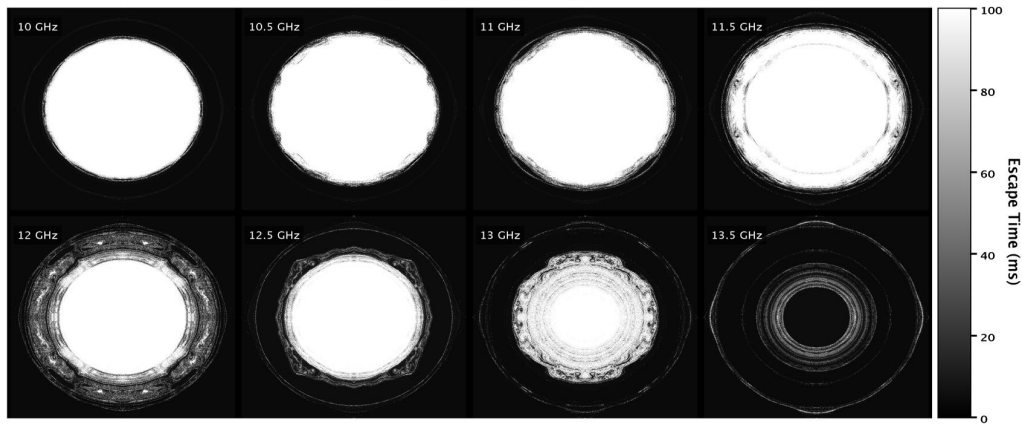
$$\frac{\partial x + \delta x}{\partial t} - \frac{\partial x}{\partial t} = F(x + \delta x, t) - F(x, t), \tag{6.17}$$

which after making various leading order subtractions and so on gives rise to:

$$\frac{\partial \delta x}{\partial t} = \frac{\partial f}{\partial x} \cdot \delta x. \tag{6.18}$$
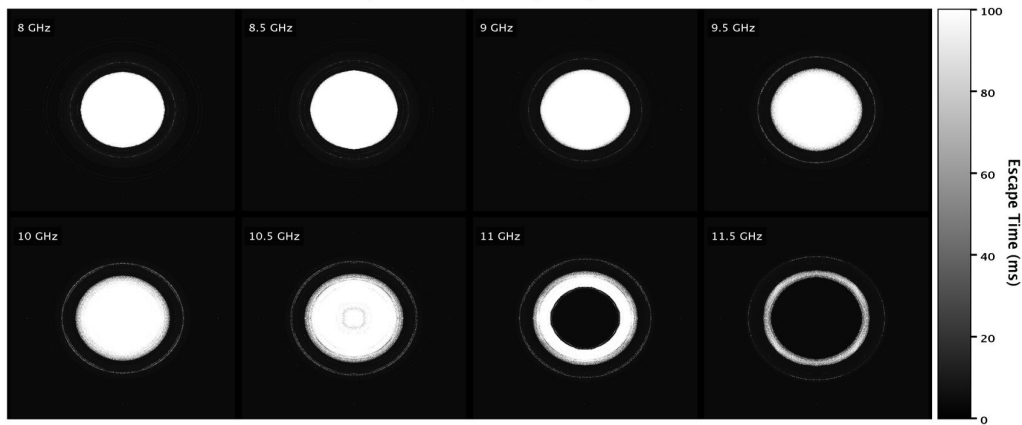
Various chaos indicators based on variational equations such as that in Eq. 6.18 may be studied, such as the perhaps more well-known Maximum Lyapunov Exponent [143]. Using a higher order variation called the OFLI$_2^{TT}$ [144], I determined the pin trap to be a highly chaotic system, as the panels shown in Fig. 6.22 indicate. A few stable orbits exist, but the majority are not. It is also useful to verify that the software I developed for studying these indicators is in fact properly functioning. In Fig. 6.21 I show how my results compare with those in [141]. The comparison is nearly identical, which is especially remarkable given that I don't make use of the analytic expression for the crossed dipole trap [141, Eq. 6], since none is available for the magnetic pin trap.

Ring Trap Escape Dynamics
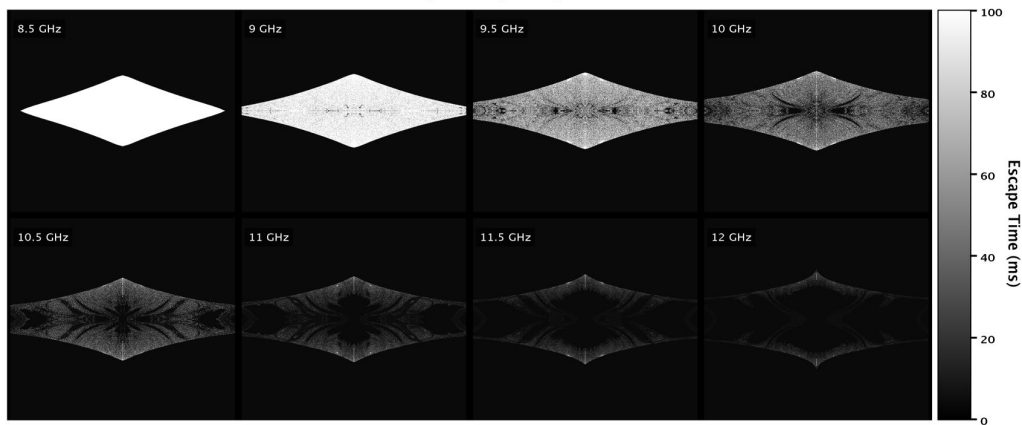
Molecules initialized in XY plane, 4mm x 4mm, with Z–velocity chosen to give total energy shown.

Tricycle Trap Escape Dynamics

Molecules initialized in XY plane, 4mm x 4mm, with Z–velocity chosen to give total energy shown.

Pin Trap Escape Dynamics

Molecules initialized in XY plane, 4mm x 4mm, with Z–velocity chosen to give total energy shown.

Figure 6.20: Molecules with the indicated total energy are initialized and their escape times indicated in grayscale. Position within a panel corresponds to initial position of the molecule in the transverse mid-plane of the trap.
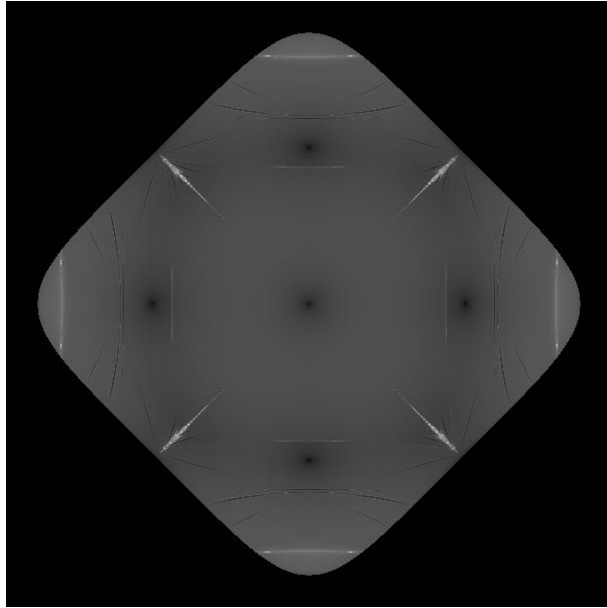
Figure 6.21: The chaos indicator OFLI^2_{TT} nicely reproduced with a spline-based computational tool, compare with [141, Fig. 5b]

Instead I use a spline to represent the potential. This is described further in my publicly available code repository [d] .

6.6   Next Generation Traps

At the time of this writing, an effort is underway to develop a next generation magnetic trap suitable for use with our 333 stage decelerator. Thanks to the development of our engineering and manufacturing capabilities as far as cryogenics are concerned, I decided to push for a cryogenic trap. This has the added benefit of addressing the vacuum and blackbody lifetime limits for OH molecules and potentially enabling ten second study times. A number of features of this design are worth discussing here.

---

[d] Chaos Indicator Codebase
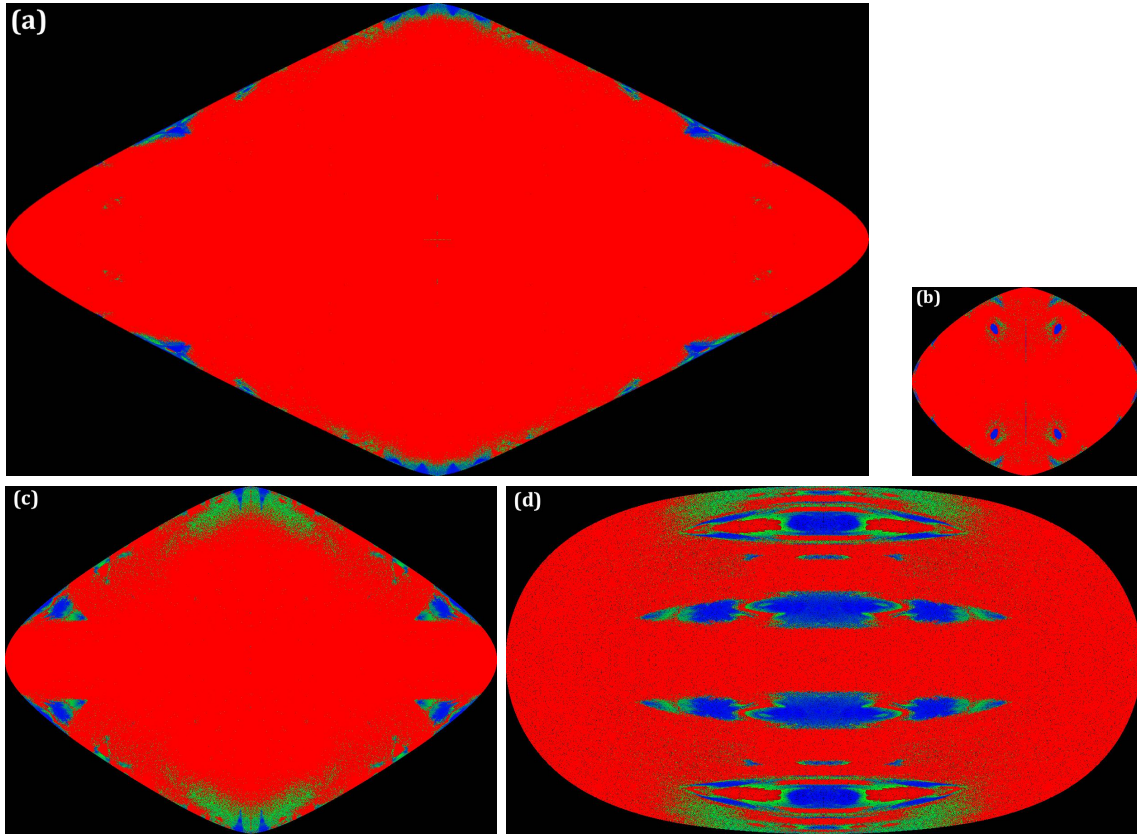
Figure 6.22: Chaos indicator OFLI_{TT}^2 is evaluated for trajectories beginning in the pin trap. Several islands of stability are engulfed within seas of chaos. Chaotic trajectories red, periodic blue, quasi-periodic green. The latter two vary on a color gradient. (a) 1.94 mm wide, all panels to the same scale. Energies in this panel are 7.5 GHz above trap minimum. Trajectories begin in the $x - y$ plane with velocity in the z direction and normal to this plane. (b) 2.5 GHz, $x - y$ plane. (c) 5 GHz, $x - y$ plane. (d) 5 GHz, $y - z$ plane.

6.6.1   Pin Trap Farewell

We decided to move back to the 3D magnetic quadrupole design, despite the success of the magnetic pin trap for addressing spin flip losses. Reasons for this include the following:

(1) Difficulty in correctly selecting and orienting the magnetic pins, which required an in-vacuum translation stage and associated high voltage concerns. We also had to carefully scan the field of the pins to identify a well-matched pair.

(2) Questions about the HV performance of the pins, which didn't condition very well. No

major arcs during normal operation were occurring, but the loaded temperature was triple that predicted by sims, a possible indication of arcing type effects during loading.

(3) Maintaining the Bias coil, which required a high pressure water boosting system [145]

(4) Expectations about collisional behavior. The pin trap resolves spin-flip losses, but substates nonetheless come quite close to one another over a broad spatial range, making inelastic loss probable. At one point Goulven Quéméner actually calculated inelastic cross sections for a map of fields and angles in the pin trap and confirmed this.

(5) Lifetime concerns for the magnetic pins themselves. We had a number of pins demagnetize during conditioning, leading us to install an in-vacuum temperature probe which could be made to touch the pins using a manipulator feedthrough or brought safely away from them during the application of voltage.

6.6.2   Magnets

Neodymium magnets reversibly demagnetize to 70% of their room temperature strength when brought to temperatures in the 10 K regime, but newer Praseodymium magnets actually enhance [146]. I was able to coordinate the manufacture of these for our application[e] .

An effort was undertaken to more systematically study the variation of the performance of the system as far as various dimensions are concerned. For each parameter of interest, the fields were exported to a MATLAB based deceleration, trap-loading, and trapping simulation to study their effectiveness. The results can be seen in Tab. 6.4. A tricycle style was selected, though with a bit of a reduction in gradient. Radiusing the rear electrode was considered, as well as variations in the thickness of extra surfaces designed to cover the imperfect surfaces of the magnets. In all cases, deceleration and loading dynamics were included, with the exception of $|f, -\frac{3}{2}\rangle$ effects. I have only once made an attempt at including these effects, for the sake of more precisely fitting the escape

---

[e] Vacuumschmelze manufactures these and has a US distribution team based in Kentucky. Thanks to Ed Narevicius for the referral. Grade 131 TP and 131 DTP.

Table 6.4: Various design parameters are studied in a loading and trapping simulation in order to make the best selection. Loading is specified as a triplet of voltage labels, which apply to the last pins, the front magnet, and the rear magnet respectively.

Name	Description	N	T
Cryo1	1 mm Front Magnet Thickness, +G- loading, 1 mm hole curvature	3151	30
Cryo2	2 mm Front Magnet Thickness, +-+ loading, 1.25 mm hole curvature	5007	45
Cryo3	Change Rear Magnet to NdFeB, +G- loading	4422	41
Cryo4	+-+ loading, 0.6 mm hole curvature	3961	40
Cryo5	1.5 mm hole curvature, center hole from 2.5 to 2 mm	4430	40
Cryo6	0.6 mm hole curvature, center hole 4 mm	4655	41
Cryo7	Remove Rear Cover	4058	42
Cryo8	Use 28 kV loading fields	4341	43
Cryo9	Rear Cover Protrusion	2739	35
Cryo10	Back to Cryo6, but finer mesh	4720	41
Cryo11	Try +G- again	4145	41
Cryo12	Back to +-+. Rear radii to 7 mm from 10 mm	4612	41
Cryo13	Front magnet OD to 16 mm from 25 mm	4620	41
Cryo14	Rear radii back to 10 mm	4710	42
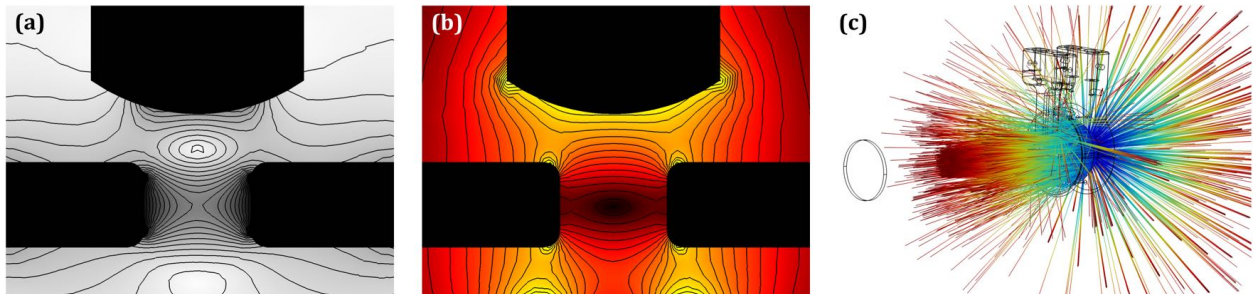
Figure 6.23: Relevant information for the Cryocycle trap under manufacture at the time of this writing. (a) Magnetic field magnitude, 500 G per contour, trap depth of ~ 2200 G transversely. (b) Electric field magnitude during loading. 10 kV/cm per contour. Curved rear surface acts to extend the region of steep trapping slope further towards the rear magnet relative to the Tricycle trap, see Fig. 6.6a. (c) Ray-trace performed in COMSOL Multiphysics for determining collection solid angle close to 4 sr for the Cryocycle.

dynamics of molecules in the tricycle trap with extra electric field turn-on events, described further in Sec. 7.3.1. The final selected geometry is shown in Fig. 6.23, and is dubbed the Cryocycle.

6.6.3   Photon Collection

The cryocycle also features what will hopefully serve as an important improvement in fluorescence collection. Mounted together with the magnet is an elliptical reflector capable of directing much of the fluorescence from the trapped molecules onto a PMT outside the vacuum. Collection solid angles close to 4 sr should be possible, an order of magnitude improvement over the previous traps, see Fig. 6.23c. Of course this assumes a highly reflective surface, only obtainable in the near ultraviolet with aluminum [147], which is fortunately a good choice for thermal conductivity as well. Aluminum may be a less ideal choice as far as high voltage is concerned however, since its surface oxide layer should enable the formation of patch charges and stray electric fields to some extent. This could prove especially problematic in the event of any sensitive long-term studies, since variations in the patch charges could lead to variations in the enhancement of spin-flip losses near the trap center. One technique to address this is to detect the magnitude of the stray field by spectroscopy, see Fig. 6.24. Because of the small magnitude of the differential Zeeman shift, slight perturbations of the electric fields on the magnetic field dependent line-shapes, especially in the vicinity of avoided crossings, are clearly discernible. Performing a full spectroscopic sequence would be slow, but similar observables could be designed to give sensitivity to stray electric fields, for example a two-point spectroscopy comparing the frequency of the dip to that of the peak. Another possibility would be to look for population transfer at a more distant frequency that would only address molecules close to avoided crossings.

6.6.4   High Voltage Considerations

In addition to the material and patch considerations mentioned above, I concentrated a significant effort towards minimizing the exposure of the magnet surfaces to high electric fields. I was motivated in this pursuit by observations of adverse effects of the magnet surfaces on decelerator electrodes, see Fig. 6.25. After the first data collection period with the tricycle trap in 2014, a vacuum break revealed significant arcing induced surface degradations. Pin pairs close to the end of
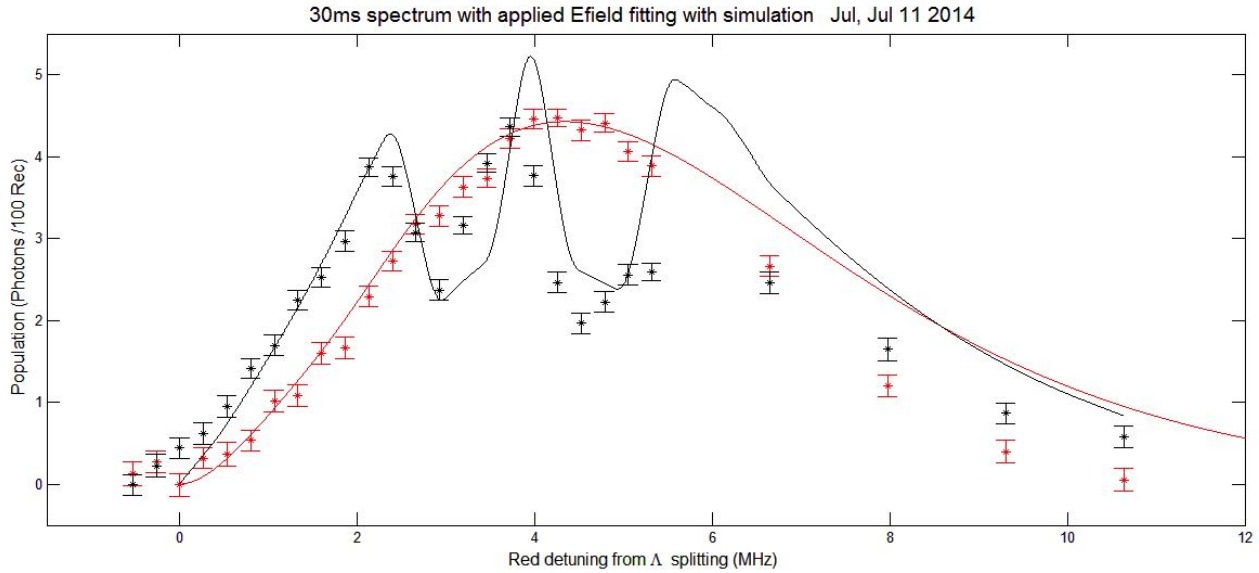
Figure 6.24: Stray fields are seen to influence spectroscopy. The black simulated line corresponds to 10 V/cm. The two dips correspond to the inability of microwaves to address molecules at those frequencies due to avoided crossings perturbing the lines at those locations. Only one crossing is significantly perturbed by small fields, that between $|e, \frac{3}{2}\rangle$ and $|f, \frac{1}{2}\rangle$, but this crossing occurs in two different locations for the two nuclear spin substates of $|f, \frac{3}{2}\rangle$.

the decelerator where the trap was located showed degraded surface lines or tracks, with a ring-like structure reminiscent of the cylindrically symmetric tricycle trap mounted in close proximity. This suggests that applying high voltage to the somewhat rough surfaces of the neodymium magnets could have been causing arcs. It is also possible that merely the presence of the magnetic field exacerbates or facilitates arcing somehow. Although we never had direct evidence that the formation of these tracks corresponded to a decline in performance of the system, at the time this observation contributed to a working hypothesis that the performance of the decelerator had degraded and needed to be addressed. In the new cryogenic system, the magnets are mounted in such a way that they are for the most part ensconced within the mounting structures, which can be better polished than the magnets themselves, which are a brittle ceramic with no available high polish surface preparation.
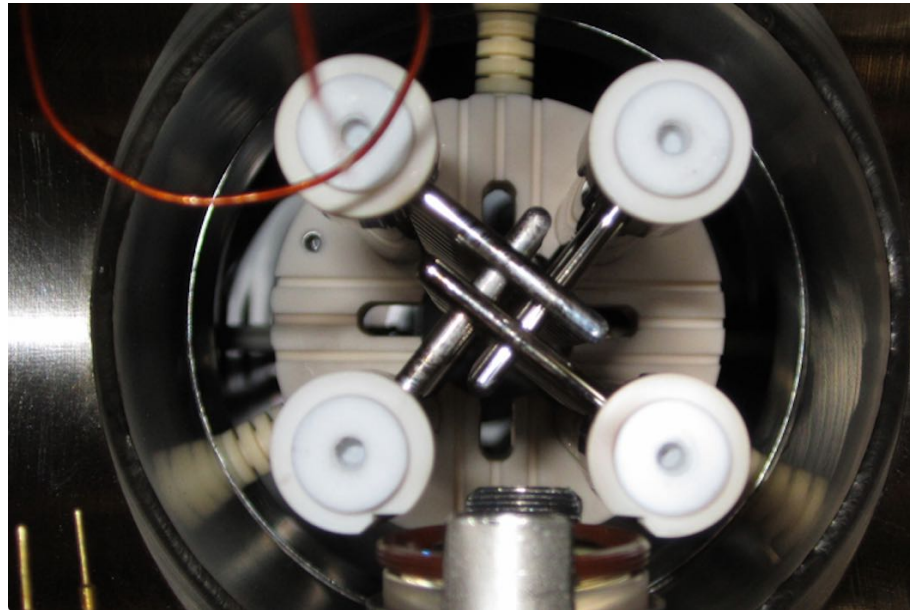
Figure 6.25: Decelerator pins after deinstallation of the Tricycle trap. Not only discoloration, but linear scratch-like patterns or tracks, are evident. These tracks appear to form concentric rings about the decelerator axis, suggesting that tricycle trap magnets were involved.

6.6.5 Blackbody Absorption

In order to benefit from a lifetime extension with cryogenic temperatures, it is necessary to carefully control the radiation environment of the molecules. OH can absorb radiation primarily at 120 μm (2.5 THz) [148], where typical radiation shielding conductors have near perfect reflection. In the case of an incomplete shield, as is required for our setup since the shield cannot approach to close to the high voltage decelerator, this can mean that the radiation relevant for the molecules is actually fully equilibrated to room temperature despite the cryogenic shield. Whatever the dominant absorbers are for the relevant wavelength will dominate the radiation environment, with conductive surfaces playing little to no role. Many materials are surprisingly transparent, including plastics such as Teflon which are actually used as lenses [f] . To address this, I opted for the addition of ceramic plates on the inside of our radiation shield to influence the radiation environment by absorbing THz radiation otherwise reflected by the shields.

---

[f] Teflon Lenses
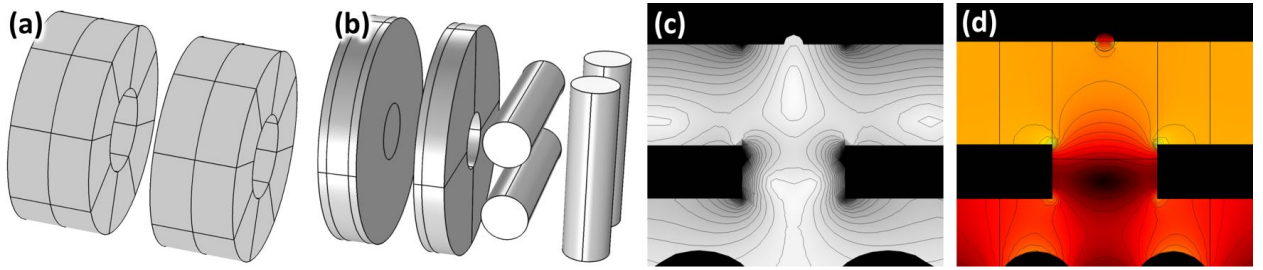
Figure 6.26: (a) Earlier Design from Matt Hummon, 32 one eighth arc segments. (b) Updated design, 8 quarter arc segments, 2 rings, 1 disk. 4 mm gap between magnets. (c) Magnetic Trap. Much longer than wide, unlike 3D quadrupole traps. Up to 1200 G deep or so, depending on tuning of extra disk magnet. (d) Loading fields, much less ideal than Tricycle trap, concave up across trap center and steepest out front.

6.6.6 Cloverleaf Trapping

Of course it would be ideal to address the issue of electric field enhanced loss once and for all with a lifted magnetic trap. This is possible with permanent magnets, and a streamlined design was identified and simulated, see Fig. 6.26. Such a trap may one day be the right choice, but it would seem unwise to tackle this simultaneously with the changes already being introduced. Moreover, without collisional effects, it may not be worth the effort. These effects should be more clearly evidenced in the Cryocycle, which should feature at least an order of magnitude improvement over any cloverleaf style design in the densities which may be loaded. The reason for this is that cloverleaf type geometries always require a delicate competition between the strengths of different fields, and can never be generated with the same trap depths or gradients as the quadrupole trap. The design shown in Fig. 6.26 loads only 20% of the Cryocycle, and is significantly less tight, likely at least twofold reduction in each direction, for a forty-fold reduction in density relative to the Cryocycle.

If at some point it becomes necessary to pursue the Cloverleaf trap in earnest, a few points are worth mentioning. Firstly, always make sure to investigate cross sections through the trap in many planes, since often the three principal orthogonal planes can miss the actual weak points of the trap. It should be sufficient to add in planes with $\theta = \pi/4$ and including the z axis, working

in cylindrical coordinates, for the Cloverleaf shown in Fig. 6.26b, but for that in Fig. 6.26a, I believe the weak points may occur in the $\theta = \pi/8$ planes. Secondly, for any given geometry it is always worth varying the magnitude of an extra bias magnetic field in the z direction before making conclusions. This extra field can have a very significant effect on the tightness and depth of the trap, and in practice may even be tuned in the experiment with an external coil or a translatable permanent magnet. I had some success with removing a small divot from the rear electrode so as to reduce loss of molecules which can access that volume. It helps the loading significantly to add conductor between the magnets and touching the front magnets closest to the decelerator, so as to push the loading hill further back and overlap the trap center better. One problem with this is that then the collection solid angle is negatively impacted. Mounting the magnets in aluminum frames that are highly polished to better allow fluorescence to escape could help with this, as planned in the Cryocycle. Finally, it will be important to study this trap outside of the the vacuum somehow, especially in order to see how closely the magnets can be packed/glued together, what the resulting field strengths are, and especially to make sure that the trap is truly plugged. This will require a highly miniaturized magnetic field probe of some kind.

6.7   Trapping of Water Isotopologues

One potentially exciting capability of our new lengthier decelerator system and advanced field distributions would be to apply it to a less Stark responsive molecule such as water [108, Sec. 2.4]. The precise feasibility depends on just how slow the beam is when produced in Xenon in an Even-Lavie valve, which may be worth investigating in the near term. With earlier generations of the experiment [69, Fig. 4], a wide range of initial speeds ($323 - 465$ m/s) were possible in a Xenon expansion depending on the discharge timing. Although a discharge would not be used, this indicates that at least with that valve a wide range of longitudinal Xenon speeds were present after supersonic expansion. This is symptomatic of an inefficient supersonic expansion process, but good news in the sense that water molecules at the low velocity wings of the expansion will have a much greater decelerability. Some very relevant guiding work should prove a useful starting ground [149].

An electrostatic quadrupole trap would be most feasible, and this could be achieved in a very similar system to the one currently planned for the Cryocycle, but with magnet-less electrodes. It is best to have at least the rear electrode bend inwards towards the others, as in this electrostatic trap [150]. The final pins of the decelerator can form one electrode of the quadrupole, which would then require an additional ring and end-cap electrode. Detection could be performed with some sort of REMPI scheme, but for initial tests of decelerability the RGA may suffice.

Chapter 7

Detecting Collisions

Collisions are an exciting area of study for low temperature molecular systems. Quantization of intermolecular degrees of freedom leads to a host of interesting dynamics, which until relatively recently could only be discerned via their contribution to measured integrated cross sections including averaging over many initial states and many partial waves of the interaction potential. However, with the ability to isolate single quantum states thanks to selective manipulation techniques, and with the reduction of collision energies afforded by deceleration, new state-resolved effects [151], and new resolution on quantum mechanical interference type effects are now achievable [128, 129]. It is even possible to study effects directly pertaining to the orientation or stereodynamics of molecular interactions [152]. Simultaneously, studies of collisions in traps have evolved from total cross section measurements [87, 124], to lower temperature determinations directly relevant to inelastic-elastic ratios [125, 130, 153].

This last result [153] from the Narevicius group is particularly exciting, as it compares quite directly with our own work, including cryogenic skimming techniques, decelerator optimization, and cryogenic trapping optimization, and is worth further discussion here. Realizing a similar observation would be an exciting outcome of the research in this thesis, though at the time of this writing it remains unclear whether the optimizations we have pursued will achieve densities comparable to [153]. In their Zeeman deceleration of oxygen, benefit is taken from oxygen's much more direct sourcing, and from the better integration of skimmer cooling with Zeeman deceleration thanks to

the possibility of affixing a long cryogenic Sapphire tube within the bore of the decelerator.[a]   In contrast, for OH our discharging yield from water may be only $1-10\%$, and skimmer cooling has only led to two-fold gains with the hexapole 4.5.

Another alternative strategy for phase space compression of molecules applicable to a wide array of species is found in the combination of centrifugal deceleration and optoelectric cooling [126]. The deceleration technique has also directly enabled collisional studies on its own [130], of CH_3F and ND_3. The optoelectric sisyphus technique requires low spatial density flat-bottomed trap geometries, but the velocity space compression is quite impressive, $420^\circ\,\mu K$ is reached. Laser-based techniques are also beginning to enable similar molecular collisional studies, notably the recently observed sympathetic cooling of NaLi molecules by sodium [154], the first successful sympathetic cooling of a molecule by an atom. Work on laser-cooled molecules has also recently progressed to the collisional stage, with the Doyle group reporting on collisions between pairs of CaF molecules loaded into optical tweezers [28].

A key challenge that has emerged during the course of my thesis work has been the verification of collisional behavior of all kinds. For this purpose, several very general techniques exist, which are now described in detail.

7.1   Controlled Density Reductions

Collisional effects always influence a population in proportion to the likelihood of such collisions, which in turn scale with the square of the number density of the population. It therefore follows that as one were to scale an experimental control parameter tuning the number density of the population, collisional effects would grow quadratically in that parameter, while single-particle effects would grow linearly. The challenge lies in whether it is really possible to achieve a tuning of this parameter which does not inadvertently lead to an unwanted change of a different nature. Several different strategies have been pursued in this regard. The molecule source is perhaps the

---

[a] In private communication with Yair Segev, we discussed the application of skimmer cooling to deceleration, and the use of such tubes in the Narevicius group.

most logically natural place to begin, but in practice all ways of tuning the initial molecule density risk disturbing the experiment in unwanted ways. For example, tuning the current of the discharge filament can easily reduce the measured number of molecules, and is simple to control and manipulate, but its most likely method of action is to make the discharging process more sporadic, in which case the measured reduction may actually be dominated by cases where no molecules are generated at all. In this scenario, densities remain as always, but some fraction of the time the discharge fails to ignite and no molecules are produced at all. This situation may masquerade as a density tuning, but in fact does not at all investigate the physics of interest.

Other source parameters include the stagnation pressure in the pulsed valve; parameters influencing the flux of the opening event such as coil current, coil voltage, pulse duration; or valve temperature. In all of these cases, there is the risk that changes in the number of molecules generated can change the efficiency of the supersonic expansion process, thereby changing the molecule distribution function across the population, and not only its number density. If we were verifiably operating in a regime where the valve dramatically overfills the decelerator's phase space acceptance, these effects could more plausibly be neglected, but this assertion is not justified, especially when seeking small effects and when using the relatively narrow initial distribution of the Even-Lavie valve. To be more concrete, let us parametrize the most likely way that phase space distributions resulting from different source parameter changes may vary from one another. Assuming that in all cases we at least maximize the signal loaded into the decelerator as far as it depends on timing parameters, we can approximate the phase space distribution downstream in the decelerator where many rotations have cleaned out variations in the angular coordinate as follows:

$$\delta(r) = e^{-\frac{r^2}{2\sigma_r^2}}, \tag{7.1}$$

where r is defined for a planar space-velocity slice of phase space as:

$$r^2 = (z - z_0)^2 + (v_z - v_0)^2/\omega^2, \tag{7.2}$$

z_0 and v_0 are the center coordinates of the phase space distribution, and σ_r parametrizes the width of the distribution.

Variations in this σ_r can eventually contribute to subtle influences in the observed lifetime of the gas, since σ_r in turn influences the extent to which the outer reaches of the trap are populated after loading. Source variations which change the initial temperature of the supersonic expansion are likely to increase the value of σ_r, leading to greater population in the wings, and faster decay rates early on during loading, a classic indicator of collisional effects, which also lead to faster decays early on which later turn off as the population reduces. The distribution proposed in Eq. 7.1 is in fact a more benign representation of what is possible. Loading a narrow distribution off of center can easily lead the radially averaged phase space distribution to actually peak away from center for example.

Another possibility for achieving density variations without changing the distribution $\delta(r)$ of molecules delivered eventually to the trap is to perturb some aspect of the deceleration process, but leave the source untouched. Any phase space manipulation based technique, such as operating in different deceleration modes or introducing gaps in the coverage of the traveling potential, would have the same possibility of disturbing the distribution ultimately loaded into the trap as just described for the case of source variations. However, in the decelerator, the population is already state selected, opening up the different possibility of directly reducing the density by spectroscopic means. Were a second LIF laser available and a region of good optical access before the trapping region, this would serve as a reliable means to achieve a 50% density reduction for example, although at the expense of writing intensity noise and other shot-to-shot variation issues of the pulsed dye laser onto the number density of the ensemble. Microwave transfer is a more compelling possibility, especially since it affords the possibility of directly transferring molecules to an un-trapped state. Applying them during deceleration presents a bit of a challenge however, especially given the usual engineering constraints imposed by the high voltage system. In the past, we've addressed this using the biased tee strategy described further in [114], but hoping for a simpler workaround, we attempted a microwave near-field probe coupler as shown in Fig. 7.1.

In the microwave engineering literature [155, Sec. 4.7], a probe is a near-field device used either for driving a waveguide or measuring its local field behavior. The chamber in which our

Figure 7.1: A microwave free space coupling probe used for addressing OH molecules even in the midst of the Stark decelerator. The brass structure is in good mechanical and electrical contact with the center pin of a coaxial vacuum feedthrough mounted in a 2.75" conflat vacuum connector. This is achieved with the 0-80 setscrew just visible towards the base of the brass structure. The thin region of the Brass structure has a 1/4" diameter, and the thick region is closer to 3/4" diameter.

decelerator sits has a 20 cm diameter, comparable to the microwave frequencies relevant for driving $|f, \frac{3}{2}\rangle$ to $|e, \frac{3}{2}\rangle$ transitions, where in zero field 1.7 GHZ corresponds to 18 cm wavelengths, so it is reasonable to expect that a simple current probe might successfully drive microwave modes of the vacuum chamber. This indeed turns out to be the case, and we successfully used this probe, not only for microwave removal of population during deceleration, as shown in Fig. 7.2, but also to perform the same in-trap spectroscopy described in the previous chapter.
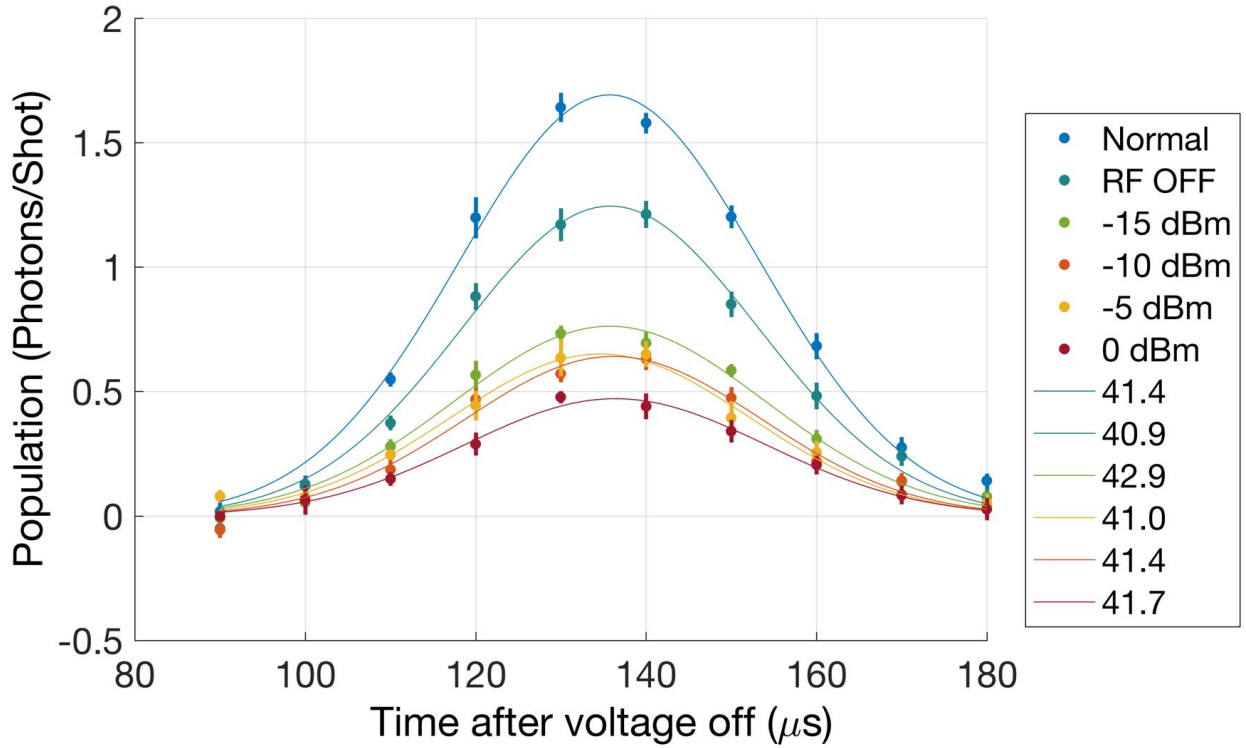
Figure 7.2: Microwaves are successfully coupled into our vacuum chamber using the probe shown in Fig. 7.1, as evidenced by the response of hydroxyl radicals to increasing powers shown here. These molecules were slowed to 43 m/s and then allowed to fly through the detection region with no trap loading. These data were collected on June 14th, 2016. Microwave powers are as measured at the vacuum feedthrough. At a later point, we were able to apply even higher RF powers by instead applying them in a pulsed manner so as to remain within the capabilities of our microwave equipment. Fitted FWHM values in μs are reported in the legend and found not to vary with power.

7.2   Fitting Trap Decay Curves

Another competing technique for observing the influence of collisions relates to the functional form of the decay that is exhibited from a trapping geometry as a function of time. If we make the naïve assumption that collisions lead to loss uniformly over a population regardless of other parameters, this can be described by the following differential equation:

$$\frac{dN}{dt} = -\beta N^2 - \alpha N, \tag{7.3}$$

where the magnitude of the two-body process is parametrized by β, and single-particle effects such as collisions with background gas molecules are included in the model and parametrized by α. This can in turn be solved by the factorization method for rational polynomial functions:

$$\int \frac{dN}{N(\alpha + \beta N)} = -t + C, \tag{7.4}$$

$$\int \frac{1}{\alpha} \left(\frac{1}{N} - \frac{\beta}{\alpha + \beta N} \right) dN = -t + C \tag{7.5}$$

$$\log N - \log(\alpha + \beta N) = -\alpha t + C' \tag{7.6}$$

$$\frac{N}{\alpha + \beta N} = C'' e^{-\alpha t} \tag{7.7}$$

$$\frac{1}{\alpha/N + \beta} = C'' e^{-\alpha t} \tag{7.8}$$

$$\alpha/N + \beta = C''' e^{\alpha t} \tag{7.9}$$

$$N(t) = \frac{\alpha}{C''' e^{\alpha t} - \beta} \tag{7.10}$$

Now by requiring that $N(0) = N_0$, we have:

$$N_0 = \frac{\alpha}{C''' - \beta} \tag{7.11}$$

$$C''' = \frac{\alpha}{N_0} + \beta. \tag{7.12}$$

Substituting and moving around:

$$N(t) = \frac{\alpha}{(\frac{\alpha}{N_0} + \beta) e^{\alpha t} - \beta} \tag{7.13}$$

$$= \frac{N_0 e^{-\alpha t}}{1 + \beta N_0 (1 - e^{-\alpha t})/\alpha} \tag{7.14}$$

This equation is rather ugly, but it can be seen to reduce to the more well known formulas describing the decay of a population subject to either single or double particle effects but not both. To see this, we simply take the corresponding α or β parameters in Eq. 7.14 to zero:

$$\lim_{\beta \to 0} \left(\frac{N_0 e^{-\alpha t}}{1 + \beta N_0 (1 - e^{-\alpha t})/\alpha} \right) = N_0 e^{-\alpha t} \tag{7.15}$$

$$\lim_{\alpha \to 0} \left(\frac{N_0 e^{-\alpha t}}{1 + \beta N_0 (1 - e^{-\alpha t})/\alpha} \right) = \frac{N_0}{1 + \beta N_0 (t e^{-\alpha t}|_{\alpha=0})} = \frac{N_0}{1 + \beta N_0 t} \tag{7.16}$$

where the penultimate step for the two-body formula is achieved via L'Hôpital's rule.

With these functional forms in hand, it is now possible to use the fitting of measured trap decays as an observable giving indication of the presence of collisional effects. Historically, this procedure was used in our experiment in both the Ring and Tricycle traps, but never in the Pin trap due to thanks to the development of our capability of performing controlled density reductions. When using decay fits, it is essential that these observations are made in the absence of any time varying single-particle loss processes, such as the potentially slow escape dynamics of some classes of molecules from the trap geometry. In the Ring trap for example, we have experimental indications that molecules do not explore the toroidal region of the trap, although they have access to it. This confirms that the ensemble loaded in this trap is in a potentially dangerous regime for the application of loss functional forms, since there should certainly be a timescale for molecules to explore the toroid which has not been easily satisfied in the first few milliseconds after trap loading.

I can take this a step further by approximating a trap with slow escape dynamics for some populations as one characterized by two different single-particle decay times:

$$N(t) = A_1 e^{-\alpha_1 t} + A_2 e^{-\alpha_2 t} \tag{7.17}$$

Now consider a trap where half the population decays with a background pressure limited lifetime of 500 ms and the other half escapes the trap on a timescale that is slow relative to a 300 μs oscillation time but faster than the background limit, say 50 ms. These numbers are somewhat representative of historical values in our traps. In the absence of any collisional effects, fitting this bi-exponential decay with Eq. 7.14 is optimal with a zero-valued α, and with $\beta = 9.9 \pm 0.1$/s/mol. Not only does the hypothesis of decay according to Eq. 7.14 give a strong slant in favor of two-body effects, it does so with high fidelity, fitting the data with an $R^2 = 0.99$, see Fig. 7.3. I should mention that in this fitting I fix the initial population to one, which reduces the ability of Eq. 7.14 to fit any arbitrary shape.

Of course one contributing factor to the success of the two-body fit in matching the bi-exponential decay curve is the timescale probed in the experiment. One more effective way for distinguishing true two-body effects could be to use a long-time measurement to fix the one-body
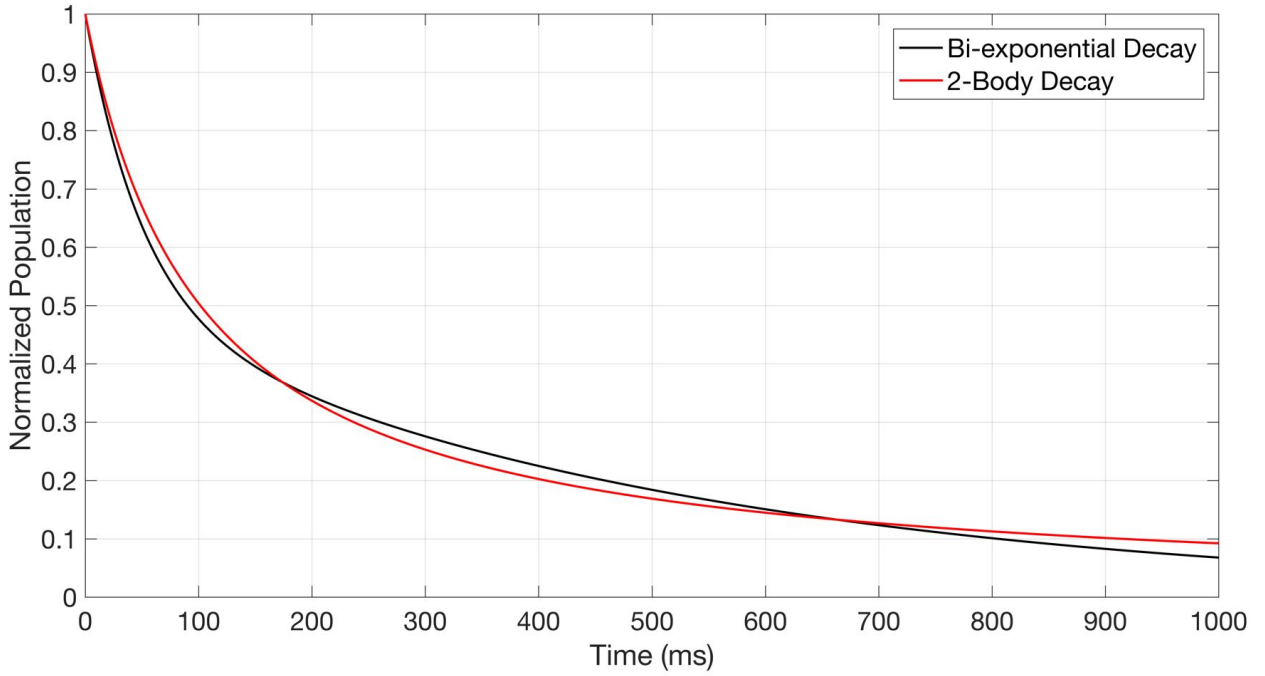
Figure 7.3: A biexponential decay curve is well fit by a two body, demonstrating the importance of either removing single-particle effects or ensuring that they occur on only a single timescale.

decay rate, since at long enough times the two-body effects reduce in relevance while the one-body rates remain fixed. In practice, this approach can lead to more trouble, since at about 3 s [148], an additional one-body process kicks in, but as long as one-body effects are well-known, pushing to long timescales can improve the reliability of the decay-fitting method for detecting collisions.

7.2.1 Electric Field Induced Losses

One area where the fitting of decay curves played a very large role was in the study of what was thought to be electric field induced inelastic loss. In the experiment [121], it was found that application of electric field led to loss from the trap. It was further found that initiating the loss after different hold times in the trap was a way of varying the initial density so as to probe the two-body process in different parameter regimes. Some example fits from [121] are shown in Fig. 7.4a. At the time, it was known that a single particle loss due to electric field existed, discussed in the appendix of [121]. Its magnitude was approximated, and fixed in Eq. 7.14 when fitting decay curves. It was
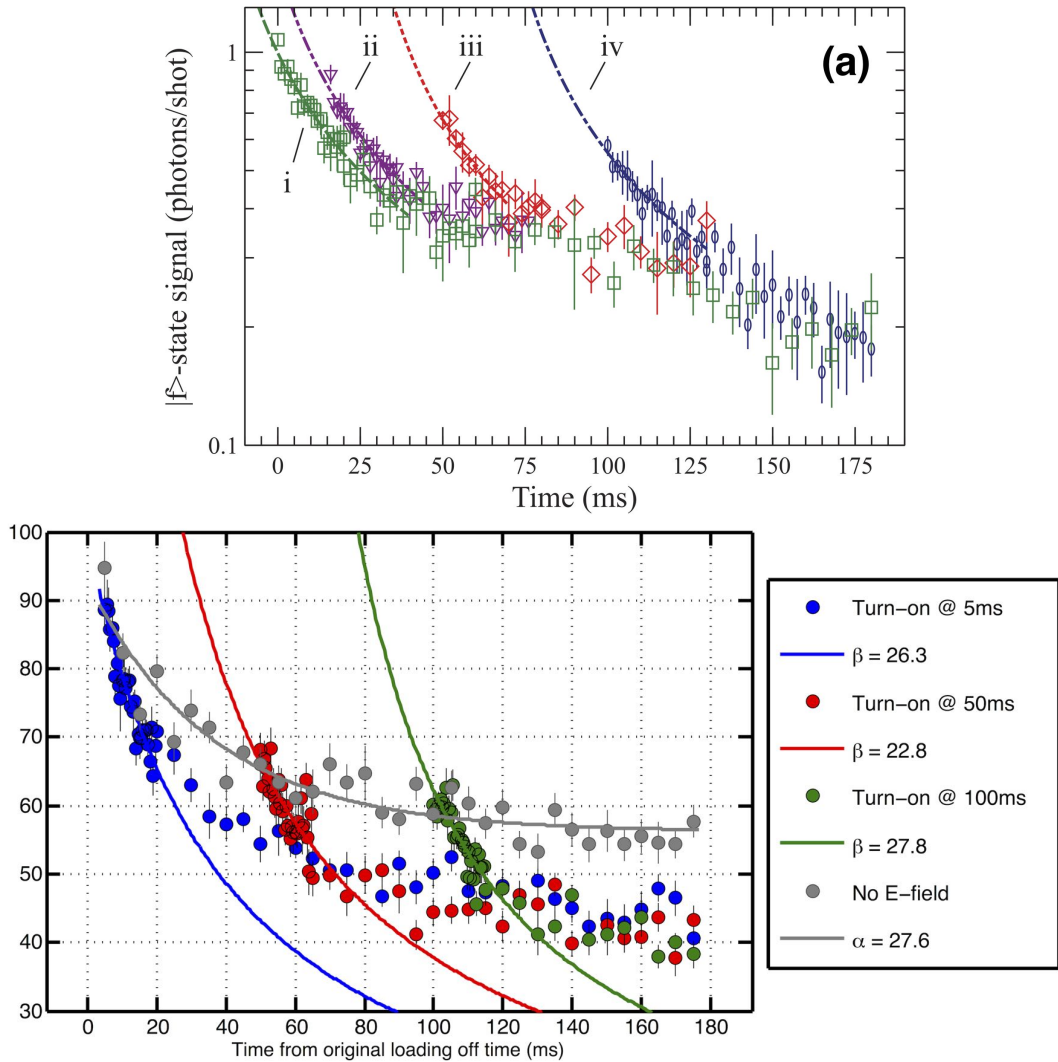
Figure 7.4: Electric field induced decays with different turn-on times of the electric field are shown. (a) Fits to decays initiated after application of a 3 kV/cm electric field after different wait times yield two body parameters β of (i) 40.4 ± 3.0, (ii) 41.2 ± 4.2, (iii) 48.4 ± 8.1, and (iv) 45.4 ± 5.5 (photons/shot)$^{-1}$s^{-1}. Intrigued by the data shown in panel (a) from [121], we took data with an emphasis on simultaneous collection for reduced systematics at longer timescales for all datasets, resulting in panel (b), collected in March of 2014 in the Tricycle trap with a similar electric field magnitude.

argued that this strategy of fitting Eq. 7.14 while varying initial population would lend robustness to the procedure despite the known difficulties of relying on Eq. 7.14 [121, Page. 1800, bottom right].

During our reinvestigation, we pushed the decay measurements out to long times, and found

the results shown in Fig. 7.4b. These results are a big challenge to the hypothesis of a fixed single particle loss timescale, and strongly suggest a time-dependence of the single particle loss, since there is no reason that either a one-body or two-body effect, initiated after various wait times, should lead to nearly overlapped traces in the long term. Note how near 180 ms in Fig. 7.4b, the 50, 100, and 150 ms traces all approach the same level. Intrigued by this observation of what seemed like a fixed magnitude trap-loss induced by the turn-on of the electric field, we also experimented with the application of multiple pulses of electric field, and obtained the results shown in Fig. 7.5. This presents an additional challenge to the hypothesis of simple electric field dependent loss parameters, which ought to respond only to the time integrated electric field application, and not whether it is pulsed or continuous. In contrast, in Fig. 7.5 we find that applying the electric field for the entirety of the time sequence (red) causes far less loss than applying it for half of the time, but in a switched manner (yellow). This is strongly suggestive of a dynamical effect, i.e. an effect which concerns the short term dynamics of molecule trajectories in their trapping potential, and not a collisional effect which ought to respond generally speaking to thermodynamically and temporally averaged quantities.

Specifically, one obvious dynamical effect would be the behavior of the population in the presence of a spin-flip loss region, discussed at length in Sec. 6.4.2. Molecules whose orbits regularly intersect the loss region are lost, but molecules may exist whose orbits never intersect the loss region. Indeed, such a class of molecules is mathematically guaranteed, thanks to the cylindrical symmetry of the ring and tricycle trap. This symmetry enforces the conservation of angular momentum about the axis of cylindrical symmetry under the evolution of the classical Hamiltonian governing molecular trap orbits. Since the loss region occurs close to this axis, molecules with enough azimuthal angular momentum never intersect the loss region under classical Hamiltonian trajectory evolution. With some collisional thermalization however, trajectories which intersect the loss region should gradually be repopulated, but at a rate that is slow relative to the initial escape dynamics. We can conclude that if thermalization is slow, electric field enhanced spin-flip loss can cause a decay rate that decreases over time. If thermalization is slow even compared to the total
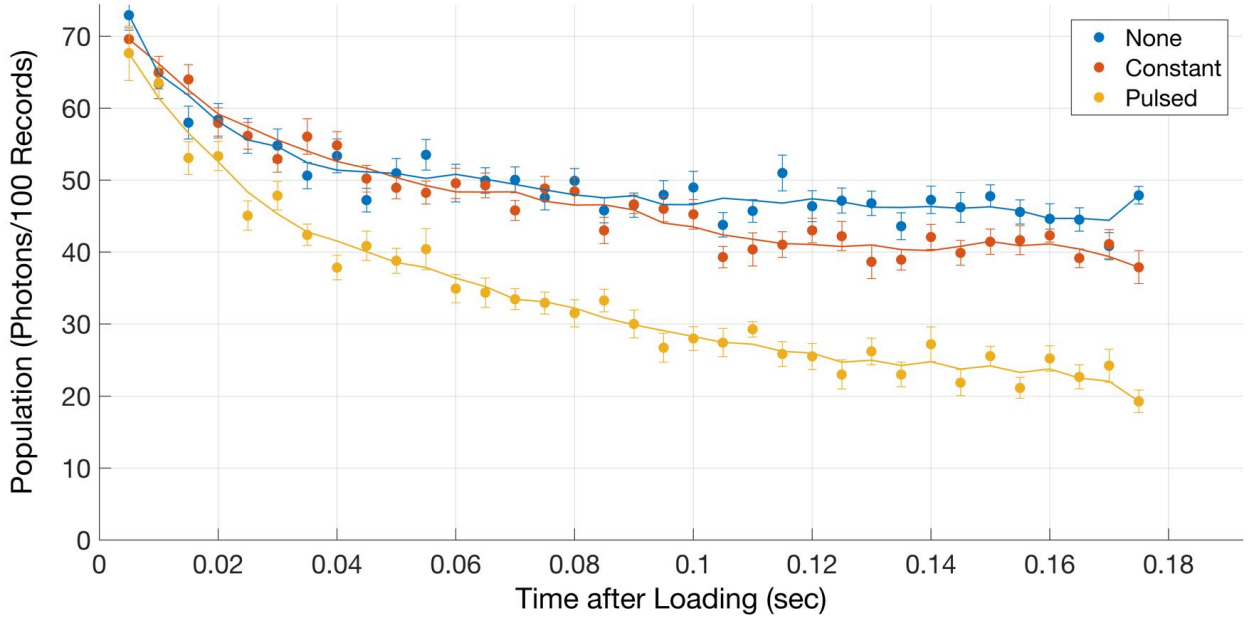
Figure 7.5: Trap decay curves under various conditions related to the timing of application of electric field. The conditions are (blue) no electric field applied, (red) constant electric field applied, (yellow) 5 ms pulses of electric field every 10 ms. Lines are five point running averages. Data collected in March of 2014.

experiment runtime, spin-flip loss should lead to the removal of a fixed subset of the population over a certain dynamical timescale, regardless of any hold-time, exactly as observed in the long-term behavior in Fig. 7.4b.

7.3 Comparison to Simulation

Comparison to simulations is a potentially favorable strategy for detecting the role of collisions in an experiment. Fast mean-field based approaches to simulating collisional gases exist, with that due to Bird [156] quite common in the literature. In the course of this thesis, significant simulation endeavors were pursued, often exactly with this goal of elucidating the relative contribution of single and double particle effects. Simulation is particularly promising in light of the role of dynamical effects described in the previous section, since any analytical forms are hopeless to shed light on dynamics, while the simulation should serve well with a suitably meshed trapping potential.

Firstly, a note of caution is in order. Similar to the fitting of decay curves, comparison to simulations can be plagued by the same sorts of fundamental flaws as are the comparison to decay fits discussed in the last section. The simulation should certainly perform better than analytic decay fits in that it does not need to make any homogeneous population or related assumptions, but at the expense of abandoning these homogeneity assumptions the simulation becomes dependent on many additional tuning parameters. Extracted collisional contributions can strongly depend on these tuning parameters. As a thought experiment, suppose that an experimental parameter like the trap strength, which may easily deviate between simulation and experiment due to manufacturing defects or variability in the permanent magnets for example, is indeed different between the simulation and the experiment. Suppose further that the simulation overestimates the trap depth by 10%. This parameter is important for the short-time dynamics of molecules from the trap, and an overestimate would result in a reduced role of these dynamics, leading the simulation to underestimate the initial decay rate due to dynamics. Consequently, it is likely that the best match between simulation and experiment would occur for a simulation with a larger number of collisions than the experiment, since these extra collisions would boost the initial decay rate to compensate for the trap depth overestimate.

These issues could be behind the incredibly large collision rates predicted in the simulation decay fitting shown in Fig. 7.6 for example. These are not unperturbed decays, but occur during the application of various forced microwave evaporation sequences. It is seen that large collision rates are rather successful at fitting the shapes observed in the trapping geometry. A key parameter governing the comparison of simulation to experiment is the removal efficiency of the microwave knife, which could have dependencies on polarization and position in the trap that are not treated, dependence on molecule velocity, etc. If this parameter is too small, the simulation will predict greater numbers of molecules remaining, and the collision rate will be reduced to match this, since the collision rate also influences molecule number remaining by influencing how successful the evaporation is. I believe the match of microwave knife between simulation and experiment is responsible for the simulation landing at the large collision rate match of 130 $\text{s}^{-1}\text{mol}^{-1}$ in Fig. 7.6.
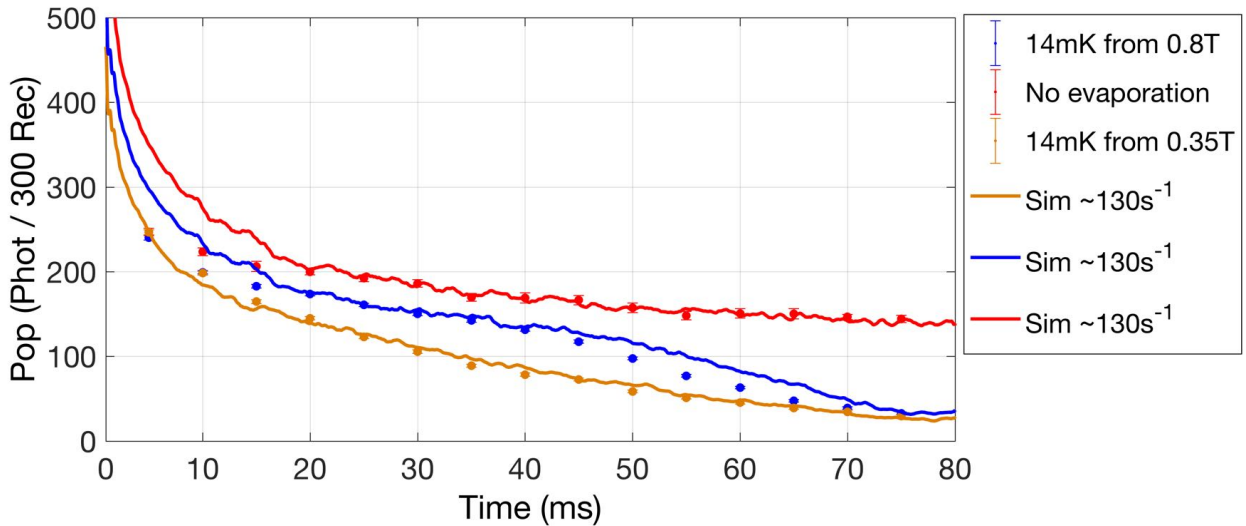
Figure 7.6: The fitting of the decays of molecules from the trap with direct Monte-Carlo simulations including collision rates are shown. Large collision rates of 130/s are found to fit best, primarily due to the initially fast decay exhibited by the population. These data were collected on June 26th, 2013. The legend describes some details of the microwave knife,

In addition to parameter tuning, there is also the question of whether the simulation correctly includes all relevant effects, since simplifying assumptions are often essential for reasonable runtimes and development times. Specifically, the influence of other substates of OH other than the doubly stretched one are pervasive and pernicious. As discussed in Sec. 6.3, molecules in the $|f, -\frac{3}{2}\rangle$ state end up in either $|f, \frac{1}{2}\rangle$ or $|e, \frac{3}{2}\rangle$, and the dynamics of these molecules should also influence the dynamical escape processes involved during early trap decay.

7.3.1 Simulating Electric Field Induced Loss

One key success achieved during my thesis work was the use of simulations to demonstrate the dynamical effects suggested by the experiments discussed above in Sec. 7.2.1. By carefully including the electric field enhanced spin flip loss in simulations but with no appreciable collision rate, and then applying the same fitting paradigm used in [121] to the decay traces obtained by simulation, a very close match is obtained to the experimental data, see Fig. 7.7. Each point corresponds to the fitting of a suite of decays occurring after different hold times at a specific electric field. We can
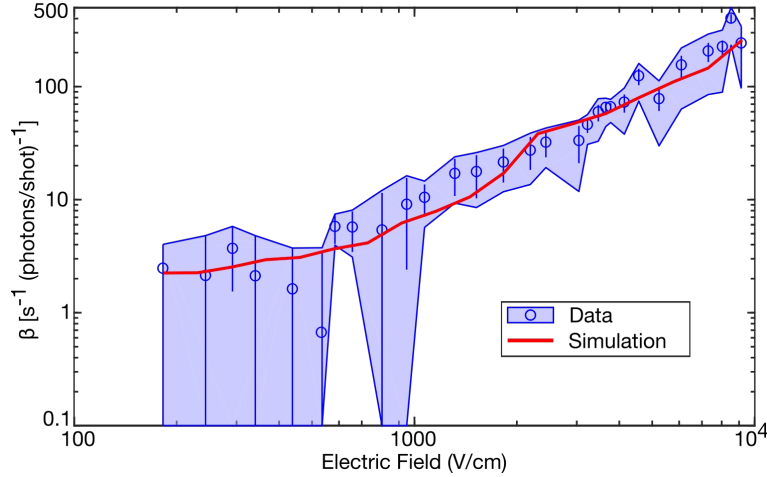
Figure 7.7: Two body fits from [121] to experimental data like that in Fig. 7.4 but at various electric fields. The blue data points and shaded region are repeated from Fig. 3 of [121], where the shading indicates the variation that would be brought about by two-fold changes in the assumed one-body loss α from spin-flip losses. The very close agreement highlights the ability of dynamical effects to masquerade as two-body decay curves.

also examine the match of individual experiments, instead of only looking at the full collection. An example of the simulated trajectories arising from a specific electric field is also shown in fig. 7.8. It is seen that the simulation overestimates the initial decay rate, but agrees fairly well with the total eventual loss.

At first it is perhaps tempting to attribute this discrepancy to the possible continued role of collisions. However, there is no reason that collisions should influence this short time discrepancy, which is much more likely a higher order dynamical effect, especially since the dynamical effects were just seen to so nicely explain the observation of fixed total electric field induced loss. And indeed, just such a higher order dynamical effect is available through the more careful inclusion of other substates of the OH ground state. Electric field induced spin-flip loss does not directly remove molecules from the trap, but instead transfers them to lower lying states, some of which remain fairly well trapped. This can be seen by viewing the energy of substates as a function of position in the trap, animated in Fig. 7.9. Along the axis, all states are connected, but as the radial coordinate increases, mostly trapped states separate away from the others. Simulating this
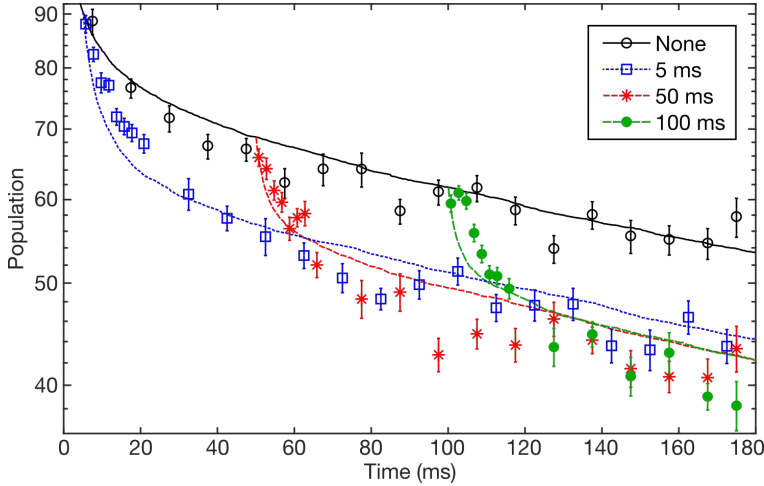
Figure 7.8: Experimental data on electric field-induced loss with an attempted overlap to spin-flip loss simulations. The case of no electric field (black, solid, circles) is compared to electric fields of 3 kV/cm turned on after a wait time indicated in the legend.

has several associated challenges. Firstly, the dynamics associated with hopping between substates must be carefully treated. This is made especially challenging by the fact that the location of hopping points between the second trapped substate and lower states varies with the magnitude of applied electric field, unlike the hopping point between the primary trapped state and the second, which is always located at the trap center. Secondly, the detection probability of molecules in other states features strong position dependence, since these states have a positional dependence to their parity character. This also increases the possibility of discrepancies between simulation and experiment associated with the power and frequency of the laser, since these will determine how much $|f\rangle$ character is required for detection. Despite all of this, the key idea is that the treatment of secondary and higher order partially trapped states should lead to a reduction in the dynamical decay timescale after application of electric field, and this is indeed observed when including the secondary trapped state, as shown in Fig. 7.10. This figure also shows a few other tuning parameters that were considered in the simulation, such as laser beam diameter and initial molecular ensemble center of mass velocity. I also spent considerable time on the question of the initial population, at one point implementing a loading reflective of the $|f, \pm\frac{3}{2}\rangle$ magnetic effects,
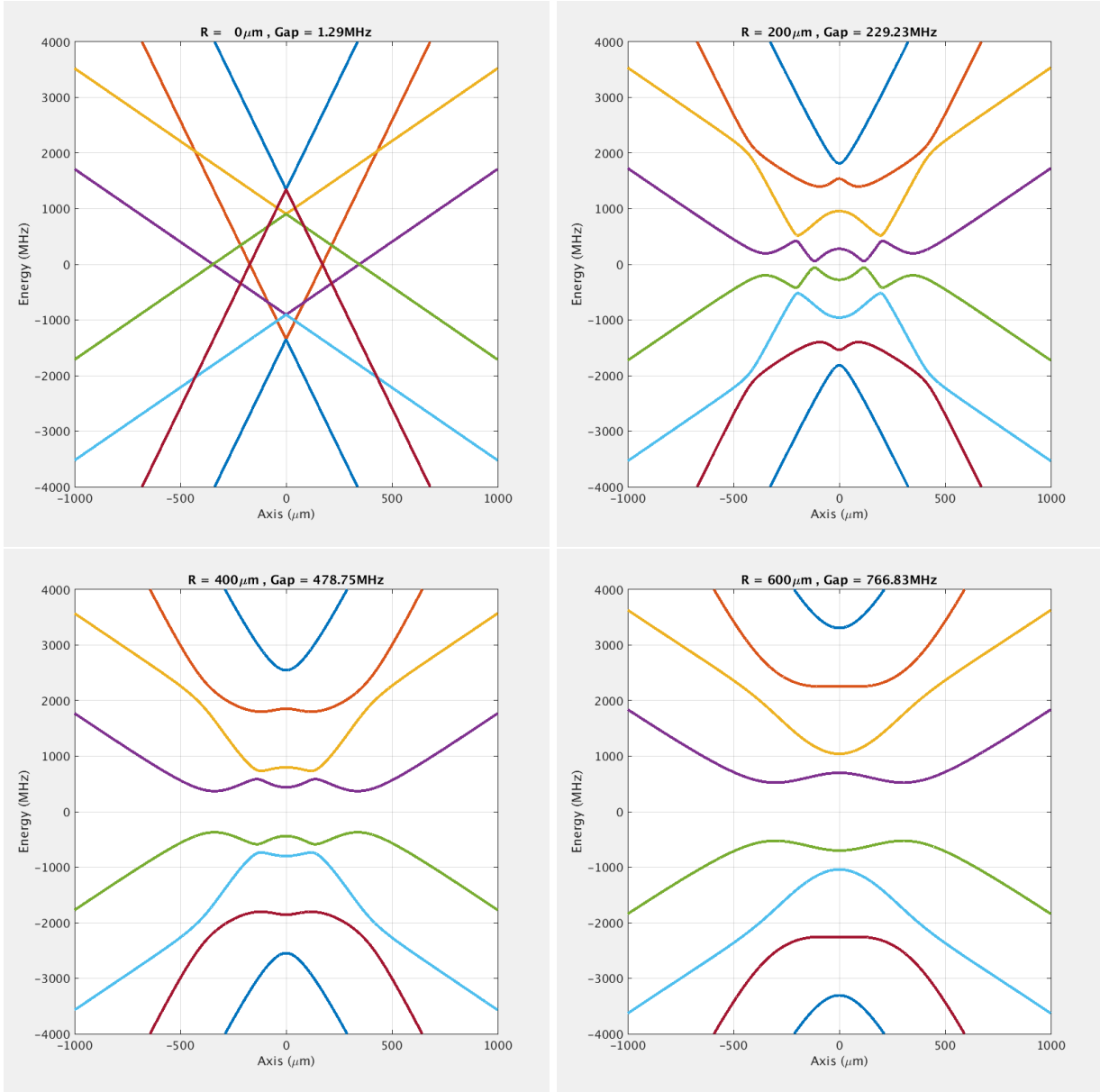
Figure 7.9: Eight ground states of OH as a function of position in a magnetic quadrupole trap with 3 kV/cm applied. In the top left, the energies of these eigenstates are plotted as a function of their position along the cylindrical axis through the quadrupole trap. The doubly stretched state appears as a dark blue V near the center, and the other states may be identified based on their Zeeman effect at larger distances. The red state is $|e, \frac{3}{2}\rangle$, and has the same slope as the dark blue, yellow is $|f, \frac{1}{2}\rangle$, purple $|e, \frac{1}{2}\rangle$, etc. In the other panels, position is plotted not along the axis, but parallel to it and offset by the distance labeled in the title of the panel, increasing in steps of 200 μs. The avoided crossings open up even for very small deviations from the axis, demonstrating that except for a few small openings, really the top four substates are predominantly trapped.
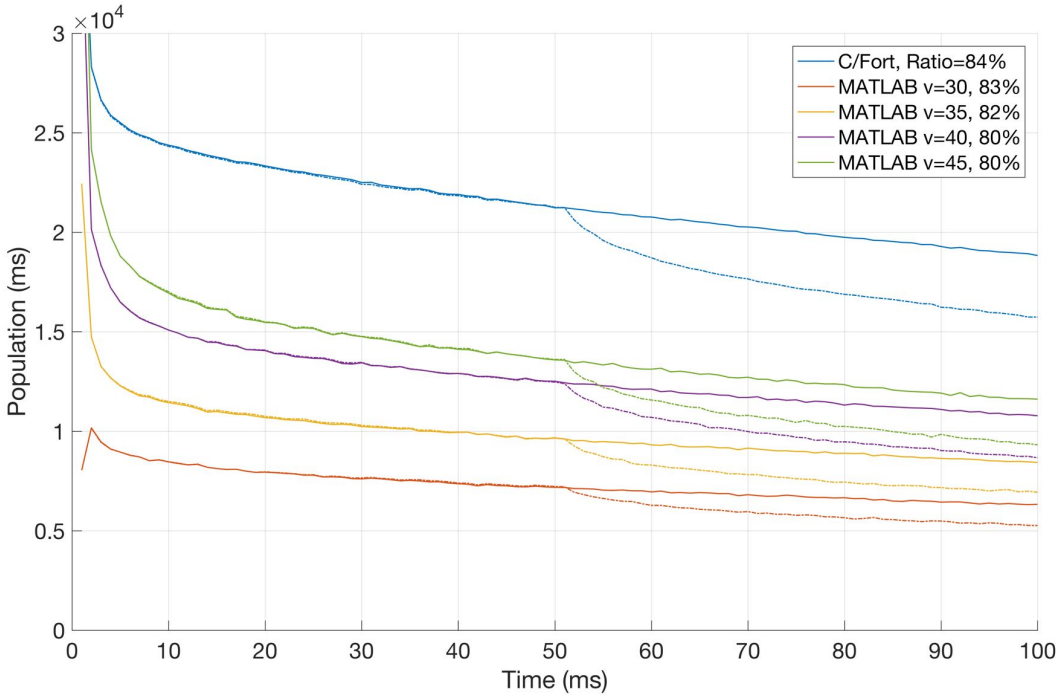
Figure 7.10: Decays after electric field turn-on are shown with and without the electric field and under varying conditions. In the legend, final fractional differences between the cases with and without electric fields are shown.

see Fig. 6.14 of Sec. 6.3. Comparing to Fig. 7.8, it is clear that a slower dynamical timescale has been obtained, and we can conclude that the remaining discrepancy in that figure is capable of being explained by the inclusion of higher order trapped states.

Simulation fitting is a powerful tool, but great care must be taken that single particle deviations between simulation and experiment are not falsely influencing the reported collision rate. Such influences are not surprising, since often single particle deviations yield the same signature as collisions. One way to address this is to explicitly study the influence of parameter variation on the best fit collisional simulation parameter. Another is to use alternative means to constrain the collision rate, such as density calibration [60, Chapter 4].

7.4   Anticipated Collision Rates

Given the challenges associated with each of the collision detection techniques discussed thus far, it is especially useful to develop alternative means of anticipating reasonable collision rates in a system of interest. One key way to do this is to estimate the molecule number via the experimental detection scheme, use theory to approximate the collision cross section, and then rely on the well-known and easily motivated expression to get an order of magnitude estimate for the collision rate:

$$\beta = n\sigma v_{\text{rel}}, \tag{7.18}$$

where n is a number density, σ a collision cross section, β the collision rate per molecule, and v_{rel} the average relative velocity.

As far as the molecule number, density calibration suggests 1.9×10^{-5} cm^{-3} molecule density in free flight [60, Sec. 4.6]. Assuming that the laser beam fills a 2 mm^3 volume or so, and detects 0.3 photons/shot during free flight, 1.5 photons/shot during trapping, we find:

$$N \quad = \quad 2 \cdot 10^{-3} \text{ cm}^3 \quad \times \quad 1.9 \cdot 10^{-5} \text{ cm}^{-3} \quad \times \quad 1.5/0.3 \quad = \quad 1900. \tag{7.19}$$

As far as the cross sections are concerned, we can take Goulven's calculations [44, Inset of Fig. 1b] at 50 mK giving an elastic cross section:

$$\sigma = 2.5 \times 10^{-12} \text{ cm}^2. \tag{7.20}$$

Now at this stage it is a bit tricky to decide what exactly to put into Eq. 7.18, because the density in the trap is not homogeneous, and in fact varies rather strongly given the tightly confining linear quadrupole geometry. For this reason, I simulated this exact question by initializing a thermal distribution of molecules in a linear quadrupole trap and studying the collision frequency per molecule, leading to the results shown in Fig. 7.11. These results are essentially a mapping that gives the relationship between molecule number and collision rate for the geometry. The fitted value scales directly with molecule number, so that in an ensemble with 10^6 molecules, each molecule would have 68 collisions per second for example. This simulation was actually performed with a
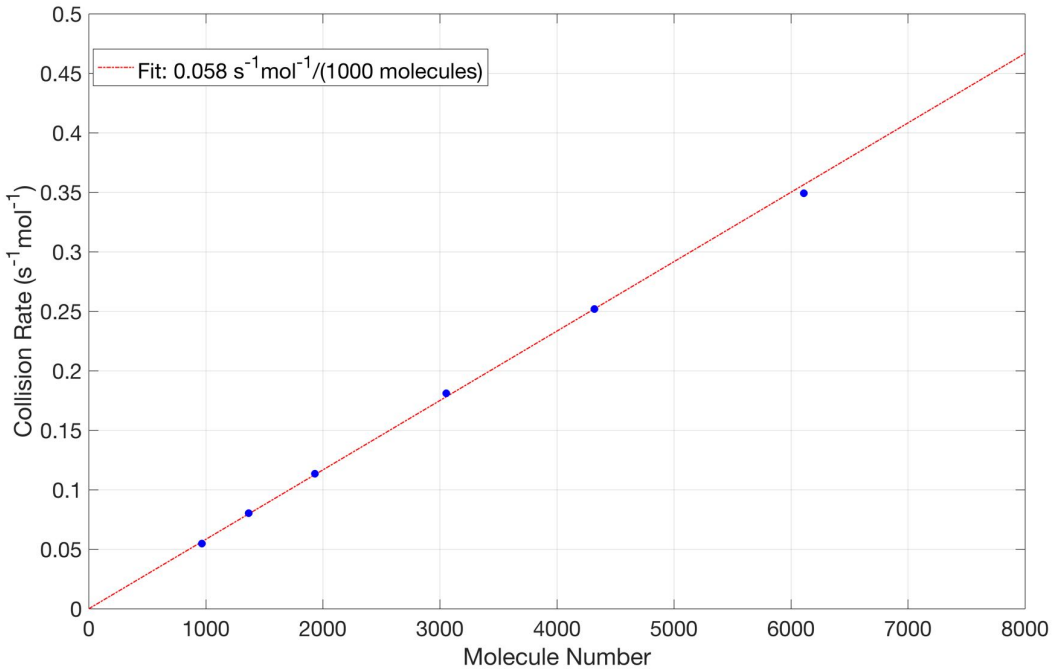
Figure 7.11: Collision rates are simulated as a function of molecule number. With 1000 molecules, a rate of 0.068 s^{-1}mol^{-1} is found.

more ideal value of the collision cross section, $\sigma = 2 \cdot 10^{-11}$ cm^2, taken from the low temperature limiting value computed by Goulven in [44, Fig. 1b]. It follows that for 50 mK temperatures, the expected mapping from number to collision rate would be 8.5 s^{-1}mol^{-1} with 10^6 molecules in the tricycle trap.

With these numbers, the discussion surrounding the collision rates in Fig. 7.6 can be placed in much better context. We can anticipate that the molecule number required to achieve a collision rate of 130 s^{-1} would be $1.5 \cdot 10^7$. Our collection system ought to detect something like one photon per three hundred molecules, or in this case $50,000$ photons, when in practice we detect only a few photons per realization of the experiment.

7.5   Forward Minus Backward Evaporation

During our careful reinvestigation of the results reported in [44], we developed a rather sensitive technique for probing the presence of slight but potentially nonzero collision rates in the
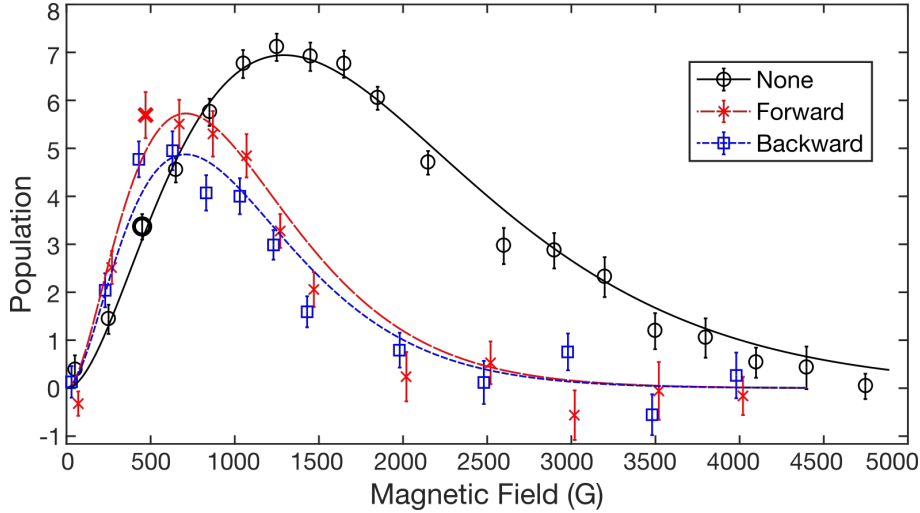
Figure 7.12: Microwave depletion spectra are shown with no evaporation, with evaporation, and with a backward evaporation sequence.

experiment. The essence of our technique is to subtract the molecule number after an evaporation sequence from the number we obtained by time-reversing the microwave frequency chirp, so that the population cut goes backwards from deep to shallow in the trap. This comparison subjects all molecules to the same integrated microwave power, and thus the two conditions should be equivalent in a situation with only single particle effects. With respect to collisional effects, the time-reversed case functions like a truncation, preventing molecules that would otherwise have collisionally thermalized to lower temperatures from doing so, see [157] for a discussion of the usual behavior of an evaporation. To whatever extent an evaporation is successful in facilitating beneficial thermalizing collisions, the time-reversed condition should yield fewer molecules. We consistently observed this in the Ring trap at the $(6 \pm 2)\%$ level, pointing to an evaporative effect despite the negative influence of spin-flip losses.

It is also interesting to look at the spectra of molecules in the trap after such sequences. This is shown in [88, App. B] only for a forward sequence, but I wish here to expand a bit on the conversation offered there, and to include a spectrum from the backward evaporation as well, see Fig. 7.12. Both forward and backward evaporations show a single point well separated from

the unevaporated spectra, and are remarkably similar overall. This similarity suggests that the two sequences are not significantly different from one another thermodynamically, and leaves one wondering whether any systematic artifact in the forward minus backward comparison could be contributing to the measured difference in molecule number.

I spent some time investigating this possibility, and eventually realized that any dynamical timescale for the escape of molecules removed by the microwave knife could indeed lead to a false positive result of the forward minus backward evaporation. Since the backward evaporation removes its molecules earlier than the forward, any extra dynamical time for their escape could result in the forward evaporation artificially showing a larger remaining molecule number. The same kinds of multi-substate dynamics discussed above in Sec. 7.3.1 could also lead to an increased dynamical timescale relative to expectations. The naïve expectation would be escape on the order of a few trap oscillations, characterized by a single exponential decay, as discussed in [114] for $|e\rangle$-state molecules. From [114, Fig. 4], the electric field applied during evaporation of 300 V/cm should be sufficient for removing $|e\rangle$-state molecules in a few milliseconds. However, even in that work, signatures of the slow escape of some molecules are evident although not discussed, note for example the inset of [114, Fig. 3], where a single exponential is supposedly fit, but reaches a nonzero baseline value of 0.1. If the dynamical timescale were slower for some molecules, say 10 ms or beyond, the forward minus backward observable could skew positive by single particle means.

To simulate this possibility, I did the hard work of including all substates in a Monte-Carlo simulation, including their differential Zeeman shifts so as to include the influence of the microwave knife on other substates and other transitions besides the $|f, \frac{3}{2}\rangle$ to $|e, \frac{3}{2}\rangle$ transition directly targeted. In Fig. 7.13, the difference between forward and backward evaporation ramps for all substates as a function of time is reported in this simulation. Note how molecules persist in $|f, \frac{1}{2}\rangle$ at the final step, and how there are actually fewer molecules in $|f, \frac{3}{2}\rangle$ with forward evaporation at the last step, at least in this realization of the Monte-Carlo simulation.

After setting up on the JILA computer cluster, I performed a suite of similar simulations aimed at studying the forward minus backward collision observable, culminating in several panels
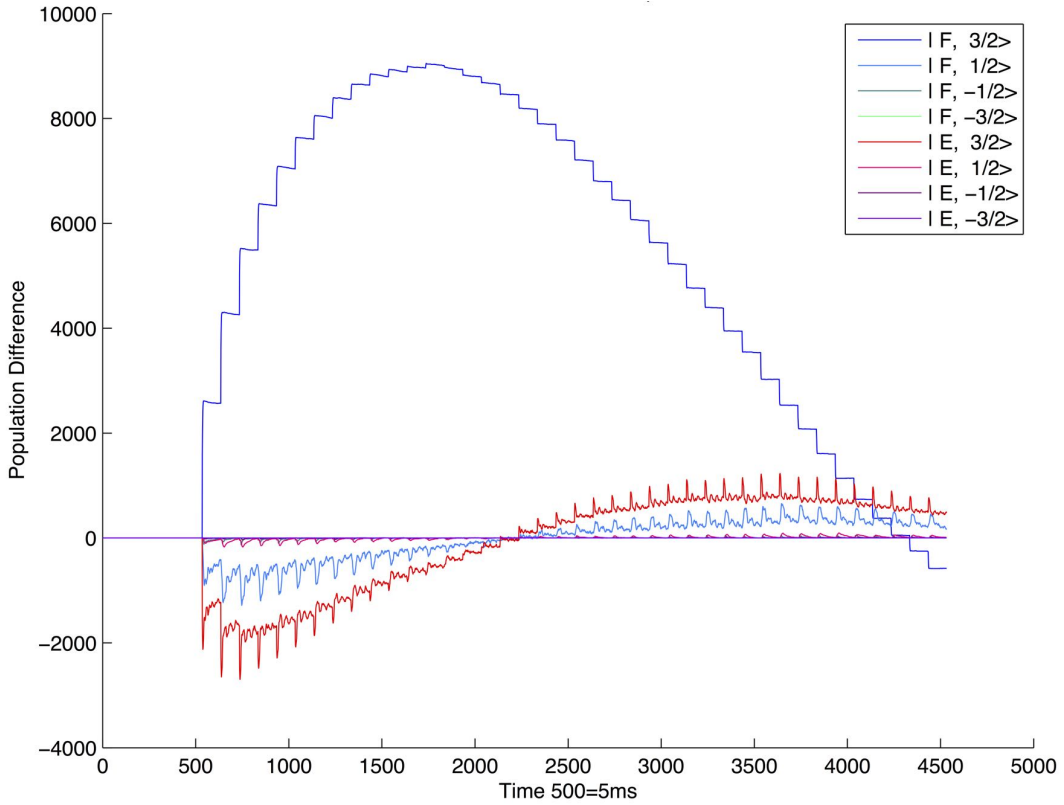
Figure 7.13: All eight substates of the OH ground state are included in a simulation of evaporation.

of data similar to that shown in Fig. 7.14. As one would expect, the forward minus backward observable really starts displaying a strong effect for the largest molecule numbers and the longest evaporation sequences. At lower molecule numbers, we see exactly the predicted effect- the forward minus backward observable reaches a small but nonzero limiting value of approximately 5% difference.

7.6 Spatial Density Enhancements by Microwave Spectroscopy

This last technique for detecting collisions plays a key role in the final claims of the legitimacy of the observation of some degree of thermalization presented in [88, App. B]. The idea is to compare normalized microwave spectroscopies in order to determine whether there is any region close to the center of the trap that ends up with a greater spatial density of molecules than it had
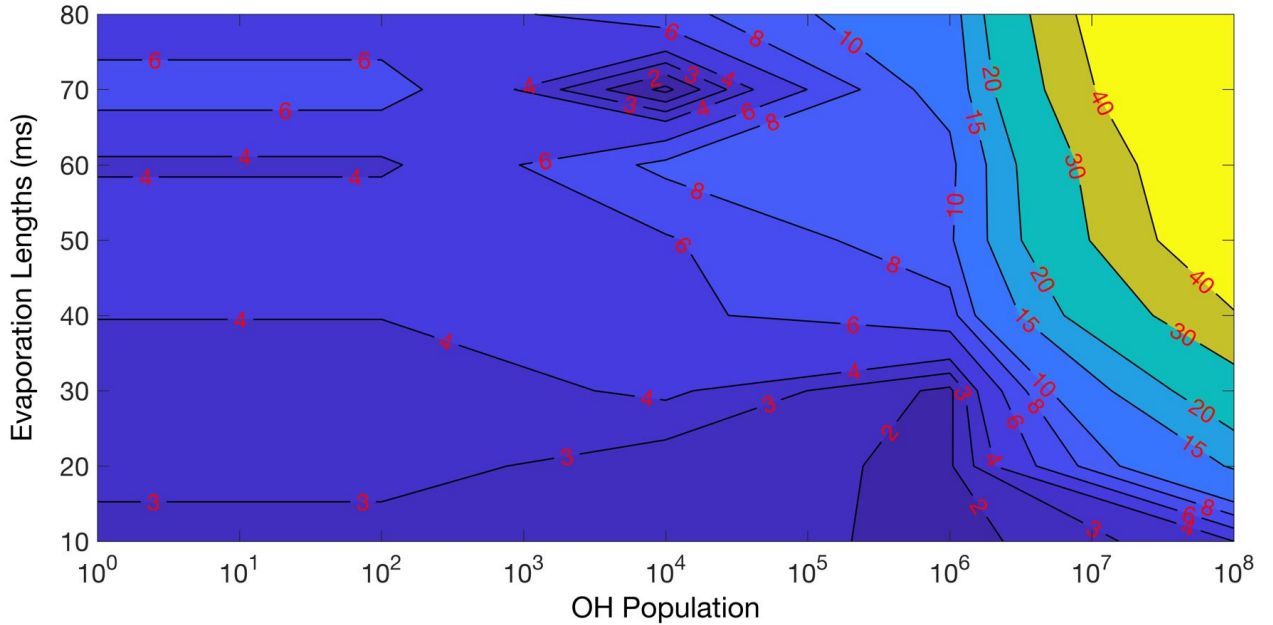
Figure 7.14: Contour plot indicating the percentage gain of forward evaporation compared with backward as a function of evaporation length and molecule number. Slower evaporations with large initial numbers show the most significant gains. Even very tiny numbers of molecules still show a forward minus backward difference, indicating a small, single-particle contribution to this collisional indicator.

originally. This is not a necessary condition for either collisions or evaporation, since phase space density increase could happen primarily through the velocity dimensions of phase space. It is also possible to enhance spatial density at the expense of velocity density, often referred to as adiabatic compression, but this cannot happen by mistake and requires work to be performed on the ensemble via the trapping potential. In this sense, the observation of a spatial density enhancement is an indisputable observable of elastic collisions in an ensemble.

A normalized spectroscopically determined density enhancement is indeed observed for the region near 500 G in both forward and backward evaporation as evident in Fig. 7.12. Nevertheless, a few additional caveats should be kept in mind, as well as those in Sec. 6.2.4. First of all, it would be ideal if a way could be found to eliminate some of the complexities of the normalization procedure. To briefly recapitulate, depletion spectroscopy transfers only a fraction of molecules to the lower parity state at a specific magnetic field value, so we integrate the total area enclosed

by the spectroscopy curve, which is scaled according to the observed total population by laser induced fluorescence. This is necessary because depletion spectroscopy is performed with a train of short microwave pulses lasting over a total time of about a quarter of a trap oscillation, so that molecules are not at all frozen in place. Relative to a very brief spectroscopy pulse that would only deplete molecules in a given region at that particular instant, the use of a train of pulses over a longer period of time allows us to sample molecules more widely to boost the signal to noise ratio of spectroscopy. The spectroscopy gives a value that is proportional to the true instantaneous population in a specific magnetic field region, but with a scaling factor that allows the signal to be constrained with the measured total number of molecules in the trap. Nevertheless, in any future experiments, I would submit that claims of absolute density enhancement should be confirmed by means of a single transfer ARP spanning the low magnetic field region, and thus serving as a direct witness on the spatial density in that region at that time, with no need to perform any careful accounting of the total molecule distribution function.

Moreover, any future demonstration of spatial density enhancement would do well to include additional observables to support the claim. One of these may be had through the use of resonantly enhanced multi-photon ionization of the molecules, as pioneered for the use of measuring population distributions recently in the Lewandowski lab [158]. The resonant process detects a small subregion of the trap, whose position may be tuned in order to access the population distribution function.

7.7   Conclusions

The detection of collisions is a challenging task, especially in the absence of a background-free exit channel as for the collisions between OH molecules discussed in this chapter. Several methods have been carefully investigated with regard to their potential for systematic effects when employed in the detection of small effects. With the possibility of enhanced molecule numbers in the near future, these methods should prove very relevant for elucidating the full collisional story of the next generation of trapped OH radicals.

Bibliography

[1] Mike H Anderson, Jason R Ensher, Michael R Matthews, Carl E Wieman, and Eric A Cornell. Observation of Bose-Einstein condensation in a dilute atomic vapor. **Science**, 269(5221):198–201, 1995. 1

[2] K. B. Davis, M. O. Mewes, M. R. Andrews, N. J. van Druten, D. S. Durfee, D. M. Kurn, and W. Ketterle. Bose-Einstein Condensation in a Gas of Sodium Atoms. **Physical Review Letters**, 75(22):3969–3973, 1995. 1, 127

[3] B. P. Abbott, R. Abbott, T. D. Abbott, M. R. Abernathy, F. Acernese, K. Ackley, C. Adams, T. Adams, P. Addesso, R. X. Adhikari, and Et Al. Observation of Gravitational Waves from a Binary Black Hole Merger. **Physical Review Letters**, 116(6):061102, 2016. 1

[4] J I Cirac and P Zoller. Quantum Computations with Cold Trapped Ions. **Phys. Rev. Lett.**, 74(20):4091–4094, 1995. 2

[5] H Haffner, C Roos, and R Blatt. Quantum computing with trapped ions. **Physics Reports**, 469(4):155–203, 2008. 2

[6] John Preskill. Quantum Computing in the NISQ era and beyond. **Quantum**, 2:79, 2018. 2

[7] I. Kassal, S. P. Jordan, P. J. Love, M. Mohseni, and A. Aspuru-Guzik. Polynomial-time quantum algorithm for the simulation of chemical dynamics. **Proceedings of the National Academy of Sciences**, 105(48):18681–18686, 2008. 2

[8] Dawei Lu, Nanyang Xu, Ruixue Xu, Hongwei Chen, Jiangbin Gong, Xinhua Peng, and Jiangfeng Du. Simulation of Chemical Isomerization Reaction Dynamics on a NMR Quantum Simulator. **Physical Review Letters**, 107(2):020501, 2011. 2

[9] Gordon W F Drake. Announcement: The Fundamental Role of Precision Measurement in Atomic, Molecular, and Optical Physics—a New Section Heading for Physical Review A. **Phys. Rev. A**, 98(1):10001, 2018. 2

[10] D. Hanneke, S. Fogwell, and G. Gabrielse. New Measurement of the Electron Magnetic Moment and the Fine Structure Constant. **Physical Review Letters**, 100(12):120801, 2008. 2

[11] B J Bloom, T L Nicholson, J R Williams, S L Campbell, M Bishof, X Zhang, W Zhang, S L Bromley, and J Ye. An optical lattice clock with accuracy and stability at the 10^{-18} level. **Nature**, 506:71, 2014. 2

[12] Lincoln D. Carr, David DeMille, Roman V. Krems, and Jun Ye. Cold and ultracold molecules: science, technology and applications. **New Journal of Physics**, 11(5):055049, 2009. 2

[13] Colin D. Bruzewicz, John Chiaverini, Robert McConnell, and Jeremy M. Sage. Trapped-Ion Quantum Computing: Progress and Challenges. 2019. 3

[14] D I Schuster, Lev S Bishop, I L Chuang, D DeMille, and R J Schoelkopf. Cavity QED in a molecular ion trap. **Phys. Rev. A**, 83(1):12311, 2011. 3

[15] M. W. Zwierlein, C. A. Stan, C. H. Schunck, S. M. F. Raupach, S. Gupta, Z. Hadzibabic, and W. Ketterle. Observation of Bose-Einstein Condensation of Molecules. **Physical Review Letters**, 91(25):250401, 2003. 3

[16] Matthias Schmitt, Matthias Wenzel, Fabian Böttcher, Igor Ferrier-Barbut, and Tilman Pfau. Self-bound droplets of a dilute magnetic quantum liquid. **Nature**, 539:259, 2016. 3

[17] L Chomaz, R M W van Bijnen, D Petter, G Faraoni, S Baier, J H Becher, M J Mark, F Wächtler, L Santos, and F Ferlaino. Observation of roton mode population in a dipolar quantum gas. **Nature Physics**, 14(5):442–446, 2018. 3

[18] William B. Cairncross, Daniel N. Gresh, Matt Grau, Kevin C. Cossel, Tanya S. Roussy, Yiqi Ni, Yan Zhou, Jun Ye, and Eric A. Cornell. Precision Measurement of the Electron's Electric Dipole Moment Using Trapped Molecular Ions. **Physical Review Letters**, 119(15):1–5, 2017. 3

[19] V. Andreev, D. G. Ang, D. DeMille, J. M. Doyle, G. Gabrielse, J. Haefner, N. R. Hutzler, Z. Lasner, C. Meisenhelder, B. R. O'Leary, C. D. Panda, A. D. West, E. P. West, and X. Wu. Improved limit on the electric dipole moment of the electron. **Nature**, 562(7727):355–360, 2018. 3

[20] Ivan Kozyryev and Nicholas R. Hutzler. Precision Measurement of Time-Reversal Symmetry Violation with Laser-Cooled Polyatomic Molecules. **Physical Review Letters**, 119(13): 133002, 2017. 3

[21] T. Zelevinsky, S. Kotochigova, and Jun Ye. Precision Test of Mass-Ratio Variations with Lattice-Confined Ultracold Molecules. **Physical Review Letters**, 100(4):043201, 2008. 3

[22] D. DeMille, S. B. Cahn, D. Murphree, D. A. Rahmlow, and M. G. Kozlov. Using Molecules to Measure Nuclear Spin-Dependent Parity Violation. **Physical Review Letters**, 100(2): 023003, 2008. 3

[23] Eric R Hudson. **Experiments on Cold Molecules Produced via Stark Deceleration**. Doctor of philosophy, University of Colorado, 2006. 4, 12, 77

[24] Luigi De Marco, Giacomo Valtolina, Kyle Matsuda, William G. Tobias, Jacob P. Covey, and Jun Ye. A degenerate Fermi gas of polar molecules. **Science**, 363(6429):853–856, 2019. 4

[25] Benjamin K. Stuhl, Brian C. Sawyer, Dajun Wang, and Jun Ye. Magneto-optical Trap for Polar Molecules. **Physical Review Letters**, 101(24):243002, 2008. 4

[26] Alejandra L Collopy, Shiqian Ding, Yewei Wu, Ian A Finneran, Loïc Anderegg, Benjamin L Augenbraun, John M Doyle, and Jun Ye. 3D Magneto-Optical Trap of Yttrium Monoxide. **Phys. Rev. Lett.**, 121(21):213201, 2018. 4, 135

[27] Matthew H. Steinecker, Daniel J. McCarron, Yuqi Zhu, and David DeMille. Improved Radio-Frequency Magneto-Optical Trap of SrF Molecules. **ChemPhysChem**, 17(22):3664–3669, 2016. 4

[28] Loïc Anderegg, Lawrence W Cheuk, Yicheng Bao, Sean Burchesky, Wolfgang Ketterle, Kang-Kuen Ni, and John M Doyle. An Optical Tweezer Array of Ultracold Molecules. **arXiv preprint**, 2019. 4, 153

[29] Loïc Anderegg, Benjamin L. Augenbraun, Yicheng Bao, Sean Burchesky, Lawrence W. Cheuk, Wolfgang Ketterle, and John M. Doyle. Laser cooling of optically trapped molecules. **Nature Physics**, 14(9):890–893, 2018. 4

[30] K. N. Jarvis, J. A. Devlin, T. E. Wall, B. E. Sauer, and M. R. Tarbutt. Blue-Detuned Magneto-Optical Trap. **Physical Review Letters**, 120(8):083201, 2018. 4

[31] Alejandra L Collopy, Matthew T Hummon, Mark Yeo, Bo Yan, and Jun Ye. Prospects for a narrow line MOT in YO. **New Journal of Physics**, 17(5):055008, 2015. 4

[32] John P. Bartolotta, Matthew A. Norcia, Julia R. K. Cline, James K. Thompson, and Murray J. Holland. Laser cooling by sawtooth-wave adiabatic passage. **Physical Review A**, 98 (2):023404, 2018. 4

[33] D.R. Miller. Free Jet expansions. In G. Scoles, editor, **Atomic and Molecular Beam Methods, Vol. 1**. Oxford University Press, 1988. 5, 14, 16, 18, 19, 20, 22

[34] Nicholas R. Hutzler, Hsin-I Lu, and John M. Doyle. The Buffer Gas Beam: An Intense, Cold, and Slow Source for Atoms and Molecules. 2011. 5

[35] W. L. Meerts and A. Dymanus. A Molecular Beam Electric Resonance Study of the Hyperfine Λ Doubling Spectrum of OH, OD, SH, and SD. **Canadian Journal of Physics**, 53(19): 2123–2141, 1975. 5

[36] Klaus P Huber and Gerhard H Herzberg. Constants of Diatomic Molecules. In P.J. Linstrom and W.G. Mallard, editors, **NIST Chemistry WebBook, NIST Standard Reference Database Number 69**. National Institute of Standards and Technology, Gaithersburg, MD 20899, 2018. 5, 8, 10

[37] David J Griffiths and Darrell F Schroeter. **Introduction to Quantum Mechanics**. Cambridge University Press, 2018. 6

[38] John M. Brown and Alan Carrington. **Rotational Spectroscopy of Diatomic Molecules**. 2003. 7, 10

[39] C.E. Fellows, R.F. Gutterres, A.P.C. Campos, J. Vergès, and C. Amiot. The RbCs X1Σ+ Ground Electronic State: New Spectroscopic Study. **Journal of Molecular Spectroscopy**, 197(1):19–27, 1999. 8

[40] Edmund R. Meyer and John L. Bohn. Electron electric-dipole-moment searches based on alkali-metal- or alkaline-earth-metal-bearing molecules. **Physical Review A**, 80(4):042508, 2009. 8

[41] Peter W Atkins and Ronald S Friedman. **Molecular quantum mechanics**. Oxford University Press, 4 edition, 2005. 9

[42] BK Stuhl. **Ultracold molecules for the masses: evaporative cooling and magneto-optical trapping**. Doctor of philosophy, University of Colorado, 2012. 12, 16

[43] Kenji Maeda, Michael L. Wall, and Lincoln D. Carr. Hyperfine structure of the hydroxyl free radical (OH) in electric and magnetic fields. **New Journal of Physics**, 17(4):045014, 2015. 12, 13

[44] Benjamin K Stuhl, Matthew T Hummon, Mark Yeo, Goulven Quéméner, John L Bohn, and Jun Ye. Evaporative cooling of the dipolar hydroxyl radical. **Nature**, 492(7429):396–400, 2012. 12, 13, 68, 106, 114, 127, 131, 136, 170, 171

[45] Brian Sawyer. **Cold Polar Molecules for Novel Collision Experiments at Low Energies**. Doctor of philosophy, University of Colorado, 2010. 12, 16, 17, 24, 27, 77

[46] Roger Campargue, editor. **Atomic and Molecular Beams**. Springer-Verlag Berlin Heidelberg, 2000. 14

[47] G. K. Batchelor. **An introduction to fluid dynamics**. Cambridge university press, 1967. 15

[48] S. Montero. Molecular description of steady supersonic free jets. **Physics of Fluids**, 29(9): 096101, 2017. 17

[49] U Even. Pulsed Supersonic Beams from High Pressure Source: Simulation Results and Experimental Measurements. **Advances in Chemistry**, 2014:636042, 2014. 17, 24

[50] H. Hulsman. **Nonequilibrium Distributions of Rotational Energies of K_2 Seeded in a Free-Jet of Argon**, pages 273–282. Springer Berlin Heidelberg, Berlin, Heidelberg, 2001. 18

[51] A E Belikov, M M Ahern, and M A Smith. **Rotational and Vibrational Relaxation of Hydrides in Free Jets: HBr and OH**, pages 283–294. Springer Berlin Heidelberg, Berlin, Heidelberg, 2001. 18

[52] H.C.W. Beijerinck and N.F. Verster. Absolute intensities and perpendicular temperatures of supersonic beams of polyatomic gases. **Physica B+C**, 111(2-3):327–352, 1981. 18, 22, 23

[53] J Peter Toennies and Klaus Winkelmann. Theoretical studies of highly expanded free jets: Influence of quantum effects and a realistic intermolecular potential. **The Journal of Chemical Physics**, 66(9):3965–3979, 1977. 18

[54] Uzi Even. "The Even-Lavie valve as a source for high intensity supersonic beam". **EPJ Techniques and Instrumentation**, 2(1):17, 2015. 20, 24, 95, 136

[55] Hao Wu, David Reens, Tim Langen, Yuval Shagam, Daniela Fontecha, and Jun Ye. Enhancing radical molecular beams by skimmer cooling. **Physical Chemistry Chemical Physics**, 20 (17):11615–11621, 2018. 20, 21, 27, 31, 36, 65

[56] D A Hite, Y Colombe, A C Wilson, K R Brown, U Warring, R Jördens, J D Jost, K S McKay, D P Pappas, D Leibfried, and D J Wineland. 100-Fold Reduction of Electric-Field Noise in an Ion Trap Cleaned with In Situ Argon-Ion-Beam Bombardment. **Phys. Rev. Lett.**, 109 (10):103001, 2012. 23

[57] T Briles. **Production, Deceleration, and Detection of OH Radicals**. Doctor of philosophy, University of Colorado Boulder, 2015. 24

[58] D. Proch and T. Trickl. A high-intensity multi-purpose piezoelectric pulsed molecular beam source. **Review of Scientific Instruments**, 60(4):713, 1989. 24

[59] Daniel Irimia, Dimitar Dobrikov, Rob Kortekaas, Han Voet, Daan A van den Ende, Wilhelm A Groen, and Maurice H M Janssen. A short pulse (7 μs FWHM) and high repetition rate (dc-5 kHz) cantilever piezovalve for pulsed atomic and molecular beams. **Review of Scientific Instruments**, 80(11):113303, 2009. 24

[60] Hao Wu. **Achieving a Large Density of Hydroxyl Radicals for Cold Collisions**. Doctor of philosophy, University of Colorado, 2019. 27, 31, 169, 170

[61] B. Yan, P. F H Claus, B. G M Van Oorschot, L. Gerritsen, A. T J B Eppink, S. Y T Van De Meerakker, and D. H. Parker. A new high intensity and short-pulse molecular beam valve. **Review of Scientific Instruments**, 84(2), 2013. 28, 29

[62] Ulf Bossel. On the Optimization of Skimmer Geometries. **Entropie**, 42:12–17, 1971. 30, 31

[63] Ulf Bossel. Skimming Molecular Beams from diverging nonequilibrium gas jets. **Archives of Mechanics**, 1974. 30

[64] R Campargue. Progress in overexpanded supersonic jets and skimmed molecular beams in free-jet zones of silence. **The Journal of Physical Chemistry**, 88(20):4466–4474, 1984. 31

[65] Yair Segev, Natan Bibelnik, Nitzan Akerman, Yuval Shagam, Alon Luski, Michael Karpov, Julia Narevicius, and Edvardas Narevicius. Molecular beam brightening by shock-wave suppression. **Science Advances**, 3(3):e1602258, 2017. 31, 136

[66] David Lancaster, Cameron Allen, Kylan Jersey, Thomas Lancaster, Gage Shaw, Mckenzie Taylor, Di Xiao, Nicholas Hutzler, and Jonathan Weinstein. Improving cryogenic buffer-gas beam collimation with de Laval nozzles. **Bulletin of the American Physical Society**, 2019. 37

[67] J.R. Clement. Liquid Helium Properties. In J.E. Jensen, W.A. Tuttle, R.B. Stewart, H. Brechna, and A.G. Prodell, editors, **Brookhaven National Laboratory Selected Cryogenic Data Notebook**, chapter 2, page 46. Brookhaven National Laboratory, revised edition, 1980. 40

[68] Moritz Kirste, Henrik Haak, Gerard Meijer, and Sebastiaan Y. T. van de Meerakker. A compact hexapole state-selector for NO radicals. **Review of Scientific Instruments**, 84 (7):073113, 2013. 44, 49

[69] J. R. Bochinski, Eric R. Hudson, H. J. Lewandowski, and Jun Ye. Cold free-radical molecules in the laboratory frame. **Physical Review A**, 70(4):043410, 2004. 47, 48, 49, 95, 150

[70] Brian C. Sawyer, Benjamin L. Lev, Eric R. Hudson, Benjamin K. Stuhl, Manuel Lara, John L. Bohn, and Jun Ye. Magnetoelectrostatic Trapping of Ground State OH Molecules. **Physical Review Letters**, 98(25):253002, 2007. 47, 95, 99, 105, 106

[71] Jack Ekin. **Experimental Techniques for Low-Temperature Measurements: Cryostat Design, Material Properties and Superconductor Critical-Current Testing**. Oxford University Press, 2006. 50, 55

[72] Günther Hartwig. **Polymer Properties at Room and Cryogenic Temperatures**. Springer Science, 2013. 51, 53

[73] R. Berman. Some experiments on thermal contact at low temperatures. **Journal of Applied Physics**, 27(4):318–323, 1956. 51

[74] John Sondericker, William DeVito, and Dieter Zantopp. Advances in Cryogenic Engineering Materials: Volum; Part A. In Richard P. Reed, Fred R. Fickett, Leonard T. Summers, and M. Stieg, editors, **Advances in Cryogenic Engineering Materials**, volume 40, chapter The Measur, pages 1099–1105. Springer US, Boston, MA, 2013. 53, 55

[75] H Craig Miller. Surface Flashover of Insulators. **IEEE Transactions on Electrical Insulation**, 24(5):765–786, 1989. 61, 99

[76] H Craig Miller. High Voltage Performance Characteristics of Solid Insulators in Vacuum. In R V Latham, editor, **High Voltage Vacuum Insulation**, pages 299–327. Elsevier, 1995. 61

[77] B Mazurek. High Voltage Vacuum Insulation at Cryogenic Temperatures. In R V Latham, editor, **High Voltage Vacuum Insulation**, pages 487–513. Elsevier, 1995. 61

[78] D C Faircloth. Technological Aspects: High Voltage. **CAS, CERN Accelerator School: Ion Sources**, pages 381–419, 2013. 66, 99

[79] Brian C. Sawyer, Benjamin K. Stuhl, Mark Yeo, Timur V. Tscherbul, Matthew T. Hummon, Yong Xia, Jacek Kłos, David Patterson, John M. Doyle, and Jun Ye. Cold heteromolecular dipolar collisions. **Physical Chemistry Chemical Physics**, 13(42):19059, 2011. 68, 105, 106, 123, 127

[80] Moritz Kirste, Xingan Wang, H Christian Schewe, Gerard Meijer, Kopin Liu, Ad van der Avoird, Liesbeth M C Janssen, Koos B Gubbels, Gerrit C Groenenboom, and Sebastiaan Y T van de Meerakker. Quantum-State Resolved Bimolecular Collisions of Velocity-Controlled OH with NO Radicals. **Science**, 338(6110):1060–1063, 2012. 68

[81] Zhi Gao, Tijs Karman, Sjoerd N. Vogels, Matthieu Besemer, Ad van der Avoird, Gerrit C. Groenenboom, and Sebastiaan Y. T. van de Meerakker. Observation of correlated excitations in bimolecular collisions. **Nature Chemistry**, 10(4):469–473, 2018. 68

[82] J. Veldhoven, J. K upper, H. L. Bethlem, B. Sartakov, A. J. A. Roij, and G. Meijer. Decelerated molecular beams for high-resolution spectroscopy. **The European Physical Journal D**, 31(2):337–349, 2004. 68

[83] Eric R. Hudson, H. J. Lewandowski, Brian C. Sawyer, and Jun Ye. Cold Molecule Spectroscopy for Constraining the Evolution of the Fine Structure Constant. **Physical Review Letters**, 96(14):143004, 2006. 68

[84] Benjamin L. Lev, Edmund R. Meyer, Eric R. Hudson, Brian C. Sawyer, John L. Bohn, and Jun Ye. OH hyperfine ground state: From precision measurement to molecular qubits. **Physical Review A**, 74(6):061402, 2006. 68

[85] Arthur Fast, John E Furneaux, and Samuel A Meek. Precision spectra of $A\,^2\Sigma^+, v' = 0 \leftarrow X\,^2\Pi_{3/2}, v'' = 0, J'' = 3/2$ transitions in ^{16}OH and ^{16}OD. **Physical Review A**, 98(5):052511, 2018. 68

[86] Sebastiaan Y. T. van de Meerakker, Hendrick L. Bethlem, Nicolas Vanhaecke, and Gerard Meijer. Manipulation and Control of Molecular Beams. **Chemical Reviews**, 112(9):4828–4878, 2012. 68, 80

[87] Brian C. Sawyer, Benjamin K. Stuhl, Dajun Wang, Mark Yeo, and Jun Ye. Molecular Beam Collisions with a Magnetically Trapped Target. **Physical Review Letters**, 101(20):203203, 2008. 68, 106, 127, 131, 133, 152

[88] David Reens, Hao Wu, Tim Langen, and Jun Ye. Controlling spin flips of molecules in an electromagnetic trap. **Physical Review A**, 96(6):063420, 2017. 68, 82, 106, 123, 126, 172, 174

[89] Edwin M. McMillan. The Synchrotron–A Proposed High Energy Particle Accelerator. **Physical Review**, 68(5-6):143–144, 1945. 68

[90] Hendrick L. Bethlem, Giel Berden, and Gerard Meijer. Decelerating Neutral Dipolar Molecules. **Physical Review Letters**, 83(8):1558–1561, 1999. 69, 70, 127

[91] Sebastiaan Y T van de Meerakker, Nicolas Vanhaecke, and Gerard Meijer. Stark deceleration and trapping of OH radicals. **Annual Review of Physical Chemistry**, 57(1):159–190, 2006. 72, 73, 74, 75, 99

[92] L. P. Parazzoli, N. Fitch, D. S. Lobser, and H. J. Lewandowski. High-energy-resolution molecular beams for cold collision studies. **New Journal of Physics**, 11(5):055031, 2009. 73

[93] B. C. Sawyer, B. K. Stuhl, B. L. Lev, J. Ye, and E. R. Hudson. Mitigation of loss within a molecular Stark decelerator. **European Physical Journal D**, 48(2):197–209, 2008. 73, 74, 77

[94] Sebastiaan Y. T. van de Meerakker, Nicolas Vanhaecke, Hendrick L. Bethlem, and Gerard Meijer. Higher-order resonances in a Stark decelerator. **Physical Review A**, 71(5):053409, 2005. 73, 76, 81

[95] Ludwig Scharfenberg, Henrik Haak, Gerard Meijer, and Sebastiaan Y. T. van de Meerakker. Operation of a Stark decelerator with optimum acceptance. **Physical Review A**, 79(2): 023410, 2009. 73, 87

[96] Dongdong Zhang, Gerard Meijer, and Nicolas Vanhaecke. Advanced switching schemes in a Stark decelerator. **Physical Review A**, 93(2):023408, 2016. 73, 84

[97] Shunyong Hou, Shengqiang Li, Lianzhong Deng, and Jianping Yin. Dependences of slowing results on both decelerator parameters and the new operating mode: taking ND 3 molecules as an example. **Journal of Physics B: Atomic, Molecular and Optical Physics**, 46 (4):045301, 2013. 73

[98] Andreas Osterwalder, Samuel A. Meek, Georg Hammer, Henrik Haak, and Gerard Meijer. Deceleration of neutral molecules in macroscopic traveling traps. **Physical Review A**, 81 (5):051401, 2010. 73, 77, 84

[99] J.E. van den Berg, S.C. Mathavan, C. Meinema, J. Nauta, T.H. Nijbroek, K. Jungmann, H.L. Bethlem, and S. Hoekstra. Traveling-wave deceleration of SrF molecules. **Journal of Molecular Spectroscopy**, 300:22–25, 2014. 73

[100] M. I. Fabrikant, Tian Li, N. J. Fitch, N. Farrow, Jonathan D. Weinstein, and H. J. Lewandowski. Method for traveling-wave deceleration of buffer-gas beams of CH. **Physical Review A**, 90(3):033418, 2014. 73

[101] Marina Quintero-Pérez, Paul Jansen, Thomas E. Wall, Joost E. van den Berg, Steven Hoekstra, and Hendrick L. Bethlem. Static Trapping of Polar Molecules in a Traveling Wave Decelerator. **Physical Review Letters**, 110(13):133003, 2013. 73, 88

[102] Shunyong Hou, Qin Wang, Lianzhong Deng, and Jianping Yin. A switched ring Stark decelerator for both light and heavy polar molecules. **Journal of Physics B: Atomic, Molecular and Optical Physics**, 49(6):065301, 2016. 73

[103] Yomay Shyur, Jason A. Bossert, and H. J. Lewandowski. Pulsed operation of a ring Stark decelerator. **Journal of Physics B: Atomic, Molecular and Optical Physics**, 51(16): 165101, 2018. 73

[104] Qin Wang, Shunyong Hou, Liang Xu, and Jianping Yin. Slowing and cooling of heavy or light (even with a tiny electric dipole moment) polar molecules using a novel, versatile electrostatic Stark decelerator. **Physical Chemistry Chemical Physics**, 18(7):5432–5443, 2016. 73, 77

[105] Edvardas Narevicius, Adam Libson, Christian G. Parthey, Isaac Chavez, Julia Narevicius, Uzi Even, and Mark G. Raizen. Stopping Supersonic Beams with a Series of Pulsed Electromagnetic Coils: An Atomic Coilgun. **Physical Review Letters**, 100(9):093003, 2008. 77, 84, 127

[106] Vikram Plomp, Zhi Gao, Theo Cremers, and Sebastiaan Y T van de Meerakker. Multistage Zeeman deceleration of NH X $^3\Sigma^-$ radicals. **Physical Review A**, 99(3):33417, 2019. 77

[107] R Golub. **On Decelerating Molecules**. Doctor of philosophy, Massachusetts Institute of Technology, 1967. 77

[108] Sebastiaan Y. T. van de Meerakker. **Deceleration and Electrostatic Trapping of OH Radicals**. Doctor of philosophy, Radboud University at Nijmegen, 2006. 78, 150

[109] Michael A Weibel, Toby D Hain, and Thomas J Curtiss. Hexapole-selected supersonic beams of reactive radicals: CF3, SiF3, SH, CH, and C2H. **The Journal of Chemical Physics**, 108(8):3134–3141, 1998. 78

[110] Hendrick L. Bethlem, Giel Berden, André J. A. van Roij, Floris M. H. Crompvoets, and Gerard Meijer. Trapping Neutral Molecules in a Traveling Potential Well. **Physical Review Letters**, 84(25):5744–5747, 2000. 84

[111] Eric R. Hudson, J. R. Bochinski, H. J. Lewandowski, Brian C. Sawyer, and Jun Ye. Efficient Stark deceleration of cold polar molecules. **The European Physical Journal D**, 31(2): 351–358, 2004. 84

[112] E. L. Surkov, J. T. M. Walraven, and G. V. Shlyapnikov. Collisionless motion and evaporative cooling of atoms in magnetic traps. **Physical Review A**, 53(5):3403–3408, 1996. 84

[113] Sebastiaan Y. T. van de Meerakker, Paul H M Smeets, Nicolas Vanhaecke, Rienk T. Jongma, and Gerard Meijer. Deceleration and Electrostatic Trapping of OH Radicals. **Physical Review Letters**, 94(2):023004, 2005. 87

[114] Benjamin K. Stuhl, Mark Yeo, Brian C. Sawyer, Matthew T. Hummon, and Jun Ye. Microwave state transfer and adiabatic dynamics of magnetically trapped polar molecules. **Physical Review A**, 85(3):033427, 2012. 88, 105, 106, 112, 113, 128, 129, 131, 137, 155, 173

[115] Samuel A. Meek, Gabriele Santambrogio, Boris G. Sartakov, Horst Conrad, and Gerard Meijer. Suppression of nonadiabatic losses of molecules from chip-based microtraps. **Physical Review A**, 83(3):033413, 2011. 91, 136

[116] T. E. Wall, S. K. Tokunaga, E. a. Hinds, and M. R. Tarbutt. Nonadiabatic transitions in a Stark decelerator. **Physical Review A**, 81(3):033414, 2010. 91, 136

[117] Ludwig Scharfenberg. **Crossed beam scattering with a Stark-decelerated molecular beam**. Doctor of philosophy, Technische Universität Berlin, 2012. 100

[118] W Steckelmacher. A review of the molecular flow conductance for systems of tubes and components and the measurement of pumping speed. **Vacuum**, 16(11):561–584, 1966. 104

[119] Jonathan D Weinstein, Robert DeCarvalho, Thierry Guillet, Bretislav Friedrich, and John M. Doyle. Magnetic trapping of calcium monohydride molecules at millikelvin temperatures. **Nature**, 395(6698):148–150, 1998. 105, 127

[120] Hendrick L Bethlem, Giel Berden, Floris M H Crompvoets, Rienk T Jongma, André J A van Roij, and Gerard Meijer. Electrostatic trapping of ammonia molecules. **Nature**, 406(6795): 491–494, 2000. 105

[121] Benjamin K. Stuhl, Mark Yeo, Matthew T. Hummon, and Jun Ye. Electric-field-induced inelastic collisions between magnetically trapped hydroxyl radicals. **Molecular Physics**, 111(12-13):1798–1804, 2013. 106, 123, 126, 128, 131, 132, 137, 160, 161, 165, 166

[122] J D Jackson. **Classical Electrodynamics**. John Wiley & Sons, 3 edition, 1999. 111

[123] J R Bochinski, Eric R Hudson, H J Lewandowski, Gerard Meijer, and Jun Ye. Phase Space Manipulation of Cold Free Radical OH Molecules. **Physical Review Letters**, 91(24):243001, 2003. 127, 132

[124] A.W. Wiederkehr, H. Schmutz, M. Motsch, and F. Merkt. Velocity-tunable slow beams of cold O 2 in a single spin-rovibronic state with full angular-momentum orientation by multistage Zeeman deceleration. **Molecular Physics**, 110(15-16):1807–1814, 2012. 127, 152

[125] S. Marx, D. Adu Smith, G. Insero, S. A. Meek, B. G. Sartakov, G. Meijer, and G. Santambrogio. Measuring and manipulating the temperature of cold molecules trapped on a chip. **Physical Review A**, 92(6):063408, 2015. 127, 152

[126] Alexander Prehn, Martin Ibrügger, Rosa Glöckner, Gerhard Rempe, and Martin Zeppenfeld. Optoelectrical Cooling of Polar Molecules to Submillikelvin Temperatures. **Physical Review Letters**, 116(6):063005, 2016. 127, 153

[127] Yang Liu, Manish Vashishta, Pavle Djuricanin, Sida Zhou, Wei Zhong, Tony Mittertreiner, David Carty, and Takamasa Momose. Magnetic Trapping of Cold Methyl Radicals. **Physical Review Letters**, 118(9):093201, 2017. 127

[128] Alexander von Zastrow, Jolijn Onvlee, Sjoerd N. Vogels, Gerrit C. Groenenboom, Ad van der Avoird, and Sebastiaan Y. T. van de Meerakker. State-resolved diffraction oscillations imaged for inelastic collisions of NO radicals with He, Ne and Ar. **Nature Chemistry**, 6(3):216–221, 2014. 127, 152

[129] Ayelet Klein, Yuval Shagam, Wojciech Skomorowski, Piotr S. Żuchowski, Mariusz Pawlak, Liesbeth M. C. Janssen, Nimrod Moiseyev, Sebastiaan Y. T. van de Meerakker, Ad van der Avoird, Christiane P. Koch, and Edvardas Narevicius. Directly probing anisotropy in atom–molecule collisions through quantum scattering resonances. **Nature Physics**, 13(1): 35–38, 2016. 127, 152

[130] Xing Wu, Thomas Gantner, Manuel Koller, Martin Zeppenfeld, Sotir Chervenkov, and Gerhard Rempe. A cryofuge for cold-collision experiments with slow polar molecules. **Science**, page 10.1126/science.aan3029, 2017. 127, 152, 153

[131] L. P. Parazzoli, N. J. Fitch, P. S. Żuchowski, J. M. Hutson, and H. J. Lewandowski. Large Effects of Electric Fields on Atom-Molecule Collisions at Millikelvin Temperatures. **Physical Review Letters**, 106(19):193201, 2011. 127

[132] Goulven Quéméner and John L. Bohn. Shielding $^2\Sigma$ ultracold dipolar molecular collisions with electric fields. **Physical Review A**, 93(1):012704, 2016. 127, 134

[133] Wolfgang Petrich, Michael H. Anderson, Jason R. Ensher, and Eric A. Cornell. Stable, Tightly Confining Magnetic Trap for Evaporative Cooling of Neutral Atoms. **Physical Review Letters**, 74(17):3352–3355, 1995. 127

[134] J. Riedel, S. Hoekstra, W. Jäger, J. J. Gilijamse, S. Y T Van De Meerakker, and G. Meijer. Accumulation of Stark-decelerated NH molecules in a magnetic trap. **European Physical Journal D**, 65(1-2):161–166, 2011. 127

[135] Marina Quintero-Pérez, Thomas E. Wall, Steven Hoekstra, and Hendrick L. Bethlem. Preparation of an ultra-cold sample of ammonia molecules for precision measurements. **Journal of Molecular Spectroscopy**, 300:112–115, 2014. 127

[136] Nitzan Akerman, Michael Karpov, Yair Segev, Natan Bibelnik, Julia Narevicius, and Edvardas Narevicius. Trapping of Molecular Oxygen together with Lithium Atoms. **Physical Review Letters**, 119(7):073204, 2017. 127

[137] Manuel Lara, Benjamin L. Lev, and John L. Bohn. Loss of molecules in magneto-electrostatic traps due to nonadiabatic transitions. **Physical Review A**, 78(3):033433, 2008. 128

[138] John L Bohn and Goulven Quéméner. Dipolar radicals in crossed electric and magnetic fields. **Molecular Physics**, 111(12-13):1931–1938, 2013. 128, 134

[139] M A Player and P G H Sandars. An experiment to search for an electric dipole moment in the 3P2 metastable state of xenon. **Journal of Physics B: Atomic and Molecular Physics**, 3(12):1620–1635, 1970. 130

[140] J. J. Hudson, B. E. Sauer, M. R. Tarbutt, and E. A. Hinds. Measurement of the Electron Electric Dipole Moment Using YbF Molecules. **Physical Review Letters**, 89(2):023003, 2002. 130

[141] Rosario González-Férez, Manuel Iñarrea, J. Pablo Salas, and Peter Schmelcher. Nonlinear dynamics of atoms in a crossed optical dipole trap. **Physical Review E**, 90(6):062919, 2014. 136, 140, 142

[142] H Scott Dumas. **The KAM Story**. World Scientific, 2014. 139

[143] Alan Wolf, Jack B Swift, Harry L Swinney, and John A Vastano. Determining Lyapunov exponents from a time series. **Physica D: Nonlinear Phenomena**, 16(3):285–317, 1985. 140

[144] Roberto Barrio. Painting Chaos: A Gallery of Sensitivity Plots of Classical Problems. **International Journal of Bifurcation and Chaos**, 16(10):2777–2798, 2006. 140

[145] David Reens. Water Pressure Boosting System, 2017. 144

[146] F H O'Shea, G Marcus, J B Rosenzweig, M Scheer, J Bahrdt, R Weingartner, A Gaupp, and F Grüner. Short period, high field cryogenic undulator for extreme performance x-ray free electron lasers. **Phys. Rev. ST Accel. Beams**, 13(7):70702, 2010. 144

[147] John Rumble. **CRC handbook of chemistry and physics**. CRC press, 2017. 146

[148] Steven Hoekstra, Joop J. Gilijamse, Boris Sartakov, Nicolas Vanhaecke, Ludwig Scharfenberg, Sebastiaan Y T Van De Meerakker, and Gerard Meijer. Optical pumping of trapped neutral molecules by blackbody radiation. **Physical Review Letters**, 98(13):1–4, 2007. 148, 160

[149] M. Motsch, L. D. van Buuren, C. Sommer, M. Zeppenfeld, G. Rempe, and P. W. H. Pinkse. Cold guided beams of water isotopologs. **Physical Review A**, 79(1):013405, 2009. 150

[150] Jacqueline van Veldhoven, Hendrick L Bethlem, Melanie Schnell, and Gerard Meijer. Versatile electrostatic trap. **Phys. Rev. A**, 73(6):63408, 2006. 151

[151] James Greenberg, Philipp C Schmid, Mikhail Miller, John F Stanton, and H J Lewandowski. Quantum-state-controlled reactions between molecular radicals and ions. **Phys. Rev. A**, 98(3):32702, 2018. 152

[152] William E Perreault, Nandini Mukherjee, and Richard N Zare. Quantum control of molecular collisions at 1 kelvin. **Science**, 358(6361):356–359, 2017. 152

[153] Yair Segev, Martin Pitzer, Michael Karpov, Nitzan Akerman, Julia Narevicius, and Edvardas Narevicius. Collisions between cold molecules in a superconducting magnetic trap. **arXiv preprint**, (1902.04549), 2019. 152

[154] Juliana Park, Hyungmok Son, Jiangtian Yao, Martin Zwierlein, Alan Jamison, and Wolfgang Ketterle. Collisional Dynamics of NaLi Molecules in the Triplet Ground State, 2019. 153

[155] David M Pozar. **Microwave engineering**. John Wiley & Sons, 4 edition, 2009. 155

[156] G. A. Bird. Transition regime behavior of supersonic beam skimmers. **Physics of Fluids**, 19(10):1486, 1976. 163

[157] O. Luiten, M. Reynolds, and J. Walraven. Kinetic theory of the evaporative cooling of a trapped gas. **Physical Review A**, 53(1):381–389, 1996. 172

[158] John M Gray, Jason A Bossert, Yomay Shyur, and H J Lewandowski. Measurements of trap dynamics of cold OH molecules using resonance-enhanced multiphoton ionization. **Phys. Rev. A**, 96(2):23416, 2017. 176